UNIVERSITY OF SÃO PAULO
SÃO CARLOS SCHOOL OF ENGINEERING
DEPARTMENT OF STRUCTURAL ENGINEERING

HEIDER DE CASTRO E ANDRADE

Enriched formulations based on the Boundary Element Method for fracture analysis of homogeneous domains and bimaterial interfaces

Formulações enriquecidas baseadas no Método dos Elementos de Contorno para a análise de fratura em domínios homogêneos e interfaces de bimateriais

São Carlos - SP
2021

HEIDER DE CASTRO E ANDRADE

Enriched formulations based on the Boundary Element Method for fracture analysis of homogeneous domains and bimaterial interfaces

Corrected version
(Original version is available at São Carlos School of Engineering)

PhD Thesis presented to the Graduate Program in Structural Engineering at the São Carlos School of Engineering, University of São Paulo, Brazil to obtain the degree of Doctor of Science.

Concentration area: Structures

Advisor: Prof. Edson Denner Leonel

São Carlos - SP
2021

Ficha catalográfica elaborada pela Biblioteca Prof. Dr. Sérgio Rodrigues Fontes da EESC/USP com os dados inseridos pelo(a) autor(a).

AA553e

Andrade, Heider
Enriched formulations based on the Boundary Element Method for fracture analysis of homogeneous domains and bimaterial interfaces / Heider Andrade; orientador Edson Leonel. São Carlos, 2021.

Tese (Doutorado) - Programa de Pós-Graduação em Engenharia Civil (Engenharia de Estruturas) e Área de Concentração em Estruturas -- Escola de Engenharia de São Carlos da Universidade de São Paulo, 2021.

1. Boundary element method. 2. Enriched formulations. 3. Isogeometric analysis. 4. Discontinuous NURBS. 5. Crack growth. 6. Interface cracks. I. Título.

Eduardo Graziosi Silva - CRB - 8/8907

FOLHA DE JULGAMENTO

Candidato: Engenheiro **HEIDER DE CASTRO E ANDRADE.**

Título da tese: " Formulações enriquecidas baseadas no método dos elementos de contorno para a análise de fratura de domínios homogêneos e interfaces bimateriais".

Data da defesa: 29/03/2021.

Comissão Julgadora	**Resultado**
Prof. Associado **Edson Denner Leonel (Orientador)** (Escola de Engenharia de São Carlos – EESC/USP)	**Aprovado**
Prof. Dr. **Leandro Palermo Junior** (Universidade Estadual de Campinas/UNICAMP)	**Aprovado**
Prof. Dr. **Gabriel Hattori da Silva** (Cambridge University)	**Aprovado**
Prof. Dr. **Rodolfo André Kuche Sanches** (Escola de Engenharia de São Carlos – EESC/USP)	**Aprovado**
Prof. Dr. **Gilberto Gomes** (Universidade de Brasília/UnB)	**Aprovado**

Coordenador do Programa de Pós-Graduação em Engenharia Civil (Engenharia de Estruturas):
Prof. Associado **Vladimir Guilherme Haach**
Presidente da Comissão de Pós-Graduação:
Prof. Titular **Murilo Araujo Romero**

Acknowledgements

The following research project would not be possible without the sponsorship from the São Paulo State Foundation for Research (FAPESP), grants #2016/23649-0 and #2019/03340-3, and their support is greatly appreciated. This study was also financed in part by the Coordenação de Aperfeiçoamento de Pessoal de Nível Superior - Brasil (CAPES) - Finance Code 001.

I am also immensely grateful to my family for their unconditional support and incentive over the course of these intense years. Special thanks go to my lovely wife Yara, who has been by my side at all times, being my fortress and my guiding light.

I also gratefully acknowledge Prof. Edson Leonel for the supervision, partnership and friendship built over these years. Special thanks are extended to Prof. Jon Trevelyan at Durham University, whose valuable guidance and assistance were essential for the developments of this thesis.

I would also like to thank all my friends from São Carlos for the enjoyable times spent together, particularly during the daily *cafezinho*, and for all the fruitful insights.

Last but not least, I acknowledge the staff at the Department of Structural Engineering (SET) and at Durham University for their support, cordiality and solicitude throughout my doctoral years.

Abstract

ANDRADE, H. C. **Enriched formulations based on the Boundary Element Method for fracture analysis of homogeneous domains and bimaterial interfaces**. 2021. 219p. Thesis (Doctorate) - São Carlos School of Engineering at the University of São Paulo, São Carlos, 2021.

The main objective of this doctoral thesis is the development of enriched numerical formulations based on the Boundary Element Method (BEM) for the fracture analysis of homogeneous materials and the investigation of cracks lying on bimaterial interfaces. Initially, an eXtended Boundary Element Method (XBEM) formulation is proposed for simulating the linear elastic crack growth in isotropic and anisotropic domains. A displacement approximation enrichment based on the first-order asymptotic expansions is used to represent the near-tip square root behaviour predicted by the linear elastic fracture mechanics. This strategy also enables the direct evaluation of the Stress Intensity Factors (SIFs) after a crack tip tying constraint is enforced at the crack tip to accommodate the additional enrichment parameters. Additionally, discontinuous functions are embedded into the displacement approximation of elements intercepted by cracks to avoid remeshing of these elements. For the discontinuous enrichment, new equations are provided by imposing displacement continuity conditions at the crack mouth. Shifted enrichment functions are used to preserve the physical meaning of the nodal parameters and reduce the singularity order of the integral kernels containing the enrichment terms in the XBEM formulation. Furthermore, an enriched traction approximation is proposed to apply concentrated forces and support points along the boundary.

Then, a new extended isogeometric boundary element method (XIGABEM) is developed for simulating multiple fatigue crack propagation in two-dimensional domains. The classical use of NURBS in isogeometric formulations is further extended by repeated knot insertion to introduce C^{-1} continuity within the approximation space as an elegant approach to representing geometrical discontinuities where cracks intersect other boundaries. This strategy is also used to restrict the enrichment term to portions of the NURBS defining the crack tip, where it is necessary. At this near-tip zone, the linear elastic fracture mechanics solutions are embedded into the displacement approximation to represent the theoretical square root behaviour. Like in the XBEM approach, the enrichment procedure introduces just two degrees of freedom per crack tip, and a crack tip tying constraint is used to yield a square linear system. This scheme also allows the SIFs to be computed directly since they appear in the solution vector.

Finally, an XIGABEM approach is introduced for the analysis of interface cracks. Considering the two-term asymptotic expansion to define the enrichment functions, the SIFs and T-stress are recovered directly from the system of equations provided by the

numerical method. For this purpose, the same tying constraint adopted in the previous enriched formulations is used to accommodate the SIFs, while a new relationship based on the NURBS derivatives at the tip is defined to solve for the T-stress parameter. The XIGABEM is also successfully applied for the direct evaluation of the tip parameters for curved cracks.

Several examples are presented to illustrate the application of the enriched direct methods for evaluating the crack parameters and for modelling the crack propagation. The accuracy of the results compares favourably against those from the literature and also against solutions obtained from unenriched and enriched indirect methods that employ the J-integral for SIF extraction.

Keywords: Boundary element method. Enriched formulations. Isogeometric analysis. Discontinuous NURBS. Crack growth. Interface cracks.

Resumo

ANDRADE, H. C. **Formulações enriquecidas baseadas no Método dos Elementos de Contorno para a análise de fratura em domínios homogêneos e interfaces de bimateriais**. 2021. 219p. Tese (Doutorado) - Escola de Engenharia de São Carlos, Universidade de São Paulo, São Carlos, 2021.

O objetivo principal desta tese de doutorado é o desenvolvimento de formulações numéricas enriquecidas baseadas no método dos elementos de contorno (MEC) para a análise de fratura em materiais homogêneos e investigação de trincas em interfaces de bimateriais. Inicialmente, uma formulação estendida do MEC (XBEM) é proposta para simular o crescimento de trincas em regime elástico-linear em domínios isotrópicos e anisotrópicos. Um enriquecimento para a aproximação de deslocamento baseado nas expansões de primeira ordem é usado para representar o comportamento próximo da ponta previsto pela mecânica da fratura elástico-linear. Essa estratégia também permite a avaliação direta dos Fatores de Intensidade de Tensão (FITs) após a aplicação de uma restrição de amarração na ponta para acomodar os parâmetros adicionais de enriquecimento. Além disso, funções descontínuas são incorporadas à aproximação de deslocamento de elementos interceptados por trincas para evitar o remalhamento desses elementos. Para o enriquecimento descontínuo, novas equações são obtidas pela imposição de condições de continuidade de deslocamento no ponto de interseção. Funções de enriquecimento *shifted* são utilizadas para preservar o significado físico dos parâmetros nodais e reduzir a ordem de singularidade dos núcleos integrais contendo os termos de enriquecimento. Ademais, uma aproximação enriquecida de força de superfície é proposta para aplicar forças concentradas e pontos de apoio ao longo do contorno.

Em seguida, é desenvolvido um novo método dos elementos de contorno isogeométrico estendido (XIGABEM) para simular a propagação de múltiplas trincas por fadiga em domínios bidimensionais. O uso clássico das NURBS em formulações isogeométricas é ampliado pela inserção sucessiva de *knots* para introduzir a continuidade C^{-1} dentro do espaço de aproximação, sendo uma elegante abordagem para representar descontinuidades geométricas onde as trincas interceptam o contorno. Essa estratégia também é utilizada para restringir o termo enriquecimento a porções das NURBS que definem a ponta da trinca, onde ele é necessário. Nessa zona próxima à ponta, as soluções da mecânica de fratura elástico-linear são incorporadas à aproximação de deslocamento para representar o comportamento analítico. Como na abordagem XBEM, a estratégia de enriquecimento introduz apenas dois graus de liberdade por ponta de trinca e uma restrição de amarração da ponta é utilizada para produzir um sistema linear quadrado. Esse esquema também permite que os FITs sejam calculados diretamente, uma vez que eles aparecem no vetor de solução.

Finalmente, uma abordagem XIGABEM é introduzida para a análise de trincas de interface. Considerando os dois primeiros termos da expansão assintótica para definir as funções de enriquecimento, os FITs e a tensão T são recuperados diretamente do sistema de equações fornecido pelo método numérico. Para este fim, a mesma restrição de amarração adotada nas formulações enriquecidas anteriores é usada para acomodar os FITs, enquanto uma nova relação baseada nas derivadas das NURBS avaliadas na ponta é definida para obter para o parâmetro da tensão T. O XIGABEM também é aplicado com sucesso para a avaliação direta dos parâmetros da ponta para trincas curvas.

Diversos exemplos são apresentados para ilustrar a aplicação dos métodos enriquecidos diretos na determinação dos parâmetros de trinca e na modelagem de propagação. A precisão dos resultados se compara de forma satisfatória às respostas da literatura e também às soluções obtidas a partir de métodos enriquecidos e não enriquecidos indiretos que empregam a integral J para a extração dos FITs.

Palavras-chave: Método dos elementos de contorno. Formulações enriquecidas. Análise isogeométrica. NURBS descontínuas. Propagação de trincas. Trincas de interface.

List of Figures

List of Tables

Nomenclature

Symbols

$\bar{P}_i^{e\lambda a}$	Element integral of enriched P_{ij}^* kernel (Second enrichment term)
$\bar{u}_j^{\bar{e}}$	Prescribed displacements
Δa	Crack length increment
ΔK_{ef}	Range of effective stress intensity factors
$\hat{P}_{ij}^{\bar{e}l}$	Element integral of enriched P_{ij}^* kernel (Discontinuous enrichment)
$\hat{S}_{kij}^{\bar{e}l}$	Element integral of enriched S_{kij}^* kernel (Discontinuous enrichment)
$\Im$	Imaginary part operator
$\mathbf{I}$	Identity matrix
$\mathbf{x}$	Field point
$\mathbf{x}^\lambda$	Crack tip position
$\mathbf{x}'$	Source point
$\mathbf{x}_F^{\bar{e}}$	Point of application of a concetrated force
$\mathfrak{i}$	Imaginary unit $\left(=\sqrt{-1}\right)$
$\mathfrak{K}_n$	N-th crack parameter
$\Re$	Real part operator
$\tilde{K}_M^\lambda$	Crack tip enrichment parameters
$\tilde{P}_{iM}^{e\lambda a}$	Element integral of enriched P_{ij}^* kernel (First enrichment term)
$\tilde{P}_{iM}^{e\lambda}$	Element integral of enriched P_{ij}^* kernel (Tip enrichment)
$\tilde{p}_j^e$	Traction approximation over an element
$\tilde{S}_{ijM}^{e\lambda}$	Element integral of enriched S_{kij}^* kernel (Tip enrichment)
$\tilde{U}_{iM}^{e\lambda I}$	Element integral of enriched U_{ij}^* kernel (First enrichment term)
$\tilde{u}_j^e$	Displacement approximation over an element

$\tilde{x}_j^e$	Coordinate approximation over an element
a	Crack length
a_{ijkl}	Elastic stiffness tensor
b_i	Body-force components
C, m	Paris law coefficients
c_{ijkl}	Elastic compliance tensor
c_{ij}	Jump term
C_s	T-stress coefficient
d_i^{em}	Control displacement parameter
D_{kij}^*	Fundamental solution obtained from the U_{ij}^* derivatives
D_{kij}^{em}	Element integral of D_{kij}^* kernel
E	Young's modulus
e_i	Components of a unit vector
$F_j^{\bar{e}}$	Force components
G	Total energy release rate
g^l	Auxiliary discontinuous function
H	Heaviside sign step function
H_i	Anisotropic trigonometric functions
J	J-integral value
J^e	Jacobian of transformation
K_1	Mode 1 stress intensity factor for interface cracks
K_2	Mode 2 stress intensity factor for interface cracks
K_{eq}	Equivalent stress intensity factor
K_{Ic}	Fracture toughness
K_{II}	Mode II stress intensity factor

K_I	Mode I stress intensity factor
K_T	T-stress parameter
$M^{(1,2)}$	M-integral value
N	Total number of collocation points
n	Number of control points
N^{lc}	Number of load cycles
N_e	Total number of elements
n_e	Number of nodes of an element
N_e^{λ}	Number of elements enriched by tip λ
N_f	Number of concentrated force enrichments
N_h	Number of discontinuous enrichments
$N_{i,p}$	B-spline functions
n_j	Components of the outward unit normal vector
N_t	Number of crack tip enrichments
p	Order of the spline
P_{ij}^*	Traction fundamental solution
P_{ij}^{em}	Element integral of P_{ij}^* kernel
p_j	Traction components
p_j^{em}	Nodal traction parameter
r	Distance between the field point and the source point
$R_{i,p}$	NURBS basis functions
R_{jk}^{λ}	Components of the rotation matrix referred to tip λ
$R_j^{\bar{e}}$	Support reactions
S_{kij}^*	Fundamental solution obtained from the P_{ij}^* derivatives
S_{kij}^{em}	Element integral of S_{kij}^* kernel

T	T-stress (lower material)
t_i^{em}	Control traction parameter
U_{ij}^*	Displacement fundamental solution
U_{ij}^{em}	Element integral of U_{ij}^* kernel
u_j	Displacement components
u_j^{em}	Nodal displacement parameter
W	Strain energy density
w_i	Weights from a NURBS
x_j	Cartesian components
x_j^{em}	Nodal (or control point) coordinates

Greek Symbols

$\alpha_j^{\bar{e}l}$	Discontinuous enrichment parameter
β_{ij}	Anisotropic coefficients
χ	Load factor
χ_{ij}	Chentsov's coefficients
$\Delta(\mathbf{x}', \mathbf{x})$	Dirac delta function
δ_{ij}	Kronecker delta
Δ_j^n, Θ_j^n	Displacement functions for interface cracks
η_{ij}	Coefficients of mutual influence
Γ	Domain boundary
Γ_e	Element boundary
Γ_J	J-integral path
Γ_s^B	External boundary
Γ_s^C	Crack boundary
Γ_s^I	Interface boundary

$\hat{\xi}$	Parent space coordinate
κ	Kolosov constant
μ	Shear modulus
μ_i	Material complex parameters
ν	Poisson's ratio
Ω	Elastic domain
ω	Crack tip orientation
ϕ^{em}	Shape functions
ψ_{kM}	Displacement crack tip functions
ψ^C_{kM}	Displacement functions over crack surfaces (first term of expansion)
ψ^I_{kM}	Displacement functions over interface (first term of expansion)
ρ	Distance from the crack tip
$\sigma_{\theta\theta}$	Tangential stress component
σ_{ij}	Stress components
$\Sigma^n_{ij}, \Upsilon^n_{ij}$	Stress functions for interface cracks
θ	Orientation according to the crack tip
θ_p	Propagation direction
Υ	Weight vector
ε	Oscillatory parameter
ε_{ij}	Strain components
φ^C	Displacement functions over crack surfaces (second term of expansion)
φ^I	Displacement functions over interface (second term of expansion)
ϖ^I_{kM}	Traction functions over interface (first term of expansion)
Ξ	Knot vector
ξ	Parametric coordinate / Knot

ξ'	Parametric coordinate at the collocation point
ξ^m	Parametric coordinate at the m-th node

Abbreviations

ACA	Adaptative cross approximation
BEM	Boundary element method
CAD	Computer-aided design
CMOD	Crack mouth opening displacement
CSTDB	Cracked straight-through Brazilian disc
DBEM	Dual boundary element method
DBIE	Displacement boundary integral equation
DOF	Degrees of freedom
EFG	Element-free galerkin
FEM	Finite element method
FMM	Fast multipole method
GFEM	Generalised finite element method
IGA	Isogeometric analysis
IGABEM	Isogeometric boundary element method
ILMF	Integrated local mesh free
LEFM	Linear elastic fracture mechanics
NNRPIM	Natural neighbor radial point interpolation method
NURBS	Non-uniform rational basis spline
PU	Partition of unity
SBFEM	Scaled boundary finite element method
SIF	Stress intensity factor
TBIE	Traction boundary integral equation

XBEM	Extended boundary element method
XFEM	Extended finite element method
XIGABEM	Extended isogeometric boundary element method
xSBFEM	Extended scaled boundary finite element method

Contents

1 Introduction

The development of reliable models for the analysis of engineering problems and the collapse prediction of deformable bodies is a major research area within the international scientific community. In particular, the search for robust methodologies is stimulated by the increasingly complex structures used in industries such as the mechanical, naval, aerospace and automotive, in which both high mechanical performance and low weight are desired. Therefore, the proposition of accurate models for failure prediction is crucial to obtain safer structures and belongs to the scope of the present investigation.

Among the usual failure mechanisms of the solids is the fracture phenomenon. The materials contain inherent flaws throughout their microstructure that, when loaded, may grow and form cracks, which leads to material degradation. The fracture mechanics, in particular, is a field of study that describes the mechanical behaviour of deformable bodies containing material discontinuities. Moreover, this field provides a set of appropriate theories that allow the consistent analysis of the crack growth process when a cracked body is loaded.

Since the seminal work of Griffith (GRIFFITH, 1921) and the rapid development of the area during the 1960s and 1970s, the fracture mechanics became one of the main tools to access material failure. One of the principal branches of this theory is the linear elastic fracture mechanics (LEFM), in which the material is admitted with linear elastic behaviour. The LEFM formulation is applicable when the fracture process zone positioned in front of the crack tip is small compared to the crack dimensions, such as in brittle materials. Besides, this formulation provides a fundamental basis for high-cycle fatigue analyses and non-linear fracture approaches. According to the LEFM, the singular stress state occurring near the crack tips is governed by the stress intensity factors (SIFs), which can thus be used to verify the crack tip stability. Several existing books (ROOKE; CARTWRIGHT, 1976; MURAKAMI et al., 1987; TADA; PARIS; IRWIN, 2000) include a compendium for the SIFs and the stress and displacement components at the region near the crack tip. However, these closed-form solutions are restricted to a limited number of problems, with simplified geometry, boundary conditions and constitutive material relations. Consequently, the response to complex applications involving cracked bodies can only be achieved by numerical techniques.

The finite element method (FEM), in particular, has been widely applied to simulate fracture problems due to its facility of implementation and popularity in the scientific community. Applications of FEM to simulate crack propagation can be found in (BITTENCOURT et al., 1996; BOUCHARD; BAY; CHASTEL, 2003; AZADI; KHOEI, 2010). Moreover, several computer programs based on FEM have been developed to analyse this

kind of problem, e.g. Franc2D (WAWRZYNEK; INGRAFFEA, 1994). As a consequence of the existing domain mesh in FEM, some difficulties emerge from the remeshing process when crack propagation is addressed. Furthermore, the approximation of the mechanical fields throughout the domain introduces inaccuracies in the responses for singular regions near the crack tips.

A suitable alternative for modelling cracked bodies is the Boundary Element Method (BEM). Straightforward application of the BEM in fracture problems presents some difficulties since the existence of coincident source points on overlapping crack surfaces leads to degeneracy in the algebraic system of equations (CRUSE, 1972). Some strategies have been developed to overcome this issue, such as the use of especial fundamental solutions (Green's functions) containing the effect of cracks (SNYDER; CRUSE, 1975), or the multi-domain technique (BLANDFORD; INGRAFFEA; LIGGETT, 1981), which introduces artificial boundaries to model the crack surfaces and the eventual crack propagation path. However, these strategies also face some challenges for fracture modelling, particularly when dealing with multiple cracks or considering crack growth.

The most successful BEM approach for dealing with fracture problems is based on the dual formulation developed by Portela, Aliabadi, and Rooke (1992) and is denoted as Dual Boundary Element Method (DBEM). In this method, two independent boundary integral equations are separately applied for the source points on each crack surface, which results in a non-singular system of equations. In DBEM, only the boundary of the analysed body is discretised, and this mesh dimensionality reduction facilitates the meshing process during crack growth. The absence of a domain mesh also allows the accurate description of the internal mechanical fields, even for the singular zones surrounding the tips. These features make the DBEM an efficient numerical approach for simulating several fracture problems, including linear-elastic (PORTELA; ALIABADI; ROOKE, 1992; MI; ALIABADI, 1992), non-linear (SALEH; ALIABADI, 1995), dynamic (FEDELINSKI; ALIABADI; ROOKE, 1993; ALBUQUERQUE; SOLLERO; ALIABADI, 2004), contact (LEITÃO; ALIABADI; ROOKE, 1995; LEONEL; VENTURINI, 2011), thermoelastic (PASTERNAK, 2012; PRASAD; ALIABADI; ROOKE, 1994) and multiple crack propagation (CARPINTERI; MONETTO, 1999; LEONEL; VENTURINI, 2010; PRICE; TREVELYAN, 2014). To reduce the computational cost of the BEM in large-scale problems, particularly those involving 3D applications in which the processing time may be prohibitive, acceleration techniques can be used, such as the Fast Multipole Method (FMM) (NISHIMURA; YOSHIDA; KOBAYASHI, 1999; LIU, 2009; LIU; LI; XIE, 2017) and the Adaptative Cross Approximation (ACA) (BENEDETTI; ALIABADI; DAVÌ, 2008; BENEDETTI; MILAZZO; ALIABADI, 2009; BENEDETTI; ALIABADI, 2010).

In conventional formulations of FEM and BEM, piecewise Lagrange polynomials are used to interpolate both the unknown quantities and geometry over discrete elements.

This strategy is widely known as the isoparametric approach. However, errors may be introduced in the analysis if the physical fields show a highly non-polynomial behaviour at the element's domain, such as near crack tips. Consequently, the accuracy of the responses for the Stress Intensity Factors (SIFs) may be compromised since they depend on the mechanical response at these singular regions. Since the SIFs play a major role in verifying the crack stability considering the LEFM, the development of numerical models that mitigate approximation errors is crucial for the fracture analysis.

Several strategies have been proposed over the years to overcome the deficiency in describing unknown quantities, among which the enriched formulations stand out. This approach consists of augmenting the conventional polynomial approximation with additional functions based on a priori knowledge about the solution space. Early enrichment strategies to incorporate singular properties within the finite element formulation are found in Tracey (1971), Fix, Gulati, and Wakoff (1973) and Benzley (1974). In particular, the latter used this approach for crack problems to compute the SIFs directly as part of the solution of the system of linear equations, without the need for a post-processing stage. In these early enrichment strategies, the enrichment functions have global support; consequently, the finite element stiffness matrix loses its local structure (BABUŠKA; BANERJEE, 2012).

Over the past two decades, the concept of the partition of unity (PU) method (MELENK; BABUSKA, 1996; BABUSKA; MELENK, 1997) has been established within the FEM framework. Using the PU enrichment, Belytschko and Black (1999) obtained accurate responses for the elastic fields at the vicinity of the crack tips with coarse discretisation, while Moës, Dolbow, and Belytschko (1999) modelled the displacement discontinuity over the crack faces without the need of a conforming finite element mesh. This numerical strategy is known as the eXtended Finite Element Method (XFEM) and is widely applied to several fracture problems (BUDYN et al., 2004; ASADPOURE; MOHAMMADI, 2007; YU; WU; GUO, et al., 2009; KUMAR; SINGH; MISHRA, 2015; KHOEI; VAHAB; HIRMAND, 2018). Nevertheless, the large amount of degrees of freedom (DOF) introduced by the enrichment degrades the conditioning of the system of equation. Besides, the existence of blending elements decreases the convergence rate of the method. Several strategies can be adopted to overcome these drawbacks as, e.g., the use of pre-conditioners (BÉCHET et al., 2005; MENK; BORDAS, 2010) and the application of special types of enrichment functions to the blending elements (CHESSA; WANG; BELYTSCHKO, 2003; LEGAY; WANG; BELYTSCHKO, 2005; FRIES, 2008; GRACIE; WANG; BELYTSCHKO, 2008). Conditioning issues for 3D crack problems have also been treated in (AGATHOS et al., 2015, 2017; AGATHOS; CHATZI; BORDAS, 2016, 2018; AGATHOS; BORDAS; CHATZI, 2019; TIAN; WEN; WANG, 2019), and many error estimation approaches have been proposed to improve the accuracy of XFEM (BORDAS; DUFLOT; LE, 2007; DUFLOT; BORDAS, 2008; RÓDENAS et al., 2010; CHEN et

al., 2012; LOEHNERT; PRANGE; WRIGGERS, 2012; PRANGE; LOEHNERT; WRIGGERS, 2012; LINS et al., 2015; JIN et al., 2017; PENG et al., 2017).

Since the pioneer works of Belytschko et al. (1996) and Fleming et al. (1997), the PU-based enrichment functions have also been adopted within meshfree methods to solve fracture mechanics problems (VENTURA; XU; BELYTSCHKO, 2002; DUFLOT; NGUYEN-DANG, 2004; RABCZUK; BELYTSCHKO, 2004; LI; LI; CHENG, 2005; ZHUANG; AUGARDE; MATHISEN, 2012; KHOSRAVIFARD et al., 2017; FALLAH; NIKRAFTAR, 2018), including three-dimensional analyses (RABCZUK; BORDAS; ZI, 2007; BORDAS; RABCZUK; ZI, 2008; RABCZUK et al., 2010). In these methods, the approximation is constructed from nodes only and does not rely on a structured mesh as the mesh-based XFEM. This feature also eliminates the difficulties arising from the mesh generation, especially when considering crack growth. Concerning a meshless boundary integral formulation, Liew, Cheng, and Kitipornchai (2007) proposed an enriched approach for two-dimensional fracture problems.

Despite the developments regarding other numerical techniques, the use of the PU concept in BEM is still incipient. Early applications of this formulation can be traced back to a series of papers in the early 2000s (PERREY-DEBAIN; TREVELYAN; BETTESS, 2002, 2003a,b; PERREY-DEBAIN et al., 2004), which were focused on Helmholtz problems and elastic waves. Later, the accuracy of the numerical integration of oscillatory functions (HONNOR; TREVELYAN; HUYBRECHS, 2010) and the definition of an adaptative enrichment strategy based on an error indicator (TREVELYAN; COATES, 2010) were also investigated. Regarding fracture problems, Simpson and Trevelyan (2011a) proposed an enriched formulation of BEM to improve the accuracy of the computed SIFs. In their work, the standard approximation space for the displacements was expanded by enrichment functions based on the PU and the LEFM formulation. Because of the similarities with XFEM, the method was termed the eXtended Boundary Element Method (XBEM). The large number of DOF introduced by the enriched formulation poses some drawbacks for this version of XBEM, such as ill-conditioning and the need for additional collocation points to yield a square system of equations.

Noting that the additional DOF in the PU-based enrichment for XBEM are all proxies for the SIFs, an alternative was proposed by Simpson and Trevelyan (2011b), in which the displacement approximation was augmented similarly to the early work of Benzley (1974). In this strategy, the number of parameters introduced by the enrichment is limited to two per tip for planar problems. Besides, an independent boundary integral equation derived from the LEFM crack tip fields was used to solve for the new DOF. In this approach, the SIFs were obtained indirectly with the J-integral technique (RICE, 1968), which is computational costly in the BEM framework since the integral kernels related to the internal points defining the integration path must be evaluated.

Including a crack tip tying constraint in the XBEM approach, Alatawi and Trevelyan

(2015) were able to accommodate the additional degrees of freedom without additional collocation points and also showed how the SIFs could be obtained directly from the system of equations with sufficient accuracy. Later, Hattori, Alatawi, and Trevelyan (2016) extended this method for directly assessing the SIFs in anisotropic materials. The direct approach is particularly beneficial in boundary element formulations since indirect techniques that require the evaluation of internal fields, such as the J-integral, could be avoided. Notwithstanding this additional cost, the enrichment strategy can also be combined with post-processing techniques to markedly improve the accuracy of computed SIF values for cases in which highly accurate solutions are required. Despite the advantages of handling fracture problems, particularly when addressing crack growth in which the SIF evaluation is needed for each new configuration, the XBEM has not yet been used for crack propagation modelling, which will be a topic of investigation of this thesis.

The aforementioned enriched formulations aim to improve the physical fields approximation by the expansion of the solution space with special functions determined from a priori knowledge of the problem's behaviour. However, errors are also introduced into the analysis when polynomials shape functions are used to describe complex geometries. To overcome this deficiency, the same functions applied in computer-aided design (CAD) packages, such as the non-uniform rational B-splines (NURBS), can be used for an accurate geometry description. These functions can also be adopted into the unknown quantities approximation, giving rise to the isogeometric analysis (IGA). Since the seminal paper of Hughes, Cottrell, and Bazilevs (2005), the IGA concepts have been extensively embedded in different numerical methods for applications in several fields. One of the advantages of this approach over the conventional polynomial-based formulations is the remarkable reduction of effort for the mesh generation process since the discretisation is provided directly by the CAD model. This is particularly beneficial for industrial applications, in which the mesh generation can take up to 80% of overall analysis time (HUGHES; COTTRELL; BAZILEVS, 2005; BAZILEVS et al., 2010). Moreover, the basis functions adopted by IGA facilitate the refinement process using knot insertion or degree elevation without changing the geometry or its parametrisation.

Over the years, particular attention has been devoted to the application of the IGA in the finite element method (FEM) framework. Non-uniform rational B-splines (NURBS) have been widely applied in IGA-FEM approximations since they are standard technology in computational design (COTTRELL et al., 2006; CHO; HA, 2008; COTTRELL; HUGHES; BAZILEVS, 2009; BENSON et al., 2010; VERHOOSEL et al., 2010; TEMIZER; WRIGGERS; HUGHES, 2011; AKHRAS et al., 2017). Nonetheless, the use of NURBS exhibits some shortcomings in numerical modellings, such as the difficulties involved in local refinement and in obtaining geometries with no gaps and overlaps (*watertight*). Several alternatives to the NURBS have been adopted in the IGA-FEM context to overcome these deficiencies, such as T-splines (BAZILEVS et al., 2010), PHT-splines

(DENG et al., 2008) and LR-Splines (DOKKEN; LYCHE; PETTERSEN, 2013). Additionally, complex topologies have been efficiently modelled by multiply-connected NURBS using trimming techniques (KIM; SEO; YOUN, 2009, 2010; SCHMIDT; WÜCHNER; BLETZINGER, 2012). To facilitate the incorporation of NURBS and T-splines into existing FEM codes, the Bézier extraction process may be employed (BORDEN et al., 2010; SCOTT et al., 2011), in which the extracted Bézier elements are expressed using Bernstein polynomials and therefore resemble the standard polynomial approximation. However, the application of Bézier extraction comes at the cost of an increase in the number of degrees of freedom in the final system of equations.

Engineering components are commonly expressed in CAD systems in the form of surface models or boundary representations. Therefore, the coupling between IGA and domain-based methods, such as FEM, requires the definition of an additional parametrisation direction to define the domain discretisation, which can be a quite complex task (AKHRAS et al., 2017). Alternatively, boundary-based numerical techniques provide a more natural and direct link between CAD models and numerical analysis since both formulations deal with quantities solely on the boundary. Early application of IGA into BEM was made by Politis et al. (2009), in which an exterior planar Neumann problem was analysed. Later, Simpson et al. (2012; 2013) introduced the fundamentals and implementation aspects of IGA for elastostatic BEM. In these works, the term IGABEM was coined for the numerical approach. The use of the IGABEM has since expanded, and the method has been applied to several problems involving geomechanics (BEER; MARUSSIG; DUENSER, 2013; BEER; DUENSER, 2018), acoustics (SIMPSON et al., 2014; COOX et al., 2017; SUN et al., 2019), shape optimisation (LIAN; KERFRIDEN; BORDAS, 2017; SUN et al., 2018; OLIVEIRA; ANDRADE; LEONEL, 2020), potential flow (GONG; DONG; QIN, 2017; CAMPOS; ALBUQUERQUE; WROBEL, 2017), heat transfer (AN et al., 2018) and fracture (NGUYEN et al., 2016; PENG et al., 2017; CORDEIRO; LEONEL, 2018; SUN; DONG; YANG, 2019). Additionally, studies concerning the accurate evaluation of the singular and near-singular integrals arising in IGABEM can be found in (TAUS; RODIN; HUGHES, 2016; TAUS et al., 2019; GONG et al., 2019).

When dealing with linear-elastic crack problems, the IGA basis functions, as the Lagrange polynomials, are not themselves capable of accurately representing the mechanical behaviour in the singular zone near the crack tips. Then, an enriched strategy can also be applied in IGA to overcome this drawback. The development of numerical methods combining the benefits of extended and isogeometric analysis (XIGA) has received much attention, especially in the FEM framework (BENSON et al., 2010; LUYCKER et al., 2011; GHORASHI; VALIZADEH; MOHAMMADI, 2011; GHORASHI et al., 2015; NGUYEN et al., 2015; SINGH et al., 2017). Meanwhile, the use of XIGA in the BEM context - resulting in the XIGABEM, also denoted as XIBEM in the literature - is still incipient. The first applications of XIGABEM were reported by Peake, Trevelyan, and

Coates (2013, 2015), in which 2D and 3D Helmholtz problems were investigated. Concerning crack analysis, Peng et al. (2016) adopted a crack tip enrichment based on the PU similar to the XBEM approach used by Simpson and Trevelyan (2011a). As previously mentioned, some shortcomings of PU-based enrichments are the number of additional DOF and the ill-conditioning of the resulting system of equations. Also, new collocation points are required to retrieve a square system of equations, and the optimal location of these points is not clear. Therefore, a direct XIGABEM formulation based on the XBEM strategy used by Alatawi and Trevelyan (2015) and Hattori, Alatawi, and Trevelyan (2016) appears as an appealing alternative for the analysis of crack problems and will be considered in the developments of this thesis.

In the present investigation, the analysis of interface cracks is also considered. Applications of composite materials have been received increasing interest in several industries over the past years. Due to their practical importance, the verification of structural integrity in these types of materials involves the investigation of fracture and delamination processes that occur at the interface between dissimilar media. Considering the linear elastic fracture mechanics (LEFM), early studies on interface cracks revealed that the stress and displacement fields near the crack tip present an oscillatory behaviour (WILLIAMS, 1959; ENGLAND, 1965; ERDOGAN, 1965; RICE; SIH, 1965). As a result of this oscillatory nature, it was shown the existence of a zone of interpenetration in regions close to the tip. According to Banks-Sills (2018), this anomalous behaviour was responsible for a hiatus of more than a decade in research on the subject. Nevertheless, since the order of magnitude of the contact zone in practical applications is small in comparison to the crack length (COMNINOU, 1990), many investigations were later conducted considering the oscillatory characteristic of the near-tip fields (HUTCHINSON; MEAR; RICE, 1987; RICE, 1988; RICE; SUO; WANG, 1990; HUTCHINSON; SUO, 1991; BANKS-SILLS, 2018).

The interface integrity can be assessed through the complex stress intensity factor, which defines the singular term in the asymptotic stress expansion. Closed-form solutions for the SIFs of interface cracks are only available for a limit number of configurations and the solutions for complex applications can be determined only by numerical formulations. Examples of papers evaluating the SIFs with numerical methods can be found in Ryoji and Sang-Bong (1989), Sukumar et al. (2004) and Gu and Zhang (2020). Additionally, some effort has been made for the direct evaluation crack parameters in the context of the XFEM (LIU; XIAO; KARIHALOO, 2004; WANG et al., 2017) and scaled boundary finite element method (SBFEM) (SONG, 2005; NATARAJAN; SONG; BELOUETTAR, 2014). Furthermore, He et al. (1991) and Kang (1994) showed that the T-stress, which is related to the second term of the asymptotic expansion for elastic stress field, plays an important role in the stability of the crack path. Several approaches have been proposed to compute this parameter, in which interaction integrals have been mainly applied (KIM;

MOON; EARMME, 2001; MUTHU et al., 2016; SLADEK; SLADEK, 1997; YU; WU; LI, 2012). Here, an XIGABEM formulation is developed to directly evaluate not only the SIFs but also the T-stress parameter for interface cracks.

1.1 Objectives and novel aspects

The main objective of this thesis is the development of enriched formulations based on the boundary element method for the fracture and fatigue analyses of two-dimensional multi-cracked structural systems. Cracks on bimaterial interfaces are also investigated with the extended approach.

Initially, an XBEM formulation is developed to simulate the linear elastic crack growth in isotropic and anisotropic domains. The main features of the proposed method are:

- Use of crack tip enrichment that allows the direct evaluation of the SIFs from the solution of the system of equations. Differently from previous XBEM investigations available in the literature, the enrichment term is based on shifted functions.
- Proposition of a novel displacement-discontinuity enrichment into the BEM framework to avoid the remeshing of existing boundary elements intercepted by cracks.
- Introduction of a traction enrichment composed of a Dirac delta term to model point boundary conditions within BEM, such as concentrated forces and support points.

Then, an XIGABEM approach is presented for the analysis of high-cycle fatigue crack growth in two-dimensional bodies. The novel aspects of the novel formulation are:

- Definition of a crack tip enrichment strategy for direct evaluation of the SIFs on homogeneous materials considering the isogeometric formulation.
- Development of a scheme to model the crack propagation, in which the new crack surfaces are created from the extension of existing NURBS. The strategy is based on the definition of a C^{-1} continuity for the rational basis between the new and old surfaces to facilitate the crack propagation modelling.
- Use of the C^{-1}-continuous NURBS basis to facilitate the isogeometric representation of discontinuities such as the intersection of cracks with other boundaries.

Finally, a new XIGABEM formulation is introduced for the analysis of interface cracks. Among the novelties of this numerical method are:

- Definition of enrichment functions based on the two-term asymptotic expansions for displacements and stresses of interface cracks. The proposed extended formulation allows the evaluation of the SIFs and T-stress parameter directly from the system of equations.

- Extension of the direct method to extract the crack parameters for curved cracks.

Several numerical applications are presented to demonstrate the accuracy of all enriched formulations herein proposed. The results are compared with analytical, experimental and numerical solutions available in the literature. Besides, the direct approach is contrasted against unenriched and enriched indirect methods that employ the J-integral for SIF extraction.

1.2 Methodology

This doctoral thesis is inserted in the developments of the research group on fracture problems using BEM of the Department of Structural Engineering from the São Carlos School of Engineering at the University of São Paulo, under supervision of Prof. Edson Denner Leonel. The main goal of this research team is the proposition of numerical formulations for the analysis of the mechanical behaviour of cracked solids, and the work presented here provides further contributions to these investigations.

The first part of this thesis can be seen as a continuation of the author's Master's degree (ANDRADE, 2017), in which the DBEM was applied for the analysis of multiple crack propagation. The proposed XBEM approach used the DBEM code as basis for the inclusion of crack tip, discontinuous and concentrated force enrichments for the analysis of crack growth in isotropic and anisotropic materials.

Then, an IGABEM code was implemented for the analysis of linear elastostatic problems. The numerical formulation was then coupled to the level set method to perform topology optimisation, which yielded the work reported in Oliveira, Andrade, and Leonel (2020). The IGABEM code was later considered for the definition of the extended isogeometric approach with the introduction of the crack tip enrichment. The resulting XIGABEM was allied to the C^{-1}-continuity of NURBS to define the numerical model for the analysis of high-cycle fatigue.

Finally, the isogeometric formulation was expanded to include new enrichment functions for the analysis of cracks along bimaterial interfaces. The BEM sub-region technique was adopted to analyse each sub-domain separately, while the interfaces were admitted with perfectly bonded conditions. In the proposed XIGABEM, the two-term asymptotic expansions near the interface tip were used for enrichment of elements in the discretisation of both crack surfaces and interfaces, which allowed the SIFs and T-stress parameter to be obtained directly from the solution vector given by the numerical method.

All BEM formulations were implemented in the FORTRAN 90 language. Additionally, the pre-processing for model generation and post-processing for data analysis were carried out in Python. For isogeometric applications, the NURBS-Python library *geomdl* (BINGOL; KRISHNAMURTHY, 2019) was adopted for defining the initial geometries.

1.3 Organisation of the text

The remainder of this thesis is structured as follows: Chapter 2 briefly describes the dual BEM formulation, which forms the basis for the enriched approaches. Chapter 3 presents the LEFM fundamentals that are used for the definition of the crack tip enrichments for homogeneous and interface cracks. The novel XBEM formulation developed in this study to simulate linear crack propagation is described in Chapter 4. Chapter 5 brings the main concepts of IGABEM and presents the new XIGABEM approach applied for fatigue simulation. In Chapter 6, the XIGABEM formulation is extended to the analysis of interface cracks. Finally, Chapter 7 draws some conclusions obtained from the present research and offers some recommendations for future work.

2 Boundary element formulation

2.1 Fundamentals of Elasticity

In this study, the BEM is applied to the solution of linear elastostatic problems. In what follows, the main concepts of the Theory of Elasticity used for the development of the BEM formulation are briefly presented.

Let Ω denotes an elastic domain with enclosing boundary Γ , as illustrated in Fig. 2.1. The static equilibrium equations for each point $\mathbf{x}$ belonging to Ω are stated as follows:

$$\sigma_{ij,j} + b_i = 0 \tag{2.1}$$

where $\sigma_{ij} = \sigma_{ji}$ represents the Cauchy stress tensor and b_i denotes the body-force components. The index notation and Einstein summation convention are adopted herein.

Figure 2.1: Representation of the elastostatic boundary value problem.

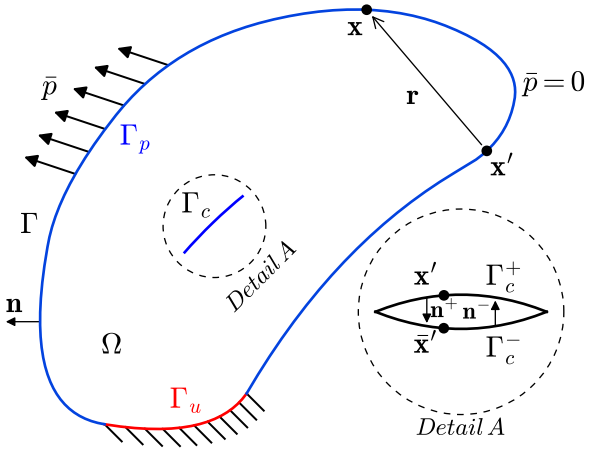

Source: Own author.

The linear strain tensor is defined as:

$$\varepsilon_{ij} = \frac{u_{i,j} + u_{j,i}}{2} \tag{2.2}$$

where $\varepsilon_{ij} = \varepsilon_{ji}$ are the strain components and u_i stands for the displacements.

The stress and strain components can be related through generalized Hooke's law. Considering a fully anisotropic media, this relation is given by:

$$\sigma_{ij} = a_{ijkl}\varepsilon_{kl} \tag{2.3}$$

in which the components a_{ijkl} define the fourth-order elastic stiffness tensor $\mathbb{A}$ and satisfy the following symmetry relations:

$$a_{ijkl} = a_{jikl} = a_{ijlk} = a_{klij} \tag{2.4}$$

Alternatively, the strain components can be defined from the stress components using the inverse of Eq. (2.3). This constitutive relation is expressed in Voigt notation by:

$$\begin{Bmatrix} \varepsilon_{11} \\ \varepsilon_{22} \\ \varepsilon_{33} \\ 2\varepsilon_{23} \\ 2\varepsilon_{13} \\ 2\varepsilon_{12} \end{Bmatrix} = \begin{bmatrix} c_{1111} & c_{1122} & c_{1133} & 2c_{1123} & 2c_{1113} & 2c_{1112} \\ c_{2211} & c_{2222} & c_{2233} & 2c_{2223} & 2c_{2213} & 2c_{2212} \\ c_{3311} & c_{3322} & c_{3333} & 2c_{3323} & 2c_{3313} & 2c_{3312} \\ 2c_{2311} & 2c_{2322} & 2c_{2333} & 4c_{2323} & 4c_{2313} & 4c_{2312} \\ 2c_{1311} & 2c_{1322} & 2c_{1333} & 4c_{1323} & 4c_{1313} & 4c_{1312} \\ 2c_{1211} & 2c_{1222} & 2c_{1233} & 4c_{1223} & 4c_{1213} & 4c_{1212} \end{bmatrix} \begin{Bmatrix} \sigma_{11} \\ \sigma_{22} \\ \sigma_{33} \\ \sigma_{23} \\ \sigma_{13} \\ \sigma_{12} \end{Bmatrix} \tag{2.5}$$

The components c_{ijkl} on the right-hand side of Eq. (2.5) represent the fourth-order elastic compliance tensor $\mathbb{C}$, given by the inverse of the stiffness tensor, i.e., $\mathbb{C} = \mathbb{A}^{-1}$. The compliance tensor can be determined from the material constants as follows:

$$\begin{Bmatrix} \varepsilon_1 \\ \varepsilon_2 \\ \varepsilon_3 \\ 2\varepsilon_4 \\ 2\varepsilon_5 \\ 2\varepsilon_6 \end{Bmatrix} = \begin{bmatrix} \frac{1}{E_1} & -\frac{\nu_{12}}{E_1} & -\frac{\nu_{13}}{E_1} & \frac{\eta_{14}}{E_1} & \frac{\eta_{15}}{E_1} & \frac{\eta_{16}}{E_1} \\ -\frac{\nu_{21}}{E_2} & \frac{1}{E_2} & -\frac{\nu_{23}}{E_2} & \frac{\eta_{24}}{E_2} & \frac{\eta_{25}}{E_2} & \frac{\eta_{26}}{E_2} \\ -\frac{\nu_{31}}{E_3} & -\frac{\nu_{32}}{E_3} & \frac{1}{E_3} & \frac{\eta_{34}}{E_3} & \frac{\eta_{35}}{E_3} & \frac{\eta_{36}}{E_3} \\ \frac{\eta_{41}}{\mu_4} & \frac{\eta_{42}}{\mu_4} & \frac{\eta_{43}}{\mu_4} & \frac{1}{\mu_4} & \frac{\chi_{45}}{\mu_4} & \frac{\chi_{46}}{\mu_4} \\ \frac{\eta_{51}}{\mu_5} & \frac{\eta_{52}}{\mu_5} & \frac{\eta_{53}}{\mu_5} & \frac{\chi_{54}}{\mu_5} & \frac{1}{\mu_5} & \frac{\chi_{56}}{\mu_5} \\ \frac{\eta_{61}}{\mu_6} & \frac{\eta_{62}}{\mu_6} & \frac{\eta_{63}}{\mu_6} & \frac{\chi_{64}}{\mu_6} & \frac{\chi_{65}}{\mu_6} & \frac{1}{\mu_6} \end{bmatrix} \begin{Bmatrix} \sigma_1 \\ \sigma_2 \\ \sigma_3 \\ \sigma_4 \\ \sigma_5 \\ \sigma_6 \end{Bmatrix} \tag{2.6}$$

in which the following index transformation is adopted:

$$1 \leftrightarrow 11 \quad 2 \leftrightarrow 22 \quad 3 \leftrightarrow 33 \quad 4 \leftrightarrow 23 \equiv 32 \quad 5 \leftrightarrow 13 \equiv 31 \quad 6 \leftrightarrow 12 \equiv 21 \tag{2.7}$$

In a fully anisotropic material, the compliance tensor is defined by 21 independent elastic constants: Young's moduli E_i, Poisson's ratios ν_{ij}, shear moduli μ_i, coefficients of mutual influence η_{ij}, and Chentsov's coefficients χ_{ij}. For isotropic materials, only two elastic constants are independent: the Young's modulus E and the Poisson's ratio ν. In this case, a compact relation between the strains and stresses can be written:

$$\varepsilon_{ij} = \frac{\sigma_{ij}}{2\mu} - \frac{\nu}{E}\sigma_{kk}\delta_{ij} \tag{2.8}$$

in which μ is the shear modulus, given by:

$$\mu = \frac{E}{2\,(1+\nu)} \tag{2.9}$$

and δ_{ij} is the Kronecker delta, defined as:

$$\delta_{ij} = \begin{cases} 1, & i = j \\ 0, & i \neq j \end{cases} \tag{2.10}$$

Let the displacement and traction boundary conditions at Γ be defined as:

$$\begin{aligned} u_i &= \bar{u}_i \quad \text{on } \Gamma_u \\ p_i &= \bar{p}_i \quad \text{on } \Gamma_p \end{aligned} \tag{2.11}$$

in which $\Gamma = \Gamma_u \cup \Gamma_p$ and $\Gamma_u \cap \Gamma_p = \emptyset$. The traction components at the boundary are defined from Cauchy's formula:

$$p_i = \sigma_{ij} n_j \tag{2.12}$$

where n_j are the components of the outward unit normal vector at the boundary.

Equations (2.1), (2.2) and (2.6) (or Eq. (2.8) for isotropic materials), along with the Dirichlet and Neumann boundary conditions expressed in Eq. (2.11), constitute the boundary value problem in linear elasticity.

The above relations are valid for the three-dimensional space, with $i, j, k = 1, 2, 3$. However, plane problems are considered in the present study. For plane stress conditions, in which $\sigma_{13} = \sigma_{23} = \sigma_{33} = 0$, the same equations hold with $i, j, k = 1, 2$. Additionally, considering the plane of analysis as a plane of elastic symmetry, Eq. (2.6) is reduced to:

$$\begin{Bmatrix} \varepsilon_1 \\ \varepsilon_2 \\ 2\varepsilon_6 \end{Bmatrix} = \begin{bmatrix} c_{11} & c_{12} & c_{16} \\ c_{21} & c_{22} & c_{26} \\ c_{61} & c_{26} & c_{66} \end{bmatrix} \begin{Bmatrix} \sigma_1 \\ \sigma_2 \\ \sigma_6 \end{Bmatrix} \tag{2.13}$$

For plane strain states, in which $\varepsilon_{13} = \varepsilon_{23} = \varepsilon_{33} = 0$, these expressions are also valid for $i, j, k = 1, 2$. Nonetheless, the following modified components of the compliance tensor should be used in Eq. (2.13):

$$c^*_{ij} = c_{ij} - \frac{c_{i3} c_{j3}}{c_{33}}, \quad i, j = 1, 2, 6 \tag{2.14}$$

When considering isotropic materials in plane strain problems, the out-of-plane normal stress component is given by:

$$\sigma_{33} = \nu \left(\sigma_{11} + \sigma_{22} \right) \tag{2.15}$$

and the following corrected Poisson's ratio should be used in Eq. (2.8):

$$\nu^* = \nu \left(1 - \nu \right) \tag{2.16}$$

In some situations, the coordinate system must be rotated to perform the mechanical

analysis. When an anisotropic material is considered, the compliance matrix must also be rotated since it depends on the frame of reference. For a new orientation, rotated by an angle of φ about the original x_1 axis as depicted in Fig. 2.2, Eq. (2.13) can be rewritten in a compact form as:

$$\{\varepsilon'\} = [C']\,\{\sigma'\} \tag{2.17}$$

where the tensors are now expressed in the new coordinate system and are obtained as follows:

$$\{\varepsilon'\} = [R]^{-T}\,\{\varepsilon\} \tag{2.18}$$

$$\{\sigma'\} = [R]\,\{\sigma\} \tag{2.19}$$

$$[C'] = [R]^{-T}\,[C]\,[R]^{-1} \tag{2.20}$$

in which $[R]$ denotes the rotation matrix given by:

$$[R] = \begin{bmatrix} c^2 & s^2 & 2cs \\ s^2 & c^2 & -2cs \\ -cs & cs & c^2 - s^2 \end{bmatrix} \tag{2.21}$$

where $c = \cos\varphi$ and $s = \sin\varphi$.

Figure 2.2: Rotation from the global to the local coordinate system.

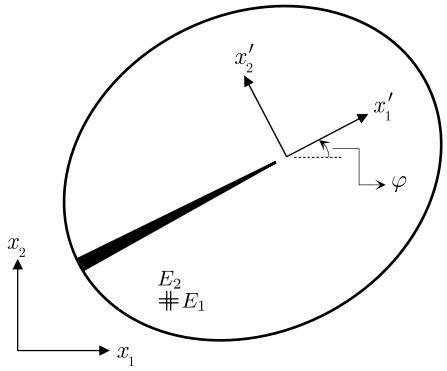

Source: Own author.

2.2 Boundary integral equations

From the equilibrium conditions shown in Eq. (2.1) and by means of the weighted residual method, the following expression can be written $\forall \mathbf{x} \in \boldsymbol{\Omega}$:

$$\int_{\Omega} \left(\sigma_{ij,j} + b_i\right) u_i^* d\Omega = 0 \tag{2.22}$$

where u_i^* is used as a weighting function and corresponds to a displacement field from a self-equilibrated auxiliary state.

Applying the divergence theorem, strain-displacement relation (2.2) and Cauchy's formula (2.12) in Eq. (2.22) results in:

$$\int_{\Omega} \sigma_{ij}\varepsilon_{ij}^* d\Omega = \int_{\Gamma} p_i u_i^* d\Gamma + \int_{\Omega} b_i u_i^* d\Omega \tag{2.23}$$

From Hooke's law (2.3), the integral on the left-hand side of Eq. (2.23) can be rewritten as:

$$\int_{\Omega} \sigma_{ij}\varepsilon_{ij}^* d\Omega = \int_{\Omega} a_{ijkl}\varepsilon_{kl}\varepsilon_{ij}^* d\Omega = \int_{\Omega} \sigma_{ij}^*\varepsilon_{ij} d\Omega \tag{2.24}$$

where the last equality is obtained after using the symmetry relations from Eq. (2.4) and applying an index change.

Observing the similarity with the first member of Eq. (2.23), the last member of Eq. (2.24) can be expressed by:

$$\int_{\Omega} \sigma_{ij}^*\varepsilon_{ij} d\Omega = \int_{\Gamma} p_i^* u_i d\Gamma + \int_{\Omega} b_i^* u_i d\Omega \tag{2.25}$$

Therefore, substituting Eqs. (2.25) and (2.24) into Eq. (2.23) leads to:

$$\int_{\Gamma} p_i^* u_i d\Gamma + \int_{\Omega} b_i^* u_i d\Omega = \int_{\Gamma} p_i u_i^* d\Gamma + \int_{\Omega} b_i u_i^* d\Omega \tag{2.26}$$

Equation (2.26) corresponds to Betti's reciprocal work theorem for two self-equilibrated elastic states. An integral representation for the elastostatic problem can be obtained from this relation by choosing the auxiliary state as a point-load problem in an infinite domain. In this case, the corresponding body force is given by:

$$b_i^* = \Delta(\mathbf{x}', \mathbf{x}) e_i \tag{2.27}$$

where $\Delta(\mathbf{x}', \mathbf{x})$ is the Dirac delta function, $\mathbf{x}'$ corresponds to the point of applied force (or source point) and e_i represents the components of a unit vector in the x_i direction. The displacement and traction fields of the point-load problem can be expressed by:

$$\begin{aligned} u_i^* &= U_{ij}^*(\mathbf{x}', \mathbf{x}) e_j \\ p_i^* &= P_{ij}^*(\mathbf{x}', \mathbf{x}) e_j \end{aligned} \tag{2.28}$$

in which U_{ij}^* and P_{ij}^* are, respectively, the displacement and traction fundamental solutions. Appendix B presents their expressions for two-dimensional problems considering

both isotropic and anisotropic materials.

Substituting Eqs. (2.27) and (2.28) into Eq. (2.26), and then using the Dirac delta sifting property, the Somigliana's identity is obtained:

$$u_i(\mathbf{x}') + \int_\Gamma P^*_{ij}(\mathbf{x}', \mathbf{x}) u_j(\mathbf{x}) d\Gamma = \int_\Gamma U^*_{ij}(\mathbf{x}', \mathbf{x}) p_j(\mathbf{x}) d\Gamma + \int_\Omega U^*_{ij}(\mathbf{x}', \mathbf{x}) b_j(\mathbf{x}) d\Omega \tag{2.29}$$

With Eq. (2.29), the displacement at internal points $\mathbf{x}' \in \Omega \backslash \Gamma$ can be computed once the displacements and tractions at the boundary points $\mathbf{x} \in \Gamma$ are known.

Differentiating Eq. (2.29) with respect to the source point $\mathbf{x}'$, then using the strain-displacement relation (2.2) and finally applying Hooke's law (2.8), the integral equation that defines the internal stress components is obtained:

$$\sigma_{ij}(\mathbf{x}') + \int_\Gamma S^*_{kij}(\mathbf{x}', \mathbf{x}) u_k(\mathbf{x}) d\Gamma = \int_\Gamma D^*_{kij}(\mathbf{x}', \mathbf{x}) p_k(\mathbf{x}) d\Gamma + \int_\Omega D^*_{kij}(\mathbf{x}', \mathbf{x}) b_k(\mathbf{x}) d\Omega \tag{2.30}$$

where D^*_{kij} and S^*_{kij} are obtained from the U^*_{ij} and P^*_{ij} derivatives, respectively. Their expressions are also presented in Appendix B.

Equations (2.29) and (2.30) are only valid for evaluation of the mechanical fields at internal points. Therefore, to compute the boundary values, $\mathbf{x}'$ must be placed at Γ. This can be achieved by performing a limiting process and analysing the behaviour of the integral kernels since they are singular as $\mathbf{x}' \to \mathbf{x}$ (see expressions of fundamental solutions in Appendix B). Details about this process can be obtained in Brebbia and Dominguez (1994) and Aliabadi (2002). Applying this procedure to Eq. (2.29) and assuming that the displacement field is continuous at $\mathbf{x}'$, the displacement boundary integral equation (DBIE) is determined as:

$$c_{ij}(\mathbf{x}') u_j(\mathbf{x}') + c_{ij}(\bar{\mathbf{x}}') u_j(\bar{\mathbf{x}}') + \fint_\Gamma P^*_{ij}(\mathbf{x}', \mathbf{x}) u_j(\mathbf{x}) d\Gamma = \int_\Gamma U^*_{ij}(\mathbf{x}', \mathbf{x}) p_j(\mathbf{x}) d\Gamma \tag{2.31}$$

in which the body forces are disregarded, as usual in the BEM, and $\fint$ denotes an integral to be evaluated in the Cauchy principal value sense. $c_{ij}(\mathbf{x}')$ represents the jump term arising from the integration of the strongly singular kernel P^*_{ij}. The explicit expressions to compute c_{ij} can be found in Guiggiani and Casalini (1987) and, for $\mathbf{x}'$ at smooth boundaries, $c_{ij} = \delta_{ij}/2$. The additional jump term $c_{ij}(\bar{\mathbf{x}}')$ only exists if another source point $\bar{\mathbf{x}}'$ is at the same position of $\mathbf{x}'$, but is placed on a different surface. Such a condition occurs for corresponding source points at opposite crack surfaces (see Fig. 2.1). When $\mathbf{x}'$ is placed at the non-crack boundaries, the term $c_{ij}(\bar{\mathbf{x}}') u_j(\bar{\mathbf{x}}')$ vanishes.

Analogously, the limiting process may also be applied for Eq. (2.30) to determine

the second integral equation required by the DBEM. After this procedure, the traction boundary integral equation (TBIE) is obtained by applying Cauchy's formula (2.12). The order of singularity of the integral kernel in the TBIE is increased in comparison to the DBIE. Hence, for the existence of the resulting finite part integrals, the TBIE must be applied to locations at which the displacement derivatives are continuous, which constrains the collocation of $\mathbf{x}'$ at a smooth boundary. Then, considering $\mathbf{x}'$ at a smooth surface, the TBIE becomes:

$$\frac{1}{2}\left[p_j(\mathbf{x}') - p_j(\bar{\mathbf{x}}')\right] + n_i(\mathbf{x}') \oint\!\!\!\!\!\!= \int_\Gamma S^*_{kij}(\mathbf{x}', \mathbf{x}) u_k(\mathbf{x}) d\Gamma = n_i(\mathbf{x}') \oint\!\!\!\!\!\!= \int_\Gamma D^*_{kij}(\mathbf{x}', \mathbf{x}) p_k(\mathbf{x}) d\Gamma \quad (2.32)$$

where $\oint\!\!\!\!\!\!=$ stands for the Hadamard principal value integral.

2.3 Dual boundary element method

When analysing bodies containing cracks, as illustrated in Fig. 2.1, the application of the same boundary integral equation at coincident source points $\mathbf{x}'$ and $\bar{\mathbf{x}}'$ on the opposing crack surfaces leads to degeneracy in the resulting system of algebraic equations. One approach to overcome this deficiency is to use the DBEM (HONG; CHEN, 1988; PORTELA; ALIABADI; ROOKE, 1992), which employs the two independent boundary integral equations shown in Eqs. (2.31) and (2.32). The DBIE is applied to $\mathbf{x}'$ on the upper crack surface Γ^C_+ and external boundary, while the TBIE is adopted to $\mathbf{x}'$ located on the lower crack surface Γ^C_-. In what follows, the numerical approximations used in the DBEM are defined by Lagrange polynomials. In Chapters 5 and 6, an isogeometric analysis is considered. In this approach, the following formulation remains valid, requiring only the replacement of the Lagrange polynomials by the NURBS basis functions.

To define the discrete forms of the boundary integral equations, Γ is firstly subdivided into boundary elements Γ_e, with $\Gamma = \cup\Gamma_e$, as illustrated in Fig. 2.3a. Each element is defined by n_e nodes, with $n_e - 1$ representing the degree of the polynomial approximation. Considering the conventional Lagrange polynomials, the Cartesian coordinates along the element e are interpolated from the nodal values by:

$$\tilde{x}^e_j(\xi) = \sum_{m=1}^{n_e} \phi^{em}(\xi) x^{em}_j \quad (2.33)$$

where x^{em}_j represents the nodal coordinates and:

$$\phi^{em}(\xi) = \prod_{l=1, l\neq m}^{n_e} \frac{(\xi - \xi^l)}{(\xi^m - \xi^l)} \quad (2.34)$$

is the Lagrange polynomial associated with the m-th node from the e-th element. A global

node n is related to a local node through a connectivity relation, i.e, $n = \text{conn}\,(e, m)$. Besides, $\xi \in [-1, 1]$ denotes the parametric space defined over the element, and the Jacobian of the transformation to the Cartesian coordinate system is given by:

$$J^e(\xi) = \frac{d\Gamma}{d\xi} = \sqrt{\left(\frac{dx_1}{d\xi}(\xi)\right)^2 + \left(\frac{dx_2}{d\xi}(\xi)\right)^2} \tag{2.35}$$

Figure 2.3: (a) Boundary discretisation with quadratic elements. The interpolation of the coordinates, tractions and displacements along three elements is also illustrated. (b) Representation of a boundary mesh for a inhomogeneous crack problem. Continuous, semi-discontinuous and discontinuous elements are depicted in different colours with their respective nodes and collocation points. The external boundary (Γ^B), the interface (Γ^I) and the upper (Γ^C_+) and lower (Γ^C_-) crack surfaces are indicated with the corresponding BIE applied for their collocation points.

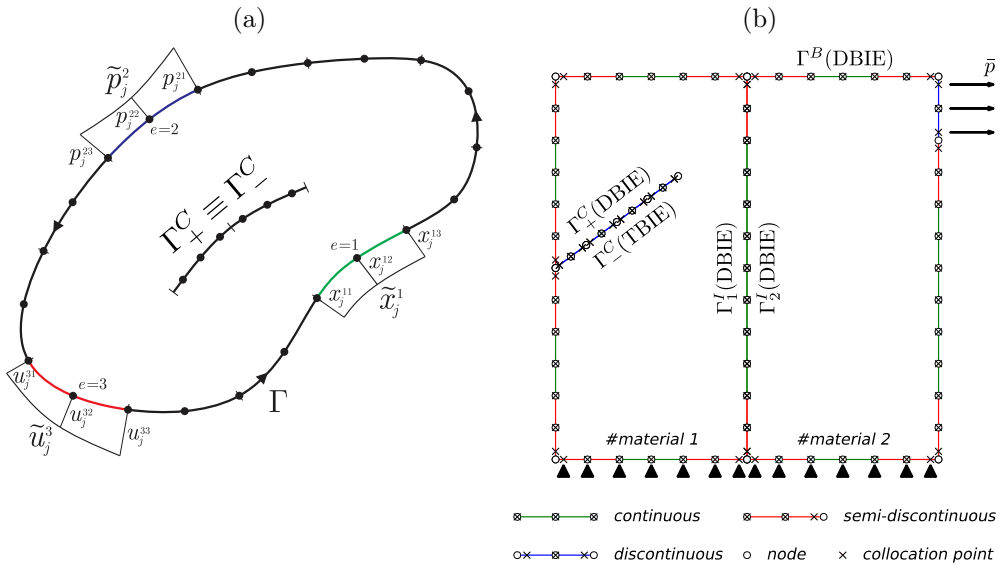

Source: Own author.

With the boundary discretisation, the DBIE (2.31) becomes:

$$\begin{aligned} c_{ij}(\mathbf{x}')u_j(\mathbf{x}') + c_{ij}(\bar{\mathbf{x}}')u_j(\bar{\mathbf{x}}') + \sum_{e=1}^{N_e} \int_{-1}^{1} P^*_{ij}(\mathbf{x}', \mathbf{x}(\xi))u^e_j(\xi)J^e(\xi)d\xi = \\ = \sum_{e=1}^{N_e} \int_{-1}^{1} U^*_{ij}(\mathbf{x}', \mathbf{x}(\xi))p^e_j(\xi)J^e(\xi)d\xi \end{aligned} \tag{2.36}$$

where N_e is the total number of elements.

Using the isoparametric approach, the mechanical fields along the elements are also interpolated with the polynomials shape functions and the nodal values as:

$$\tilde{u}^e_j(\xi) = \sum_{m=1}^{n_e} \phi^{em}(\xi)u^{em}_j \tag{2.37}$$

$$\tilde{p}_j^e(\xi) = \sum_{m=1}^{n_e} \phi^{em}(\xi) p_j^{em} \tag{2.38}$$

Substituting Eqs. (2.37) and (2.38) into Eq. (2.36) results in:

$$c_{ij}(\mathbf{x}')u_j(\mathbf{x}') + c_{ij}(\bar{\mathbf{x}}')u_j(\bar{\mathbf{x}}') + \sum_{e=1}^{N_e}\sum_{m=1}^{n_e} P_{ij}^{em} u_j^{em} = \sum_{e=1}^{N_e}\sum_{m=1}^{n_e} U_{ij}^{em} p_j^{em} \tag{2.39}$$

where:

$$P_{ij}^{em} = \fint_{-1}^{1} P_{ij}^*(\mathbf{x}', \mathbf{x}(\xi))\phi^{em}(\xi) J^e(\xi) d\xi \tag{2.40}$$

$$U_{ij}^{em} = \int_{-1}^{1} U_{ij}^*(\mathbf{x}', \mathbf{x}(\xi))\phi^{em}(\xi) J^e(\xi) d\xi \tag{2.41}$$

Similarly, the discrete TBIE (2.32) is determined as:

$$\frac{1}{2}\left[p_j(\mathbf{x}') - p_j(\bar{\mathbf{x}}')\right] + n_i(\mathbf{x}') \sum_{e=1}^{N_e}\sum_{m=1}^{n_e} S_{kij}^{em} u_k^{em} = n_i(\mathbf{x}') \sum_{e=1}^{N_e}\sum_{m=1}^{n_e} D_{kij}^{em} p_k^{em} \tag{2.42}$$

where:

$$S_{kij}^{em} = \fint_{-1}^{1} S_{kij}^*(\mathbf{x}', \mathbf{x}(\xi))\phi^{em}(\xi) J^e(\xi) d\xi \tag{2.43}$$

$$D_{kij}^{em} = \fint_{-1}^{1} D_{kij}^*(\mathbf{x}', \mathbf{x}(\xi))\phi^{em}(\xi) J^e(\xi) d\xi \tag{2.44}$$

With the discrete forms of the DBIE and TBIE, given by Eqs. (2.39) and (2.42), respectively, the algebraic system of equations provided by DBEM can be assembled by applying the collocation method. Here, the DBIE is used for collocation on nodes at the external boundary and one of the crack surfaces, while the TBIE is used for collocation on the other surface to obtain a non-singular system of equations (see Fig. 2.3b). Therefore, these nodes become the source point $\mathbf{x}'$ of their respective BIE.

The existence of the Hadamard principal value in the TBIE requires the continuity of the displacement derivatives, given by Eq. (2.37), at the collocation points. This condition is automatically satisfied by the use of discontinuous elements, in which the collocation points do not coincide with the end nodes but are positioned inside the element. Hence, this type of element is used in the crack surfaces mesh (see Fig. 2.3b). Moreover, in the present work, discontinuous or semi-discontinuous elements are also used to ensure a smooth boundary at the collocations points, as depicted in Fig. 2.3b.

Due to the singularities of the fundamental solutions when $\mathbf{x}' \to \mathbf{x}$, the integral kernels in Eqs. (2.40), (2.41), (2.43) and (2.44) must be assessed with different strategies depend-

ing on the distance of the source point to the integrated element. Appendix C presents the different approaches applied to evaluate the integrands for each case.

After the integration process, the resulting algebraic system of equation is determined, and it can be summarised into matrix form as:

$$\mathbf{Hu} = \mathbf{Gp} \tag{2.45}$$

in which $\mathbf{H}$ is a $2N \times 2N$ matrix containing the influence coefficients obtained from the kernels P_{ij}^{em} and S_{kij}^{em} and from the jump terms of the DBIE. $\mathbf{G}$ is also a $2N \times 2N$ matrix with the coefficients determined from U_{ij}^{em} and D_{kij}^{em} and from the jump terms of the TBIE. $\mathbf{u}$ and $\mathbf{p}$ are $2N$ vectors with the displacements and tractions on the boundary, respectively, and N is the total number of collocation points on the boundary mesh. Imposing the prescribed boundary conditions to the system (2.45), the final linear system of equations is obtained:

$$\mathbf{Ax} = \mathbf{f} \tag{2.46}$$

where $\mathbf{A}$ is a $2N \times 2N$ matrix composed by the coefficients from $\mathbf{H}$ and $\mathbf{G}$ related to the unknown boundary values, $\mathbf{x}$ is a $2N$ vector containing the unknown nodal parameters and $\mathbf{f}$ is a $2N$ vector obtained from the multiplication of the prescribed boundary values and their respective influence coefficients from matrices $\mathbf{H}$ and $\mathbf{G}$. The solution of Eq. (2.46) provides a response to the elastostatic boundary value problem determined by DBEM.

2.4 Internal points

If the mechanical fields at an internal point are desired, the discrete forms of Eqs.(2.29) and (2.30) can be used once the boundary values are determined from the solution of Eq. (2.46). Thus, the displacement and stress components at an internal point $\mathbf{x}'$ are given as follows:

$$u_i(\mathbf{x}') = \sum_{e=1}^{N_e} \sum_{m=1}^{n_e} U_{ij}^{em} p_j^{em} - \sum_{e=1}^{N_e} \sum_{m=1}^{n_e} P_{ij}^{em} u_j^{em} \tag{2.47}$$

$$\sigma_{ij}(\mathbf{x}') = \sum_{e=1}^{N_e} \sum_{m=1}^{n_e} D_{kij}^{em} p_k^{em} - \sum_{e=1}^{N_e} \sum_{m=1}^{n_e} S_{kij}^{em} u_k^{em} \tag{2.48}$$

Note that the integral kernels on the right-hand side of Eqs. (2.47) and (2.48) are non-singular and can be evaluated without numerical difficulties. Nonetheless, the third-degree polynomial transformation (see Appendix C.2) can be considered when $\mathbf{x}'$ approaches the boundary to improve the accuracy of the quasi-singular integration.

2.5 Stress on the boundary

In many application, the state of stress at a particular point on the boundary is required. One possibility to define the stress components on a boundary point is to use the equation determined from Eq. (2.30) after the limiting process is considered to take the source point to the boundary. This process gives an expression similar to the TBIE (2.32) - in fact, the TBIE is obtained after Cauchy's formula is applied over the equation obtained from the limiting process. However, the use of this relation is computationally costly since the integral kernels must be evaluated.

Alternatively, the stresses on the boundary can be determined from the tractions and displacements approximations used in the boundary discretisation. Figure 2.4a illustrates the traction components related to a global frame of reference that are determined after the BEM analysis. These components can be rotated to a local coordinate system, as depicted in Fig. 2.4b, by the following:

$$\left\{ \begin{array}{c} p'_1 \\ p'_2 \end{array} \right\} = \left[\begin{array}{cc} n_1 & n_2 \\ -n_2 & n_1 \end{array} \right] \left\{ \begin{array}{c} p_1 \\ p_2 \end{array} \right\} \tag{2.49}$$

where the matrix:

$$\mathbf{R}^T = \left[\begin{array}{cc} n_1 & n_2 \\ -n_2 & n_1 \end{array} \right] \tag{2.50}$$

is the transpose of the rotation matrix $\mathbf{R}$.

Figure 2.4: Traction components at a boundary point related to a (a) global and (b) local coordinate system.

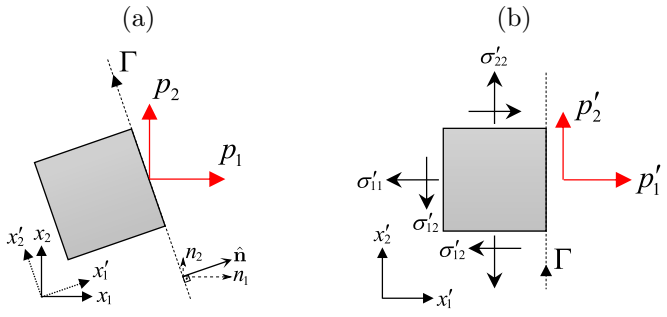

Source: Own author.

With the traction components referred to the local coordinate system, the local stress components σ'_{11} and σ'_{12} can be determined with Cauchy's formula (2.12) and are given as follows:

$$\sigma'_{11} = p'_1 \tag{2.51}$$

$$\sigma'_{12} = p'_2 \tag{2.52}$$

The stress component σ'_{22} can be obtained using the approximations applied in the boundary discretisation and presented in Section 2.3. Firstly, Eq. (2.13) is rewritten considering the strain-displacement relation (2.2) and the local coordinate system as:

$$\left\{ \begin{array}{c} u'_{1,1} \\ u'_{2,2} \\ u'_{1,2} + u'_{2,1} \end{array} \right\} = \left[\begin{array}{ccc} c'_{11} & c'_{12} & c'_{16} \\ c'_{21} & c'_{22} & c'_{26} \\ c'_{61} & c'_{26} & c'_{66} \end{array} \right] \left\{ \begin{array}{c} \sigma'_{11} \\ \sigma'_{22} \\ \sigma'_{12} \end{array} \right\} \tag{2.53}$$

Then, the derivatives of the displacement components can be obtained from the approximation in Eq. (2.37) by:

$$\frac{du'_i}{d\xi} = \sum_{m=1}^{n_e} \frac{d\phi^{em}}{d\xi} u_i'^{em} = A_i \tag{2.54}$$

in which the nodal displacement components can be rotated as the traction components in Eq. (2.49).

The displacement derivatives in Eq. (2.54) can also be determined by the chain rule as follows:

$$\frac{du'_i}{d\xi} = \frac{du'_i}{dx'_l} \frac{dx'_l}{d\xi} = u'_{i,l} T_l \tag{2.55}$$

where $\frac{dx'_l}{d\xi} = \sum_{m=1}^{n_e} \frac{d\phi^{em}}{d\xi}(\xi) x_l'^{em} = T_l$.

From Eqs. (2.54) and (2.55), the following expressions can be written:

$$u'_{1,1} = \frac{A_1 - u'_{1,2} T_2}{T_1} \tag{2.56}$$

$$u'_{2,2} = \frac{A_2 - u'_{2,1} T_1}{T_2} \tag{2.57}$$

Using Eqs. (2.53), (2.56) and (2.57), the expression that gives σ'_{22} is obtained as follows:

$$\sigma'_{22} = \frac{A_1 T_1 + A_2 T_2 - T_1^2 \left(c'_{11}\sigma'_{11} + c'_{16}\sigma'_{12}\right) - T_2^2 \left(c'_{21}\sigma'_{11} + c'_{26}\sigma'_{12}\right) - T_1 T_2 \left(c'_{61}\sigma'_{11} + c'_{66}\sigma'_{12}\right)}{T_1^2 c'_{12} + T_2^2 c'_{22} + T_1 T_2 c'_{62}} \tag{2.58}$$

Equation (2.58) is valid for anisotropic materials in plane problems. It can also be applied to isotropic materials, with the particularity that $c'_{16} = c'_{61} = c'_{26} = c'_{62} = 0$ and the other components of the compliance matrix are constant with the material orientation.

Finally, the state of stress in the global coordinate system can be obtained by the inverse of Eq. (2.19).

2.6 Sub-region technique

In this study, the BEM sub-region technique (BANERJEE, 1976; BLANDFORD; INGRAFFEA; LIGGETT, 1981) is applied for the solution of inhomogeneous structural systems composed of piecewise homogeneous materials interconnected by interfaces. In this strategy, the DBIE (2.31) can be applied independently for each subdomain Ω_s - which is composed exclusively of one material - to define a set of linear equations. Hence, the resulting system of equation assumes the following form:

$$\left[\begin{array}{cc} \mathbf{H}_s^B & \mathbf{H}_s^I \end{array} \right] \left\{ \begin{array}{c} \mathbf{u}_s^B \\ \mathbf{u}_s^I \end{array} \right\} = \left[\begin{array}{cc} \mathbf{G}_s^B & \mathbf{G}_s^I \end{array} \right] \left\{ \begin{array}{c} \mathbf{p}_s^B \\ \mathbf{p}_s^I \end{array} \right\} \tag{2.59}$$

where the subscript s indicates the s-th subdomain and the superscripts I and B denote the sub-matrices and sub-vectors related to the degrees of freedom on the interface and external boundary, respectively.

The system in Eq. (2.59) is, in principle, under-determined since both displacements and tractions are unknown along the interfaces. Therefore, additional equations regarding the compatibility and equilibrium conditions at the interface must be considered. Here, the interaction between two adjacent sub-regions Ω_1 and Ω_2 is assumed perfectly bonded at the interface boundaries Γ_1^I and Γ_2^I. Hence, the following conditions hold:

$$\begin{array}{c} \mathbf{u}_1^I = \mathbf{u}_2^I \\ \mathbf{p}_1^I = -\mathbf{p}_2^I \end{array} \tag{2.60}$$

Thus, applying the relations of Eq. (2.60), the system of equations is coupled as follows:

$$\left[\begin{array}{ccc} \mathbf{H}_1^B & \mathbf{H}_1^I & \mathbf{0} \\ \mathbf{0} & \mathbf{H}_2^I & \mathbf{H}_2^B \end{array} \right] \left\{ \begin{array}{c} \mathbf{u}_1^B \\ \mathbf{u}_1^I \\ \mathbf{u}_2^B \end{array} \right\} = \left[\begin{array}{ccc} \mathbf{G}_1^B & \mathbf{G}_1^I & \mathbf{0} \\ \mathbf{0} & -\mathbf{G}_2^I & \mathbf{G}_2^B \end{array} \right] \left\{ \begin{array}{c} \mathbf{p}_1^B \\ \mathbf{p}_1^I \\ \mathbf{p}_2^B \end{array} \right\} \tag{2.61}$$

After considering all the subdomains and imposing the boundary conditions of the problem, the final system of equations in the form of Eq. (2.46) is obtained. The solution of the resulting system provides the unknown values at the external boundary and interface.

3 Fracture mechanics

3.1 LEFM fundamentals

One of the goals of the LEFM is the description of the singular stress fields around the crack tip. Since the body is assumed with linear elastic mechanical behaviour, these fields can be obtained through the stress function approach of the Theory of Elasticity. Using this strategy, Williams (1957) determined the asymptotic expansion for the stress components near a crack tip for the Griffith problems considering homogeneous and isotropic materials. For plane problems, the first-order Williams solution for the stress components referred to the local Cartesian coordinate system (Fig. 3.1) is given by:

$$\left\{ \begin{array}{c} \sigma_{11} \\ \sigma_{22} \\ \sigma_{12} \end{array} \right\} = \frac{1}{\sqrt{2\pi\rho}} \left[\begin{array}{cc} \cos\left(\frac{\theta}{2}\right)\left[1-\sin\left(\frac{\theta}{2}\right)\sin\left(\frac{3\theta}{2}\right)\right] & -\sin\left(\frac{\theta}{2}\right)\left[2+\cos\left(\frac{\theta}{2}\right)\cos\left(\frac{3\theta}{2}\right)\right] \\ \cos\left(\frac{\theta}{2}\right)\left[1+\sin\left(\frac{\theta}{2}\right)\sin\left(\frac{3\theta}{2}\right)\right] & \sin\left(\frac{\theta}{2}\right)\cos\left(\frac{\theta}{2}\right)\cos\left(\frac{3\theta}{2}\right) \\ \sin\left(\frac{\theta}{2}\right)\cos\left(\frac{\theta}{2}\right)\cos\left(\frac{3\theta}{2}\right) & \cos\left(\frac{\theta}{2}\right)\left[1-\sin\left(\frac{\theta}{2}\right)\sin\left(\frac{3\theta}{2}\right)\right] \end{array} \right] \left\{ \begin{array}{c} K_I \\ K_{II} \end{array} \right\} \quad (3.1)$$

in which ρ and θ are polar coordinates represented in Fig. 3.1. Note from Eq. (3.1) that the stress fields near the tip present a singularity order $\mathcal{O}(\rho^{-1/2})$. Moreover, the SIFs values K_I and K_{II} completely define all stress components near the crack tip. Consequently, the SIFs can be applied to verify the crack tip stability, which is the basis of the LEFM for homogeneous materials.

Figure 3.1: Stress components in the vicinity of the crack tip.

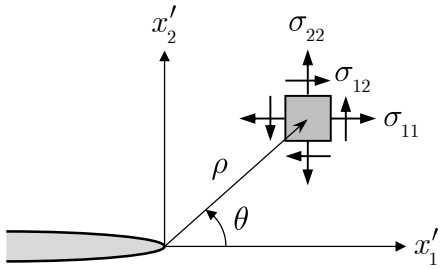

Source: Own author.

The SIFs values are associated with the basic fracture modes, characterised by the relative displacements between the crack surfaces. K_I is related to the opening mode, or mode I (Fig. 3.2a), while K_{II} is related to the sliding mode, or mode II (Fig. 3.2b). Every crack tip loading in plane problems can be decoupled into these basic fracture modes.

The displacements components near the crack tip can also be determined from the SIFs values, being expressed by:

Figure 3.2: Basic modes of fracture for two-dimensional problems: (a) opening mode and (b) sliding mode.

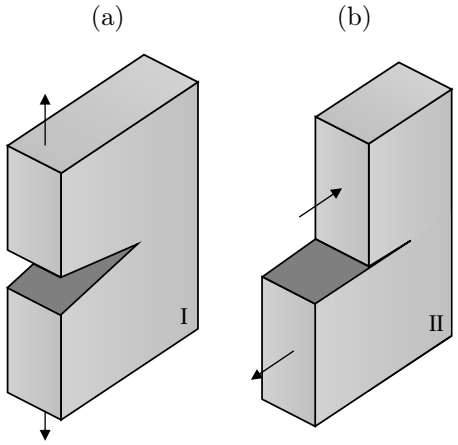

Source: Own author.

$$\left\{ \begin{array}{c} u_1 \\ u_2 \end{array} \right\} = \frac{1}{2\mu}\sqrt{\frac{\rho}{2\pi}} \left[\begin{array}{cc} \cos\left(\frac{\theta}{2}\right)(\kappa - \cos\theta) & \sin\left(\frac{\theta}{2}\right)(\kappa + 2 + \cos\theta) \\ \sin\left(\frac{\theta}{2}\right)(\kappa - \cos\theta) & -\cos\left(\frac{\theta}{2}\right)(\kappa - 2 + \cos\theta) \end{array} \right] \left\{ \begin{array}{c} K_I \\ K_{II} \end{array} \right\} \tag{3.2}$$

where $\mu = E/2(1+\nu)$ is the shear modulus and κ represents the Kolosov constant defined as $\kappa = (3-\nu)/(1+\nu)$ for plane stress and $\kappa = 3 - 4\nu$ for plane strain. E and ν are, respectively, the Young's modulus and the Poisson's ratio of the material. The displacement derivatives are often required (see Section 3.2.2), and they can be computed as follows:

$$\left\{ \begin{array}{c} u_{1,1} \\ u_{1,2} \\ u_{2,1} \\ u_{2,2} \end{array} \right\} = \frac{1}{8\mu\sqrt{2\pi\rho}} \left[\begin{array}{cc} (2\kappa - 3)\cos\left(\frac{\theta}{2}\right) + \cos\left(\frac{5\theta}{2}\right) & -(2\kappa + 1)\sin\left(\frac{\theta}{2}\right) - \sin\left(\frac{5\theta}{2}\right) \\ (2\kappa + 1)\sin\left(\frac{\theta}{2}\right) + \sin\left(\frac{5\theta}{2}\right) & (2\kappa + 5)\cos\left(\frac{\theta}{2}\right) + \cos\left(\frac{5\theta}{2}\right) \\ -(2\kappa + 3)\sin\left(\frac{\theta}{2}\right) + \sin\left(\frac{5\theta}{2}\right) & -(2\kappa - 1)\cos\left(\frac{\theta}{2}\right) + \cos\left(\frac{5\theta}{2}\right) \\ (2\kappa - 1)\cos\left(\frac{\theta}{2}\right) - \cos\left(\frac{5\theta}{2}\right) & -(2\kappa - 5)\sin\left(\frac{\theta}{2}\right) + \sin\left(\frac{5\theta}{2}\right) \end{array} \right] \left\{ \begin{array}{c} K_I \\ K_{II} \end{array} \right\} \tag{3.3}$$

Regarding anisotropic materials, Sih, Paris, and Irwin (1965) developed the mechanical fields near the crack tip for the Griffith crack problems through the Lekhnitskii formalism (LEKHNITSKII, 1968). As the isotropic case, it was found that the stress singularity components present a singularity of the order $\mathcal{O}(\rho^{-1/2})$ and they are fully defined by the SIFs. For plane problems, the stress components are given as follows:

$$\left\{ \begin{array}{c} \sigma_{11} \\ \sigma_{22} \\ \sigma_{12} \end{array} \right\} = \frac{1}{\sqrt{2\pi\rho}} \left[\begin{array}{cc} \Re\left[\left(\frac{\mu_1\mu_2}{\mu_1-\mu_2}\right)\left(\frac{\mu_2}{H_2} - \frac{\mu_1}{H_1}\right)\right] & \Re\left[\left(\frac{1}{\mu_1-\mu_2}\right)\left(\frac{\mu_2^2}{H_2} - \frac{\mu_1^2}{H_1}\right)\right] \\ \Re\left[\left(\frac{1}{\mu_1-\mu_2}\right)\left(\frac{\mu_1}{H_2} - \frac{\mu_2}{H_1}\right)\right] & \Re\left[\left(\frac{1}{\mu_1-\mu_2}\right)\left(\frac{1}{H_2} - \frac{1}{H_1}\right)\right] \\ \Re\left[\left(\frac{\mu_1\mu_2}{\mu_1-\mu_2}\right)\left(\frac{1}{H_1} - \frac{1}{H_2}\right)\right] & \Re\left[\left(\frac{1}{\mu_1-\mu_2}\right)\left(\frac{\mu_1}{H_2} - \frac{\mu_2}{H_1}\right)\right] \end{array} \right] \left\{ \begin{array}{c} K_I \\ K_{II} \end{array} \right\} \tag{3.4}$$

where $\Re$ denotes the real part operator, μ_i are the material complex parameters with

positive imaginary part (see Appendix B for more details) and H_i is obtained from:

$$H_i = \sqrt{\cos\theta + \mu_i \sin\theta} \tag{3.5}$$

The displacement components near the crack tip for anisotropic materials are also defined by the SIFs as follows:

$$\left\{ \begin{array}{c} u_1 \\ u_2 \end{array} \right\} = \sqrt{\frac{2\rho}{\pi}} \left[\begin{array}{cc} \Re\left[\frac{\mu_1 p_2 H_2 - \mu_2 p_1 H_1}{\mu_1 - \mu_2}\right] & \Re\left[\frac{p_2 H_2 - p_1 H_1}{\mu_1 - \mu_2}\right] \\ \Re\left[\frac{\mu_1 q_2 H_2 - \mu_2 q_1 H_1}{\mu_1 - \mu_2}\right] & \Re\left[\frac{q_2 H_2 - q_1 H_1}{\mu_1 - \mu_2}\right] \end{array} \right] \left\{ \begin{array}{c} K_I \\ K_{II} \end{array} \right\} \tag{3.6}$$

in which:

$$p_i = c_{11}\mu_i^2 + c_{12} - c_{16}\mu_i \tag{3.7}$$

$$q_i = c_{12}\mu_i + c_{22}\mu_i - c_{16} \tag{3.8}$$

The displacement derivatives for anisotropic materials are expressed by:

$$\left\{ \begin{array}{c} u_{1,1} \\ u_{1,2} \\ u_{2,1} \\ u_{2,2} \end{array} \right\} = \frac{1}{\sqrt{2\pi\rho}} \left[\begin{array}{cc} \Re\left[\left(\frac{1}{\mu_1-\mu_2}\right)\left(\frac{\mu_1 p_2}{H_2} - \frac{\mu_2 p_1}{H_1}\right)\right] & \Re\left[\left(\frac{1}{\mu_1-\mu_2}\right)\left(\frac{p_2}{H_2} - \frac{p_1}{H_1}\right)\right] \\ \Re\left[\left(\frac{\mu_1\mu_2}{\mu_1-\mu_2}\right)\left(\frac{p_2}{H_2} - \frac{p_1}{H_1}\right)\right] & \Re\left[\left(\frac{1}{\mu_1-\mu_2}\right)\left(\frac{\mu_2 p_2}{H_2} - \frac{\mu_1 p_1}{H_1}\right)\right] \\ \Re\left[\left(\frac{1}{\mu_1-\mu_2}\right)\left(\frac{\mu_1 q_2}{H_2} - \frac{\mu_2 q_1}{H_1}\right)\right] & \Re\left[\left(\frac{1}{\mu_1-\mu_2}\right)\left(\frac{q_2}{H_2} - \frac{q_1}{H_1}\right)\right] \\ \Re\left[\left(\frac{\mu_1\mu_2}{\mu_1-\mu_2}\right)\left(\frac{q_2}{H_2} - \frac{q_1}{H_1}\right)\right] & \Re\left[\left(\frac{1}{\mu_1-\mu_2}\right)\left(\frac{\mu_2 q_2}{H_2} - \frac{\mu_1 q_1}{H_1}\right)\right] \end{array} \right] \left\{ \begin{array}{c} K_I \\ K_{II} \end{array} \right\} \tag{3.9}$$

As shown by first-order asymptotic expansions for the stress and displacements components, the SIFs represent the local behaviour of the elastic fields at the vicinity of the crack tip. However, for linear elastic materials, they can be related to the energy release rate of the body, which is a global parameter. For plane problems, the total energy release rate G is given by the superposition of the energy release rate of each mode, resulting in:

$$G = G_I + G_{II} \tag{3.10}$$

For isotropic materials, the energy release rate of each mode $M = I, II$ can be related to the SIFs as follows (IRWIN, 1957):

$$G_M = \frac{K_M^2}{E^*} \tag{3.11}$$

in which $E^* = E$ for plane stress and $E^* = E/(1-\nu^2)$ for plane strain. Substituting Eq. (3.11) into Eq. (3.10) leads to the following expression that relates G and the SIFs for isotropic materials:

$$G = \frac{K_I^2 + K_{II}^2}{E^*} \tag{3.12}$$

Regarding the anisotropic case, Sih, Paris, and Irwin (1965) showed that the relations between the energy release rate for each mode and the SIFs are expressed as follows:

$$G_I = -\frac{c_{22}}{2}\Im\left[\frac{K_I^2\left(\mu_1+\mu_2\right)+K_I K_{II}}{\mu_1\mu_2}\right] \tag{3.13}$$

$$G_{II} = \frac{c_{11}}{2}\Im\left[K_{II}^2\left(\mu_1+\mu_2\right)+K_I K_{II}\mu_1\mu_2\right] \tag{3.14}$$

where $\Im$ denotes the imaginary part operator. Substituting Eqs. (3.13) and (3.14) into Eq. (3.10) results in:

$$G = \beta_{11}K_I^2 + \beta_{12}K_I K_{II} + \beta_{22}K_{II}^2 \tag{3.15}$$

in which:

$$\beta_{11} = -\frac{c_{22}}{2}\Im\left[\frac{\mu_1+\mu_2}{\mu_1\mu_2}\right] \tag{3.16}$$

$$\beta_{22} = \frac{c_{11}}{2}\Im\left[\mu_1+\mu_2\right] \tag{3.17}$$

$$\beta_{12} = -\frac{c_{22}}{2}\Im\left[\frac{1}{\mu_1\mu_2}\right] + \frac{c_{11}}{2}\Im\left[\mu_1\mu_2\right] \tag{3.18}$$

3.2 Stress intensity factor evaluation

As mentioned in the previous section, the crack tip stability can be assessed through the SIFs values when considering LEFM. Thus, when dealing with fracture problems, the accurate evaluation of these factors is of great importance. For a limited number of simple applications, the SIFs can be determined analytically. However, for problems involving complex geometry and boundary conditions, the SIFs can only be computed by numerical techniques.

In general, the numerical strategies to evaluate the SIFs can be subdivided into two classes: the indirect and the direct methods. In the indirect methods, the mechanical response for the cracked body is obtained and then, in a post-processing phase, the SIFs are computed. Examples of indirect methods are the correlation displacement technique (PARIS; SIH, 1965), the crack closure integral (RYBICKI; KANNINEN, 1977) and the energy approach based on the conservative J-integral (RICE, 1968), being the latter widely applied in the literature. In the J-integral technique, the use of the energy balance over a region is able to mitigate errors in the mechanical fields that may occur at particular points, leading to accurate values for the SIFs.

In the direct methods, the SIFs are obtained directly from the solution vector of the system of equations determined by the numerical technique. In this approach, the approx-

imation space is extended to include enrichment functions, which contains the features of the analytical solution to the problem. An advantage of the direct methods over the indirect approaches is that no post-processing is required for the SIF evaluation, which can represent a reduction in computational cost. Also, since in the direct approach the solution space is augmented to capture the theoretical near-tip behaviour, the values obtained for the FITs present good accuracy. In this case, the errors in the crack parameters are in the same order of magnitude as those determined by energy-based indirect approaches that employ unenriched numerical methods to compute the mechanical fields. The application of the direct methods to extract the SIFs in the XBEM framework, including comparisons with indirect approaches, is reported in (ALATAWI; TREVELYAN, 2015; HATTORI; ALATAWI; TREVELYAN, 2016; ANDRADE; LEONEL, 2020).

In this study, both indirect and direct approaches are applied to compute the SIFs. In what follows, the indirect method based on the J-integral is presented for both isotropic and anisotropic materials. The proposed direct formulations are detailed in Chapters 4, 5 and 6.

3.2.1 J-integral

The path-independent J-integral proposed by Rice (1968), also known as the first component of the vector J_k (i.e. J_1), is evaluated along a path Γ_J enclosing the crack tip and is expressed by:

$$J = \int_{\Gamma_J} W n_1 - p_j u_{j,1} d\Gamma \tag{3.19}$$

where $W = \sigma_{ij} u_{i,j}/2$ is the strain energy density, $p_j = \sigma_{ij} n_i$ are the tractions along the integration path, u_j are the displacements along Γ_J and n_i are the components of the outward unit normal vector to the path.

In the proposed model, the path Γ_J is assumed as circular and centred at the crack tip. Such path starts in the collocation point of the BEM mesh at one crack surface and finishes at the symmetric collocation point at the opposite surface, as illustrated in Fig. 3.3. Moreover, the integration path must be contained within the domain. To satisfy this condition, a simple scheme that accounts for intersection distances is used to adjust the length of the path radius.

To evaluate the J-integral, a set of internal points is positioned over Γ_J to define the discretisation of the integration path. The internal fields are computed in a post-processing phase by Eqs. (2.47) and (2.48), respectively. Then, the displacement vector and the state of stress for each internal point are rotated accounting for the crack tip orientation.

For linear elastic materials, it is possible to show that the J-integral value, J, is equal to the energy release rate. In this case, J can be related to the SIFs by Eq. (3.12) or

Figure 3.3: Path used for evaluating the J-integral.

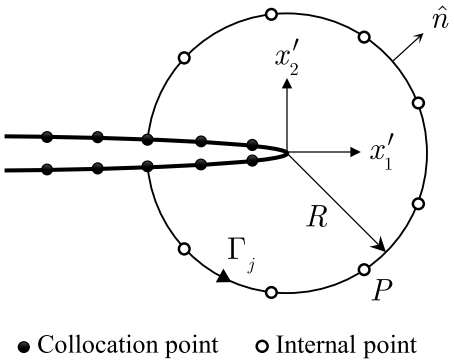

Source: Own author.

Eq. (3.15), depending on whether the material is isotropic or anisotropic, respectively. However, solely with the J-integral value given by Eq. (3.19), it is not possible to obtain the SIFs for mixed-mode problems due to the coupling of the SIFs in the energy release rate expression. Therefore, a mode decoupling strategy should be used to define K_I and K_{II} separately. Here, the interaction integral strategy is adopted, which is described in the following section.

3.2.2 Mode decoupling strategy

In the present investigation, the interaction integral technique (CHEN; SHIELD, 1977; WANG; YAU; CORTEN, 1980) is used to achieve mode decoupling. This approach is based on the definition of a conservative integral for two equilibrium states of a linear-elastic body. In what follows, the formulation applied for anisotropic materials will be presented. Then, the isotropic case is recovered as a particular condition of the anisotropic problem.

By defining a state (0) obtained from the superposition of two equilibrium states, denoted as (1) and (2), the following relations between the mechanical fields can be written:

$$\sigma_{ij}^{(0)} = \sigma_{ij}^{(1)} + \sigma_{ij}^{(2)} \tag{3.20}$$

$$u_i^{(0)} = u_i^{(1)} + u_i^{(2)} \tag{3.21}$$

$$K_M^{(0)} = K_M^{(1)} + K_M^{(2)} \tag{3.22}$$

The substitution of Eqs. (3.20) and (3.21) into the J-integral expression (3.19) written for the problem (0) leads to:

$$J^{(0)} = J^{(1)} + J^{(2)} + M^{(1,2)} \tag{3.23}$$

in which $J^{(k)}$ corresponds to the J-integral expression assessed with the mechanical fields of problem (k). Additionally, $M^{(1,2)}$ is defined as the M-integral, which represents an interaction integral between the equilibrium states (1) and (2) and is given by:

$$M^{(1,2)} = \int_{\Gamma_J} \left[\frac{\sigma_{ij}^{(1)} u_{i,j}^{(2)} + \sigma_{ij}^{(2)} u_{i,j}^{(1)}}{2} n_1 - \left(\sigma_{ij}^{(1)} u_{j,1}^{(2)} + \sigma_{ij}^{(2)} u_{j,1}^{(1)} \right) n_i \right] d\Gamma \tag{3.24}$$

Since the equality $J = G$ holds for linear-elastic materials, the J-integral of state (0) can be related to the SIFs of states (1) and (2) by combining Eqs. (3.15) and (3.22):

$$J^{(0)} = \beta_{11} \left(K_I^{(1)} + K_I^{(2)} \right)^2 + \beta_{12} \left(K_I^{(1)} + K_I^{(2)} \right) \left(K_{II}^{(1)} + K_{II}^{(2)} \right) + \beta_{22} \left(K_{II}^{(1)} + K_{II}^{(2)} \right)^2 \tag{3.25}$$

Equation (3.25) can be reorganised as follows:

$$J^{(0)} = J^{(1)} + J^{(2)} + 2\beta_{11} K_I^{(1)} K_I^{(2)} + \beta_{12} \left(K_I^{(1)} K_{II}^{(2)} + K_I^{(2)} K_{II}^{(1)} \right) + 2\beta_{22} K_{II}^{(1)} K_{II}^{(2)} \tag{3.26}$$

where:

$$J^{(k)} = \beta_{11} \left(K_I^{(k)} \right)^2 + \beta_{12} K_I^{(k)} K_{II}^{(k)} + \beta_{22} \left(K_{II}^{(k)} \right)^2 \tag{3.27}$$

represents the $J - K$ relation for problem (k).

Comparing Eqs. (3.23) and (3.26), the M-integral can also be written in terms of the interaction between the SIFs of the states (1) and (2) as follows:

$$M^{(1,2)} = 2\beta_{11} K_I^{(1)} K_I^{(2)} + \beta_{12} \left(K_I^{(1)} K_{II}^{(2)} + K_I^{(2)} K_{II}^{(1)} \right) + 2\beta_{22} K_{II}^{(1)} K_{II}^{(2)} \tag{3.28}$$

Equation (3.24) together with Eq. (3.28) allow the determination of the SIFs values of a mixed-mode fracture problem when the problems (1) and (2) are properly chosen. For this purpose, the state (1) is taken as the investigated problem, for which the values of K_I and K_{II} are desired. The state (2) is chosen as an auxiliary solution, with known mechanical fields. The first auxiliary solution, denoted here by the superscript (I), is taken as a cracked body subjected to a pure mode I loading. Therefore:

$$K_I^{(I)} = 1 \qquad K_{II}^{(I)} = 0 \tag{3.29}$$

Combining Eqs. (3.24) and (3.28) and applying the conditions of Eq. (3.29), the following relation is obtained:

$$2\beta_{11}K_I + \beta_{12}K_{II} = \int_{\Gamma_J} \left[\frac{\sigma_{ij}u_{i,j}^{(I)} + \sigma_{ij}^{(I)}u_{i,j}}{2} n_1 - \left(\sigma_{ij}u_{j,1}^{(I)} + \sigma_{ij}^{(I)}u_{j,1} \right) n_i \right] d\Gamma \tag{3.30}$$

in which the fields without the superscript are related to the investigated problem and are obtained from the numerical analysis. The components $\sigma_{ij}^{(I)}$ and $u_i^{(I)}$ correspond to the asymptotic stress and displacement fields determined, respectively, from Eqs. (3.4) and (3.6) after the conditions of Eq. (3.29) are imposed.

Similarly, the second auxiliary solution, denoted here by the superscript (II), is chosen as the problem of a cracked body subjected to a pure mode II loading. This case is represented by the following conditions:

$$K_I^{(II)} = 0 \qquad K_{II}^{(II)} = 1 \tag{3.31}$$

For this situation, the combination of Eqs. (3.24) and (3.28) after the conditions of Eq. (3.31) are imposed leads to:

$$\beta_{12}K_I + 2\beta_{22}K_{II} = \int_{\Gamma_J} \left[\frac{\sigma_{ij}u_{i,j}^{(II)} + \sigma_{ij}^{(II)}u_{i,j}}{2} n_1 - \left(\sigma_{ij}u_{j,1}^{(II)} + \sigma_{ij}^{(II)}u_{j,1} \right) n_i \right] d\Gamma \tag{3.32}$$

where $\sigma_{ij}^{(II)}$ and $u_i^{(II)}$ are the components of stress and displacement obtained, respectively, from Eqs. (3.4) and (3.6) after the conditions of Eq. (3.31) are prescribed.

After the numerical integration of the right-hand sides of Eqs. (3.30) and (3.32), which results, respectively, in $M^{(1,I)}$ and $M^{(1,II)}$, the following system of equations is obtained:

$$\begin{bmatrix} 2\beta_{11} & \beta_{12} \\ \beta_{12} & 2\beta_{22} \end{bmatrix} \begin{Bmatrix} K_I \\ K_{II} \end{Bmatrix} = \begin{Bmatrix} M^{(1,I)} \\ M^{(1,II)} \end{Bmatrix} \tag{3.33}$$

The solution of Eq. (3.33) gives the SIFs values for the investigated mixed-mode anisotropic fracture problem.

A similar approach can be applied to derive the expressions to determine the SIFs for isotropic materials. Alternatively, Eq. (3.33) can be particularised for the isotropic case by noting that $\beta_{11} = \beta_{22} = 1/E^*$ and $\beta_{12} = 0$ in this situation. Hence, the SIFs for isotropic materials are simply given by:

$$K_I = \frac{E^*}{2} \int_{\Gamma_J} \left[\frac{\sigma_{ij}u_{i,j}^{(I)} + \sigma_{ij}^{(I)}u_{i,j}}{2} n_1 - \left(\sigma_{ij}u_{j,1}^{(I)} + \sigma_{ij}^{(I)}u_{j,1} \right) n_i \right] d\Gamma \tag{3.34}$$

$$K_{II} = \frac{E^*}{2} \int_{\Gamma_J} \left[\frac{\sigma_{ij}u_{i,j}^{(II)} + \sigma_{ij}^{(II)}u_{i,j}}{2} n_1 - \left(\sigma_{ij}u_{j,1}^{(II)} + \sigma_{ij}^{(II)}u_{j,1} \right) n_i \right] d\Gamma \tag{3.35}$$

where the components of stress and displacement for the auxiliary states (I) and (II) are now given, respectively, by Eqs. (3.1) and (3.2) after the conditions of Eq. (3.29) or Eq. (3.31) are prescribed.

3.3 Propagation criterion

For mixed-mode problems, it is necessary to define an equivalent loading that results from the combination of the SIFs to establish a propagation criterion. Several approaches have been introduced in the literature to this end, and they are commonly based on either stress or energy methods. In the present study, the maximum circumferential stress criterion is applied for both isotropic and anisotropic materials and its formulation is presented in what follows.

3.3.1 Isotropic materials

The maximum circumferential stress criterion, proposed originally by Erdogan and Sih (1963), is related to the critical value of the tangential stress $\sigma_{\theta\theta}$. This stress component is obtained from the rotation of the stress tensor to the θ direction, being expressed as follows:

$$\sigma_{\theta\theta}(\theta) = \sigma_{11}\sin^2\theta + \sigma_{11}\cos^2\theta - 2\sigma_{12}\sin\theta\cos\theta \tag{3.36}$$

From the value of $\sigma_{\theta\theta}$, an equivalent SIF K_{eq} is defined as:

$$K_{eq}(\theta) = \sigma_{\theta\theta}(\theta)\sqrt{2\pi\rho} \tag{3.37}$$

Substituting Eq. (3.1) into Eq. (3.36) and then Eq. (3.36) into Eq. (3.37), the equivalent SIF is written in terms of K_I and K_{II} as follows:

$$K_{eq}(\theta) = \cos\left(\frac{\theta}{2}\right)\left[K_I\cos^2\left(\frac{\theta}{2}\right) - \frac{3}{2}K_{II}\sin\theta\right] \tag{3.38}$$

In the case of isotropic materials, the fracture toughness K_{Ic} is the same for every angle θ. Therefore, if the propagation occurs, the crack will grow along the direction θ_p that maximises K_{eq}. This propagation angle is given by:

$$\theta_p = \sin^{-1}\left(\frac{K_I K_{II} - 3K_{II}\sqrt{8K_{II}^2 + K_I^2}}{9K_{II}^2 + K_I^2}\right) \tag{3.39}$$

The value of K_{eq} evaluated by Eq. (3.38) along the direction computed from Eq. (3.39) can be compared to the fracture toughness to verify the crack tip stability. Then, the crack will grow if the following inequality is satisfied:

$$K_{Ic} - K_{eq}(\theta_p) \leq 0 \tag{3.40}$$

3.3.2 Anisotropic materials

Based on the isotropic case, Saouma, Ayari, and Leavell (1987) proposed a modified maximum circumferential stress criterion to anisotropic media. An equivalent SIF can be readily obtained by substituting Eq. (3.4) into Eq. (3.37), which leads to:

$$K_{eq}(\theta) = K_I \Re \left[\frac{\mu_1 H_2^3(\theta) - \mu_2 H_1^3(\theta)}{\mu_1 - \mu_2} \right] + K_{II} \Re \left[\frac{H_2^3(\theta) - H_1^3(\theta)}{\mu_1 - \mu_2} \right] \tag{3.41}$$

Due to the directional dependence of the mechanical properties in anisotropic materials, the propagation criterion can now be written as:

$$K_{Ic}(\theta) - K_{eq}(\theta) \leq 0 \tag{3.42}$$

in which the fracture toughness also vary with the direction θ. Therefore, propagation is considered to occur if the inequality is verified for any angle θ.

Saouma, Ayari, and Leavell (1987) characterised the variation of the fracture toughness in anisotropic materials with a two-parameter relationship. In their work, the fracture toughness is assumed as a second-order tensor and is evaluated from:

$$K_{Ic}(\theta) = K_{Ic}^{(1)} \cos^2(\theta - \gamma) + K_{Ic}^{(2)} \sin^2(\theta - \gamma) \tag{3.43}$$

in which $K_{Ic}^{(1)}$ and $K_{Ic}^{(2)}$ represent the fracture toughness along two orthogonally material directions and γ is the material orientation referenced to the local Cartesian coordinate system, as depicted in Fig. 3.4. Essentially, Eq. (3.43) admits the resistance to fracture as orthotropic.

According to Saouma, Ayari, and Leavell (1987), when only one of the fracture toughness parameters in Eq. (3.43) is known, the other can be estimated from the ratio between the elastic moduli as follows:

$$K_{Ic}^{(2)} \approx K_{Ic}^{(1)} \frac{E_1}{E_2} \tag{3.44}$$

Finally, the crack is assumed to grow if the condition in Eq. (3.42) is verified along the propagation direction determined by:

$$\theta_p = \arg\max \left[\frac{K_{eq}(\theta)}{K_{Ic}(\theta)} \right] \tag{3.45}$$

where arg max defines the argument θ that maximise the ratio between $K_{eq}(\theta)$ and $K_{Ic}(\theta)$. Naturally, the propagation only occurs if the ratio is greater than or equal to one.

Figure 3.4: Representation of the material directions near the crack tip.

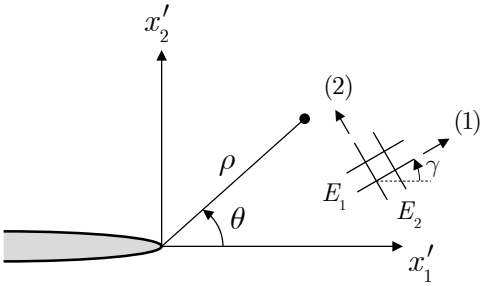

Source: Own author.

3.4 Interface fracture mechanics

The LEFM theory establishes that the stress field near the crack tip inside a homogeneous material develops the singularity of order $\mathcal{O}\left(\rho^{-1/2}\right)$, ρ being the distance from the tip. Moreover, as the crack grows, the behaviour of the stress singularity at the crack front remains the same, and the magnitude of the stress field continues to be defined by the SIFs. Therefore, instead of using the stress state, which is singular at the tip, the crack stability analysis is appropriately performed with the SIFs values.

On the other hand, in inhomogeneous domains, different orders of singularity may appear if a crack tip is positioned at a bimaterial interface. In Chapter 6, the problem of a crack lying along the interface is investigated. This configuration is of significant practical relevance since it allows the assessment of delamination between dissimilar media. In what follows, the interface fracture theory considering piecewise isotropic materials is briefly discussed. This formulation is explored in Chapter 6 to develop an enriched approach for the analysis of interface cracks.

Let Ω be a 2D-domain consisting of two dissimilar isotropic and elastic materials. The material above the interface is denoted as material 1, while the material below is defined as material 2. Consider a crack lying along the interface, as illustrated in Fig. 3.5, with Γ_1^C and Γ_2^C representing the upper and lower crack surfaces, respectively. Moreover, assume that the interface boundary Γ_1^I from material 1 is perfectly bonded with the interface boundary Γ_2^I from material 2. In this situation, the complete expansion for the crack-tip stress field is given by Deng (1993) and expressed as follows:

$$\sigma_{ij}(\rho,\theta,s)=\sum_{n=1}^{\infty}\frac{\rho^{\frac{n-2}{2}}}{\sqrt{2\pi}}\left\{\Re\left[\mathfrak{K}_n\rho^{\mathrm{i}\varepsilon_n}\right]\Sigma_{ij}^n(\theta,s)+\Im\left[\mathfrak{K}_n\rho^{\mathrm{i}\varepsilon_n}\right]\Upsilon_{ij}^n(\theta,s)\right\} \tag{3.46}$$

where $i,j=1,2$ denote the direction in the crack-tip coordinate system x_1x_2, (ρ,θ) are the crack-tip polar coordinates shown in Fig. 3.5, $s=1,2$ indicates the material 1 and 2, respectively, $\mathfrak{K}_n\in\mathbb{C}$ represents the n-th crack parameter, and $\Sigma_{ij}^n(\theta,s)$ and $\Upsilon_{ij}^n(\theta,s)$ are the stress functions given in Appendix A. The symbols $\Re$ and $\Im$ denote, respectively, the

real and imaginary parts of the quantity in brackets $[\bullet]$ and $\mathfrak{i} = \sqrt{-1}$ is the imaginary unit. Besides, ε_n is given as follows:

$$\varepsilon_n = \begin{cases} \varepsilon = \frac{1}{2\pi} \log \frac{\mu_2 \kappa_1 + \mu_1}{\mu_1 \kappa_2 + \mu_2}, & \text{if } n = 1, 3, 5, ... \\ 0, & \text{if } n = 2, 4, 6, ... \end{cases} \tag{3.47}$$

where ε is known as oscillatory parameter since it is related to the oscillatory behaviour of the odd terms, $\mu_s = E_s/[2(1+\nu_s)]$ is the shear modulus and κ_s is the Kolosov constant defined as $\kappa_s = 3 - 4\nu_s$ for plane strain and $\kappa_s = (3-\nu_s)/(1+\nu_s)$ for plane stress. E_s and ν_s represent, respectively, the Young's modulus and the Poisson's ratio of material $s = 1, 2$.

The general form of the crack-tip displacement field is also provided by Deng (1993) and is expressed by:

$$u_j(\rho, \theta, s) = \sum_{n=1}^{\infty} \frac{\rho^{n/2}}{\sqrt{2\pi}} \left\{ \Re \left[\mathfrak{K}_n \rho^{\mathfrak{i}\varepsilon_n} \right] \Delta_j^n(\theta, s) + \Im \left[\mathfrak{K}_n \rho^{\mathfrak{i}\varepsilon_n} \right] \Theta_j^n(\theta, s) \right\} \tag{3.48}$$

where $\Delta_j^n(\theta, s)$ and $\Theta_j^n(\theta, s)$ are the displacement functions given in Appendix A.

Figure 3.5: Interface crack between two dissimilar materials.

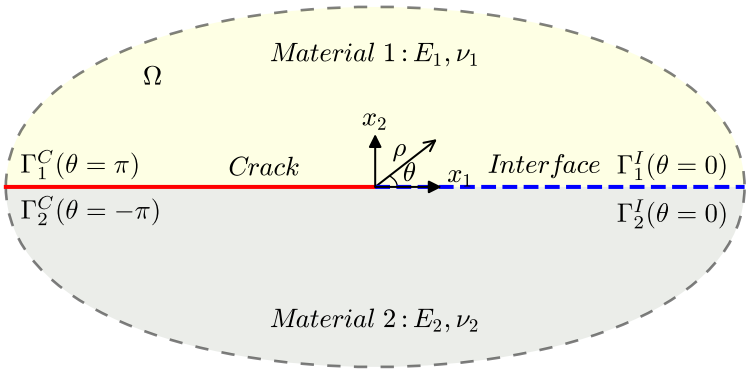

Source: Own author.

The numerical approach presented in Chapter 6 aims at the evaluation of the SIFs and T-stress for interface cracks. The SIFs are related to the leading term of the expansions in Eqs. (3.46) and (3.48), whereas the T-stress is associated to the second term in these expressions. Therefore, in the XIGABEM formulation for interface cracks, the expansion given in Eqs. (3.46) and (3.48) are truncated at $n = 1, 2$. For $n = 1$, the corresponding $\mathfrak{K}_n$ is acknowledged as complex SIF and is given by:

$$\mathfrak{K}_1 = K_1 + \mathfrak{i} K_2 \tag{3.49}$$

where K_1 and $K_2 \in \mathbb{R}$ are the modes 1 and 2 SIFs. For an interface crack of length $2a$ in an infinite body, subjected to remote stresses σ^∞ (normal to the crack surfaces) and τ^∞ (in-plane shear), the complex SIF is given by (RICE, 1988):

$$K_1 + \mathfrak{i}K_2 = (\sigma^\infty + \mathfrak{i}\tau^\infty)\sqrt{\pi a}\,(1 + 2\mathfrak{i}\varepsilon)\,(2a)^{-\mathfrak{i}\varepsilon} \tag{3.50}$$

Note from Eq. (3.50) that, unlike the homogeneous case, the SIFs cannot be unambiguously associated with the normal tension and the in-plane shear stresses. Therefore, the Arabic subscripts $1, 2$ are adopted to denote these factors instead of the classical Roman numerals I, II. Additionally, a dimensional analysis of Eq. (3.50) reveals that the physical units of the complex SIF are $FL^{-1.5-\mathfrak{i}\varepsilon}$, where F denotes force and L length. To recover the same units from the homogeneous case ($FL^{-1.5}$), the complex SIF must be multiplied by a factor $l^{\mathfrak{i}\varepsilon}$, where l is an arbitrary length. Also, note that homogeneous relationships are recovered from the above solutions if the oscillatory parameter is taken as $\varepsilon = 0$.

Using Eq. (3.49) and Euler's formula, the term in brackets that appears in Eqs. (3.46) and (3.48) can be rewritten as:

$$\mathfrak{K}_1\rho^{\mathfrak{i}\varepsilon} = [K_1\cos(\varepsilon\log\rho) - K_2\sin(\varepsilon\log\rho)] + \mathfrak{i}\,[K_1\sin(\varepsilon\log\rho) + K_2\cos(\varepsilon\log\rho)] \tag{3.51}$$

For $n = 2$, after examination of the stress functions given in Appendix A, it can be observed that $\Upsilon^2_{ij}(\theta, s) = 0$ for $i, j = 1, 2$. Consequently, only the real part of $\mathfrak{K}_2$ is related to the T-stress term in the stress expansion. Therefore, without loss of generality, the crack parameter $\mathfrak{K}_2$ is adopted as:

$$\mathfrak{K}_2 = K_T \tag{3.52}$$

where $K_T \in \mathbb{R}$ and the subscript T indicates that this factor is related to the T-stress.

Using Eq. (3.46), the stress functions given in Appendix A and Eq. (3.51), the two-term asymptotic expansion for stresses can be written as follows:

$$\sigma_{ij}(\rho,\theta,s) = \frac{1}{\sqrt{2\pi\rho}}\left\{\begin{array}{cc}\Sigma^1_{ij}(\theta,s) & \Upsilon^1_{ij}(\theta,s)\end{array}\right\}\left[\begin{array}{cc}\cos(\varepsilon\log\rho) & -\sin(\varepsilon\log\rho)\\ \sin(\varepsilon\log\rho) & \cos(\varepsilon\log\rho)\end{array}\right]\left\{\begin{array}{c}K_1\\ K_2\end{array}\right\} + \\ + C_s T\delta_{i1}\delta_{j1} \tag{3.53}$$

where $\Sigma^1_{ij}(\theta, s)$ and $\Upsilon^1_{ij}(\theta, s)$ are the stress functions for $n = 1$, δ_{ij} is the Kronecker delta and:

$$C_s = \begin{cases}\frac{(\kappa_2+1)\mu_1}{(\kappa_1+1)\mu_2}, & \text{if } s = 1\\ 1, & \text{if } s = 2\end{cases} \tag{3.54}$$

$$T = \frac{4}{\sqrt{2\pi}} \frac{(\kappa_1 + 1)\,\mu_2}{[(\kappa_1 + 1)\,\mu_2 + (\kappa_2 + 1)\,\mu_1]} K_T \tag{3.55}$$

where T denotes the T-stress.

By examination of Eq. (3.53), it can be noted that the SIFs K_1 and K_2 characterise the singular and oscillatory stress field related to the distance ρ. On the other hand, the T-stress defines the homogeneous term in the expansion, with $T_1 = C_1 T$ and $T_2 = T$ representing the contribution on the normal stress parallel to the crack surfaces at the tip in materials 1 and 2, respectively.

Analogously, the two-term asymptotic expansion for displacements can be defined from Eq. (3.48) and is given by:

$$u_j(\rho,\theta,s) = \sqrt{\frac{\rho}{2\pi}} \left\{ \begin{array}{cc} \Delta_j^1(\theta,s) & \Theta_j^1(\theta,s) \end{array} \right\} \left[\begin{array}{cc} \cos(\varepsilon \log \rho) & -\sin(\varepsilon \log \rho) \\ \sin(\varepsilon \log \rho) & \cos(\varepsilon \log \rho) \end{array} \right] \left\{ \begin{array}{c} K_1 \\ K_2 \end{array} \right\} + \\ + \frac{\rho}{\sqrt{2\pi}} \Delta_j^2(\theta,s) K_T \tag{3.56}$$

where $\Delta_j^1(\theta,s)$, $\Delta_j^2(\theta,s)$ and $\Theta_j^1(\theta,s)$ are displacement functions for $n = 1, 2$ that can be computed from Appendix A.

In the expansion shown in Eq. (3.56), the SIFs K_1 and K_2 are related to the square-root and oscillatory behaviour of the displacement field near the tip, while the T-stress parameter K_T is associated with a linear contribution related to the distance ρ.

4 Extended boundary element method

4.1 Initial considerations

In the DBEM formulation presented in Section 2.3, the polynomial functions used for the approximations are not suitable to capture the near-tip solutions defined by the LEFM shown in Section 3.1. This is clearly illustrated in Fig. 4.1, which presents the differences in the displacement field between the LEFM solution and the DBEM approximation using a discontinuous quadratic element adjacent to the tip. As the tip is approached, the square root behaviour in the analytical solution becomes dominant and cannot be properly represented by the polynomial function. Additionally, even the displacement continuity at the crack tip is not ensured in DBEM, with the crack tip opening displacement δ generally being non-zero.

Some approaches have been proposed to overcome the difficulties arising when modelling the near tip region, such as the use of quarter-point element (ALIABADI; ROOKE, 1991; BARSOUM, 1976; HENSHELL; SHAW, 1975) or the application of special singular shape functions for elements close to the tip (AKIN, 1976; TANAKA; ITOH, 1987; YAMADA et al., 1979). These strategies are simple to implement, but they are restricted to crack-tip elements while, in reality, the singular region may extend beyond their domain. Besides, the optimum choice for the size of the special elements is not clear (HARROP, 1982; INGRAFFEA; MANU, 1980; MARTÍNEZ; DOMÍNGUEZ, 1984; YEHIA; SHEPHARD, 1985).

A general strategy to include the analytical response into the approximations is the extended approach. Particularly, the enriched formulation based on Benzley (1974) allows the extension of the singular zone over several elements while the number of degrees of freedom remains fixed. Hence, the conditioning of the resulting system of equations is not significantly degraded as observed in PU-based enrichments.

In this chapter, an extended boundary element method (XBEM) formulation to model the crack growth in two-dimensional bodies is presented. Differently from previous investigations within XBEM, shifted enrichment functions are used to preserve the physical meaning of the nodal parameters. This strategy also prevents the distribution of the jump term from the boundary integral equations and reduces the singularity order from the integral kernels containing the enrichment functions. In addition, a novel displacement-discontinuity enrichment is introduced into the BEM framework to avoid the remeshing of existing boundary elements intercepted by cracks. The continuity conditions at the crack mouth are imposed to accommodate the additional DOF included by this enrichment. A traction enrichment composed of a Dirac delta term is also developed. This enriched approximation is able to model point boundary conditions within BEM, such as concen-

Figure 4.1: Crack tip displacements determined analytically by LEFM and the DBEM response defined with a quadratic approximation.

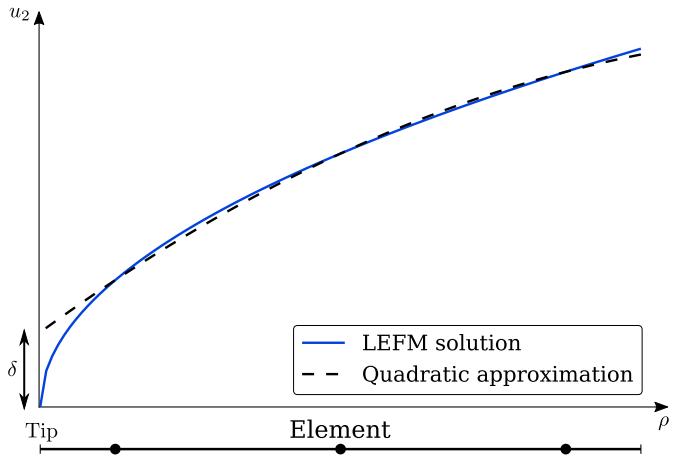

Source: Adapted from Simpson (2010).

trated forces and support points. Five numerical examples are presented to demonstrate the efficiency of the proposed XBEM formulation for the crack analysis of isotropic and anisotropic domains. The results are compared with the responses provided by unenriched DBEM and other solutions available in the literature. The main findings of this chapter are reproduced from Andrade and Leonel (2020).

4.2 Crack tip enrichment

4.2.1 Displacement approximation enrichment

According to the LEFM, the displacement field near a crack tip referred to a global coordinate system (Fig. 4.2) can be determined from the first-order expansions as:

$$u_j^{\lambda}(\rho,\theta) = \sum_{M=I,II} K_M^{\lambda} R_{jk}^{\lambda} \psi_{kM}(\rho,\theta) \tag{4.1}$$

where K_I^{λ} and K_{II}^{λ} are, respectively, the mode I and mode II stress intensity factors (SIFs) related to the crack tip λ. R_{jk}^{λ} represents the components of the rotation matrix referred to the crack tip orientation, which is given by:

$$\begin{bmatrix} R_{11} & R_{12} \\ R_{21} & R_{22} \end{bmatrix} = \begin{bmatrix} \cos\omega & -\sin\omega \\ \sin\omega & \cos\omega \end{bmatrix} \tag{4.2}$$

where ω is the angle between the local and global coordinates systems (see Fig. 4.2).

For isotropic materials, the terms ψ_{kM} are obtained from the Williams solution (WILLIAMS, 1957). These functions are determined from Eq. (3.2) and are expressed in matrix notation as:

$$\begin{bmatrix} \psi_{1I} & \psi_{1II} \\ \psi_{2I} & \psi_{2II} \end{bmatrix} = \frac{1}{2\mu}\sqrt{\frac{\rho}{2\pi}} \begin{bmatrix} \cos\left(\frac{\theta}{2}\right)(\kappa - \cos\theta) & \sin\left(\frac{\theta}{2}\right)(\kappa + 2 + \cos\theta) \\ \sin\left(\frac{\theta}{2}\right)(\kappa - \cos\theta) & -\cos\left(\frac{\theta}{2}\right)(\kappa - 2 + \cos\theta) \end{bmatrix} \tag{4.3}$$

Analogously, for anisotropic materials, ψ_{kM} are obtained from the solutions represented by Eq. (3.6) and are expressed in matrix notation as:

$$\begin{bmatrix} \psi_{1I} & \psi_{1II} \\ \psi_{2I} & \psi_{2II} \end{bmatrix} = \sqrt{\frac{2\rho}{\pi}} \begin{bmatrix} \Re\left[\frac{\mu_1 p_2 H_2 - \mu_2 p_1 H_1}{\mu_1 - \mu_2}\right] & \Re\left[\frac{p_2 H_2 - p_1 H_1}{\mu_1 - \mu_2}\right] \\ \Re\left[\frac{\mu_1 q_2 H_2 - \mu_2 q_1 H_1}{\mu_1 - \mu_2}\right] & \Re\left[\frac{q_2 H_2 - q_1 H_1}{\mu_1 - \mu_2}\right] \end{bmatrix} \tag{4.4}$$

Figure 4.2: Representation of the global displacement components near a crack tip.

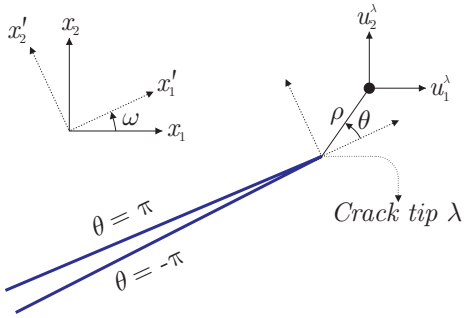

Source: Own author.

The polynomial approximation for the displacements given by Eq. (2.37) is not capable of accurately describing the $\sqrt{\rho}$ behaviour near the crack tip from the LEFM solution (Eq. (4.1)), as illustrated in Fig. 4.1. To confer the expected behaviour to this region and, consequently, improve the numerical responses, an enrichment strategy can be used. Here, the displacement approximation for an element e near a crack tip λ is augmented with functions based on ψ_{kM} as follows:

$$\tilde{u}_j^{e\lambda}(\xi) = \sum_{m=1}^{n_e} \phi^{em}(\xi) u_j^{em} + \sum_{M=I,II} \tilde{K}_M^\lambda R_{jk}^\lambda \sum_{m=1}^{n_e} \phi^{em}(\xi) \left[\psi_{kM}\left(\mathbf{x}^\lambda, \mathbf{x}(\xi)\right) - \psi_{kM}\left(\mathbf{x}^\lambda, \mathbf{x}(\xi^m)\right)\right] \tag{4.5}$$

where $\mathbf{x}^\lambda$ is the crack tip coordinates, ξ^m is the parametric coordinate at the m-th node and $\tilde{K}_M^\lambda$, for now, does not denote the SIFs but represents additional parameters introduced by the enrichment. The physical meaning of SIFs for these parameters will be recovered by imposition of the supplementary conditions, as will be further explained in Section 4.2.2.

The first term of the right-hand side of Eq. (4.5) is the same piecewise polynomial approximation used in conventional BEM, and it is capable of capturing rigid-body motions for the element. The second term is a shifted enrichment function that contains the $\sqrt{\rho}$ behaviour for the displacement approximation. Since this enrichment function is zero

at the nodes of enriched elements, the physical meaning of displacements is preserved for the nodal parameters u_j^{em}, i.e., $\tilde{u}_j^{e\lambda}(\xi^m) = u_j^{em}$. Consequently, the displacement components related to the jump term of the DBIE are not modified by this shifted enrichment. These conditions are not observed in the enrichment functions adopted in (SIMPSON; TREVELYAN, 2011b; ALATAWI; TREVELYAN, 2015; HATTORI; ALATAWI; TREVELYAN, 2016), in which the analytical expansion given in Eq. (4.1) is embedded directly into the approximation.

Introducing the displacement approximation presented by Eq. (4.5) in Eq. (2.36), the discrete form of the DBIE becomes:

$$c_{ij}(\mathbf{x}')u_j(\mathbf{x}') + c_{ij}(\bar{\mathbf{x}}')u_j(\bar{\mathbf{x}}') + \sum_{e=1}^{N_e}\sum_{m=1}^{n_e} P_{ij}^{em}u_j^{em} + \sum_{\lambda=1}^{N_t}\sum_{M=I,II}\tilde{K}_M^{\lambda}\sum_{e=1}^{N_e^{\lambda}}\tilde{P}_{iM}^{e\lambda} = \sum_{e=1}^{N_e}\sum_{m=1}^{n_e} U_{ij}^{em}p_j^{em} \tag{4.6}$$

where N_t is the number of tips in the analysis, N_e^{λ} is the number of elements enriched by tip λ and:

$$\tilde{P}_{iM}^{e\lambda} = \int_{-1}^{1} P_{ij}^{*}(\mathbf{x}', \mathbf{x}(\xi))J^e(\xi)R_{jk}^{\lambda}\sum_{m=1}^{n_e}\phi^{em}(\xi)\left[\psi_{kM}\left(\mathbf{x}^{\lambda}, \mathbf{x}(\xi)\right) - \psi_{kM}\left(\mathbf{x}^{\lambda}, \mathbf{x}(\xi^m)\right)\right]d\xi \tag{4.7}$$

From Eq. (4.6), it can be noted that the crack tip enrichment only introduces two additional degrees of freedom per crack tip, as in (SIMPSON; TREVELYAN, 2011b; ALATAWI; TREVELYAN, 2015; HATTORI; ALATAWI; TREVELYAN, 2016), regardless of the number of enriched elements. This feature is not observed in PU-based enrichment methods (SIMPSON; TREVELYAN, 2011a), in which extra parameters are created per enriched node. Consequently, the adopted approximation has no significant effect on the conditioning of the final system of equations when compared to other enrichment strategies.

Analogously, the discrete form of the TBIE considering the crack tip enrichment is obtained as:

$$\begin{aligned}\frac{1}{2}\left[p_j(\mathbf{x}') - p_j(\bar{\mathbf{x}}')\right] + n_i(\mathbf{x}')\left(\sum_{e=1}^{N_e}\sum_{m=1}^{n_e} S_{kij}^{em}u_k^{em} + \sum_{\lambda=1}^{N_t}\sum_{M=I,II}\tilde{K}_M^{\lambda}\sum_{m=1}^{N_e^{\lambda}}\tilde{S}_{ijM}^{e\lambda}\right) = \\ = n_i(\mathbf{x}')\sum_{e=1}^{N_e}\sum_{m=1}^{n_e} D_{kij}^{em}p_k^{em}\end{aligned} \tag{4.8}$$

where:

$$\tilde{S}_{ijM}^{e\lambda} = \fint_{-1}^{1} S_{kij}^{*}(\mathbf{x}', \mathbf{x}(\xi)) J^{e}(\xi) R_{kp}^{\lambda} \sum_{m=1}^{n_e} \phi^{em}(\xi) \left[\psi_{pM}\left(\mathbf{x}^{\lambda}, \mathbf{x}(\xi)\right) - \psi_{pM}\left(\mathbf{x}^{\lambda}, \mathbf{x}(\xi^{m})\right) \right] d\xi \quad (4.9)$$

The numerical evaluation of the new kernels $\tilde{P}_{iM}^{e\lambda}$ and $\tilde{S}_{ijM}^{e\lambda}$ follows the same approach used for P_{ij}^{em} and S_{kij}^{em}, respectively. To integrate singular elements, the SSM is applied and the corresponding formulation is presented in Appendix D. As shown in the referred appendix, the use of shifted enrichment functions reduces the singularity order of $\tilde{P}_{iM}^{e\lambda}$ and $\tilde{S}_{ijM}^{e\lambda}$. The former kernel becomes regular and can be assessed with the Gauss-Legendre rule, while the latter becomes strongly singular and can be evaluated semi-analytically by the SSM.

4.2.2 Crack tip tying constraint

To accommodate the degrees of freedom introduced by the enrichment and, consequently, recover a square system of equations, additional conditions are necessary. Here, a crack tip tying constraint similar to the one proposed by Alatawi and Trevelyan (2015) is applied. This condition enforces the continuity of the displacements between the upper and lower crack surfaces at the tip, which is not guaranteed in conventional DBEM since discontinuous elements are used to model the crack surfaces (see Fig. 4.1). In this strategy, a macro element is defined over the upper and lower surfaces, as shown in Fig. 4.3. Then, the displacements are extrapolated to the crack tip. For the upper surface, the expression for the displacement components at the crack tip, where the non-dimensional coordinate is $\xi_U = +1$, is given by:

$$\tilde{u}_{j}^{U}(+1) = \sum_{m=1}^{n_c} \phi^{Um}(+1) u_{j}^{Um} + \sum_{M=I,II} \tilde{K}_{M}^{\lambda} R_{jk}^{\lambda} \sum_{m=1}^{n_c} \phi^{Um}(+1) \left[-\psi_{kM}^{U}\left(\mathbf{x}^{\lambda}, \mathbf{x}(\xi^{m})\right) \right] \quad (4.10)$$

where n_c is the number of nodes used to define the extrapolation and the superscript U in the function ψ_{Mk} indicates that it is assessed in the upper surface, i.e. $\theta = \pi$. Better results are obtained when the extrapolation is carried out over more than one element. However, n_c should not exceed much more than ten nodes since the polynomial approximation will suffer from Runge's phenomenon.

Similarly, the extrapolation over the macro element on the lower surface at the local coordinate $\xi_L = -1$, which represents the tip, gives:

$$\tilde{u}_{j}^{L}(-1) = \sum_{m=1}^{n_c} \phi^{Lm}(-1) u_{j}^{Lm} + \sum_{M=I,II} \tilde{K}_{M}^{\lambda} R_{jk}^{\lambda} \sum_{m=1}^{n_c} \phi^{Lm}(-1) \left[-\psi_{kM}^{L}\left(\mathbf{x}^{\lambda}, \mathbf{x}(\xi^{m})\right) \right] \quad (4.11)$$

where the superscript L in the function ψ_{Mk} indicates that it is assessed in the lower surface, i.e. $\theta = -\pi$.

Enforcing the continuity of the displacements at the tip by making $\tilde{u}_j^U(+1) - \tilde{u}_j^L(-1) = 0$, leads to:

$$\sum_{m=1}^{n_c} \left[\phi^{Um}(+1)u_j^{Um} - \phi^{Lm}(-1)u_j^{Lm}\right] + \tag{4.12}$$
$$+ \sum_{M=I,II} \tilde{K}_M^\lambda R_{jk}^\lambda \sum_{m=1}^{n_c} \left[\phi^{Lm}(-1)\psi_{kM}^L\left(\mathbf{x}^\lambda, \mathbf{x}(\xi^m)\right) - \phi^{Um}(+1)\psi_{kM}^U\left(\mathbf{x}^\lambda, \mathbf{x}(\xi^m)\right)\right] = 0$$

Equation (4.12) provides two supplementary relations per crack tip that yield a square system of equations. Since the continuity condition is the same as observed in the asymptotic expansions (Eq. (4.1)), the enrichment parameters represent a good approximation for the SIFs. Hence, the XBEM formulation introduces the crack parameters as additional DOF for the problem and allows K_I and K_{II} to be computed directly from the solution of the resulting system of equations.

Figure 4.3: Auxiliary elements used to extrapolate the displacements for the crack tip.

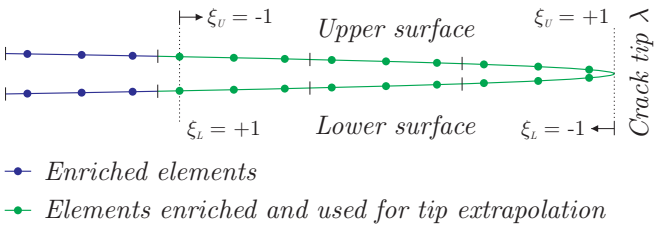

Source: Own author.

4.2.3 Resulting system of equations

With the presented crack tip enrichment, the resulting system of equations determined by the XBEM takes the following form:

$$\begin{bmatrix} \mathbf{H} & \mathbf{H}_C^K \\ \mathbf{H}_R^T & \mathbf{H}_R^K \end{bmatrix} \begin{Bmatrix} \mathbf{u} \\ \tilde{\mathbf{K}} \end{Bmatrix} = \begin{bmatrix} \mathbf{G} \\ \mathbf{0} \end{bmatrix} \{\mathbf{p}\} \tag{4.13}$$

Comparing Eqs. (2.45) and (4.13), it can be noted that the coefficients associated with the extra parameters introduce additional columns in the system given by the $2N \times 4N_t$ sub-matrix $\mathbf{H}_C^K$. Moreover, the crack tip tying constraint given by Eq. (4.12) is responsible for introducing the $2N_t \times 2N$ sub-matrix $\mathbf{H}_R^T$ and the $2N_t \times 2N_t$ sub-matrix $\mathbf{H}_R^K$ that accommodate the additional degrees of freedom stored in the $2N_t$ sub-vector $\tilde{\mathbf{K}}$.

After imposing the boundary conditions over Eq. (4.13), the following linear system is obtained:

$$\begin{bmatrix} \mathbf{A} & \mathbf{H}_C^K \\ \mathbf{H}_R^T & \mathbf{H}_R^K \end{bmatrix} \begin{Bmatrix} \mathbf{x} \\ \tilde{\mathbf{K}} \end{Bmatrix} = \begin{Bmatrix} \mathbf{f} \\ \mathbf{0} \end{Bmatrix} \tag{4.14}$$

The solution of Eq. (4.14) provides the unknown mechanical responses for the body, given by $\mathbf{x}$, as well as the enrichment parameters in $\tilde{\mathbf{K}}$, which are an approximation for the SIFs. Comparing Eqs. (4.14) and (2.46), it can be noted that the ordinary BEM system of equations is preserved, with the enrichment only introducing new sub-matrices associated with the additional parameters.

4.3 Heaviside enrichment

4.3.1 Discontinuous displacement enrichment

If an element $\bar{e}$ is crossed by a crack, a displacement discontinuity occurs at the intersection point. When using the ordinary DBEM approach, a local remeshing of the intersected element is necessary, in which discontinuous elements are adopted. This is followed by the reconstruction of the DBEM matrices in the positions related to the DOF from the original element, and by the addition of new rows and columns associated with the newly created nodes (see Andrade and Leonel (2019) for more details). To avoid these laborious procedures, the following discontinuous enrichment is introduced to capture the displacement discontinuity at element $\bar{e}$:

$$\tilde{u}_j^{\bar{e}}(\xi) = \sum_{m=1}^{n_{\bar{e}}} \phi^{\bar{e}m}(\xi) u_j^{\bar{e}m} + \sum_{l=a,b} g^l(\xi_P^{\bar{e}}, \xi) \alpha_j^{\bar{e}l} \sum_{m=1}^{n_{\bar{e}}} \phi^{\bar{e}m}(\xi) \left[H(\xi_P^{\bar{e}}, \xi) - H(\xi_P^{\bar{e}}, \xi^m) \right] \tag{4.15}$$

Figure 4.4: Representation of the discontinuous approximation for a quadratic element.

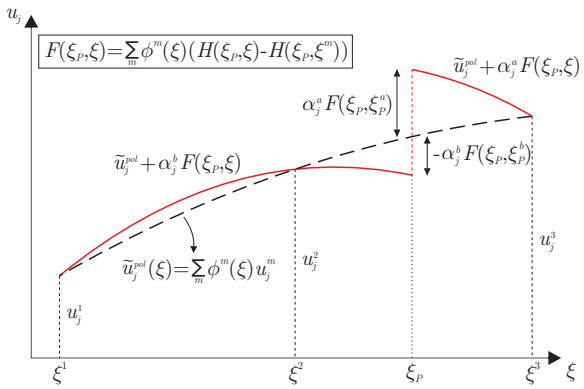

Source: Own author.

The approximation given by Eq. (4.15) is illustrated in Fig. 4.4 for a quadratic element. The first term of the right-hand side of Eq. (4.15) corresponds to the standard polynomial

displacement approximation used in the DBEM (Eq. (2.37)) and can represent rigid-body motions. The second term is a shifted enrichment function that has a discontinuity at the intersection point, represented by the non-dimensional coordinate $\xi_P^{\bar{e}}$. The discontinuous feature of the approximation is provided by the Heaviside sign step function, given by:

$$H(\xi_P^{\bar{e}}, \xi) = \begin{cases} -1, & \xi < \xi_P^{\bar{e}} \\ 1, & \xi \geq \xi_P^{\bar{e}} \end{cases} \tag{4.16}$$

The function $g^l(\xi_P^{\bar{e}}, \xi)$ is used to separate the approximation over the portion before the intersection, in which $l = b$, from the approximation over the portion after the intersection, where $l = a$. This function is defined by:

$$g^a(\xi_P^{\bar{e}}, \xi) = \begin{cases} 0, & \xi < \xi_P^{\bar{e}} \\ 1, & \xi \geq \xi_P^{\bar{e}} \end{cases} \qquad g^b(\xi_P^{\bar{e}}, \xi) = \begin{cases} 1, & \xi < \xi_P^{\bar{e}} \\ 0, & \xi \geq \xi_P^{\bar{e}} \end{cases} \tag{4.17}$$

Each discontinuous enrichment introduces four new DOF into the analysis, represented by $\alpha_j^{\bar{e}l}$ in Eq. (4.15). These additional parameters are responsible for giving the magnitude of the displacement jump at $\xi_P^{\bar{e}}$, as illustrated in Fig. 4.4. Furthermore, $\alpha_j^{\bar{e}a}$ and $\alpha_j^{\bar{e}b}$ separately control the behaviour of the displacements along the portions after and before the intersection point, respectively. This independence between the enrichment parameters has a beneficial effect on the conditioning of the system of equations.

Introducing Eq. (4.15) in the DBIE (Eq. (2.36)), the following discrete equation is obtained:

$$c_{ij}(\mathbf{x}')u_j(\mathbf{x}') + c_{ij}(\bar{\mathbf{x}}')u_j(\bar{\mathbf{x}}') + \sum_{e=1}^{N_e}\sum_{m=1}^{n_e} P_{ij}^{em}u_j^{em} + \sum_{\bar{e}=1}^{N_h}\sum_{l=a,b} \alpha_j^{\bar{e}l}\hat{P}_{ij}^{\bar{e}l} = \sum_{e=1}^{N_e}\sum_{m=1}^{n_e} U_{ij}^{em}p_j^{em} \tag{4.18}$$

where N_h is the number of Heaviside enrichments in the analysis and:

$$\hat{P}_{ij}^{\bar{e}l} = \int_{-1}^{1} P_{ij}^*(\mathbf{x}', \mathbf{x}(\xi))J^{\bar{e}}(\xi)g^l(\xi_P^{\bar{e}}, \xi)\sum_{m=1}^{n_{\bar{e}}} \phi^{\bar{e}m}(\xi)\left[H(\xi_P^{\bar{e}}, \xi) - H(\xi_P^{\bar{e}}, \xi^m)\right] d\xi \tag{4.19}$$

Analogously to the crack tip enrichment, the shifted discontinuous enrichment adopted here removes the singularity from kernel $\hat{P}_{ij}^{\bar{e}l}$. However, special attention is required to integration since the integrand is now discontinuous at $\xi_P^{\bar{e}} \in [-1, 1]$. For this purpose, a sub-element strategy can be applied. In this approach, the integrals over each portion of the element are computed separately, resulting in the following expressions:

$$\hat{P}_{ij}^{\bar{e}a} = \int_{-1}^{1} P_{ij}^*(\mathbf{x}', \mathbf{x}(\eta))J^{\bar{e}}(\eta)J^a(\eta)\sum_{m=1}^{n_{\bar{e}}} \phi^{\bar{e}m}(\eta)\left[1 - H(\xi_P^{\bar{e}}, \xi^m)\right] d\eta \tag{4.20}$$

$$\hat{P}_{ij}^{\bar{e}b} = \fint_{-1}^{1} P_{ij}^{*}(\mathbf{x}', \mathbf{x}(\eta)) J^{\bar{e}}(\eta) J^{b}(\eta) \sum_{m=1}^{n_{\bar{e}}} \phi^{\bar{e}m}(\eta) \left[-1 - H(\xi_P^{\bar{e}}, \xi^m)\right] d\eta \tag{4.21}$$

where $J^a(\eta) = (1 - \xi_P^{\bar{e}})/2$ and $J^b(\eta) = (\xi_P^{\bar{e}} + 1)/2$ represent the Jacobian of the linear transformation from η to ξ, in which η defines the local coordinate in each sub-element. The integrals in Eqs. (4.20) and (4.21) can be computed with the standard Gauss-Legendre quadrature to give the contributions over $\alpha_j^{\bar{e}a}$ and $\alpha_j^{\bar{e}b}$, respectively.

Substituting the discontinuous approximation into the TBIE gives:

$$\frac{1}{2}\left[p_j(\mathbf{x}') - p_j(\bar{\mathbf{x}}')\right] + n_i(\mathbf{x}') \left(\sum_{e=1}^{N_e} \sum_{m=1}^{n_e} S_{kij}^{em} u_k^{em} + \sum_{\bar{e}=1}^{N_h} \sum_{l=a,b} \alpha_k^{\bar{e}l} \hat{S}_{kij}^{\bar{e}l} \right) = n_i(\mathbf{x}') \sum_{e=1}^{N_e} \sum_{m=1}^{n_e} D_{kij}^{em} p_k^{em} \tag{4.22}$$

in which:

$$\hat{S}_{kij}^{\bar{e}l} = \fint_{-1}^{1} S_{kij}^{*}(\mathbf{x}', \mathbf{x}(\xi)) J^{\bar{e}}(\xi) g^{l}(\xi_P^{\bar{e}}, \xi) \sum_{m=1}^{n_{\bar{e}}} \phi^{\bar{e}m}(\xi) \left[H(\xi_P^{\bar{e}}, \xi) - H(\xi_P^{\bar{e}}, \xi^m)\right] d\xi \tag{4.23}$$

Again, the integrand in Eq. (4.23) is discontinuous due to the enrichment function. Therefore, the same sub-element approach used for $\hat{P}_{ij}^{\bar{e}l}$ should be applied to evaluate $\hat{S}_{kij}^{\bar{e}l}$, yielding:

$$\hat{S}_{kij}^{\bar{e}a} = \fint_{-1}^{1} S_{kij}^{*}(\mathbf{x}', \mathbf{x}(\eta)) J^{\bar{e}}(\eta) J^{a}(\eta) \sum_{m=1}^{n_{\bar{e}}} \phi^{\bar{e}m}(\eta) \left[1 - H(\xi_P^{\bar{e}}, \xi^m)\right] d\eta \tag{4.24}$$

$$\hat{S}_{kij}^{\bar{e}b} = \fint_{-1}^{1} S_{kij}^{*}(\mathbf{x}', \mathbf{x}(\eta)) J^{\bar{e}}(\eta) J^{b}(\eta) \sum_{m=1}^{n_{\bar{e}}} \phi^{\bar{e}m}(\eta) \left[-1 - H(\xi_P^{\bar{e}}, \xi^m)\right] d\eta \tag{4.25}$$

These kernels are regular for elements far from the source points. However, the SSM is applied for integrating elements containing the source point. The resulting expressions to be used in this case are shown in Appendix D.

It is worth mentioning that when the boundary integral equations were derived in Section 2.2, it was assumed continuity of displacements at the source points. Therefore, the intersection point must not coincide with a collocation point and, consequently, the inequality $\mathbf{x}' \neq \mathbf{x}(\xi_P)$ must always be verified. Otherwise, new jump terms associated with the additional parameters should be considered. In the proposed model, if this situation occurs, the node's position is modified according to the strategy presented in Section 4.7.

4.3.2 Continuity conditions at the crack mouth

To accommodate the additional parameters introduced by the Heaviside enrichment and recover square XBEM matrices, the continuity conditions at the crack mouth are used. For this purpose, macro elements are defined over the upper and lower crack surfaces, as illustrated in Fig. 4.5. Over each macro element, the displacements are extrapolated to the crack mouth. Then, the continuity between the displacements determined for the upper surface and the point immediately after $\xi_P^{\bar{e}}$ at the enriched element is enforced as:

$$\tilde{u}_j^U(+1) = \tilde{u}_j^{\bar{e}}(\xi_P^{\bar{e}a}) \tag{4.26}$$

where $\xi_P^{\bar{e}a}$ denotes the point immediately after $\xi_P^{\bar{e}}$.

An equivalent condition can be defined for the lower crack surface:

$$\tilde{u}_j^L(-1) = \tilde{u}_j^{\bar{e}}(\xi_P^{\bar{e}b}) \tag{4.27}$$

where $\xi_P^{\bar{e}b}$ represents the point immediately before $\xi_P^{\bar{e}}$.

Figure 4.5: Auxiliary elements used to extrapolate the displacements for the crack mouth.

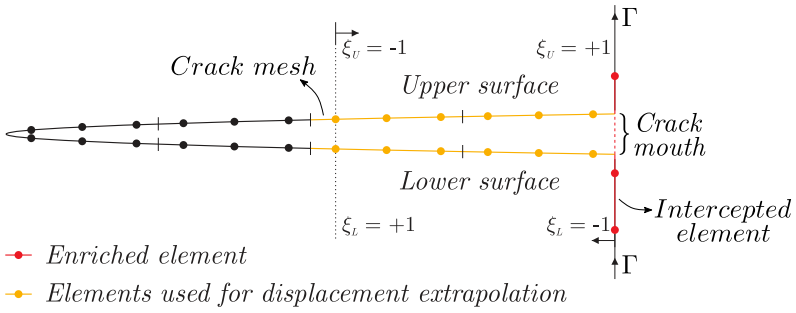

Source: Own author.

Substituting the discontinuous displacement approximation from Eq. (4.15) in Eqs. (4.26) and (4.27) and expanding the expressions for the displacement extrapolation over the macro elements on the crack surfaces leads to:

$$\sum_{m=1}^{n_c} \phi^{Um}(+1) u_j^{Um} - \sum_{m=1}^{n_{\bar{e}}} \phi^{\bar{e}m}(\xi_P^{\bar{e}}) u_j^{\bar{e}m} + \alpha_j^{\bar{e}a} \sum_{m=1}^{n_{\bar{e}}} \phi^{\bar{e}m}(\xi_P^{\bar{e}}) \left[-1 + H(\xi_P^{\bar{e}}, \xi^m)\right] = 0 \tag{4.28}$$

$$\sum_{m=1}^{n_c} \phi^{Lm}(-1) u_j^{Lm} - \sum_{m=1}^{n_{\bar{e}}} \phi^{\bar{e}m}(\xi_P^{\bar{e}}) u_j^{\bar{e}m} + \alpha_j^{\bar{e}b} \sum_{m=1}^{n_{\bar{e}}} \phi^{\bar{e}m}(\xi_P^{\bar{e}}) \left[1 + H(\xi_P^{\bar{e}}, \xi^m)\right] = 0 \tag{4.29}$$

Equations (4.28) and (4.29) produce four supplementary relations required to accommodate the additional parameters introduced by the discontinuous enrichment.

4.3.3 Resulting system of equations

The use of the Heaviside enrichment results in the following system of algebraic equations:

$$\begin{bmatrix} \mathbf{H} & \mathbf{H}_C^{\alpha} \\ \mathbf{H}_R^H & \mathbf{H}_R^{\alpha} \end{bmatrix} \begin{Bmatrix} \mathbf{u} \\ \boldsymbol{\alpha} \end{Bmatrix} = \begin{bmatrix} \mathbf{G} \\ \mathbf{0} \end{bmatrix} \{\mathbf{p}\} \tag{4.30}$$

where $\mathbf{H}_C^H$ is a $2N \times 4N_h$ sub-matrix representing additional columns obtained from kernels $\hat{P}_{ij}^{\bar{e}l}$ and $\hat{S}_{kij}^{\bar{e}l}$, $\mathbf{H}_R^H$ and $\mathbf{H}_R^{\alpha}$ are, respectively, $4N_h \times 2N$ and $4N_h \times 4N_h$ sub-matrices defined by the supplementary conditions and $\boldsymbol{\alpha}$ is a $4N_h$ sub-vector containing the parameters introduced by the discontinuous enrichment.

The imposition of the boundary condition in Eq. (4.30) results in:

$$\begin{bmatrix} \mathbf{A} & \mathbf{H}_C^{\alpha} \\ \mathbf{H}_R^H & \mathbf{H}_R^{\alpha} \end{bmatrix} \begin{Bmatrix} \mathbf{x} \\ \boldsymbol{\alpha} \end{Bmatrix} = \begin{Bmatrix} \mathbf{f} \\ \mathbf{0} \end{Bmatrix} \tag{4.31}$$

Comparing Eqs. (4.31) and (2.46), it can be noted that the proposed discontinuous enrichment only introduces new sub-matrices associated with the enrichment parameters, keeping the other components of the Eq. (4.31) the same as they would be in conventional DBEM.

4.4 Concentrated force enrichment

4.4.1 Traction approximation enrichment

In the conventional DBEM, the boundary conditions imposed over small areas, usually idealised as a point in the mechanical analyses, can become quite a cumbersome task. One of the alternatives to model such a case is to reduce the size of the element with prescribed conditions. This may result in short vicinity between source points, which has a negative effect on the conditioning of the system of equations. To overcome this drawback, for situations with concentrated forces, the following enrichment is proposed for the element $\bar{e}$ that contains the loading point $\mathbf{x}_F^{\bar{e}}$:

$$\tilde{p}_j^{\bar{e}}(\xi) = \sum_{m=1}^{n_{\bar{e}}} \phi^{\bar{e}m}(\xi) p_j^{\bar{e}m} + F_j^{\bar{e}} \Delta(\mathbf{x}_F^{\bar{e}}, \mathbf{x}(\xi)) \tag{4.32}$$

The first term of the right-hand side of Eq. (4.32) is the same piecewise polynomial approximation used in classical DBEM. The second corresponds to the enrichment part, which is composed of the force component $F_j^{\bar{e}}$ multiplied by the Dirac delta function at the point $\mathbf{x}_F^{\bar{e}}$. This enrichment term makes $\tilde{p}_j^{\bar{e}} \to \infty$ at the loading point, representing the effect of an idealised concentrated force. Evidently, the integration of the enrichment term over a region containing $\mathbf{x}_F^{\bar{e}}$ results in $F_j^{\bar{e}}$. The approximation given by Eq. (4.32) is in

accordance with a recent paper from Zhou et al. (2019). Nevertheless, Zhou et al. (2019) considered elements with a singular approximation for the displacements, with singularity at the point of application of the force, whereas, in the present study, the displacements are kept finite and given by the polynomial approximation in Eq. (2.37). The purpose to assume finite displacements is to be able to use the support point enrichment presented in Section (4.5).

Introducing the approximation from Eq. (4.32) in Eq. (2.36) and using the Dirac delta sifting property results in:

$$c_{ij}(\mathbf{x}')u_j(\mathbf{x}')+c_{ij}(\bar{\mathbf{x}}')u_j(\bar{\mathbf{x}}')+\sum_{e=1}^{N_e}\sum_{m=1}^{n_e} P_{ij}^{em}u_j^{em} = \sum_{e=1}^{N_e}\sum_{m=1}^{n_e} U_{ij}^{em}p_j^{em}+\sum_{\bar{e}=1}^{N_f} U_{ij}^{*}(\mathbf{x}',\mathbf{x}_F^{\bar{e}})F_j^{\bar{e}} \quad (4.33)$$

where N_f is the number of concentrated force enrichments.

Proceeding in a similar fashion to the TBIE yields:

$$\begin{aligned}\frac{1}{2}\left[p_j(\mathbf{x}')-p_j(\bar{\mathbf{x}}')\right]+n_i(\mathbf{x}')\sum_{e=1}^{N_e}\sum_{m=1}^{n_e} S_{kij}^{em}u_k^{em} = n_i(\mathbf{x}')\sum_{e=1}^{N_e}\sum_{m=1}^{n_e} D_{kij}^{em}p_k^{em}+ \\ + n_i(\mathbf{x}')\sum_{\bar{e}=1}^{N_f} D_{kij}^{*}(\mathbf{x}',\mathbf{x}_F^{\bar{e}})F_k^{\bar{e}}\end{aligned} \quad (4.34)$$

It can be noted from Eqs. (4.33) and (4.34) that the concentrated enrichment introduces new terms given by the product between the force components and the fundamental solutions assessed at the loading point. Since $F_j^{\bar{e}}$, $U_{ij}^{*}(\mathbf{x}',\mathbf{x}_F^{\bar{e}})$ and $D_{kij}^{*}(\mathbf{x}',\mathbf{x}_F^{\bar{e}})$ are known, the resulting term will be an additional constant for each equation that will contribute to the constant vector of the algebraic system. It is worth mentioning that, since the fundamental solutions are singular at $\mathbf{x}'$, the loading point must not coincide with a source point. Here, the position of a collocation point is modified if a concentrated force is prescribed at the same location, following the strategy presented in Section 4.7.

4.4.2 Resulting system of equations

The resulting system of linear equations considering the concentrated force enrichment is assembled as follows:

$$[\mathbf{H}]\{\mathbf{u}\} = \begin{bmatrix} \mathbf{G} & \mathbf{G}_C^F \end{bmatrix} \begin{Bmatrix} \mathbf{p} \\ \mathbf{F} \end{Bmatrix} \quad (4.35)$$

where $\mathbf{G}_C^F$ denotes additional columns obtained from the fundamental solutions U_{ij}^{*} and D_{kij}^{*} assessed at the loading point, and $\mathbf{F}$ represents the components of the applied forces.

The boundary conditions can be applied over Eq. (4.35) to define the final system of equations as follows:

$$\mathbf{A}\mathbf{x} = \mathbf{f} + \bar{\mathbf{f}} \tag{4.36}$$

where $\bar{\mathbf{f}}$ is a $2N$ constant vector given by the product between $\mathbf{G}_C^F$ and $\mathbf{F}$ that is added to the vector $\mathbf{f}$ in the final system of equations (Eq. (2.46)). Thus, the vector $\bar{\mathbf{f}}$ is the only change in the conventional DBEM approach when the concentrated force enrichment is considered.

4.5 Support point enrichment

4.5.1 Displacement boundary condition

To enforce a displacement restriction at one boundary point, the same traction enrichment presented in Eq. (4.32) can be used. However, the force components $F_j^{\bar{e}}$ are unknowns in this case, and correspond to the support reactions $R_j^{\bar{e}}$. The amount of additional parameters introduced by the enrichment depends on the number of directions with prescribed displacement. Consequently, new equations are necessary to recover a square system of equations. For this purpose, the boundary conditions at the support point are imposed using the displacement approximation for the element as follows:

$$\sum_{m=1}^{n_{\bar{e}}} \phi^{\bar{e}m}(\xi_S^{\bar{e}}) u_j^{\bar{e}m} = \bar{u}_j^{\bar{e}} \tag{4.37}$$

where $\xi_S^{\bar{e}}$ is the non-dimensional coordinate of the support point and $\bar{u}_j^{\bar{e}}$ denotes the prescribed displacement values.

4.5.2 Resulting system of equations

Regarding the support enrichment, the following system of linear equations is determined:

$$\begin{bmatrix} \mathbf{H} \\ \mathbf{H}_R^S \end{bmatrix} \{\mathbf{u}\} = \begin{bmatrix} \mathbf{G} & \mathbf{G}_C^F & \mathbf{0} \\ \mathbf{0} & \mathbf{0} & \mathbf{I} \end{bmatrix} \begin{Bmatrix} \mathbf{p} \\ \mathbf{R} \\ \bar{\mathbf{u}} \end{Bmatrix} \tag{4.38}$$

where $\mathbf{I}$ corresponds to the identity matrix and $\mathbf{R}$ contains the unknown support reactions. The supplementary conditions expressed by Eq. (4.37) give the additional rows $\mathbf{H}_R^S$ and the sub-vector with the prescribed displacement values $\bar{\mathbf{u}}$.

After the boundary conditions are imposed in Eq. (4.38), the following system is determined:

$$\begin{bmatrix} \mathbf{A} & -\mathbf{G}_C^F \\ \mathbf{H}_R^S & \mathbf{0} \end{bmatrix} \begin{Bmatrix} \mathbf{x} \\ \mathbf{R} \end{Bmatrix} = \begin{Bmatrix} \mathbf{f} \\ \bar{\mathbf{u}} \end{Bmatrix} \tag{4.39}$$

Again, when comparing the system of Eq. (4.39) with the system obtained with the unenriched DBEM approach (Eq. (2.46)), note that the proposed enrichment only introduces new sub-matrices related to the additional DOF, while the coefficients from the conventional formulation are preserved.

4.6 Flowchart for XBEM

The integration process considering the enriched boundary element formulation presented in this chapter is summarised in the flowchart shown in Fig. 4.6. The module containing the enrichment routines is highlighted. It can be noted that the changes in a conventional BEM code are minimal and, consequently, the extended formulation can be easily coupled to existing BEM codes.

4.7 Crack propagation analysis

In the numerical applications presented in Section 4.8, three different approaches are adopted for the crack analyses and the solutions provided by each one are compared. The first approach is the unenriched DBEM formulation, in which the SIFs are computed indirectly with the J-integral strategy (see Section 3.2). The second is the direct XBEM, which is able to determine the SIFs from the solution vector of the system given in Eq. (4.14). The third approach is the indirect XBEM, in which the crack enrichment is employed, but the SIFs are defined in a post-processing stage with the J-integral. It is worth mentioning that in the latter approach, the enrichment terms should be included in Eqs. (2.47) and (2.48) for computing the internal fields.

After evaluation of the SIFs, the crack stability is verified with the maximum circumferential stress criterion (ERDOGAN; SIH, 1963) (see Section 3.3). To perform the propagation analysis, a simple crack length control scheme is applied. In this strategy, only the critical crack tip is allowed to grow, as in (CARPINTERI; MONETTO, 1999; BUDYN et al., 2004). To achieve this condition, a load factor χ is defined as:

$$\chi = \left(\frac{K_{Ic}}{K_{eq}} \right)_{cr} \tag{4.40}$$

which corresponds to the minimum ratio K_{Ic}/K_{eq} in the analysis related to the critical tip.

Since the problem is linear elastic, the mechanical response determined by the numerical method can be weighted by χ to define a new state in which only the critical tip satisfies the propagation criterion $K_{eq} \geqslant K_{Ic}$. This tip is then extended by a prescribed

Figure 4.6: Integration process for XBEM.

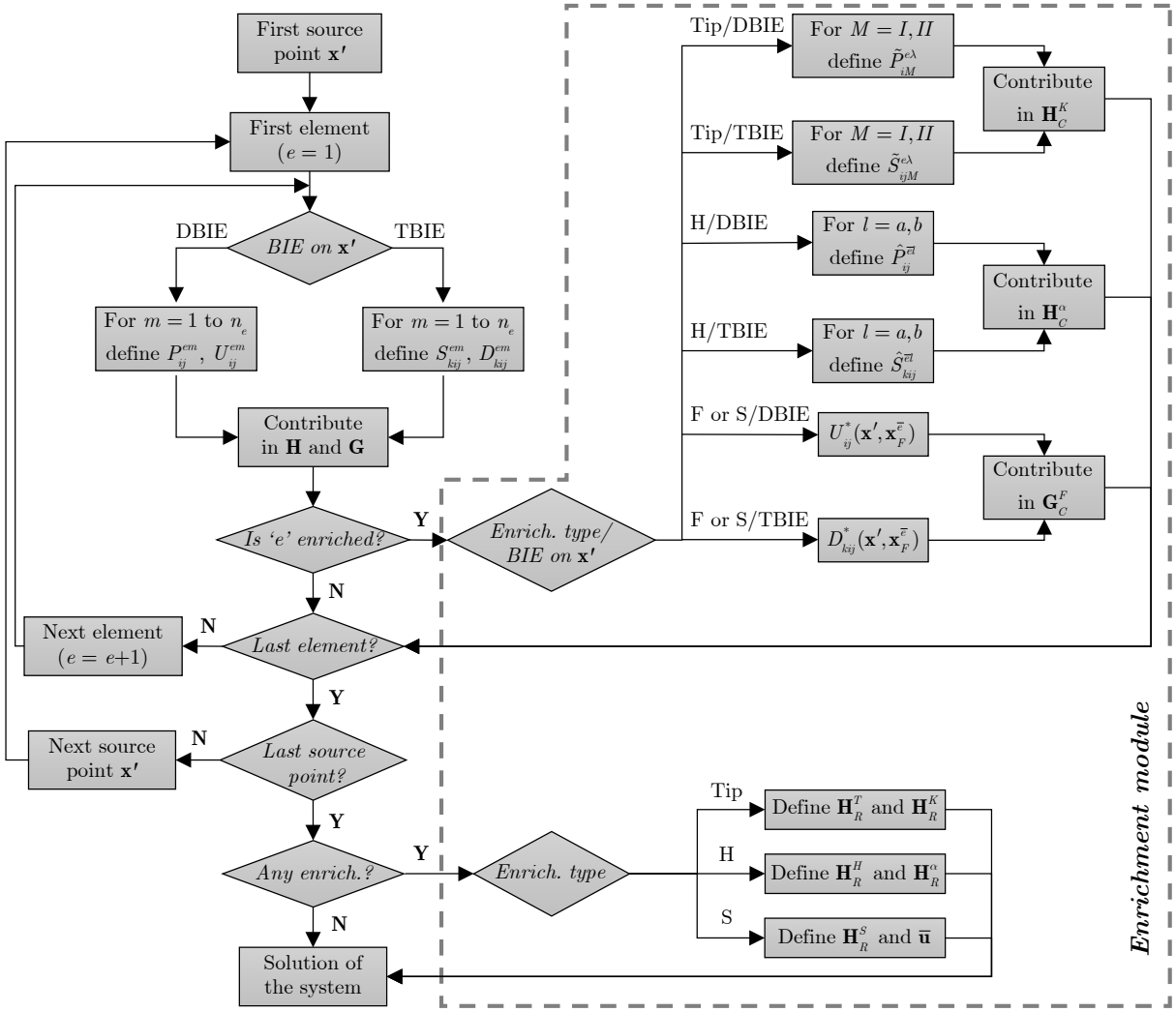

Source: Own author.

crack length increment Δa, which is defined as a straight segment. Another tip can only grow simultaneously if its ratio K_{Ic}/K_{eq} is equal to the lowest value in the analysis. After a new crack configuration is obtained following the propagation phase, the same process is repeated until there is no remaining active tip.

Inasmuch as the crack length of the critical tip is a monotonically increasing function during the propagation phase, the crack length control scheme allows the representation of the snap-back instability branch that may exist in the structural response. Despite simple, this strategy is able to provide good solutions for the applications considered in this study. It is worth mentioning that in problems involving competing cracks, a stability analysis may be performed to define the growing crack tip, as shown in the three-part paper of Sutula et al. (SUTULA et al., 2018a,c,b) within the FEM framework. However, this analysis is beyond the scope of the present investigation.

Therefore, the crack propagation scheme used in this study can be summarised in the

following steps:

1. Define the system of linear equations and solve it to obtain the nodal and enrichment parameters.

2. After solving the algebraic system, take the SIFs values directly from the solution vector or compute them indirectly through the J-integral technique.

3. Determine the equivalent SIF for each tip in the analysis with the maximum circumferential stress criterion (Section 3.3).

4. Take the minimum ratio K_{Ic}/K_{eq} in the analysis and compute the scaling factor χ from Eq. (4.40). Then, scale the mechanical solution (displacements, tractions and enrichment parameters) obtained in Step 1.

5. Extend the crack(s) with minimum ratio K_{Ic}/K_{eq} in the direction defined by the propagation criterion (Section 3.3).

6. Define the boundary element mesh for the new configuration and return to Step 1.

During the propagation phase, for problems in which the Heaviside enrichment is not considered, the modifications into the boundary element mesh and system of equations follow the same approach reported in previous work (ANDRADE; LEONEL, 2019). Instead, if a pre-existing element is crossed by a crack when the discontinuous enrichment is considered, the strategy proposed in Section 4.3 is used to represent the intersection. Furthermore, to handle the contact between the crack surfaces, the same node-to-node scheme also applied in (ANDRADE; LEONEL, 2019) is adopted here.

As pointed out in Section 4.3, the discontinuous enrichment is not applicable when an intersection coincides with a collocation point. Moreover, if a crack intersects an element close to a node, the accuracy of the integration over the tip elements when the node is taken as the source point can be compromised due to the quasi-singularity of the integral kernels. To overcome both issues, the node near the intersection is moved away from the crossing point, as depicted in Fig. 4.7. Evidently, the rows and columns in the BEM matrices associated with the node's DOF should also be modified to consider the new position. A similar approach is applied for the force and support enrichments to avoid the singularity occurring at the components of the sub-matrix $\mathbf{G}_C^F$.

The event involving the crack intersection of a discontinuous element in the discontinuity region requires special attention in the Heaviside enrichment. In this case, both columns related to the parameters $\alpha_j^{\bar{e}l}$ are zero, in which $l = a$ or $l = b$ if the intersection point is at the discontinuous region at the beginning or end of the element, respectively. This issue occurs since the shifted enrichment function is nil in the respective scenarios. Therefore, a special solution strategy should be used to deal with the resulting singular

Figure 4.7: Modification of the node position for a near intersection.

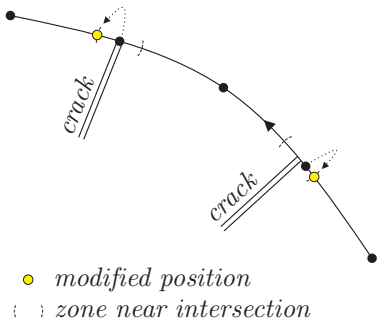

Source: Own author.

matrix as, e.g., the iterative scheme proposed in (STROUBOULIS; BABUŠKA; COPPS, 2000).

The XBEM approach proposed here also adaptively handle the changes of enriched elements during the crack growth. When a tip propagates, the new elements enriched by the tip and used for displacement extrapolation are restricted to the crack length increment Δa, whereas the crack tip enrichment is removed from elements enriched by the tip when it was in the former position. Hence, the tip functions are always included in the approximation of elements near the crack tip, where the square root behaviour for displacements is dominant. Besides, when a tip intercepts another element, the tip becomes inactive, and the parameters related to the crack tip enrichment are eliminated from the system of equations. The intercepted element is then enriched with the discontinuous displacement function, and the new elements defined for the growing crack are used to write the compatibility conditions at the crack mouth.

4.8 Numerical applications

In this section, five numerical examples are presented to validate the proposed XBEM formulation for isotropic and anisotropic materials. In the first and second, the accuracy of the responses obtained by the enriched formulation is analysed. The use of the XBEM approach in crack growth problems is addressed in the third and fourth examples. Finally, the last application demonstrates the applicability of the proposed method to simulate crack propagation in multi-cracked bodies.

In the examples, the enriched models are identified by the type of enrichment used, whether the crack tip enrichment (Tip) and/or the Heaviside enrichment (H) and by the approach used to define the SIFs, whether the direct method (Dir) or the indirect method based on the J-integral (J). The responses obtained by unenriched DBEM are simply denoted by 'DBEM'. In the results of deformed shapes, the elements are depicted in different colours and denoted by the type of enrichment applied to them: Tip, H, Support or Force. When an element is used for displacement extrapolation to provide

the supplementary constraints, it is identified as Ext.(Tip) or Ext.(H) if associated with a crack tip enrichment or to a Heaviside enrichment, respectively. For comparison purposes, all deformed shapes obtained by the XBEM formulation overlay the solutions determined by the conventional DBEM, which are depicted in grey.

4.8.1 Square plate with an edge crack

Consider a plate containing an edge crack and tensioned by a uniform loading $\bar{p}$, as shown in Fig. 4.8a. The dimensions of the structure are such that $2h = w$ and the crack length is defined as a. The material is assumed with Poisson's ratio $\nu = 0$. The top corner of the right edge is fixed along the x_1 direction, while the bottom corner is fixed in both directions. These restrictions are imposed in the models by the support enrichment developed in Section 4.5 to avoid rigid body motions.

Figure 4.8: (a) Tensioned plate containing an edge crack. (b) Boundary element mesh for $a/w = 0.5$ (Example 4.8.1).

(a) (b)

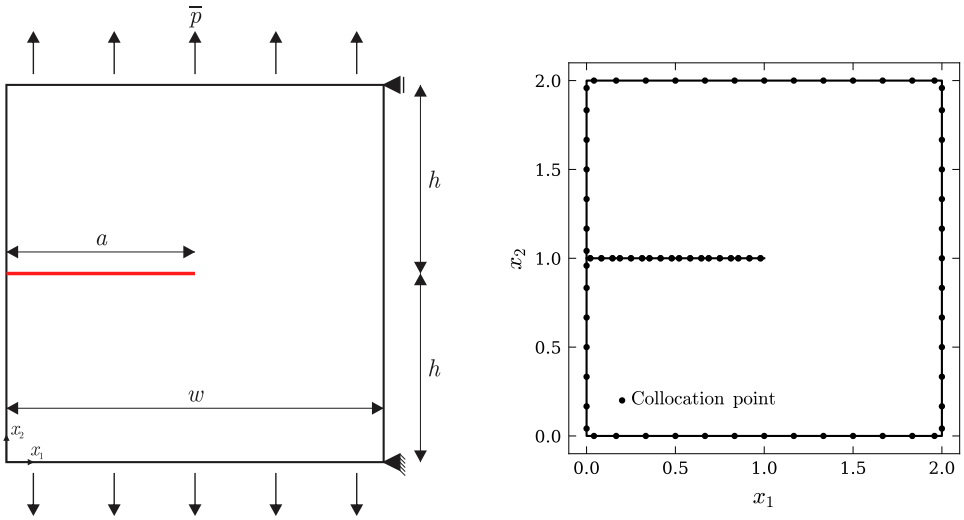

Source: Own author.

Initially, the accuracy of the crack tip enrichment is assessed considering the direct and indirect approaches for the evaluation of K_I at the right tip. The following values for ratio a/w are considered: 0.2, 0.3, 0.4 and 0.5. For the XBEM analyses, each edge of the plate and each crack surface is discretised with six quadratic elements, as depicted in Fig. 4.8b for $a/w = 0.5$. The crack tip enrichment is applied to elements on the entire right half of the crack (three elements per crack surface) to capture the near tip behaviour at the right tip. The same three elements at each crack surface are also used to define the crack tip tying constraint, which provides the required additional equations to XBEM.

Table 4.1 presents the results determined directly and indirectly by the proposed XBEM formulation. Good accuracy is observed when the responses are compared to

the reference values (Ref.) provided by Civelek and Erdogan (1982). The relative errors obtained by the direct method are inferior to 0.6%, while the combination of the enriched scheme with J-integral results in relative errors below 0.3%. Nevertheless, the indirect method requires the evaluation of internal fields along the J-integral path in a post-processing stage, increasing computational cost. The table also shows the numerical solutions determined by Portela, Aliabadi, and Rooke (1992) using the dual BEM (DBEM), by Oliveira and Portela (2019) using the Integrated Local Mesh Free (ILMF) model and by Belinha et al. (2016) using the Natural Neighbor Radial Point Interpolation Method (NNRPIM). For the analysed problem, the solutions obtained by the XBEM are, in general, more accurate than other numerical solutions available in the literature when compared with the reference values given by Civelek and Erdogan (1982). However, it is worth mentioning that the accuracy also depends on the intrinsic features of each numerical method and the technique used for SIF extraction.

Table 4.1: Normalised mode I stress intensity factor for the edge crack in a square plate (Example 4.8.1).

a/w	$K_I/(\bar{p}\sqrt{\pi a})$						Error (%)				
	XBEM(Dir)	XBEM(J)	DBEM	ILMF	NNRPIM	Ref.	XBEM(Dir)	XBEM(J)	DBEM	ILMF	NNRPIM
0.2	1.493	1.492	1.495	1.520	1.524	1.488	0.322	0.256	0.470	2.151	2.419
0.3	1.848	1.850	1.858	1.967	1.986	1.848	0.018	0.116	0.541	6.439	7.468
0.4	2.317	2.325	2.338	2.413	2.479	2.324	0.281	0.029	0.602	3.830	6.670
0.5	2.992	3.009	3.028	2.973	3.032	3.010	0.598	0.039	0.598	1.229	0.731

Source: Own author.

To verify the convergence of the proposed extended formulation, the same plate illustrated in Fig. 4.8a is considered with a fixed ratio $a/w = 0.5$. The number of quadratic elements used in the discretisation of each edge of the plate and each crack surface is varied from six to twenty in steps of two elements. Again, the displacement approximation of elements positioned at the right half of the crack are augmented with the crack tip enrichment to represent the near tip behaviour at the right tip, and three elements at each crack surface are used to define the crack tip tying constraint. The Heaviside enrichment is also applied to represent the intersection between the left crack tip with the structural boundary, with three elements used for defining the displacement extrapolation that provides the required supplementary equations.

Figure 4.10a presents the convergence of K_I, normalised by $\bar{p}\sqrt{\pi a}$, as a function of the number of DOF in the boundary element mesh for different enrichment scenarios. The results are compared with those obtained by the conventional DBEM approach - in which neither the crack tip enrichment nor the Heaviside enrichment is used - and the solution provided by Civelek and Erdogan (1982). Figure 4.10a shows that the responses obtained by the different approaches converge towards the reference solution available

in the literature. The models with crack tip enrichment present better accuracy when compared to the unenriched J-integral approach, as shown by the relative error plot depicted in Fig. 4.10b, which demonstrates the effectiveness of the proposed enriched formulation. The enrichment remarkably improves the accuracy of the indirect method, with the enriched J-integral approach giving the lowest relative error, around 0.05%. The solutions obtained by Alatawi and Trevelyan (2015) considering an XBEM formulation are also presented in Figs. 4.10a and 4.10b. From the results obtained in the present study and by Alatawi and Trevelyan (2015), it can be noted that the use of shifted enrichment functions can reduce the errors in the XBEM responses.

Figure 4.9: Variations of (a) the mode-I SIF (normalised by $\bar{p}\sqrt{\pi a}$) and (b) the relative error with the number of degrees of freedom in the boundary element model. The error is measured considering the result given by Civelek and Erdogan (1982) as reference (Example 4.8.1).

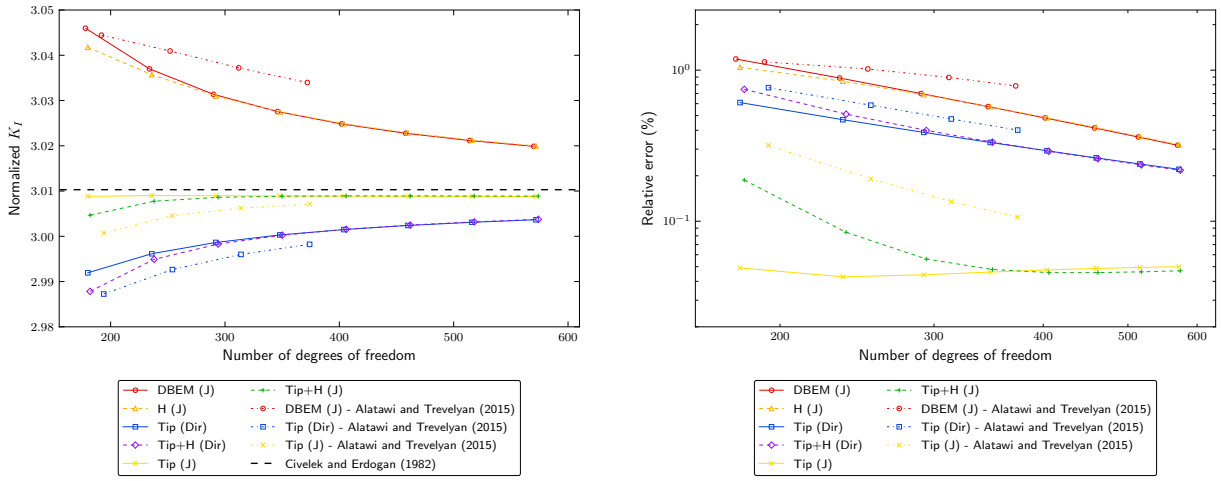

(a) (b)

Source: Own author.

Regarding the Heaviside enrichment, when coarser meshes are considered, the values given by scenarios with this enrichment are slightly lower than similar cases in which it is disregarded, as shown in Fig. 4.10a. These differences occur especially due to the size of the element enriched with the step function, ranging up to 0.14% for the coarsest mesh. Moreover, it is worth mentioning that in models without the Heaviside enrichment, a local refinement is performed by adding a node at the intersection point, which contributes to the differences in the solutions. However, as the mesh density increases, the responses obtained considering the Heaviside enrichment converge towards the solutions from similar models.

The ability of the Heaviside enrichment to represent the crack mouth opening displacement (CMOD) is illustrated in Fig. 4.10. The convergence between the responses of similar models with and without the discontinuous enrichment is also observed for normalised CMOD values. Besides, the differences between the solutions for coarser meshes

are also noted for this parameter. For models considering the crack tip enrichment, the normalised values of CMOD stabilise around 12.27, whereas the results keep varying with mesh refinement for models not considering this type of enrichment.

Figure 4.10: Variation of the CMOD (normalised by $\bar{p}w/E$) with the number of degrees of freedom in the analysis (Example 4.8.1).

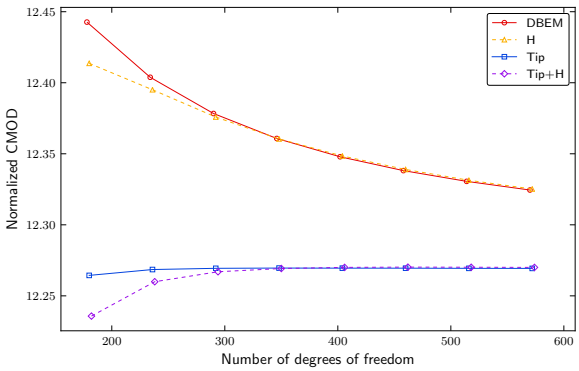

Source: Own author.

Figure 4.11: Deformed shape for the coarsest boundary element mesh used in the analysis. The XBEM result overlays the DBEM solution for comparison, and details of the crack tip and crack mouth are provided for better visualisation of these regions. Elements with enriched approximation and/or used for displacement extrapolation are depicted in different colours (Example 4.8.1).

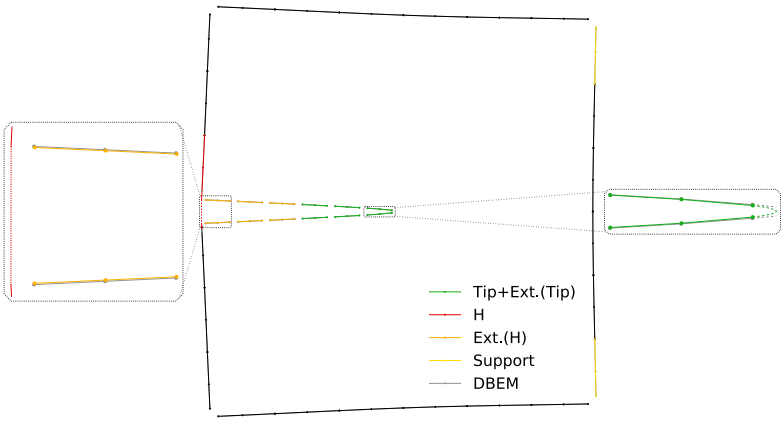

Source: Own author.

Figure 4.11 presents the deformed shape considering the coarsest mesh (six elements on each edge and each crack surface) obtained by the fully enriched model and the conventional DBEM approach. The XBEM result, in which enriched elements and elements used for displacement are depicted in different colours, overlays the DBEM solution, which is represented in grey. The details of the crack tip and the crack mouth show that the

differences between results from the enriched and unenriched formulations are more pronounced in these regions. These differences occur due to the features introduced by the enrichment terms and the imposition of the displacement constraints to define the additional equations needed in XBEM, whereas no restriction is made to guarantee continuity in the unenriched case. In particular, the details of the crack tip show that the tip enrichment can represent the square root behaviour expected for displacements. Besides, the crack tip is closed in this situation due to the imposition of the tying constraint. On the other hand, the polynomial approximation used in the conventional formulation is not capable of recovering the analytical displacement behaviour in this region; also, the crack tip remains opened in this case.

4.8.2 Anisotropic plate with a slanted crack

Figure 4.12a shows an anisotropic plate containing a centre crack submitted to a uniform tension $\bar{p}$. The dimensions of the structure are such that $h/w = 2$ and the crack length is defined as $a = 0.2w$. The slope of the crack is assumed constant and equal to $\theta = 45°$. The material is a glass-epoxy composite with the following elastic properties: $E_1 = 48.26$ GPa, $E_2 = 17.24$ GPa, $\mu_{12} = 6.89$ GPa and $\nu_{12} = 0.29$. Besides, plane stress condition is assumed. In this example, different values for material orientation γ are considered, and the SIFs are computed for each configuration considering the unenriched DBEM and the direct and indirect XBEM approaches. The solutions are compared with the responses provided by Sollero and Aliabadi (1995) and García, Sáez, and Domínguez (2004) using BEM and by Hattori, Alatawi, and Trevelyan (2016) using an XBEM formulation based on Stroh formalism.

The external boundary and each crack surface are discretised, respectively, with thirty-six and six quadratic elements, as illustrated in Fig. 4.12b. In the enriched models, each crack tip enriches the closest three elements on each crack surface, and the same elements are used to define the crack tip tying constraint.

Figures 4.14a and 4.14b show the results for K_I and K_{II} - normalised by $\bar{p}\sqrt{\pi a}$ - determined directly by XBEM and indirectly through the J-integral approach by unenriched DBEM and XBEM. The numerical solutions found in the literature are also provided. The shaded region in the figures represents the envelope defined by a 1% deviation from the average of the reference values. Good agreement is found between the results determined here and the reference solutions. The direct approach provides slightly greater values than the other two indirect methods applied in the present study, whereas the solutions obtained with the J-integral are quite similar. Nonetheless, all responses determined by the XBEM formulation are comprised within the 1% error envelope defined from the reference results. This demonstrates that the proposed direct method can provide accurate SIFs solutions for cracks in anisotropic domains.

Figure 4.12: (a) Tensioned anisotropic plate with centre slanted crack. (b) Boundary element mesh (Example 4.8.2).

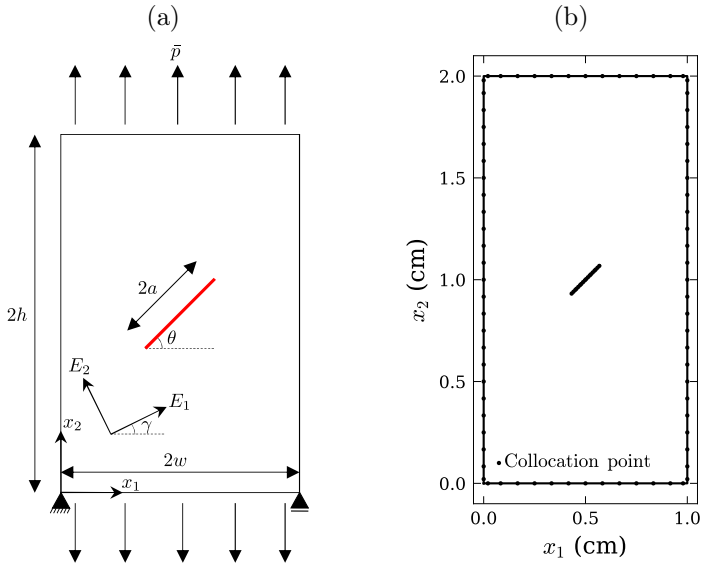

Source: Own author.

Figure 4.13: Variations of (a) mode-I and (b) mode-II SIF with the material orientation. The SIFs values are normalised by $\bar{p}\sqrt{\pi a}$. The shaded area corresponds to the 1% error envelope defined from the average of the reference solutions (Example 4.8.2).

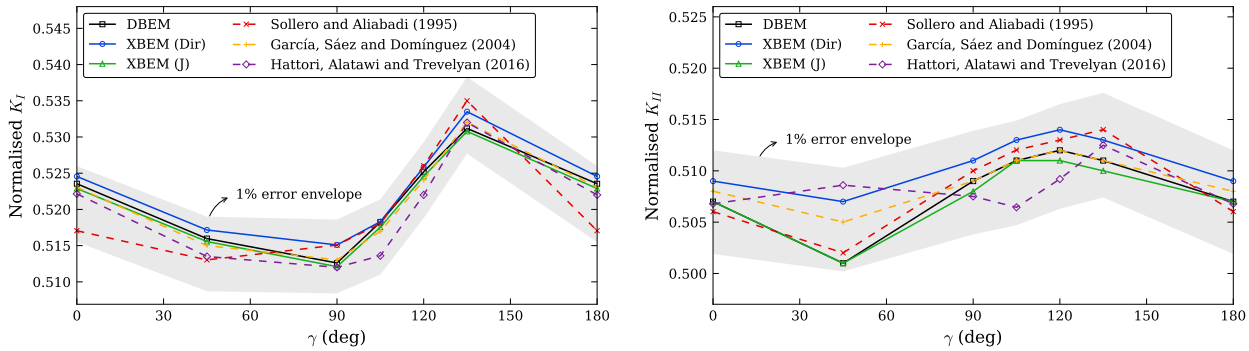

(a) (b)

Source: Own author.

4.8.3 Cracked three-point bending specimen

To illustrate the application of the proposed XBEM approach in the simulation of crack growth phenomenon, the experimental test conducted by Ingraffea and Grigoriu (1990) using the structure shown in Fig. 4.14a is numerically reproduced. The specimen is a $20d \times 8d$ rectangle, with thickness $0.5d$, made from acrylic glass with the following mechanical properties: $E = 3.10$ GPa (450 ksi), $\nu = 0.37$ and $K_{Ic} = 32.8$ Mpa$\sqrt{\text{mm}}$ (944 psi$\sqrt{\text{in}}$). The plate contains an edge crack of length $a = 2.5d$ and three holes positioned as indicated by Fig. 4.14a. The characteristic length d is 25.4 mm (1 in). A three-point bending test is performed, and the point boundary conditions are enforced

following the traction enrichment strategy presented in Sections 4.4 and 4.5. Besides, plane stress state is assumed.

Figure 4.14: (a) Three-point bending specimen containing an edge crack and three holes. (b) Boundary discretisation (Example 4.8.3).

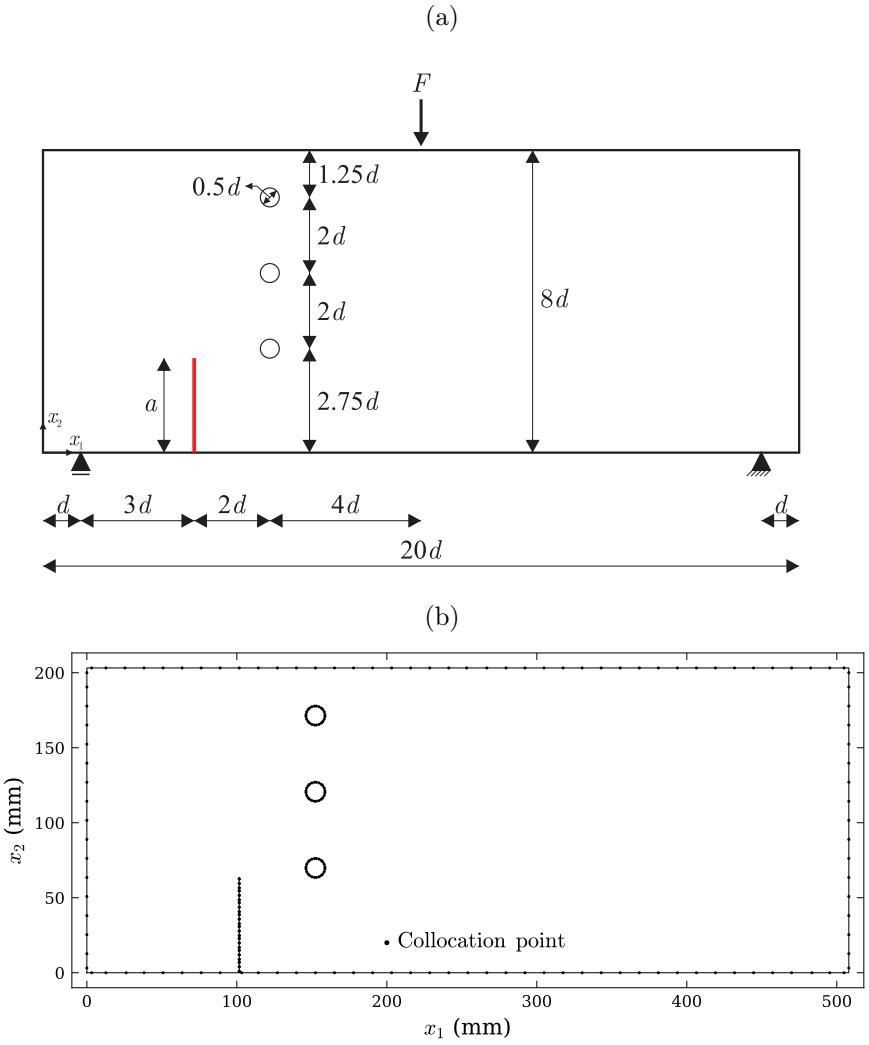

Source: Own author.

The boundary discretisation considered in the XBEM analysis consists of elements with quadratic approximation. Fifty-six elements are used for the external boundary, eight elements are adopted for each hole and eight elements are employed for each crack surface (Fig. 4.14b). Initially, four elements on each crack surface are enriched with the crack tip enrichment, while two elements are used for displacement extrapolation, as depicted in Fig. 4.15a. The Heaviside enrichment is utilised to represent the discontinuity occurring at the intersection between the crack and the bottom edge of the structure, with three crack elements used to define the displacement continuity constraint (see Fig. 4.15a).

During the propagation phase, the crack length increment is taken as $0.2d$, and two elements are used for the discretisation of each new crack surface. As the crack grows, the elements added to the new surfaces are enriched with the tip functions and used to

Figure 4.15: Evolution of the crack for three-point bending specimen obtained by XBEM considering the direct method for SIF computation. The XBEM results overlay the DBEM solutions for comparison. Elements with enriched approximation and/or used for displacement extrapolation are depicted in different colours and the solutions defined by the DBEM are represented in grey (Example 4.8.3).

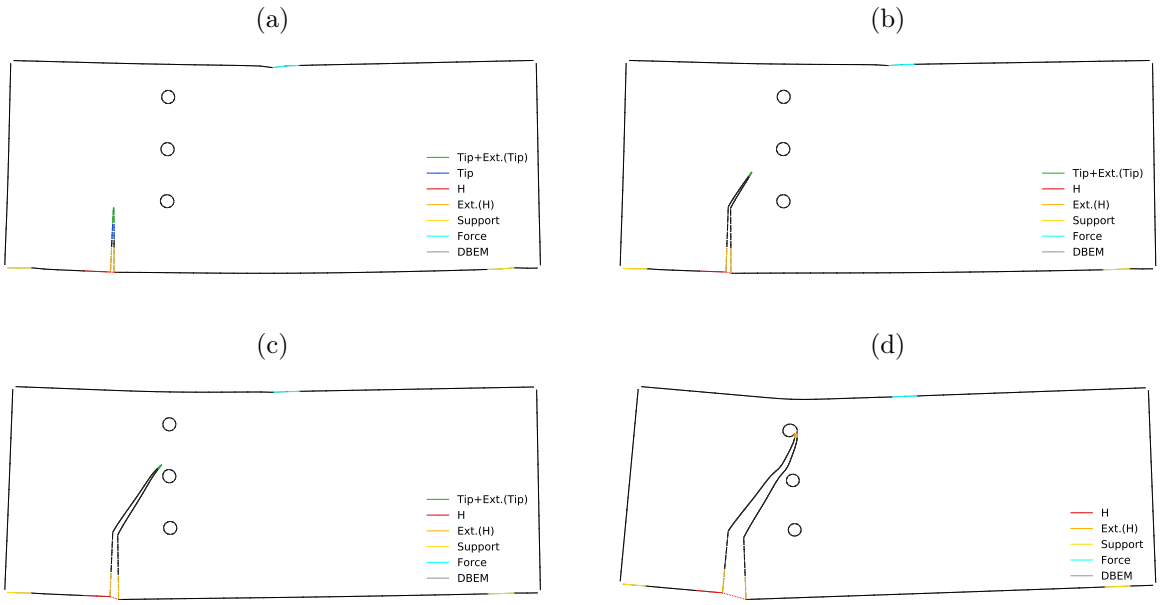

Source: Own author.

Figure 4.16: Comparison between the crack paths determined by different numerical approaches and the experimental response reported by Ingraffea and Grigoriu (1990) (Example 4.8.2).

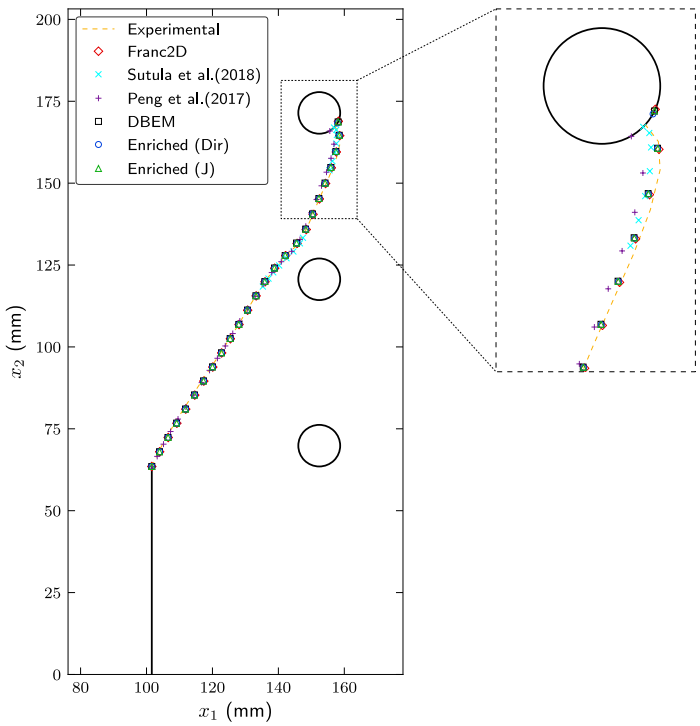

Source: Own author.

defined the crack tip tying constraint, whereas the crack tip enrichment is removed from the elements enriched by the former tip. The crack growth process determined by the XBEM formulation using the direct method for SIF extraction is illustrated in Fig. 4.15a to Fig. 4.15d. For comparison, the XBEM solutions overlay the responses defined by the unenriched DBEM approach, for which the J-integral is used to compute the SIFs. Good correspondence is observed between the deformed shapes determined by the two strategies, with the direct method having the advantage of avoiding the computationally expensive post-processing step for SIF definition. Furthermore, the Heaviside enrichment adopted in the XBEM formulation is capable of successfully representing the opening of the crack mouth at the bottom of the specimen and at the intersection of the crack with a curved element representing the edge of the top hole.

The final crack paths obtained by the enriched formulation considering both the direct and indirect methods for SIF evaluation are shown in Fig. 4.16. Figure 4.16 also presents the experimental results obtained by Ingraffea and Grigoriu (1990) and the numerical solutions determined by conventional DBEM, by Peng et al. (2017) and Sutula et al. (2018b) using XFEM and by the FEM-based software Franc2D (WAWRZYNEK; INGRAFFEA, 1994). Good agreement is observed between the paths determined by the XBEM approach and the experimental results reported by Ingraffea and Grigoriu (1990). The results also agree well with the XFEM solutions obtained by Peng et al. (2017) and Sutula et al. (2018b) and the responses provided by the unenriched DBEM and Franc2D. The main differences between the crack paths are observed at the end of the analysis, when the singular stress field is disturbed as the tip approaches the top hole. In this situation, the differences in the numerical solutions become more evident due to the selection of different propagation criteria and/or crack length increments.

Figure 4.17 shows the variation of the SIFs with the crack length for an applied force $F = 4.45$ kN (1000 lbf). Initially, the mode II SIF values are high and the crack develops a mixed-mode growth. After the initial increments, mode I propagation prevails until the crack approaches the holes. At these moments, the mode II SIF varies significantly, leading to changes in the crack direction, as shown by Fig. 4.16. The SIF values determined directly by the XBEM formulation are in excellent agreement with the results obtained through the J-integral approach by conventional DBEM, enriched DBEM and Franc2D. This demonstrates the efficiency of the direct method for computing the SIFs during the crack growth process with associated reduction of computational cost.

The variation of the vertical support reactions with the crack length is presented in Fig. 4.18. The values are related to the equilibrium state recovered by the crack length strategy, in which the applied force induces an equivalent SIF (K_{eq}) at the tip that is equal to the fracture toughness (K_{Ic}). Since the structure is an isostatic beam with symmetric boundary conditions, the numerical values of both vertical reactions are practically the same. Besides, the sum of the vertical components matches the magnitude of the

Figure 4.17: Variation of (a) mode I and (b) mode II SIFs with the crack length determined by enriched and unenriched DBEM and by Franc2D (Example 4.8.3).

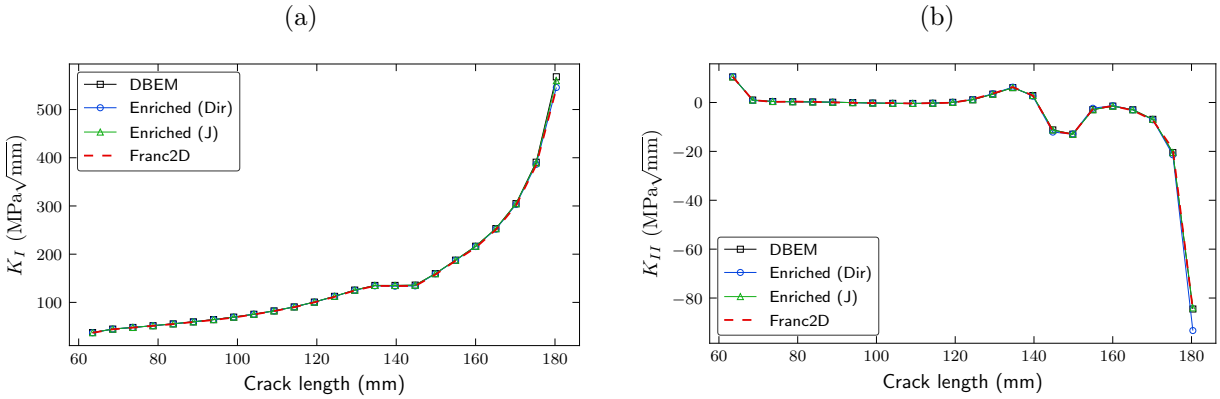

Source: Own author.

applied force, as expected by equilibrium consideration. Therefore, good correspondence is observed between the responses provided by the force and support enrichments herein proposed.

Figure 4.18: Vertical reactions (R_2) acting at the left and right supports. The total vertical reaction is also shown and is compared to the magnitude of the applied force (F) (Example 4.8.3).

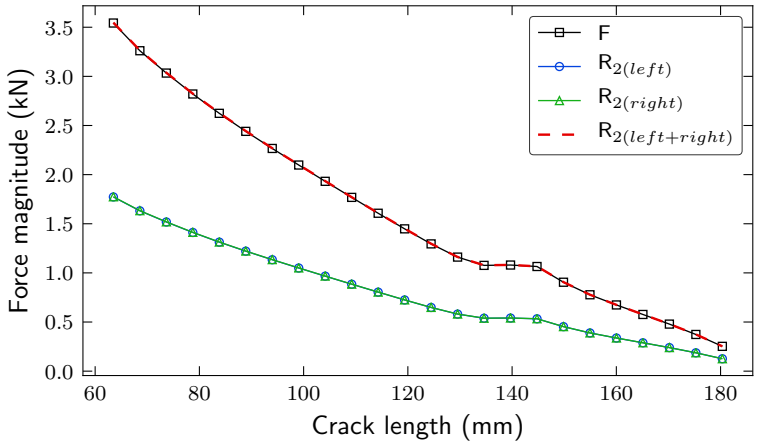

Source: Own author.

Finally, Fig. 4.19 illustrates the force-displacement curves considering the point of application of the force F obtained by the enriched and conventional DBEM formulations. The crack length strategy adopted here allows the representation of the snap-back branch of the global mechanical response. The good agreement between the SIFs determined by the unenriched and enriched DBEM approaches, shown in Figs. 4.17, leads to the good correspondence between the force-displacement curves since the crack length control relies on the equivalent SIF to define the structural behaviour.

Figure 4.19: Force-displacement curves for the cracked three-point bending specimen considering the enriched and unenriched DBEM approaches. The displacements are the vertical components taken at the point of application of the force.

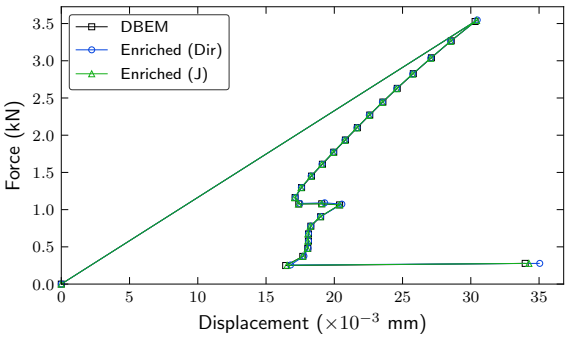

Source: Own author.

4.8.4 Crack propagation in anisotropic CSTBD specimens

In this example, three experimental tests on anisotropic materials conducted by Chen, Pan, and Amadei (1998) are numerically reproduced with the proposed enriched formulation. The tests were carried out on CSTDB (cracked straight-through Brazilian disc) specimens of shale of thickness t, with general geometry depicted in Fig. 4.20. The shale is considered transversely isotropic with the following elastic properties: $E_1 = E_3 = 20.326$ GPa, $E_2 = 16.605$ GPa, $\mu_{12} = \mu_{23} = 6.683$ GPa, $\mu_{13} = 7.590$ GPa, $\nu_{12} = \nu_{23} = 0.462$ and $\nu_{13} = 0.339$. Table 4.2 presents the characteristics of each specimen analysed, being the material orientation γ the main difference between them. Here, the numerical analyses are performed using the conventional DBEM and direct XBEM to simulate the crack propagation in the anisotropic domain. Twenty discontinuous quadratic elements are used to discretise each crack surface, while thirty-two discontinuous elements are applied to the external boundary - being two linear in the region of application of boundary conditions and the others quadratic (see Figure 4.21 for mesh detail). In the unenriched model, the boundary conditions are considered distributed over the linear elements, while in the enriched formulation the concentrated force and support points are simulated with the traction enrichments shown in Sections 4.4 and 4.5, respectively. Plane strain is assumed. The maximum circumferential stress criterion is adopted to define the crack growth direction (see Section 3.3.2) and the crack length increment during propagation is taken as $\Delta a = 1.0$ mm.

Chen, Pan, and Amadei (1998) determined the crack orientation β as the angle that caused only mode II loading at the tips in their numerical simulations using DBEM. Then, the same β values defined numerically were used to fabricate the testing specimens. In the present work, the values of β for pure mode II are also computed using the DBEM and XBEM, and the results are presented in Table 4.3. Only for specimen S1, the crack orientation defined here is slightly lower than in Chen, Pan, and Amadei (1998). Table 4.3 also presents the numerical results determined for K_{II} considering the application of the

Figure 4.20: CSTBD specimen of shale rock (Example 4.8.4).

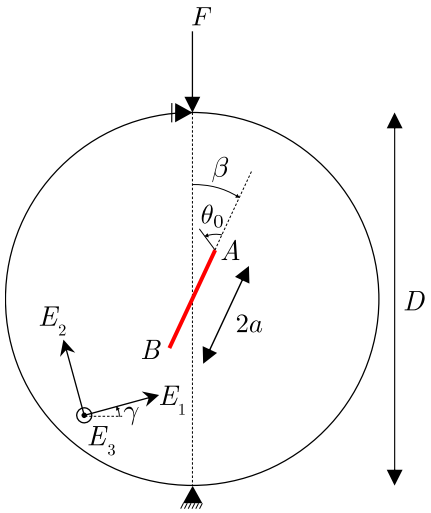

Source: Own author.

Table 4.2: Characterisation of CSTBD specimens (Example 4.8.4).

Specimen	D(mm)	t (mm)	$2a$ (mm)	γ (°)
S1	70.10	9.50	19.61	0
S2	70.10	9.50	19.20	-45
S3	70.10	9.42	20.19	-90

Source: Own author.

failure load F obtained experimentally. Good agreement is attained between the numerical responses.

Table 4.3: Numerical values obtained for β and K_{II}. Mode II SIF corresponds to the application of the failure load F obtained from the experimental results determined by Chen, Pan, and Amadei (1998) (Example 4.8.4).

Specimen	F(kN)	β (°)			K_{II} (Mpa×mm$^{0.5}$)		
		DBEM	XBEM (Dir)	Ref.	DBEM	XBEM (Dir)	Ref.
S1	2.95	27.8	27.8	28.2	-28.44	-28.79	-28.01
S2	2.23	27.6	27.6	27.6	-21.27	-21.55	-20.87
S3	2.68	25.9	25.9	25.9	-25.84	-26.06	-26.06

Source: Own author.

The crack initiation angle θ_0 is also compared with the reference. Table 4.4 shows the results obtained in the present work using DBEM and direct XBEM and those determined numerically and experimentally by Chen, Pan, and Amadei (1998). Again, good agreement is found between the numerical results. Moreover, when compared to experimental results, the solutions provided by the extended approach are near to the responses defined for at least one of the tips.

Table 4.4: Numerical and experimental crack initiation angles $\theta_0\,(^\circ)$ (Example 4.8.4)

Specimen	Numerical			Experimental		
	DBEM	XBEM (Dir)	Ref.	Tip A	Tip B	Average
S1	70.48	70.50	71.87	78.6	70.5	74.6
S2	70.41	70.43	70.46	67.8	73.5	70.7
S3	69.48	69.50	69.44	67.5	63.3	65.4

Source: Own author.

Finally, Figure 4.21 provides the propagation paths determined in the present investigation using DBEM and XBEM. An excellent agreement is observed between the responses, demonstrating that the direct approach can be successfully applied to simulate the crack growth in anisotropic materials with the advantage of dismissing the post-processing strategy to compute the SIFs. The experimental results reported by Chen, Pan, and Amadei (1998) are also presented. Again, the XBEM solutions are capable of representing the crack path in all three testing specimens until the tips reach the compression zone near the applied force and support point. After this stage, the numerical solution becomes unstable and the propagation path starts to zigzag. Nevertheless, most of the XBEM solutions agrees well with the experimental results, which demonstrates the efficiency of the proposed model to simulate real problems.

4.8.5 Multi-cracked square plate

The final example of this chapter presents the application of the XBEM for the crack propagation modelling of a multi-cracked domain, represented by the square plate depicted in Fig. 4.22a. The plate contains ten randomly distributed cracks and is tensioned by a uniform loading $\bar{p}$. The dimension w is equal to 50.8 mm (2 in) and Table 4.5 presents the initial coordinates for the crack tips. The material has Young's modulus $E = 689.5$ MPa (100 ksi), Poisson's ratio $\nu = 0.3$ and material toughness $K_{Ic} = 27.8$ Mpa$\sqrt{\text{mm}}$ (800 psi$\sqrt{\text{in}}$). Besides, the plate is considered with unit thickness and plane strain condition is assumed for the analyses. This problem was also investigated by Budyn et al. (2004) using the XFEM and by Azadi and Khoei (2010) using the FEM, and their solutions are used as references.

The initial boundary element discretisation contains forty-eight elements distributed along the plate's edges and six elements placed at each crack surface, as illustrated by Fig. 4.22b. A quadratic approximation is used for all elements. During the propagation phase, the crack length increment is $\Delta a = 1.778$ mm (0.07 in) and two elements are used for each newly created crack surface.

Figure 4.21: Comparison between the propagation paths obtained experimentally and the numerical solutions determined by DBEM and XBEM for the CSTBD specimens (a) S1, (b) S2 and (c) S3 (Example 4.8.4).

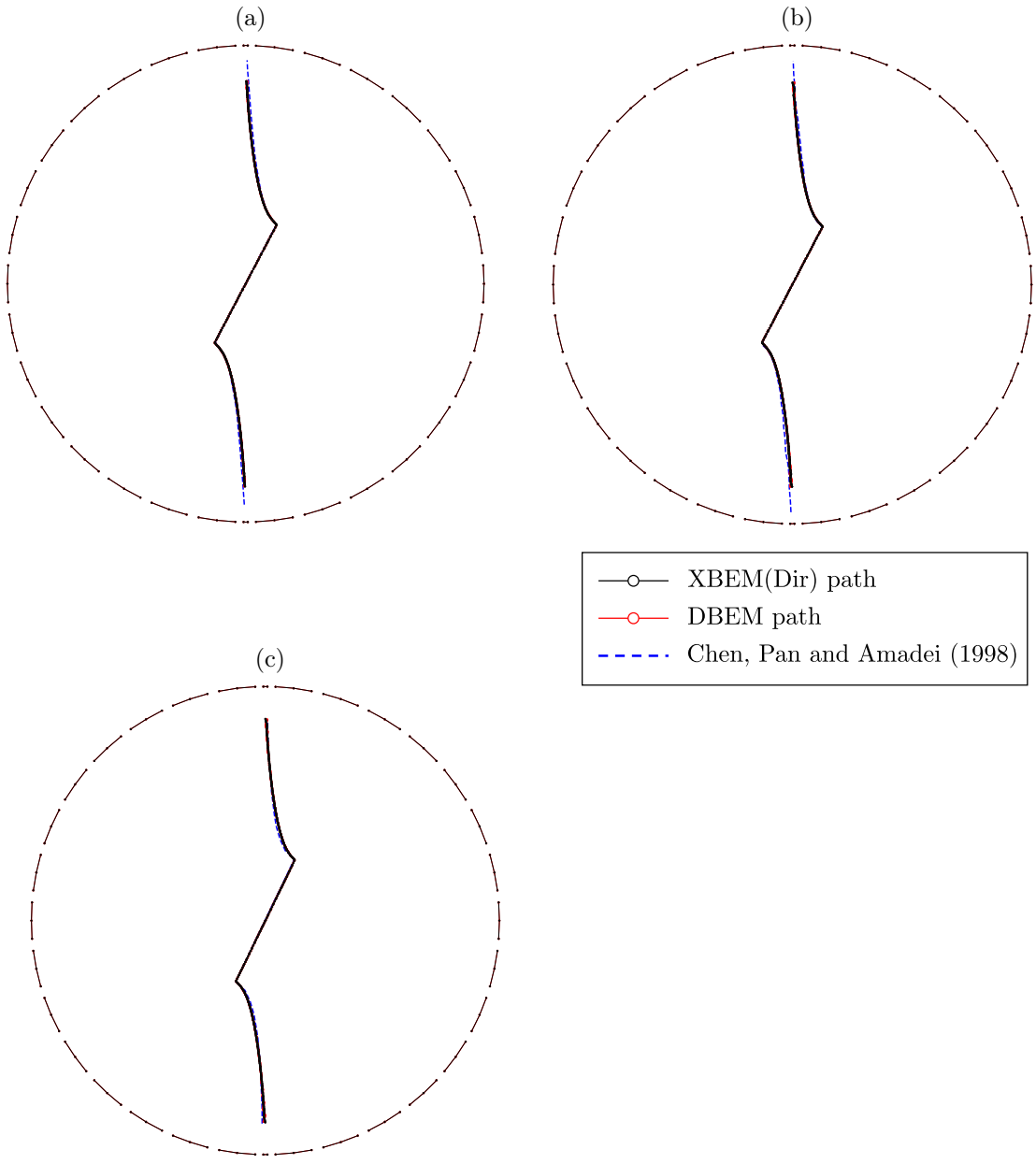

Source: Own author.

Figure 4.22: (a) Tensioned square plate containing ten randomly distributed cracks. (b) Boundary discretisation (Example 4.8.5).

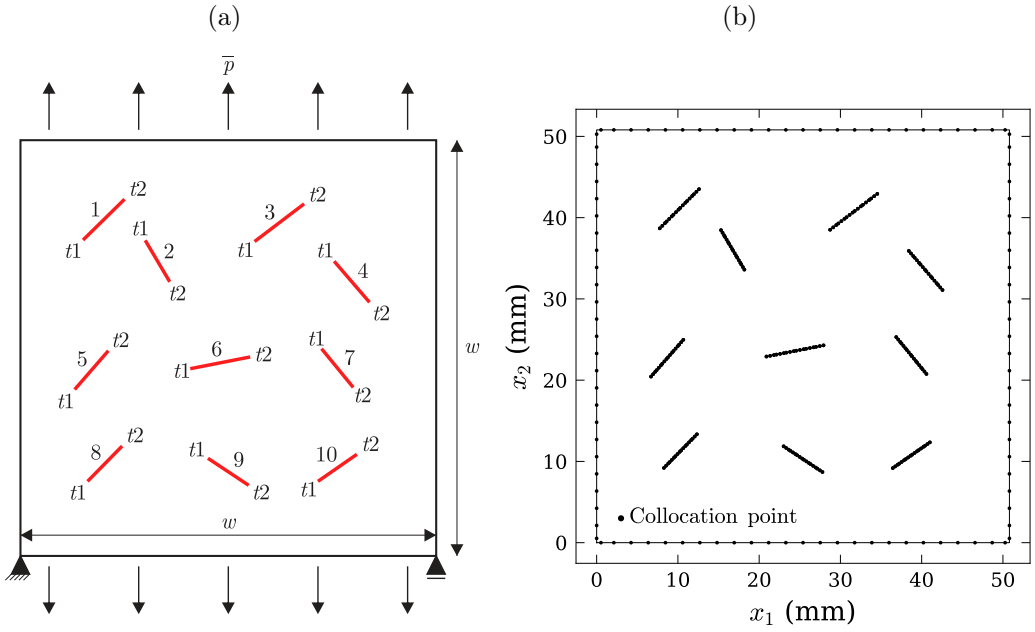

Source: Own author.

Table 4.5: Crack tip coordinates for the multi-cracked square plate (Example 4.8.5).

Crack	$t1$		$t2$	
	x_1 (mm)	x_2 (mm)	x_1 (mm)	x_2 (mm)
1	7.666	38.583	12.699	43.607
2	18.240	33.500	15.244	38.562
3	28.607	38.419	34.661	43.020
4	42.649	30.991	38.331	36.009
5	6.607	20.343	10.752	25.063
6	20.748	22.878	28.069	24.312
7	36.792	25.399	40.664	20.667
8	8.195	9.112	12.425	13.426
9	22.911	11.930	27.889	8.628
10	36.349	9.112	41.107	12.414

Source: Own author.

Initially, the extended formulation is applied considering the crack tip enrichment and the support point enrichment, the latter being used to avoid rigid body motion. Each half of the cracks is enriched by the corresponding tip, and the displacement constraint is defined over three elements. As the cracks grow, the two elements introduced per crack surface are enriched with the tip functions and used for displacement extrapolation. When a crack intersection occurs during the propagation, the Heaviside enrichment is included in the analysis to reproduce the discontinuity in the crossed elements. In this case, the new crack elements are considered to define the displacement continuity constraint. Both

Figure 4.23: Evolution of the fracture through the plate determined by the unenriched DBEM formulation and XBEM considering the direct approach. The XBEM results overlay the DBEM solutions for comparison. Elements with enriched approximation and/or used for displacement extrapolation are depicted in different colours, and the solutions defined by DBEM are represented in grey (Example 4.8.5).

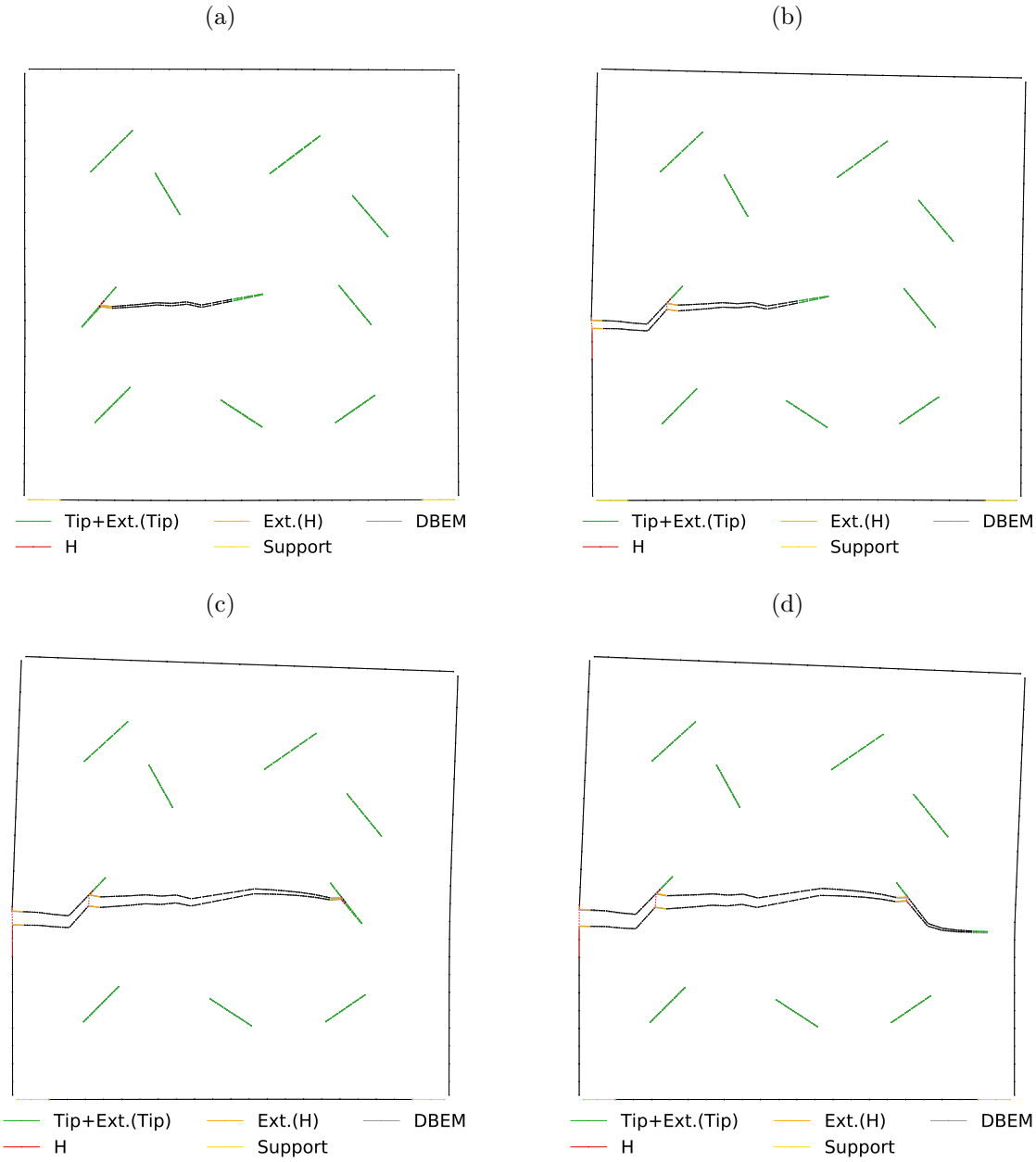

Source: Own author.

direct and the indirect J-integral approaches are used to compute the SIFs, which are later used to define the propagation path. An ordinary DBEM analysis is also carried out to provide additional reference solutions for the XBEM responses.

The sequence shown in Fig. 4.23 represents the fracture process through the plate determined by XBEM considering the direct approach to evaluate the SIFs. Initially, tip $t1$ of crack 6 grows to the left and crosses crack 5 (Fig. 4.23a). Then, tip $t1$ of crack 5 becomes critical and moves towards the left edge of the plate (Fig. 4.23b). After the edge is intersected, tip $t2$ of crack 6 starts to propagate and crosses crack 7 (Fig. 4.23c). Finally, tip $t2$ of crack 7 runs to the right (Fig. 4.23d), dividing the plate into two parts. The sequence shown in Fig. 4.23 demonstrates that the developed model is capable of automatically handling new enrichments during the crack growth. Besides, the discontinuous enrichment can successfully represent the discontinuity over elements crossed by cracks. Fig. 4.23 also presents the responses obtained by the conventional DBEM, and good correspondence with the deformed shapes determined by the direct method is observed.

The ability of the XBEM to represent the fracture process can also be noted from Fig. 4.24, in which the crack paths defined by the enriched approach are compared with the responses determined by DBEM and other numerical solutions available in the literature. The results obtained by XBEM present the same behaviour of the references, demonstrating the efficiency of the proposed enriched formulation for predicting the propagation direction in multi-cracked structures.

Figure 4.24: Comparison between the crack path determined by the enriched and unenriched DBEM formulations and the numerical responses provided by Budyn et al. (2004) and Azadi and Khoei (2010) (Example 4.8.5).

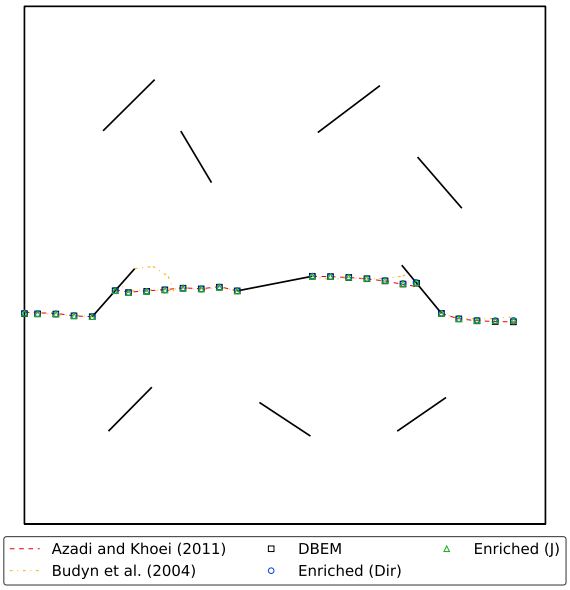

Source: Own author.

The global mechanical response of the cracked plate is represented in Fig. 4.25 by the nominal stress-strain curves. The nominal stress corresponds to the applied uniform loading $\bar{p}$, while the nominal strain is defined by the average vertical displacement of the nodes at the top edge divided by the dimension w. Excellent correspondence is observed between the responses determined by the enriched and unenriched DBEM formulations. Besides, good agreement is found with the solutions available in the literature, especially with the one reported by Azadi and Khoei (2010). Again, the crack length strategy used here leads to a stable representation of the snap-back branch of the structural response. This set of results demonstrates that the proposed XBEM formulation is capable of successfully describing the behaviour of structures containing multiple cracks. In particular, good solutions are achieved by the direct approach without requiring a post-processing technique to compute the SIFs.

Figure 4.25: Nominal stress-strain curves for the multi-cracked plate considering the enriched and unenriched DBEM and the reference results provided by Budyn et al. (2004) and Azadi and Khoei (2010) (Example 4.8.5).

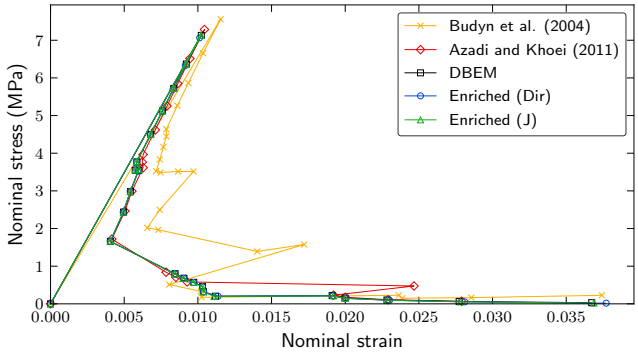

Source: Own author.

5 Extended isogeometric boundary element method

5.1 Initial considerations

In Chapter 4, an XBEM formulation is proposed for the analysis of linear crack growth. The enriched approximations used there are defined from the conventional Lagrange polynomials and the enrichment terms that are responsible for introducing a particular behaviour to the solutions space. In this chapter, an extended isogeometric formulation is developed. The Lagrange polynomials are thus replaced by the non-uniform rational B-splines (NURBS) basis functions, which are commonly applied in CAD packages to describe geometries. The use of the isogeometric approach within the BEM framework provides a direct link between CAD models and the numerical analysis since both deal with quantities solely on the boundary. Besides, the higher-order continuity provided by NURBS facilitates the definition of collocation points on the crack with the required continuity for the existence of the finite part integrals presented in the dual boundary element formulation (HONG; CHEN, 1988; PORTELA; ALIABADI; ROOKE, 1992) adopted here (see Section 2.3).

In this chapter, the parametric functions B-splines and NURBS are briefly described. The unenriched isogeometric boundary element method (IGABEM) is then presented, including implementation aspects that differ from conventional DBEM. In the sequence, an extended approximation is introduced to develop an XIGABEM formulation for the direct evaluation of the SIFs. A propagation scheme considering the enriched approach is also proposed for the analysis of multiple fatigue crack growth in two-dimensional isotropic bodies.

For the crack propagation analysis, the new crack surfaces are created from the extension of existing NURBS. A C^{-1} continuity for the rational basis is enforced between the new and old surfaces to limit the enrichment term to the portion near the crack tip, where it is necessary. The availability of C^{-1} continuity is also elegantly exploited to represent the geometrical discontinuity in elements intersected by cracks simply by inserting the required knots, maintaining a NURBS description throughout. Therefore, the discontinuous enrichment presented in the last chapter is not applied in the isogeometric formulation.

Two sets of examples are presented to demonstrate the accuracy of the proposed XIGABEM formulation. The first set is concerned with the evaluation of SIFs, whereas the second deals with fatigue crack propagation problems, including the prediction of fatigue life. The results are compared against analytical, experimental and numerical solutions available in the literature. Besides, the direct XIGABEM approach is contrasted with unenriched and enriched indirect methods that employ the J-integral for SIF extraction.

A comparison between run times of the direct and indirect strategies is also illustrated in the last example of the chapter.

5.2 B-splines

5.2.1 Initial definitions

B-splines are parametric functions that are able to map a curve in the geometrical space ($\mathbb{R}^d$). In the two-dimensional space ($\mathbb{R}^2$), as the one considered for the applications in this study, this function is described by one independent non-dimensional coordinate ξ defined in the parametric space. In this case, a B-spline is completely defined by the following three properties:

- The curve degree (or order) p, that is equivalent to the degree of the polynomial used in the isoparametric formulation.
- A set of n control points $\mathbf{p}^i = (x_1^i, x_2^i)$ defined in $\mathbb{R}^2$, that is similar to the nodes in conventional BEM.
- A knot vector $\Xi = \{\xi_1, \xi_2, ..., \xi_q\}$ containing q values of parameter ξ (or knots) that are used to define the basis functions for the B-spline. Moreover, the entries in Ξ are positioned in non-decreasing order. The knots resemble the non-dimensional nodal coordinates that are used to define the Lagrange polynomials (see Eq. (2.34)) in isoparametric BEM; however, the knot vector components are not indistinctively associated with the control points.

When the knots are repeated $p + 1$ times at the start and end of Ξ, the knot vector is termed as open knot vector. A consequence of the use of an open knot vector is that the corresponding B-spline is interpolatory at the first and last control points, which is usually not observed for interior control points. Besides, the total number of entries in the knot vector of this type is $q = n + p + 1$. The use of open knot vectors is recurrent in the CAD packages, and it will be also considered in the applications of the present investigation.

5.2.2 Basis functions

In a B-spline, the number of basis functions is equal to the number of control points that define the curve. These functions are determined over the parametric space $\xi \in [\xi_1, \xi_{n+p+1}]$ and are denoted by $N_{i,p}$, with $i = 1, ..., n$ and p indicating the order of the spline. For a constant B-spline ($p = 0$), the basis functions are obtained by:

$$N_{i,0}(\xi) = \begin{cases} 1, & \xi_i \leq \xi < \xi_{i+1} \\ 0, & otherwise \end{cases}, \tag{5.1}$$

and for $p \geq 1$, they are given recursively by Cox-de Boor formula (COX, 1972; DE BOOR, 1972):

$$N_{i,p}(\xi) = \frac{\xi - \xi_i}{\xi_{i+p} - \xi_i} N_{i,p-1}(\xi) + \frac{\xi_{i+p+1} - \xi}{\xi_{i+p+1} - \xi_{i+1}} N_{i+1,p-1}(\xi) \tag{5.2}$$

Note from Eqs. (5.1) and (5.2) that the B-spline basis functions constitute a partition of unity, i.e. $\sum_{i=1}^{n} N_{i,p}(\xi) = 1$, $\forall \xi$. Besides, they are non-negative at every point.

To illustrate the recursive nature of the basis functions, a B-spline with $p = 2$, $n = 5$ and $\Xi = \{0, 0, 0, 1, 1, 2, 2, 2\}$ is taken as an example. The following diagram shows how the functions $N_{i,p}$ are constructed, in which the arrows denote the dependence of higher order basis functions with respect to lower order basis.

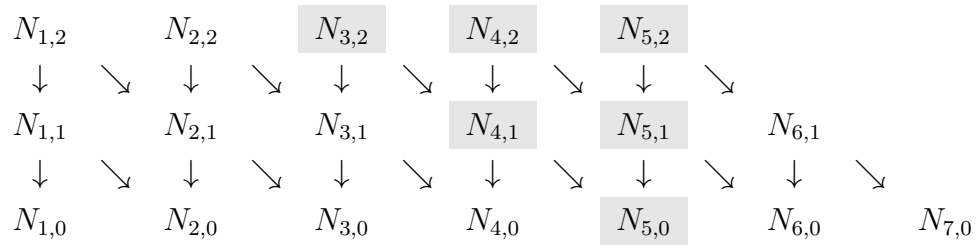

Suppose we want to define the basis functions for this B-spline at the point $\xi = 1.2$. Due to the definition of the constant terms shown in Eq. (5.1), only $N_{5,0}$ is different from zero. Consequently, from the recursive relation of Eq. (5.2), only $N_{3,2}$, $N_{4,2}$ and $N_{5,2}$ will be non-zero for $p = 2$. In the above diagram, the non-zero basis functions that should be evaluated are highlighted, whereas the others are identically zero. In general, for a point $\xi \in [\xi_a, \xi_{a+1}[$, the terms that will assume non-zero values are $N_{a-p,p}, N_{a-p+1,p}, ..., N_{a,p}$. This property is useful during definition of the basis functions in order to reduce the computational effort since not all terms must be evaluated.

The derivatives of the B-spline basis functions are also given recursively, and they can be obtained as follows:

$$N_{i,p}^{(k)}(\xi) = \frac{d^k}{d\xi^k} N_{i,p}(\xi) = p \left(\frac{N_{i,p-1}^{(k-1)}(\xi)}{\xi_{i+p} - \xi_i} - \frac{N_{i+1,p-1}^{(k-1)}(\xi)}{\xi_{i+p+1} - \xi_{i+1}} \right) \tag{5.3}$$

where k indicates the order of the derivative.

5.2.3 B-splines curves

A B-spline curve is defined by a linear combination of the basis functions with the control points positions. This approach is analogous to the polynomial approximation shown in Eq. (2.33). Then, the positions over a B-spline are given by:

$$\tilde{x}_i^b(\xi) = \sum_{m=1}^{n} N_{m,p}(\xi) x_i^m \tag{5.4}$$

where x_i^m represents the coordinates of the m-th control point.

In general, a B-spline curve is C^{p-1} continuous over $[\xi_1, \xi_{n+p+1}]$. However, the order of continuity can be reduced at a particular point if the knot value at that point is repeated in the knot vector. If an interior knot value is repeated k times (i.e. has multiplicity equals to k), the continuity of the B-spline at that knot becomes C^{p-k}. Therefore, if an interior knot has multiplicity p, the curve is C^0 continuous, i.e. the B-spline is interpolatory at the point.

5.3 NURBS

Non-Uniform Rational B-Splines (NURBS) have been extensively applied in CAD software for geometry modelling. Among their advantages are the exact representation of conic sections and quadric surfaces and the ability to describe complex forms, such as industrial components. In the present investigation, NURBS basis functions are adopted in the isogeometric formulation, and a brief description is given in what follows. Further details about NURBS can be obtained in Piegl and Tiller (1995).

NURBS are constructed from B-splines and an additional coordinate denoted as weight. NURBS curves in the Euclidean space $\mathbb{R}^d$ can be interpreted as a projection of B-splines curves from the space $\mathbb{R}^{d+1}$ (see Hughes, Cottrell, and Bazilevs (2005)). Considering a set of positive weights $\Upsilon = \{w_1, w_2, ..., w_n\}$, in which each value w_i is associated with $N_{i,p}$, the rational basis functions $R_{i,p}$ are given from the B-splines basis functions as follows:

$$R_{i,p}(\xi) = \frac{N_{i,p}(\xi) w_i}{\sum_{j=1}^{n} N_{j,p}(\xi) w_j} \tag{5.5}$$

The NURBS basis functions given in Eq. (5.5) are also non-negative and form a partition of unity. Moreover, it can be noted that the B-spline approximation is recovered if all weights are equal. Like the B-splines, NURBS functions are, in general, C^{p-1} continuous over $[\xi_1, \xi_{n+p+1}]$; additionally, the continuity of the NURBS can be reduced at a particular point by increasing the multiplicity of the corresponding knot value.

The first order derivative of NURBS basis functions are often required when dealing with isogeometric approaches, and they can be obtained by the following:

$$R^{(1)}_{i,p}(\xi) = \frac{d}{d\xi} R_{i,p}(\xi) = w_i \frac{N^{(1)}_{i,p}(\xi) \sum_{j=1}^{n} N_{j,p}(\xi) w_j - N_{i,p}(\xi) \sum_{j=1}^{n} N^{(1)}_{j,p}(\xi) w_j}{\left(\sum_{j=1}^{n} N_{j,p}(\xi) w_j \right)^2} \tag{5.6}$$

where $N^{(1)}_{i,p}(\xi)$ is the first order derivative of the B-spline given by Eq. (5.3). In addition, higher order NURBS derivatives can be computed from:

Figure 5.1: (a) NURBS basis functions and (b) NURBS curve representing a unit circle. The order of the NURBS is $p = 2$.

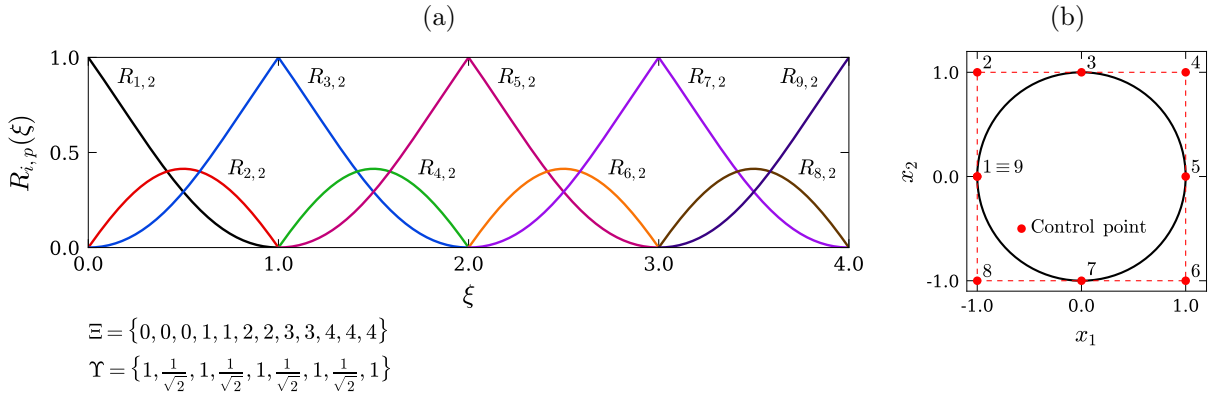

Source: Own author.

Figure 5.2: (a) NURBS basis functions after $p + 1$ knot insertions at $\bar{\xi} = 1.5$. (b) Representation of the NURBS curve and new control points positions. Control points 5 and 6 end up in the same position after the successive knot insertions; however, the NURBS curve may be discontinuous at this point if the coincident control points are moved to different locations.

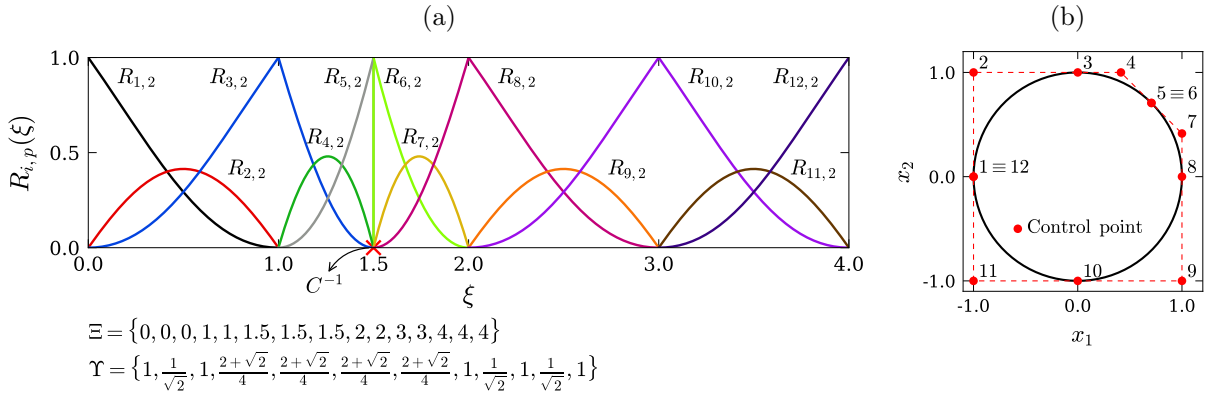

Source: Own author.

$$R_{i,p}^{(k)}(\xi) = \frac{w_i N_{i,p}^{(k)}(\xi) - \sum_{l=1}^{k} \left[\begin{pmatrix} k \\ l \end{pmatrix} \sum_{j=1}^{n} N_{j,p}^{(l)}(\xi) w_j R_{i,p}^{(k-l)}(\xi) \right]}{\sum_{j=1}^{n} N_{j,p}(\xi) w_j} \tag{5.7}$$

where:

$$\begin{pmatrix} k \\ l \end{pmatrix} = \frac{k!}{l!\,(k-l)!} \tag{5.8}$$

Similarly to the B-spline, the NURBS curve can be defined from Eq. (5.4) by switching the shape function $N_{m,p}(\xi)$ to $R_{m,p}(\xi)$.

To illustrate the NURBS concepts, Fig. 5.1a shows the distribution of the rational basis functions obtained with the knot vector and weights presented in the figure and

considering $p = 2$. It can be observed that the functions are C^0 continuous in knots with multiplicity $k = p$, whereas they are smooth elsewhere (C^1 continuous). Figure 5.1b shows how the rational functions from Fig. 5.1a can be associated with a set of control points to describe a unit circle exactly.

5.3.1 H-refinement of NURBS: knot insertion

When adopting the isogeometric approach in a numerical method, the refinement of NURBS is often required to increase the mesh density for the analysis. Here, the refinement is performed with the knot insertion strategy, which is analogous to the h-refinement of conventional isoparametric elements. There are some other alternatives for NURBS refinement, such as order elevation or k-refinement (HUGHES; COTTRELL; BAZILEVS, 2005), but they are not considered in the present investigation.

In the knot insertion strategy, knots are introduced into the knot vector and the control point locations and weights are modified to preserve the exact geometry of the resulting spline. Given an open knot vector $\Xi = \{\xi_1, \xi_2, ..., \xi_{n+p+1}\}$, let $\bar{\xi} \in [\xi_a, \xi_{a+1}[$ be a desired new knot. The new $n+1$ rational basis functions are constructed in the standard way from Eq. (5.5) considering the new knot vector $\bar{\Xi} = \left\{\xi_1, \xi_2, ..., \xi_a, \bar{\xi}, \xi_{a+1}, ...\xi_{n+p+1}\right\}$. To define the new control points positions and weights for the 2-D NURBS, firstly the coordinate $\mathbf{q}^i = (x_1^i, x_2^i, w^i)$ can be defined. The components of $\mathbf{q}^i$ are obtained from the coordinates $\mathbf{p}^i = (x_1^i, x_2^i)$ and weight w^i of the i-th original control point. Then, the NURBS curve in $\mathbb{R}^2$ is converted to a B-spline curve in $\mathbb{R}^3$ by considering the following control points:

$$\mathbf{Q}^i = \left(x_1^i w^i, x_2^i w^i, w^i\right) \tag{5.9}$$

The knot insertion can be performed to this 3-D B-spline with the following relation (PIEGL; TILLER, 1995):

$$\bar{\mathbf{Q}}^i = \alpha^i \mathbf{Q}^i + \left(1 - \alpha^i\right) \mathbf{Q}^{i-1} \tag{5.10}$$

where $\bar{\mathbf{Q}}^i$ denotes the new control points for the B-spline and:

$$\alpha^i = \begin{cases} 1, & 1 \leq i \leq a - p \\ \frac{\bar{\xi} - \xi_i}{\xi_{i+p} - \xi_i}, & a - p + 1 \leq i \leq a \\ 0, & a + 1 \leq i \leq n + p + 2 \end{cases} \tag{5.11}$$

After application of Eq. (5.10), the new control points positions are obtained:

$$\bar{\mathbf{Q}}^i = \left(\bar{x}_1^i \bar{w}^i, \bar{x}_2^i \bar{w}^i, \bar{w}^i\right) \tag{5.12}$$

This new set of control points in $\mathbb{R}^3$ related to the 3-D B-spline can be projected back to $\mathbb{R}^2$ to recover the new set of control points and weights for the given NURBS after

the knot insertion. Hence, the new control points positions for the NURBS are given by $\bar{\mathbf{p}}^i = (\bar{x}_1^i, \bar{x}_2^i)$, with corresponding weight equals to $\bar{w}^i$.

Successive knot insertions can also be applied to introduce discontinuities into a NURBS when necessary. This is achieved by performing multiple knot insertions until a knot value reaches multiplicity $k = p + 1$. In other words, using the knot insertion strategy shown above so that a given knot $\bar{\xi}$ has multiplicity $p + 1$, the rational basis becomes C^{-1} continuous (i.e. discontinuous) at $\bar{\xi}$. In this study, the C^{-1} continuity is used to facilitate the remeshing process during crack propagation. Details about this strategy are given in Section 5.6.2.

Considering the illustrative example shown in Fig. 5.1a, the NURBS basis functions presented in Fig. 5.2a are obtained after three successive knot insertions at $\bar{\xi} = 1.5$. Note that the knot insertions modify the rational functions defined over the knot span $[1.0, 2.0[$, which contains the considered $\bar{\xi}$. Three new basis functions are created - each one introduced by a knot insertion - while the former three rational functions defined over the interval are altered. Essentially, the knot spans on the left and right of $\bar{\xi} = 1.5$ behave as two independent NURBS due to the C^{-1} continuity that has been introduced. Figure 5.2b presents the new control point positions generated after the knot insertions for the unit circle geometry. At the end of the process, control points 5 and 6 are coincident. Since the NURBS basis functions are discontinuous at this point, a geometric discontinuity may be represented if the coincident control points are moved to different locations.

5.4 IGABEM

For an accurate numerical computation of the DBIE (2.31) and TBIE (2.32), the NURBS describing the geometry may be subdivided into boundary elements, following a concept similar to the conventional isoparametric BEM presented in Section 2.3. For the isogeometric analysis, a boundary element (or cell) is defined in the parametric space as the span between two distinct knots of a NURBS, or formally $\xi \in [\xi_a, \xi_{a+1}[: \xi_a \neq \xi_{a+1}$. From the recursive nature of the rational basis functions presented in Section 5.3, the only non-zero functions over an element are $R_{a-p,p}, R_{a-p+1,p}, ..., R_{a,p}$ (see Figs. 5.1a and 5.2a for graphical examples). It is interesting to note that the number of non-zero functions is equal to $p + 1$, as observed when adopting Lagrange elements in DBEM. In addition, the connectivity of an isogeometric element is defined by the control points associated with the non-zero basis functions. Hence, the coordinates along an element e can be evaluated from:

$$\tilde{x}_j^e(\xi) = \sum_{m=1}^{p+1} \phi^{em}(\xi) x_j^{em} \qquad \xi \in [\xi_a, \xi_{a+1}[: \xi_a \neq \xi_{a+1} \tag{5.13}$$

where the terms $\phi^{em}(\xi) = R_{i,p}(\xi)$ represent the m-th shape function of order p from element e, with $i = m + a - p - 1$. Additionally, x_j^{em} denotes the coordinates of the m-th local control point from the element.

Figure 5.3 highlights an element along a NURBS curve defined from the parametric space. However, it is suitable to define the boundary elements over the parent space $\hat{\xi} \in [-1, 1]$ (see Fig. 5.3) to apply Gauss-Legendre quadrature for numerical integration. The linear transformation that maps the parameter ξ from $\hat{\xi}$ is given by:

$$\xi = \frac{(\xi_{a+1} - \xi_a)\,\hat{\xi} + (\xi_{a+1} + \xi_a)}{2} \tag{5.14}$$

Thus, the Jacobian of the transformation from the parent space $\hat{\xi}$ to the Cartesian coordinate system is evaluated by the chain rule as:

$$J^e(\hat{\xi}) = \frac{d\Gamma^e}{d\xi}\frac{d\xi}{d\hat{\xi}} \tag{5.15}$$

in which $d\Gamma^e/d\xi$ is obtained from:

$$\frac{d\Gamma^e}{d\xi}(\xi) = \sqrt{\left(\frac{d\tilde{x}_1^e}{d\xi}(\xi)\right)^2 + \left(\frac{d\tilde{x}_2^e}{d\xi}(\xi)\right)^2} \tag{5.16}$$

and $d\xi/d\hat{\xi}$ is determined from Eq. (5.14) as follows:

$$\frac{d\xi}{d\hat{\xi}} = \frac{(\xi_{a+1} - \xi_a)}{2} \tag{5.17}$$

Figure 5.3: Mapping between the Cartesian, parametric and the parent spaces.

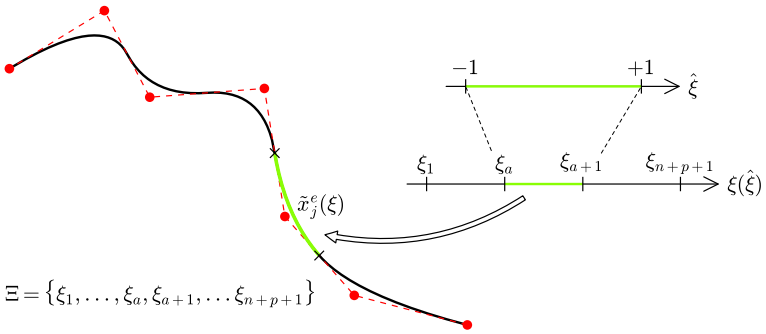

Source: Own author.

Following the isogeometric approach, the mechanical fields along the elements are also interpolated with the rational basis functions and the control points parameters as:

$$\tilde{u}_j^e(\xi) = \sum_{m=1}^{p+1} \phi^{em}(\xi) d_j^{em} \tag{5.18}$$

$$\tilde{p}_j^e(\xi) = \sum_{m=1}^{p+1} \phi^{em}(\xi) t_j^{em} \tag{5.19}$$

in which d_j^{em} and t_j^{em} are, respectively, displacement and traction parameters associated with the m-th local control point from element e. Since the NURBS basis functions are usually not interpolatory - i.e. do not exhibit the Kronecker delta property at the control points (see NURBS curve in Fig. 5.3) - these parameters do not directly represent displacements or tractions on the boundary of the body.

The approximations in Eqs. (5.13), (5.18) and (5.19) can be used in the dual BEM formulation to define the discrete forms of the DBIE (2.31) and TBIE (2.32). The strategy is analogous to conventional Lagrange BEM (see Section 2.3), with the main difference being the substitution of the Lagrange polynomials by the rational bases. Hence, the discrete DBIE considering the isogeometric approximation is given by:

$$c_{ij}(\mathbf{x}')u_j(\mathbf{x}') + c_{ij}(\bar{\mathbf{x}}')u_j(\bar{\mathbf{x}}') + \sum_{e=1}^{N_e}\sum_{m=1}^{p+1} P_{ij}^{em} d_j^{em} = \sum_{e=1}^{N_e}\sum_{m=1}^{p+1} U_{ij}^{em} t_j^{em} \tag{5.20}$$

where N_e is the total number of elements and:

$$P_{ij}^{em} = \int\!\!\!\!\!\!-_{-1}^{1} P_{ij}^*(\mathbf{x}', \mathbf{x}(\hat{\xi}))\phi^{em}(\hat{\xi}) J^e(\hat{\xi}) d\hat{\xi} \tag{5.21}$$

$$U_{ij}^{em} = \int_{-1}^{1} U_{ij}^*(\mathbf{x}', \mathbf{x}(\hat{\xi}))\phi^{em}(\hat{\xi}) J^e(\hat{\xi}) d\hat{\xi} \tag{5.22}$$

are the integral kernels defined in the parent space $\hat{\xi} \in [-1, 1]$.

Similarly, the discrete TBIE is determined as:

$$\frac{1}{2}\left[p_j(\mathbf{x}') - p_j(\bar{\mathbf{x}}')\right] + n_i(\mathbf{x}') \sum_{e=1}^{N_e}\sum_{m=1}^{p+1} S_{kij}^{em} d_k^{em} = n_i(\mathbf{x}') \sum_{e=1}^{N_e}\sum_{m=1}^{p+1} D_{kij}^{em} t_k^{em} \tag{5.23}$$

where:

$$S_{kij}^{em} = \int\!\!\!\!\!\!-_{-1}^{1} S_{kij}^*(\mathbf{x}', \mathbf{x}(\hat{\xi}))\phi^{em}(\hat{\xi}) J^e(\hat{\xi}) d\hat{\xi} \tag{5.24}$$

$$D_{kij}^{em} = \int\!\!\!\!\!\!-_{-1}^{1} D_{kij}^*(\mathbf{x}', \mathbf{x}(\hat{\xi}))\phi^{em}(\hat{\xi}) J^e(\hat{\xi}) d\hat{\xi} \tag{5.25}$$

The collocation method can also be applied to define the algebraic system of equations given by IGABEM. However, collocation at the control points is not possible since some of the source points would be placed outside the boundary. In the present investigation, the collocation is carried out at Greville abscissae (GREVILLE, 1964; JOHNSON, 2005) define as:

$$\xi_i' = \frac{\sum_{j=1}^{p} \xi_{i+j}}{p} \tag{5.26}$$

in which ξ_i' is the knot corresponding to the i-th collocation point. The Cartesian coordinates for this point can be determined with Eq. (5.13).

For the analysis of fracture problems, the discrete DBIE (5.20) is used for the collocation points at the external boundary and one of the crack surfaces, whereas the discrete TBIE (5.23) is applied for the collocation points on the other surface to obtain a non-singular system of equations. During the collocation process, the collocation points become the source point $\mathbf{x}'(\xi')$ of their respective boundary integral equations.

The existence of the Hadamard principal value in the TBIE places certain requirements on the continuity of the displacement derivatives at the collocation points. To satisfy this condition, the collocation points at the start and end of the NURBS at crack surfaces are placed inside the NURBS. For the first, the coordinate in the parametric space is updated to $\xi_1' = \xi_1' + 0.2\,(\xi_2' - \xi_1')$, and for the last, it is altered to $\xi_n' = \xi_n' - 0.2\left(\xi_n' - \xi_{n-1}'\right)$.

Special attention should be taken to the jump terms in the boundary integral equations. These terms should be distributed over the element e' that contains a particular source point $\mathbf{x}'(\xi')$ using the basis functions $\phi^{em}(\xi')$. This process is necessary since the displacement and the traction components at the collocation point is defined, respectively, with the application of Eqs. (5.18) and (5.19) assessed at ξ'. Therefore, the jump terms in the DBIE and TBIE are rewritten as:

$$c_{ij}(\mathbf{x}')u_j(\mathbf{x}') + c_{ij}(\bar{\mathbf{x}}')u_j(\bar{\mathbf{x}}') = \sum_{m=1}^{p+1} c_{ij}(\mathbf{x}')\phi^{e'm}(\xi')d_j^{e'm} + \sum_{m=1}^{p+1} c_{ij}(\bar{\mathbf{x}}')\phi^{\bar{e}'m}(\bar{\xi}')d_j^{\bar{e}'m} \tag{5.27}$$

$$\frac{1}{2}\left[p_j(\mathbf{x}') - p_j(\bar{\mathbf{x}}')\right] = \frac{1}{2}\left[\sum_{m=1}^{p+1} \phi^{e'm}(\xi')t_j^{e'm} - \sum_{m=1}^{p+1} \phi^{\bar{e}'m}(\bar{\xi}')t_j^{\bar{e}'m}\right] \tag{5.28}$$

where $\bar{e}'$ denotes the element containing the source $\bar{\mathbf{x}}'$ that is at the same position of $\mathbf{x}'$ but in the opposite crack surface. If $\mathbf{x}'$ does not belong to a crack surface, then $c_{ij}(\bar{\mathbf{x}}') = p_j(\bar{\mathbf{x}}') = 0$.

The integral kernels involved in the IGABEM are similar to the traditional DBEM approach, and they can be evaluated in the same manner as presented in Appendix C. After the integration process, the resulting algebraic system of equation is determined as follows:

$$\mathbf{Hd} = \mathbf{Gt} \tag{5.29}$$

where $\mathbf{H}$, like conventional DBEM, is a $2N \times 2N$ matrix determined from the boundary integrals P_{ij}^{em} and S_{kij}^{em} and from the distribution of the jump terms in the DBIE and

$\mathbf{G}$ is a $2N \times 2N$ matrix obtained from the boundary integrals U_{ij}^{em} and D_{kij}^{em} and from the distribution of the jump terms in the TBIE. $\mathbf{d}$ and $\mathbf{t}$ are $2N$ vectors containing, respectively, the displacement and traction control parameters and N is the total number of collocation points in the model.

Imposing the prescribed boundary conditions to the system (5.29) leads to the the final system of equations defined by IGABEM:

$$\mathbf{Ax} = \mathbf{f} \tag{5.30}$$

which has the same form of the system determined by traditional DBEM (Eq. (2.46)).

After the solution of Eq. (5.30), the unknown control variables stored in $\mathbf{x}$ are defined. Then, the mechanical response for any point ξ at the boundary, including the collocation points, can be evaluated from Eqs. (5.18) and (5.19) considering the element e that contains the point.

5.5 Extended formulation

5.5.1 Approximations

When considering the isogeometric approach, the unknown boundary fields along the elements are also approximated through the rational bases. However, the NURBS functions, as the Lagrange polynomials in conventional BEM, fail to accurately represent the square root behaviour near crack tips predicted by the LEFM theory (Section 3.1). To capture the analytical behaviour and, consequently, improve the near-tip numerical solution, an extended formulation may be employed. Unlike the XBEM formulation presented in Chapter 4, the displacement enrichment terms used for the XIGABEM approach is not composed of shifted functions but is introduced directly in the approximation as in Benzley (1974) and Simpson and Trevelyan (2011b). The option of not considering shifted functions in the isogeometric approach is because the control parameters do not represent physical displacements on the boundary of the body - as is the case of the nodal parameters in conventional BEM - and, therefore, there is no reason in preserving their meaning. Nonetheless, it is possible to develop a shifted formulation taking as reference the enrichment functions assessed at the collocation points to reduce the singularity order of the resulting enriched integral kernels, as in the XBEM formulation presented in the previous chapter.

From the previous discussion, the displacement approximation for an element e near a crack tip λ in the proposed XIGABEM approach is written as:

$$\tilde{u}_j^{e\lambda}(\xi) = \sum_{m=1}^{p+1} \phi^{em}(\xi) d_j^{em} + \sum_{M=I,II} \tilde{K}_M^{\lambda} R_{jk}^{\lambda} \psi_{kM}(\mathbf{x}^{\lambda}, \mathbf{x}(\xi)) \tag{5.31}$$

The first term on the right-hand side of Eq. (5.31) is the standard IGABEM expansion of the displacement (Eq. (5.18)) into products of the NURBS basis functions ϕ^{em} and the displacement control variables d_i^{em} associated with the m-th local control point. This term is responsible for capturing rigid-body motions. The second term of the right-hand side of Eq. (5.31) exactly represents the leading-order term from Williams expansion for displacements (WILLIAMS, 1957) (see Eq. (3.2)), and it is introduced in the approximation to capture the near-tip behaviour. This term contains the additional parameters $\tilde{K}_M^\lambda = \tilde{K}_I^\lambda, \tilde{K}_{II}^\lambda$ included by the enrichment, and these become unknowns that, when found as part of the BEM solution vector, provide the stress intensity factors. As in XBEM, the enrichment parameters become accurate approximations of the SIFs only if the continuity of displacement at the crack tip is enforced (see Section 5.5.2). The crack tip functions ψ_{kM} are extracted directly from the asymptotic solution given by Williams (1957). Assuming isotropic materials, they are expressed in matrix notation as:

$$\begin{bmatrix} \psi_{1I} & \psi_{1II} \\ \psi_{2I} & \psi_{2II} \end{bmatrix} = \frac{1}{2\mu}\sqrt{\frac{\rho}{2\pi}} \begin{bmatrix} \cos\left(\frac{\theta}{2}\right)(\kappa - \cos\theta) & \sin\left(\frac{\theta}{2}\right)(\kappa + 2 + \cos\theta) \\ \sin\left(\frac{\theta}{2}\right)(\kappa - \cos\theta) & -\cos\left(\frac{\theta}{2}\right)(\kappa - 2 + \cos\theta) \end{bmatrix} \tag{5.32}$$

where ρ is the distance to the tip and θ is the angular variation according to the local coordinate system positioned at the crack tip $\mathbf{x}^\lambda$, as shown in Fig. 5.4. κ represents the Kolosov constant defined as $\kappa = 3 - 4\nu$ for plane strain and $\kappa = (3 - \nu)\,/\,(1 + \nu)$ for plane stress.

To transform the contribution of the enrichment functions from the local to the global coordinate system, the components R_{jk}^λ of the rotation matrix are also included in the enrichment term of Eq. (5.31), in which:

$$\begin{bmatrix} R_{11} & R_{12} \\ R_{21} & R_{22} \end{bmatrix} = \begin{bmatrix} \cos\omega & -\sin\omega \\ \sin\omega & \cos\omega \end{bmatrix} \tag{5.33}$$

where ω is the angle between the local and global coordinates systems (see Fig. 5.4).

The displacement approximation expressed in Eq. (5.31) is used only for boundary elements on NURBS defining the crack tips. Then, the $\sqrt{\rho}$ behaviour observed in the near-tip solution can be captured through the enrichment term. For the other elements, only the rational basis contribution is considered in the displacement approximation (Eq. (5.18)). For the traction field, the approximation used for elements at NURBS defining both the external boundaries and cracks is expressed solely through the NURBS basis functions as in Eq. (5.19).

Considering the XIGABEM approximations, the discrete form of the DBIE (2.31) becomes:

Figure 5.4: Local coordinate system at an enriched crack tip.

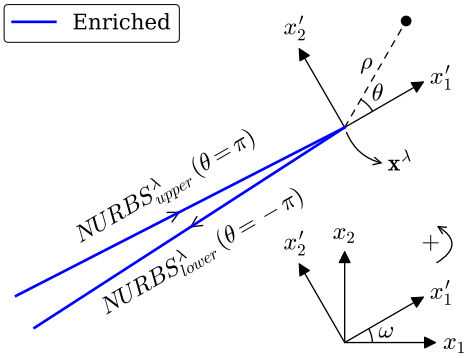

Source: Own author.

$$\sum_{m=1}^{p+1} c_{ij}(\mathbf{x}')\phi^{e'm}(\xi')d_j^{e'm} + \sum_{m=1}^{p+1} c_{ij}(\bar{\mathbf{x}}')\phi^{\bar{e}'m}(\bar{\xi}')d_j^{\bar{e}'m} + \\ + \sum_{e=1}^{N_e}\sum_{m=1}^{p+1} P_{ij}^{em}d_j^{em} + \sum_{\lambda=1}^{N_t}\sum_{M=I,II}\tilde{K}_M^\lambda \sum_{e=1}^{N_e^\lambda}\tilde{P}_{iM}^{e\lambda} = \sum_{e=1}^{N_e}\sum_{m=1}^{p+1} U_{ij}^{em}t_j^{em} \tag{5.34}$$

where N_e is the total number of elements, N_t is the number of crack tips and N_e^λ is the number of elements enriched in the vicinity of the tip λ. It is worth mentioning that the enrichment functions do not modify the jump terms in the DBIE since the crack tip functions ψ_{kM} for coincident source points $\mathbf{x}'$ and $\bar{\mathbf{x}}'$ cancel each other out during implementation. The kernel related to the enrichment parameter in Eq. (5.34) is computed from:

$$\tilde{P}_{iM}^{e\lambda} = \fint_{-1}^{1} P_{ij}^*(\mathbf{x}', \mathbf{x}(\hat{\xi}))R_{jk}^\lambda \psi_{kM}(\mathbf{x}^\lambda, \mathbf{x}(\hat{\xi}))J^e(\hat{\xi})d\hat{\xi} \tag{5.35}$$

Analogously, the discrete TBIE (2.32) is determined as:

$$n_i(\mathbf{x}')\left(\sum_{e=1}^{N_e}\sum_{m=1}^{p+1} S_{kij}^{em}d_k^{em} + \sum_{\lambda=1}^{N_t}\sum_{M=I,II}\tilde{K}_M^\lambda\sum_{m=1}^{N_e^\lambda}\tilde{S}_{ijM}^{e\lambda}\right) = \\ = -\frac{1}{2}\left[\sum_{m=1}^{p+1}\phi^{e'm}(\xi')t_j^{e'm} - \sum_{m=1}^{p+1}\phi^{\bar{e}'m}(\bar{\xi}')t_j^{\bar{e}'m}\right] + n_i(\mathbf{x}')\sum_{e=1}^{N_e}\sum_{m=1}^{p+1} D_{kij}^{em}t_k^{em} \tag{5.36}$$

where:

$$\tilde{S}_{ijM}^{e\lambda} = \fint_{-1}^{1} S_{kij}^*(\mathbf{x}', \mathbf{x}(\hat{\xi}))R_{kp}^\lambda \psi_{pM}(\mathbf{x}^\lambda, \mathbf{x}(\hat{\xi}))J^e(\hat{\xi})d\hat{\xi} \tag{5.37}$$

The use of the enriched displacement approximation in Eq. (5.31) only introduces the terms related to the enrichment parameters $\tilde{K}_I^\lambda$ and $\tilde{K}_I^\lambda$ in Eqs. (5.34) and (5.36), while the other terms are exactly the same as they would be in an unenriched formulation (see Section 5.4). The enriched kernels shown in Eqs. (5.35) and (5.37) can be computed with standard Gauss-Legendre quadrature when the integrated element does not contain the source point. Otherwise, they can be evaluated with the SSM shown in Appendix D.1.

The number of degrees of freedom introduced by the enrichment is limited to two per crack tip, regardless of the number of enriched elements, which is an advantage of the applied strategy over PU-based enrichments (SIMPSON; TREVELYAN, 2011a; PENG et al., 2016). This reduced number of enrichment parameters is also beneficial for the conditioning of the system of equations. The next section presents the additional relations adopted in the proposed XIGABEM formulation that accommodate the additional enrichment parameters and allow the direct evaluation of the SIFs.

5.5.2 Crack tip tying constraint

To accommodate the degrees of freedom introduced by the enrichment and, consequently, recover a square system of equations, the crack tip tying constraint proposed by Alatawi and Trevelyan (2015) is extended to the XIGABEM framework. This condition aims to enforce the continuity of the displacements between the upper and lower crack surfaces at the tip, which is not guaranteed in the unenriched approach as independent NURBS are used to model each crack surface (see Fig. 5.4). When compared to XBEM, the definition of the constraint is simplified by the use of NURBS functions to replace the conventional Lagrangian basis.

Using the displacement approximation shown in Eq. (5.31), and since open knot vectors are employed in the definition of the basis functions, the displacement at the crack tip considering the NURBS at the upper surface ($\theta = \pi$) is $\tilde{u}_j^U(\xi_{n+p+1}) = d_j^{U_{tip}}$, where $d_j^{U_{tip}}$ is the displacement parameter of the control point positioned at the end of the upper NURBS (crack tip). Similarly, the displacement at the crack tip considering the NURBS at the lower surface ($\theta = -\pi$) is $\tilde{u}_j^L(\xi_1) = d_j^{L_{tip}}$, where $d_j^{L_{tip}}$ is the displacement parameter of the control point positioned at the start of the lower NURBS (crack tip). Thus, the displacement continuity condition at the tip is simply expressed as:

$$d_j^{U_{tip}} - d_j^{L_{tip}} = 0 \tag{5.38}$$

Equation (5.38) provides two supplementary equations per crack tip and this is exactly sufficient to yield a square system of equations. Since the continuity condition at the tip is the same as observed in the Williams expansions, the additional parameters $\tilde{K}_I^\lambda$ and $\tilde{K}_{II}^\lambda$ represent a good approximation for mode I (K_I^λ) and mode II (K_{II}^λ) SIFs. Therefore, the proposed XIGABEM strategy allows the SIFs to be computed directly from the system of

equations, eliminating the need for computationally expensive post-processing techniques, such as the J-integral.

5.5.3 Assembly of the system of equations

Using the collocation method to assembly the system of equations as in conventional IGABEM (Section 5.4), and including the crack tip tying constraint given by Eq. (5.38), the resulting algebraic system of equations defined by XIGABEM is assembled as:

$$\begin{bmatrix} \mathbf{H} & \mathbf{H}_C^\lambda \\ \mathbf{H}_R^\lambda & \mathbf{0} \end{bmatrix} \begin{Bmatrix} \mathbf{d} \\ \tilde{\mathbf{K}} \end{Bmatrix} = \begin{bmatrix} \mathbf{G} \\ \mathbf{0} \end{bmatrix} \{\mathbf{t}\} \tag{5.39}$$

in which $\tilde{\mathbf{K}}$ is $2N_t$ vector storing the additional enrichment parameters $\tilde{K}_I^\lambda$ and $\tilde{K}_{II}^\lambda$ for each crack tip λ. The sub-matrix related to the enriched parameters $\mathbf{H}_C^\lambda$ is composed of the enriched integrals $\tilde{P}_{iM}^{e\lambda}$ (Eq. (5.35)) and $\hat{S}_{ijM}^{e\lambda}$ (Eq. (5.37)), while $\mathbf{H}_R^\lambda$ is defined from the crack tip tying constraints.

Imposing the prescribed boundary conditions to the system in Eq. (5.39), the final system of linear equations is determined as follows:

$$\begin{bmatrix} \mathbf{A} & \mathbf{H}_C^\lambda \\ \mathbf{H}_R^\lambda & \mathbf{0} \end{bmatrix} \begin{Bmatrix} \mathbf{x} \\ \tilde{\mathbf{K}} \end{Bmatrix} = \begin{Bmatrix} \mathbf{f} \\ \mathbf{0} \end{Bmatrix} \tag{5.40}$$

Note that the crack tip enrichment given by Eq. (5.31) only introduces the sub-matrices $\mathbf{H}_C^\lambda$ and $\mathbf{H}_R^\lambda$ into the system of equations. The other components of the system are the same as they would be in an unenriched IGABEM formulation (Section 5.4).

The solution of the linear system of equations defined by XIGABEM, Eq. (5.40), yields values for the unknown control parameters and also for the SIFs, which appear in the solution vector.

5.6 XIGABEM for fatigue crack growth

For the XIGABEM analyses described in this study, the structural boundary is imported directly from CAD software. Flat cracks are then inserted in the model, with each surface defining one crack tip given by a NURBS, as illustrated by Fig. 5.5a. The knot vector for the NURBS at the upper surface is defined over $\xi^U \in [0, 1]$, whereas at the lower surface it is described over $\xi^L \in [-1, 0]$. Therefore, the parameters ξ for corresponding points at each crack surface satisfy $\xi^U = -\xi^L$. As also illustrated in Fig. 5.5a, the whole NURBS containing a crack tip in the initial configuration is enriched with the tip functions.

Then, the NURBS are refined by splitting the knot vector in uniform knot spans corresponding to the boundary elements. Furthermore, if a crack is defined such that it intersects a geometric boundary, a knot refinement at the intersection point is performed

until a C^{-1} continuity is reached for the crossed NURBS. Hence, this scheme utilises the intrinsic properties of NURBS and is an elegant way to represent the discontinuity at the crack mouth.

After defining the boundary element mesh, the linear system of equations can be assembled following the formulation described in Section 5.5. The solution of the system given by XIGABEM leads to direct evaluation of the SIFs for the crack tips. The XIGABEM can also be employed in conjunction with post-processing techniques, such as the J-integral (see Section 3.2), to improve the accuracy of the indirect method, as will be discussed in the examples in Section 5.7.

5.6.1 Fatigue model and structural life prediction

In the present investigation, the structures are subjected to oscillatory loadings that induce fatigue crack growth. High-cycle fatigue is assumed, in which the stress levels introduced by the oscillatory loading are well below the material's yield strength. Consequently, the strains observed within the structure are predominantly elastic and the inelastic process zone surrounding the crack tip is small in comparison with the crack length and other dimensions of the cracked body. Because of the resemblance with brittle fracture, the LEFM can also be applied for modelling high-cycle fatigue crack propagation.

The crack growth rates are defined from the Paris law (PARIS, 1961) as follows:

$$\frac{da}{dN^{lc}} = C\left(\Delta K_{ef}\right)^{m} \tag{5.41}$$

where C and m are material constants and da/dN^{lc} represents the crack extension per load cycle, in which a is the crack length and N^{lc} is the number of load cycles. The range of effective stress intensity factors for mixed-mode can be computed, according to Tanaka (1974), as $\Delta K_{ef} = \sqrt[4]{\Delta K_I^4 + 8\Delta K_{II}^4}$, in which $\Delta K_M = K_M^{max} - K_M^{min}$, with K_M^{max} and K_M^{min} representing, respectively, the maximum and minimum values of the considered SIF within a load cycle. For simplicity, it is assumed that the crack propagation follows the power law in Eq. (5.41) throughout the analyses. Alternatively, any other growth law could be coupled to the XIGABEM formulation developed herein.

For applications involving multiple cracks, each crack tip grows proportionally to its growth rate following the relationship:

$$\Delta a = \Delta L \frac{C\left(\Delta K_{ef}\right)^{m}}{\left[da/dN^{lc}\right]^{\lambda_d}} \tag{5.42}$$

where Δa is the crack length increment, ΔL is the standard crack length increment defined in the analysis and $\left[da/dN^{lc}\right]^{\lambda_d}$ is the highest crack growth rate observed during one load cycle and related to the dominant tip λ_d.

It is worth emphasising that in mechanical problems involving multiple cracks, some

of them may grow faster than others. Different crack growth rates may lead to very small crack length increments and, consequently, collocation points may be positioned very close to their neighbours. This situation introduces numerical instabilities into the final system of algebraic equations given by the DBEM because of the singular nature of the fundamental solutions. To avoid such issue, the virtual crack extension scheme proposed by Price and Trevelyan (2014) is adopted in the numerical approach. In this strategy, the crack tip only propagates if the crack length increment is higher than a prescribed ratio of ΔL, assumed here as $0.1\Delta L$. If this condition is not satisfied, then Δa is accumulated as a virtual length. During the course of the analysis, if the total virtual extension attends the growth condition, the crack is extended by the accumulated length.

The number of load cycles ΔN_{i+1}^{lc} to extend a crack by $\Delta a = a_{i+1} - a_i$ can be computed by integration of the Paris law (5.41). Assuming a linear variation of ΔK_{ef} between a_i and a_{i+1}, the following discrete expression is defined (ANDRADE; LEONEL, 2019):

$$\Delta N_{i+1}^{lc} = \frac{\Delta a}{C\,(m-1)} \frac{\left[(\Delta K_i)^{1-m} - (\Delta K_{i+1})^{1-m}\right]}{(\Delta K_{i+1} - \Delta K_i)} \tag{5.43}$$

where ΔK_i and ΔK_{i+1} are the values of ΔK_{ef} at the crack lengths a_i and a_{i+1}, respectively.

5.6.2 Propagation and remeshing

To define the direction of the discrete length increment given by Eq. (5.42), the predictor-corrector scheme proposed by Portela, Aliabadi, and Rooke (1993) is applied, with the maximum circumferential stress criterion (see Section 3.3) used for the prediction of each iteration. This strategy aims to take into account the variation of the SIFs during the stable fatigue crack growth to obtain the same crack path independently of the crack length increment considered. The steps of the predictor-corrector scheme can then be listed as follows:

1. For the current crack configuration η, compute the propagation direction $\theta_{p(\eta)}^{i}$ for the first iteration considering Eq. (3.39).

2. Extend the crack tip by Δa, computed from Eq. (5.42), along the direction determined in the previous step.

3. Compute the SIFs for the new crack configuration $\eta + 1$.

4. Evaluate a new propagation direction $\theta_{p(\eta+1)}^{i}$ from Eq. (3.39) considering the new SIFs obtained from step 3.

5. Define the correction angle $\beta^i = \theta_{p(\eta+1)}^{i}/2$.

6. Correct the crack tip increment defined in the second step to the new growth direction given by $\theta_{p(\eta)}^{i+1} = \theta_{p(\eta)}^{i} + \beta^i$.

7. Return to step 2 while $|\beta^i| < |\beta^{i-1}|$ and $\left|\beta^i/\theta^i_{p(\eta)}\right| > \delta$, where $\delta = 10^{-3}$ in the present study.

After evaluating the propagation direction, the NURBS defining the growing tip are extended to the new tip position, as shown by Fig. 5.5b. This is achieved by expanding the corresponding knot vectors by a unit and defining new control points along the new crack surfaces. In the example given in Fig. 5.5b, after the propagation of tip $\lambda = 1$, the NURBS at the upper and lower surfaces become defined over $\xi^U \in [0, 2]$ and $\xi^L \in [-2, 0]$, respectively. Additionally, the multiplicity of the knot corresponding to the former tip is kept equal to $p + 1$, so that a C^{-1} continuity occurs between the new and old crack surfaces. This discontinuity is adopted in the present work to make the approximations over the newly created crack surfaces completely independent from the quantities in the existing surfaces. As illustrated in Fig. 5.5b, the enrichment is applied only to the elements over the new crack surfaces, where the dominant square root behaviour is captured by the enriched displacement approximation given in Eq. 5.31. For the elements defining the old crack surfaces, the unenriched approximation is adopted, which is able to represent the displacement fields since there is no singular behaviour along this region.

The changes in the geometry during the crack propagation are accompanied by modifications to the system of equations given by Eq. (5.40). After a crack increment, as illustrated in Fig. 5.5b, most of the system remains unaltered since a C^{-1} continuity is enforced between the old and new crack surfaces. As represented by the graphical representation of the algebraic system in Fig. 5.6a, only the enrichment sub-matrices related to the growing tip need to be reconstructed in this case, whereas the other terms are expanded to include the degrees of freedom associated with the new crack surfaces.

If a crack tip intersects a boundary during propagation, as shown by Fig. 5.5c, successive knot insertions are considered for the crossed NURBS until a C^{-1} continuity is obtained at the intersection point so that a displacement discontinuity may be represented. The additional columns and rows associated with the enrichment parameters of the intersecting tip are removed from the system of equations (Fig. 5.6b) as the tip becomes inactive and no longer benefits from enrichment. Moreover, the positions related to the modified control and collocation points in the intersected NURBS are also reconstructed in the original system.

As a final remark before moving on to study some numerical applications, it is stressed that the implementation of knot insertion to achieve C^{-1} continuity along the growing crack and at crack intersections appears a particularly elegant use of the properties of NURBS and is restricted to IGABEM. This simple expedient removes the need for the definition of discontinuous and semi-discontinuous elements in Lagrangian formulations, and therefore saves a considerable amount of careful data management and the use of different sets of shape functions.

Figure 5.5: (a) Representation of enriched NURBS for an interior crack. (b) NURBS and their enriched parts after a crack tip propagation. The multiplicity for the knot at the former tip is kept equal to $p+1$. (c) Intersection between the crack tip $\lambda = 1$ with another NURBS. In this case, the respective crack NURBS no longer benefit from enrichment. Besides, the crossed NURBS is made discontinuous at the intersection by increasing the multiplicity of the intersection knot $\bar{\xi}$ to $p+1$ through successive knot insertions.

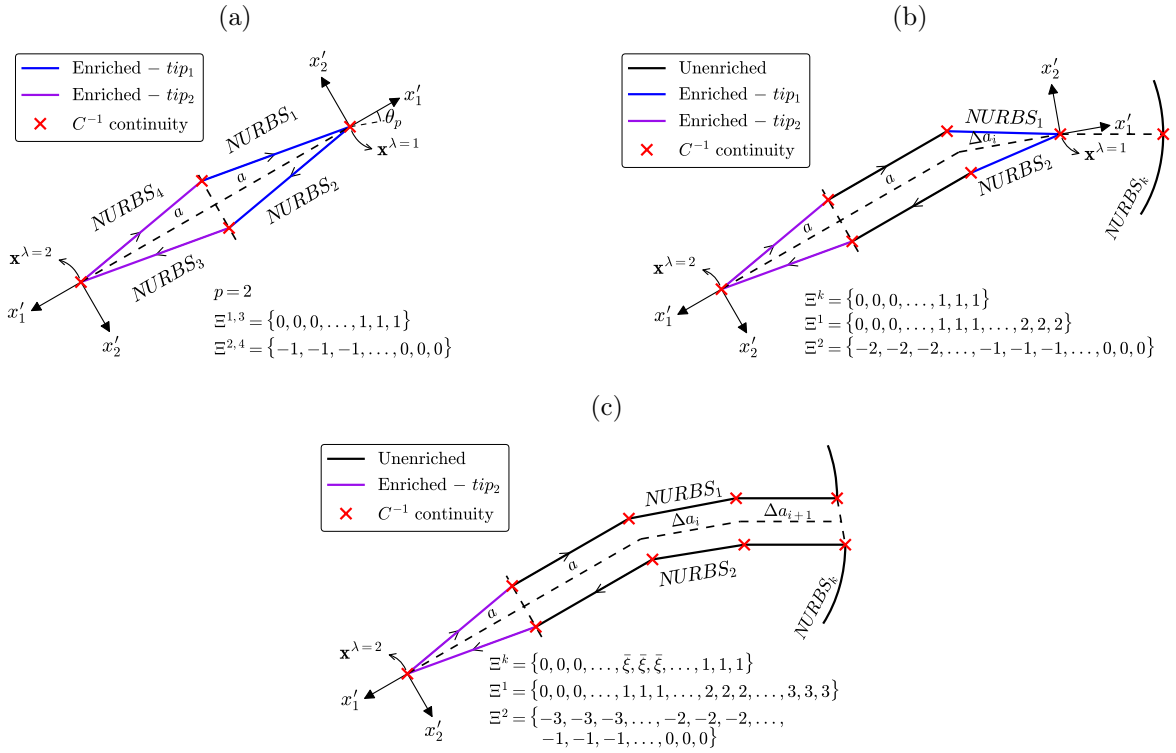

Source: Own author.

5.7 Numerical applications

Two sets of examples are presented to illustrate the application of the proposed direct XIGABEM formulation to simulate crack problems. In the first group, composed of the first three examples, it is analysed the effect of the enrichment in the accuracy and the convergence rate of the SIFs values for different crack configurations. The first example of this set shows how the enrichment strategy performs when simulating a problem with an exact solution. In the second, the finite plate effect is analysed. In the final example of the first set, the accuracy of XIGABEM for interior and inclined cracks is assessed.

In the second group of problems, the numerical approach is applied for fatigue crack propagation modelling. The first example of this part shows the application of XIGABEM for simulating a fatigue test. The second presents the analysis of an edge crack emanating from a curved boundary. The third deals with the intersection between cracks and the boundary of the structure. Finally, the last example shows the use of XIGABEM for simulating multiple crack fatigue propagation. The results obtained by the enriched approach

Figure 5.6: Graphical representation of the changes in the sub-matrices from the system of equations resulting from (a) the crack propagation illustrated in Fig. 5.5b and (b) the crack propagation followed by the intersection of a NURBS depicted in Fig. 5.5c. Note that most of the sub-matrices remain unaltered (represented by solid lines). The changes in the system (represented by dashed lines) are related to the enrichment parameters associated with the growing tip and the new control/collocation points defined along the new crack surfaces and intersected NURBS.

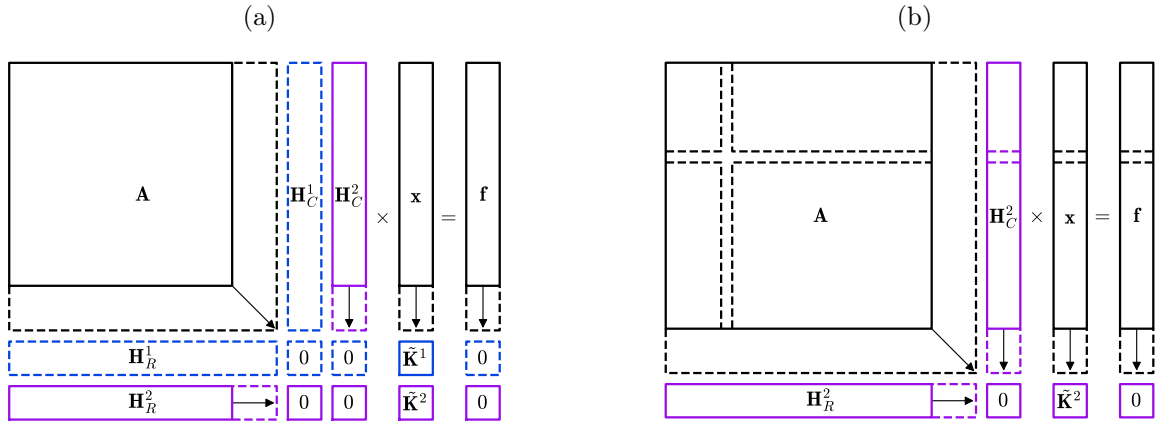

Source: Own author.

are compared with those determined using unenriched IGABEM and other solutions available in the literature. Additionally, the reduction in computational cost provided by the direct method is illustrated in the last example.

As illustrated by the numerical examples, the enrichment term in the extended formulation is responsible for representing the near-tip behaviour, while the NURBS basis captures the difference between the analytical solution and the real response. For the numerical analyses, the order of these NURBS functions is selected as $p = 2$. Moreover, a 30-point Gaussian quadrature rule is considered for the evaluation of the integral kernels, the same amount used by Peng et al. (2016). The use of this high order scheme is motivated by a desire to present errors as those resulting from the formulation and its discretisation, i.e. with negligible pollution of the results from integration errors.

It is worth emphasising that in the proposed direct approach the stress intensity factors are found directly in the solution vector (see terms $\tilde{\mathbf{K}}_I^{\lambda}$ and $\tilde{\mathbf{K}}_{II}^{\lambda}$ at the bottom of the solution vector in Fig. 5.6a, for example). The applications show how these direct evaluations of the SIFs are of appropriate engineering accuracy without the requirement for further post-processing, e.g. a J-integral, which can save a significant amount of computational time as will be demonstrated in the last example of the chapter. However, the further enhancement of the accuracy of the SIFs that can be realised by including such a post-processing stage is also investigated, and it is for this purpose that the crack parameters are also computed indirectly using the interaction integral strategy based on the J-integral. When considering the unenriched formulation, the SIFs are also computed

using this scheme. For this post-processing strategy, the integration path is considered circular, centred at the crack tip and starting at the third collocation point counting from the tip. Consistent with the isogeometric philosophy, the integration path is defined as a NURBS discretised into sixteen elements.

5.7.1 Square plate with an edge crack

In this first example, the square plate containing an edge crack shown in Fig. 5.7 is analysed. Pure mode loadings are considered by prescribing the analytical displacements given by Eq. (3.2) as Dirichlet boundary conditions along the plate's edges, while the crack surfaces are treated as traction-free. For the analyses, it is assumed $a = 1$, $L = 2$, $E = 1$, $\nu = 0.3$ and plane strain state. The numerical solutions are compared with the exact solutions and also with the results provided by Peng et al. (2016), in which the IGABEM and an XIGABEM formulation based on PU-enrichment were applied.

Figure 5.7: Square plate with an edge crack (Example 5.7.1).

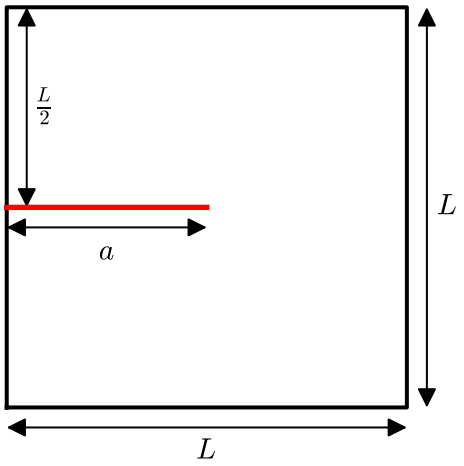

Source: Own author.

Initially, the accuracy and convergence rate of the proposed XIGABEM formulation are assessed with respect to the displacements in a pure mode I problem ($K_I = 1$ and $K_{II} = 0$). A fixed number of eight elements is used in the discretisation of each edge of the plate, while the number of elements along the crack surfaces is varied. Figure 5.8 shows the deformed shape for the upper crack surface determined by the unenriched and enriched formulations considering five elements along the crack. It can be noted that the result obtained by IGABEM differs from the analytical solution particularly near the crack tip since the NURBS basis functions are not capable of capturing the $\sqrt{\rho}$ behaviour in this region. On the other hand, the enriched approximation can approximate the exact response with remarkable precision. Figure 5.9 shows the convergence of the errors in the

relative L^2 displacement error norm e_{L2}, which is defined as:

$$e_{L2} = \frac{\|u^{num} - u^{ana}\|_{L^2(\Gamma_c)}}{\|u^{ana}\|_{L^2(\Gamma_c)}} \tag{5.44}$$

in which u^{num} and u^{ana} are the displacement solutions given numerically and analytically, respectively, and Γ_c denotes the crack surfaces. The L^2 norm of a vector quantity $\mathbf{g} = (g_x, g_y)^T$ is evaluated using $\|\mathbf{g}\|_{L^2(\Gamma_c)} = \sqrt{\int_{\Gamma_c} \mathbf{g}^T \mathbf{g} d\Gamma}$.

Figure 5.8: Deformed shape for the upper crack surface determined by IGABEM and XIGABEM (Example 5.7.1).

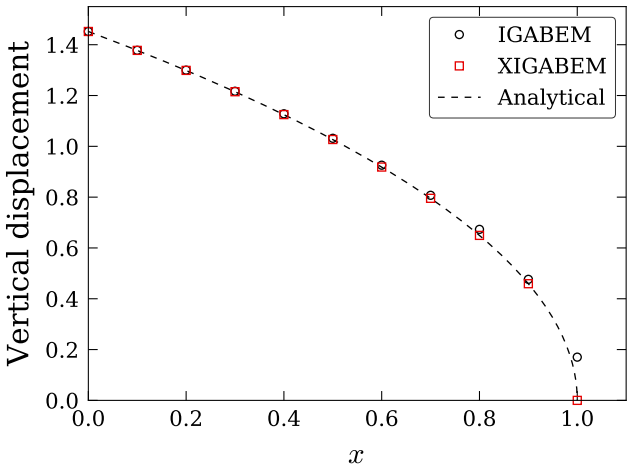

Source: Own author.

The results in Fig. 5.9 show that the accuracy and convergence rate obtained by the unenriched IGABEM model are similar to those determined by Peng et al. (2016). Regarding the enriched formulations, the PU-enrichment approach used by Peng et al. (2016) is capable of improving the convergence rate to 1.53 for a sufficiently fine mesh. This strategy includes the $\sqrt{\rho}$ behaviour of the displacements near the tip, which improves the accuracy when compared to the unenriched approach, but continuity at the crack tip is not guaranteed. In the proposed XIGABEM formulation, the crack tip function embedded into the displacement approximation can markedly improve the accuracy of the results, giving errors around 2.0×10^{-5} even for coarse crack meshes. The errors in this case depend fundamentally on how well the analytical displacement can be represented by the basis functions along the external boundary. This can be observed by the curve presented in Fig. 5.9 for an enriched model considering just four elements along each edge of the plate, in which the errors are increased to approximately 2.0×10^{-4}.

The reason for the errors in displacements to be practically constant in the XIGABEM model is that the displacements along the crack surfaces are fundamentally given by the enrichment term in the displacement approximation (see Eq. (5.18)), whereas the contribution from the NURBS basis functions is negligible. Consequently, the crack mesh refinement has little effect on the error convergence. The contribution of each term in the

Figure 5.9: Relative L^2 displacement error norm e_{L2} (Eq. (5.44)) along the crack surfaces. The reference results are taken from Peng et al. (2016) (Example 5.7.1).

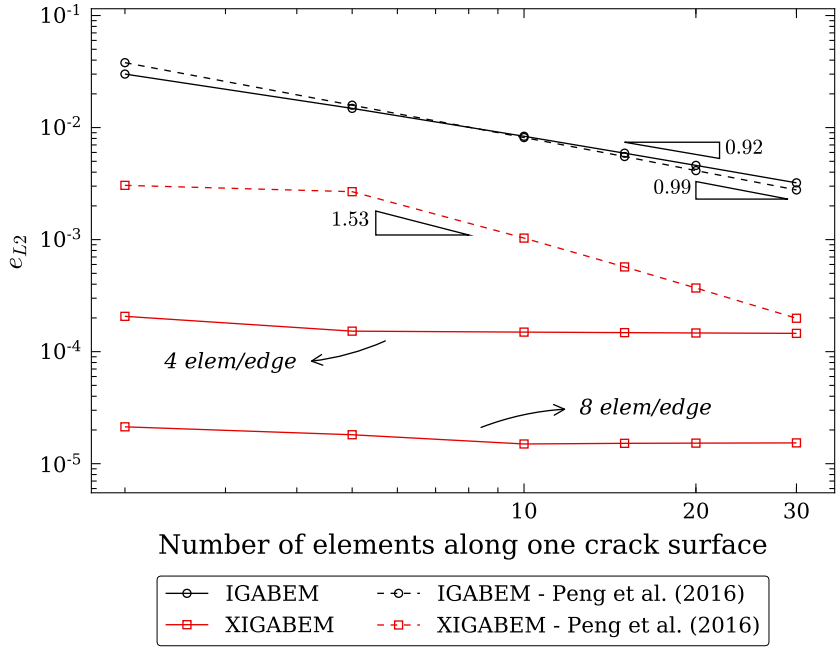

Source: Own author.

Figure 5.10: Deformed shapes considering the contribution from (a) the NURBS basis functions and (b) the enrichment term. (c) Final deformed shape for pure mode I problem, given by the superposition of solutions (a) and (b). The enriched NURBS are depicted in blue (please refer to the coloured version). A scale factor of 0.01 is adopted for the displacements (Example 5.7.1).

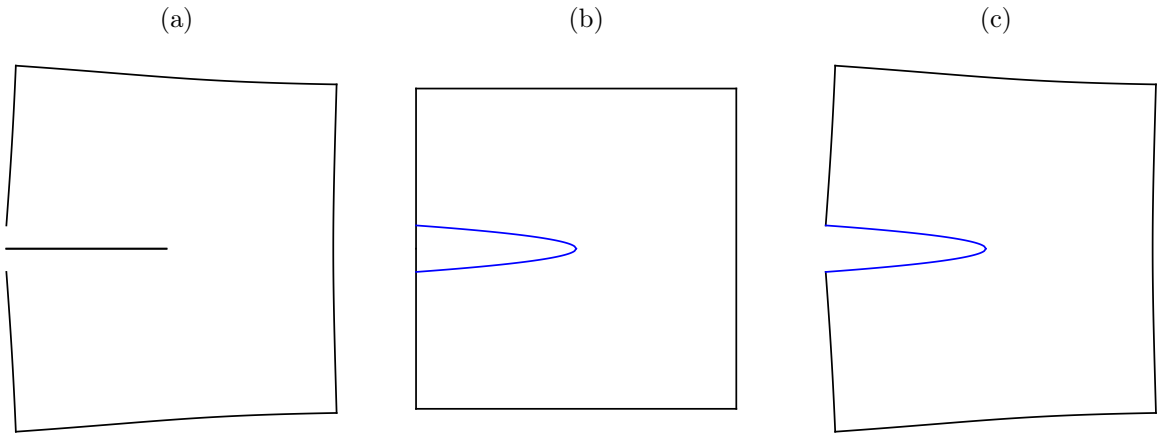

Source: Own author.

displacements is illustrated in the sequence depicted in Fig. 5.10. Figures 5.10a and 5.10b present the deformed shape considering the contribution from the NURBS basis functions and the enrichment term, respectively, while the superposition of both responses gives the deformed shape in Fig. 5.10c. From the sequence, it can be noted that the displacements along the crack are indeed controlled by the enrichment term, while the deformed shape of the external boundary is exclusively given by the basis functions since the corresponding NURBS are not enriched.

Considering now a mixed-mode problem in which $K_I = 1$ and $K_{II} = 1$, the accuracy of the SIF values determined by the numerical models is investigated. The SIFs are computed directly from the system of equations provided by the XIGABEM formulation and also indirectly with the J-integral approach. Figure 5.11 shows the convergence for K_I and K_{II} with the number of DOF in the numerical model. As in the displacement analysis, the accuracy and convergence rate for IGABEM are similar to the solutions obtained by Peng et al. (2016). Moreover, the direct approach is capable of giving very accurate solutions, with errors in the order of 0.011% for both SIFs even for coarse meshes. Furthermore, the combination of the enriched formulation and the J-integral approach can significantly improve the accuracy, giving errors as low as 0.0004%, but at the expense of computing internal points fields. Again, the mesh refinement has little effect in the convergence of the SIFs values since the near-tip behaviour is mainly controlled by the enrichment term.

Figure 5.11: Convergence of (a) mode I and (b) mode II SIF (Example 5.7.1).

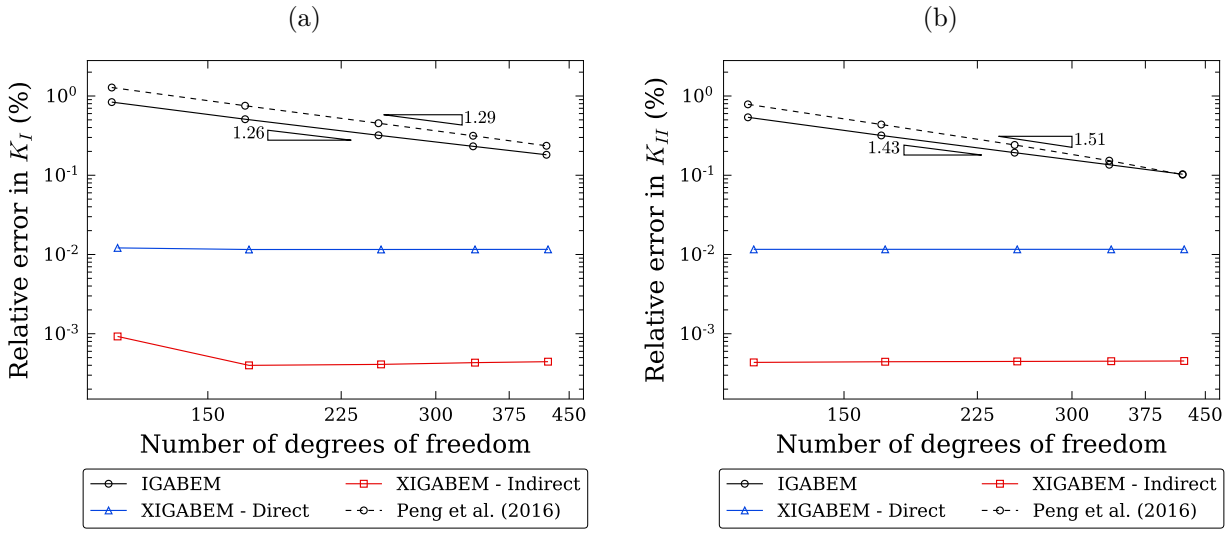

Source: Own author.

It is, of course, expected that for these pure mode problems the enriched formulation should give excellent results because the solution is contained in the approximation space. In what follows, examples in which this is not the case are explored.

5.7.2 Finite rectangular plate with an edge crack under bending

The rectangular plate containing an edge crack shown in Fig. 5.12 is considered in this second example. The structure is submitted to pure bending applied through linearly varying distributed loads ranging from -$\bar{\sigma}$ to $\bar{\sigma}$, as depicted in Fig. 5.12. The dimensions of the plate and crack are related by $h = 2.5w$ and $a = 0.5w$, and the values $\bar{\sigma} = 1$, $w = 2$, $E = 1$ and $v = 0$ are taken to perform the analyses. Alatawi and Trevelyan (2015) also simulated this problem considering an XBEM formulation similar to the one adopted in this chapter, but instead of the NURBS basis functions, they applied the conventional Lagrange polynomials in the displacement approximation. The reference solution provided by Fett (2008) is used to assess the accuracy of the numerical models.

Figure 5.12: Rectangular plate with an edge crack under uniform loading (Example 5.7.2).

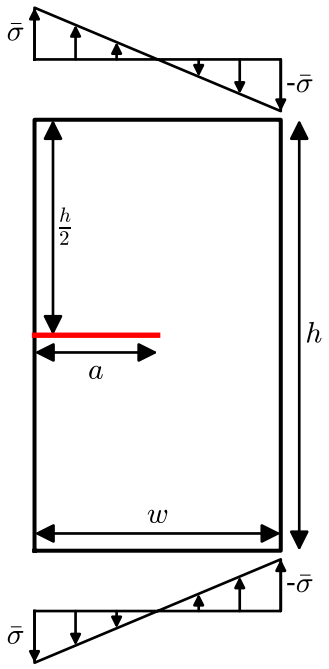

Source: Own author.

Figure 5.13a presents the evolution of K_I (normalised by $\bar{\sigma}\sqrt{\pi a}$) with mesh refinement. It can be noted that the solutions obtained by the present study and by Alatawi and Trevelyan (2015) tend to converge towards the reference value given by Fett (2008), plotted as a horizontal dashed line. Figure 5.13b shows the convergence pattern in each scenario. Concerning the unenriched formulations, the IGABEM is able to increase both the accuracy and the convergence rate when compared to conventional BEM. Besides, the enriched formulations increase the accuracy and convergence rate over their unenriched counterparts. Regarding the direct method for SIF extraction, XIGABEM solutions are more accurate than those determined using XBEM. However, the convergence rates obtained by these formulations are similar. For both XBEM and XIGABEM, the lowest errors and highest convergence rate are given by associating the enriched formulation

Figure 5.13: Variation of (a) mode I SIF (normalised by $\bar{\sigma}\sqrt{\pi a}$) and (b) relative error with the mesh refinement obtained by the present work and by Alatawi and Trevelyan (2015). The reference value for normalised K_I is taken from Fett (2008) (Example 5.7.2).

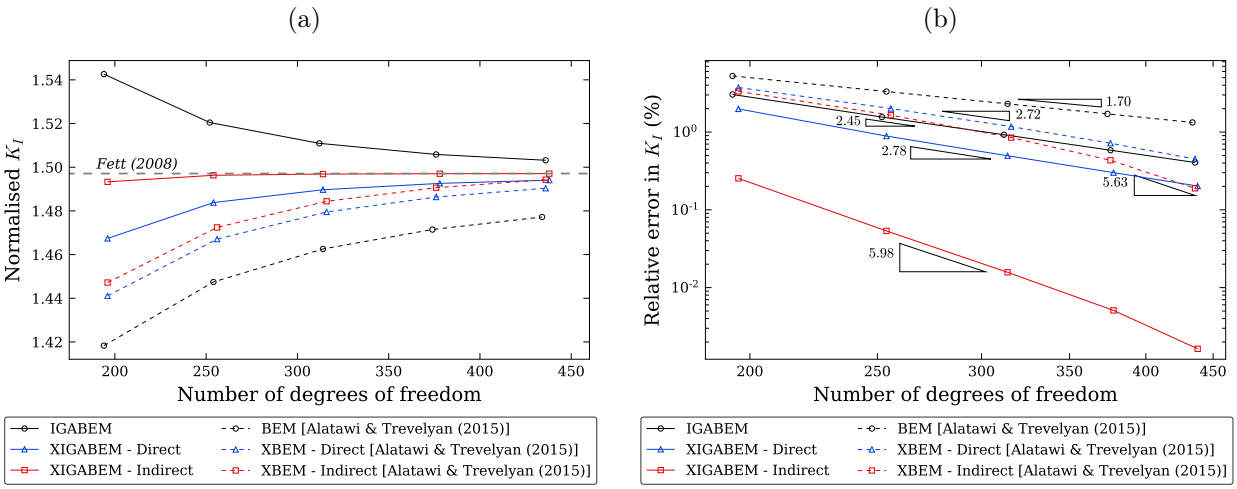

Source: Own author.

Figure 5.14: Deformed shapes considering the contribution from (a) the NURBS basis functions and (b) the enrichment term. (c) Final deformed shape for pure mode I problem, given by the superposition of solutions (a) and (b). The enriched NURBS are depicted in blue (please refer to the coloured version). A scale factor of 0.05 is adopted for the displacements (Example 5.7.2).

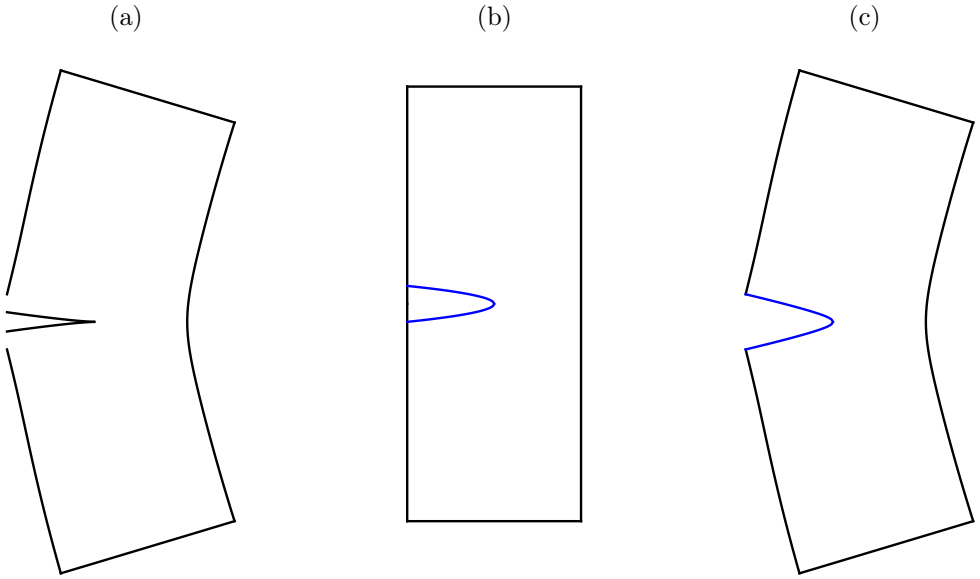

Source: Own author.

with the J-integral technique. When the XIGABEM is considered in this case, the error in K_I is around 0.25% for the coarsest mesh used, reducing to 0.0016% with mesh refinement.

The contribution of each term in the displacement approximation to the deformed shape of the structure is illustrated in Fig. 5.14. Unlike the previous example, there is now a non-zero contribution from the NURBS basis functions to the crack response since the enrichment functions are unable to describe the behaviour over the entire crack. However, the near tip behaviour continues to be strongly influenced by the enrichment term.

5.7.3 Inclined crack in an infinite domain

Figure 5.15 shows an inclined crack immersed in an infinite domain that is subjected to a far-field vertical loading $\bar{p}$. Mode I and mode II SIFs are computed with IGABEM and XIGABEM for different crack orientations θ. The infinite domain formulation proposed by Telles, Mansur, and Wrobel (1984) is applied, so only the crack surfaces are discretised. The following parameters are assumed: $2a = 1$, $\bar{p} = 1$, $E = 1$, $\upsilon = 0.3$ and plane strain conditions. The results for the SIFs are compared with the analytical solutions expressed by:

$$\begin{aligned} K_I &= \bar{p}\sqrt{\pi a}\cos^2\theta \\ K_{II} &= \bar{p}\sqrt{\pi a}\cos\theta\sin\theta \end{aligned} \tag{5.45}$$

Figure 5.15: Inclined crack in an infinite domain submitted to far-field vertical loading (Example 5.7.3).

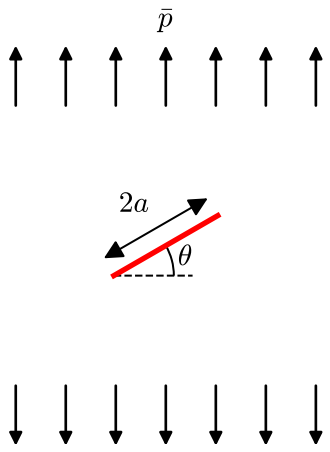

Source: Own author.

The variations of K_I and K_{II} with the crack angle θ are presented in Fig. 5.16a. The numerical results were obtained considering ten elements along each crack surface.

The responses provided by Liu, Xiao, and Karihaloo (2004) using an XFEM formulation to extract the SIFs directly are also shown in the figure. Good agreement is observed between the solutions determined by IGABEM and XIGABEM and the analytical responses. Furthermore, it can be noted that, in general, the results determined here better approximate the analytical results when compared to the XFEM approach. This occurs especially because the boundary integral formulation allows the simulation of the infinite domain, whereas a finite plate was considered in Liu, Xiao, and Karihaloo (2004), which introduced errors due to the mesh truncation.

Figure 5.16: (a) Results for normalised SIFs considering ten elements in each crack surface. (b) Relative error evolution with crack mesh refinement (Example 5.7.3).

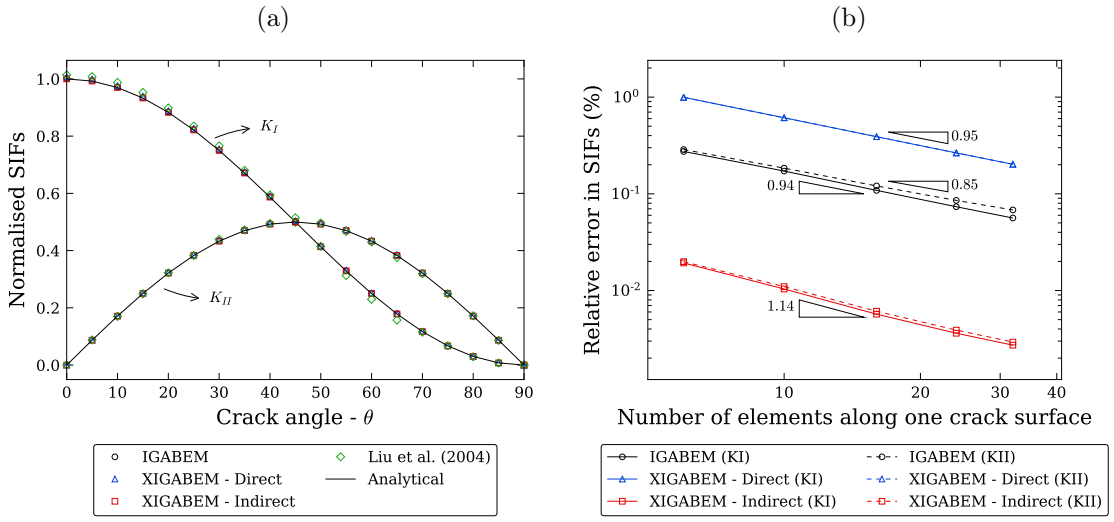

Source: Own author.

In the IGABEM and XIGABEM models, the errors in the SIF values are independent of the crack angle. Figure 5.16b shows typical curves for the error variation with crack mesh refinement. As in the previous examples, the combination of the enriched formulation with the J-integral significantly improves the convergence rate and the accuracy of the SIFs recovered. On the other hand, the direct method is less accurate than the unenriched IGABEM due to the interaction between the crack tips. However, the errors obtained by the direct approach remain low, with the same order of magnitude observed in the previous example, ranging from 1% down to 0.2%.

Figure 5.17 illustrates the interaction between displacement solutions for the two crack tips considering the XIGABEM formulation. The enrichment term provides a deformed shape for each tip considering both tips in isolation, as shown in Fig. 5.17b. The addition of the contribution from the NURBS basis functions, depicted in Fig. 5.17a, allows the scheme to recover the ellipse-like deformed shape in Fig. 5.17c. This is a good illustration of the role that the NURBS basis functions are required to play over enriched portions of the boundary; this role can be viewed as the capturing of the difference between the pure mode behaviour (expressed in the enrichment terms) and the true solution we seek.

Figure 5.17: Deformed shapes for $\theta = 30°$ considering the contribution from (a) the NURBS basis functions and (b) the enrichment term. (c) Final deformed shape for slanted crack, given by the superposition of solutions from (a) and (b). Enriched NURBS are depicted in blue (please refer to the coloured version). A scale factor of 0.1 is adopted for the displacements (Example 5.7.3).

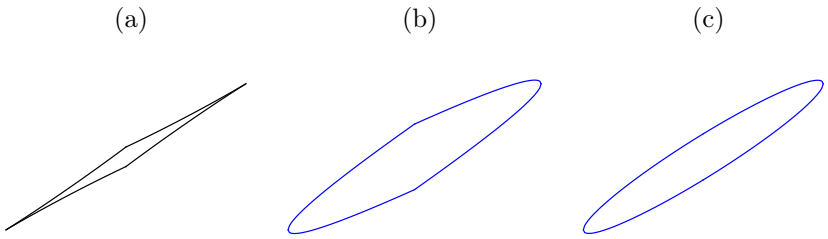

Source: Own author.

5.7.4 Titanium plate with a central inclined crack

Figure 5.18 shows a rectangular titanium plate containing a central crack of length $2a = 13.462$ mm inclined of an angle $\theta = 47°$ with respect to the horizontal direction. The dimensions of the structure are $w = 76.2$ mm and $h = 304.8$ mm. A fatigue test of such a plate was conducted by Pustejovsky (1979) considering a loading amplitude $\bar{\sigma}$ ranging from 17.24 to 172.37 MPa. This experiment is reproduced numerically with the XIGABEM model considering the following Paris law parameters : $C = 3.781 \times 10^{-15}$ and $m = 3.81$, with da/dN^{lc} given in mm/cycles and ΔK_{ef} in MPa $\times$ mm$^{0.5}$. To perform the numerical analysis, each crack surface is discretised in fifteen elements, while fifty elements are adopted along the external boundary. A crack length increment $\Delta a = 0.5$ mm is used for the fatigue growth, with two elements inserted along each new crack surface.

Figure 5.18: Specimen of a titanium plate with a central inclined crack (Example 5.7.4).

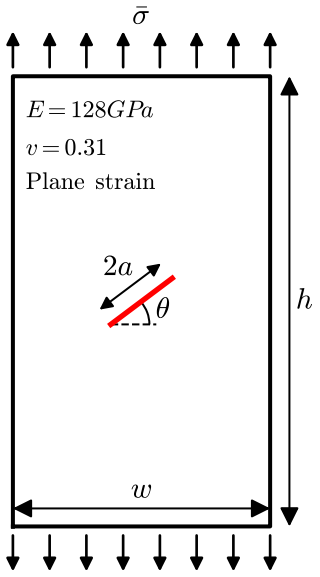

Source: Own author.

Figure 5.19 shows the propagation path determined by the XIGABEM model considering the direct method for evaluating the SIFs. The experimental result obtained by Pustejovsky (1979) and the numerical response provided by Pereira, Duarte, and Jiao (2010) using generalised FEM (GFEM) are also depicted in the figure. Good agreement is attained between the solution determined by the proposed enriched formulation and the experimental and numerical results found in the literature.

Figure 5.19: Comparison between the propagation path obtained by the XIGABEM model considering the direct approach for SIFs extraction and the experimental results determined by Pustejovsky (1979). The numerical solution obtained by Pereira, Duarte, and Jiao (2010) using GFEM is also provided (Example 5.7.4).

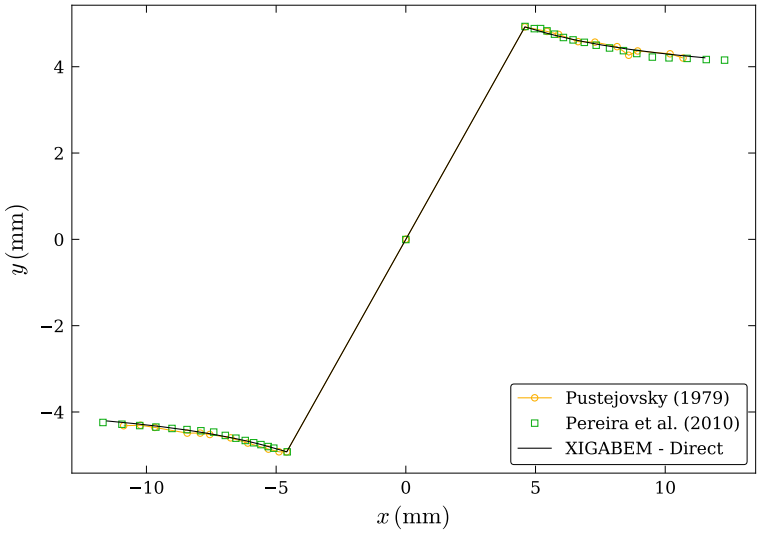

Source: Own author.

The crack length evolution with the number of loading cycles is presented in Fig. 5.20. There is a good correspondence between the unenriched and enriched formulations adopted in the present study. At the end of 14 increments, the fatigue life determined by the numerical approaches is approximately 16 thousand cycles, which agrees particularly well with the experimental results for the right tip given by Pustejovsky (1979).

5.7.5 Open spanner

In this example, the advantage of using the isogeometric formulation to deal with geometries taken directly from CAD is explored. For this purpose, consider the open spanner subjected to a cyclic loading $\bar{p}$ with range $0 \sim 10$, as illustrated in Fig. 5.21. The knot-vector and the positions of the main control points for the definition of the B-spline representing the external boundary are also presented in the figure. An initial edge flaw with length $a = 0.15$ is located in a region of high stress concentration given by an elastostatic analysis (SIMPSON et al., 2012). The geometry of this problem was originally proposed by Simpson et al. (2012), and a crack propagation analysis was later

Figure 5.20: Crack length evolution with number of load cycles. The solutions obtained experimentally by Pustejovsky (1979) are also provided (Example 5.7.4).

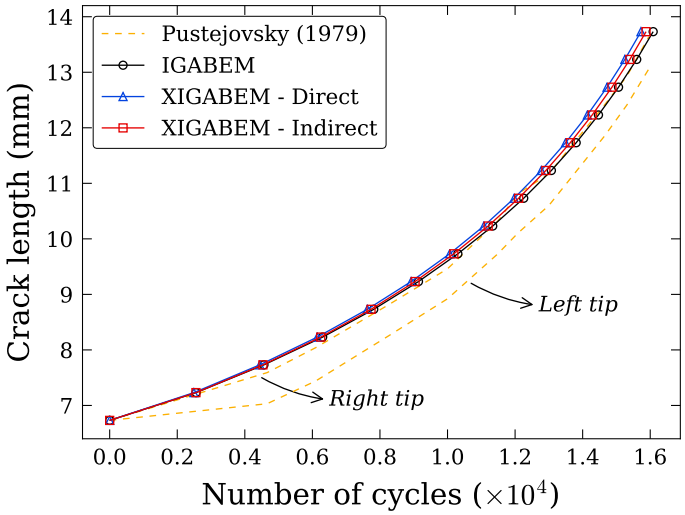

Source: Own author.

conducted by Peng et al. (2016). Here, a fatigue analysis is carried out with the proposed XIGABEM formulation considering the following parameters: $C = 10^{-13}$, $m = 2.6$ and $\Delta a = 0.1$. Each crack surface is initially discretised in three elements, and two elements are added to each surface after the crack extension.

Figure 5.21: Open spanner with an edge crack. The repeated knot 5.478 in the knot vector defining the external boundary indicates the position of the crack mouth. Besides, the weights associated with the control points are taken as a unit (Example 5.7.5).

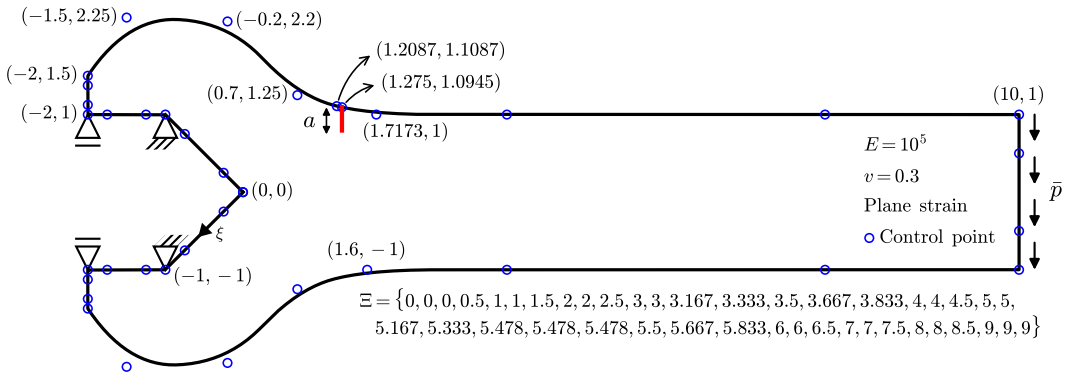

Source: Own author.

Figure 5.22 illustrates the deformed shape after 10 crack increments determined by the direct XIGABEM model. Good agreement is noted between the crack paths obtained here and the reference solution given by Peng et al. (2016). The variation of the SIF values with crack length is presented in Fig. 5.23a. At the initial configuration, the magnitude of K_{II} is significant; however, as the crack grows, the magnitude of K_{II} remains low, and the propagation becomes mode I dominant. A small difference can be observed between the values obtained by IGABEM and XIGABEM, a difference also reflected

in the results for the evolution of the crack length with the number of load cycles, as shown in Fig. 5.23b. For the XIGABEM models, the final configuration is achieved after approximately 3.74 million load cycles, whereas this number is around 3.68 million cycles considering IGABEM.

Figure 5.22: Deformed shape after 10 crack increments obtained with the XIGABEM model considering the direct method for SIF extraction. The segments near the crack tip containing the enrichment term for the displacement approximation are depicted in blue (please refer to the coloured version). The solution provided by Peng et al. (2016) is also shown for comparison (Example 5.7.5).

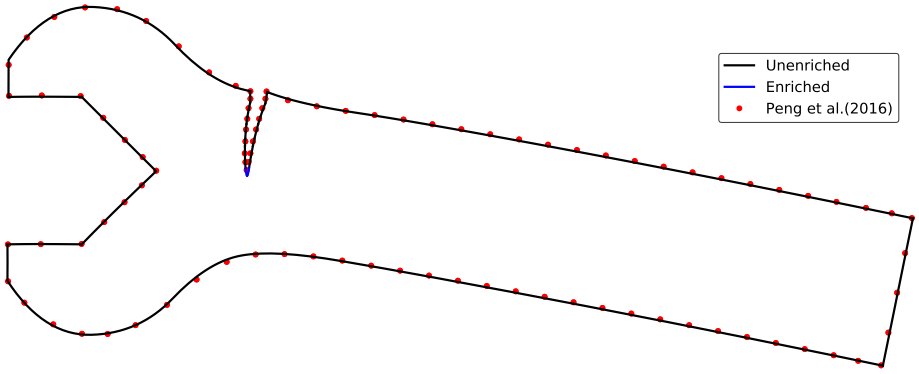

Source: Own author.

Figure 5.23: Variation of (a) SIFs and (b) the number of load cycles with crack evolution (Example 5.7.5).

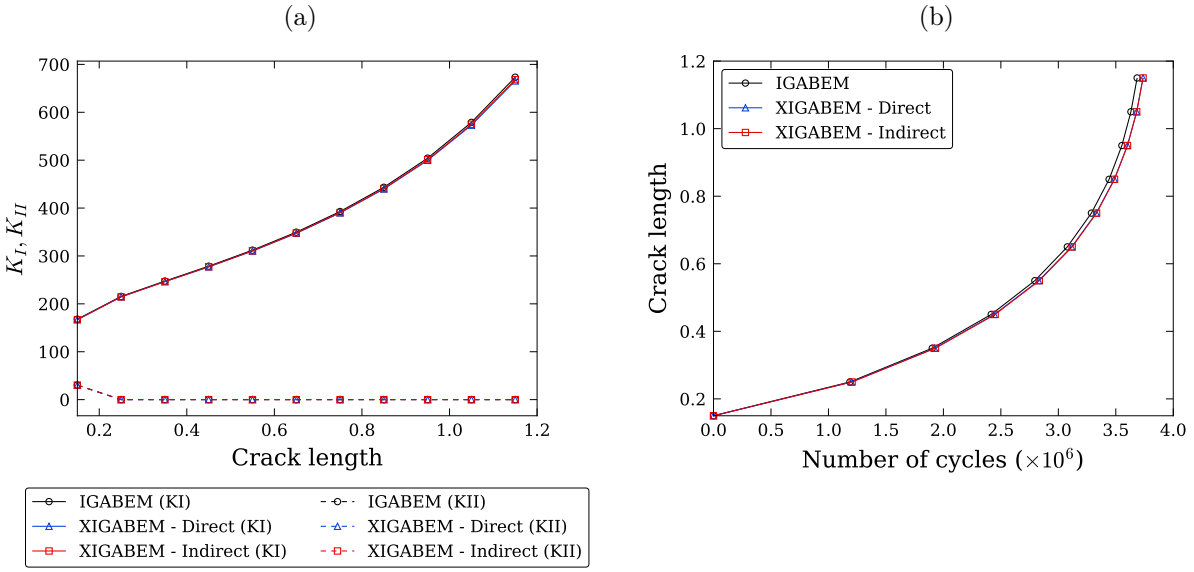

Source: Own author.

5.7.6 Perforated plate with an edge crack

Figure 5.24 shows a rectangular plate containing two holes of diameter $\phi = 0.4$ and subjected to an uniform cyclic loading $\bar{p}$ with magnitude $0 \sim 10$. The length and height

of the structure are $2L$ and L, respectively, with $L = 1$. A vertical crack emanates from the bottom edge and has initial length $a = 0.05$. In this example, different values are considered for l, the parameter defining the initial position of the defect, to assess its effect on the crack path and fatigue life. The following values are adopted: $l = \{0.95, 1.025, 1.1, 1.175, 1.25\}$. Furthermore, the parameter values $C = 10^{-10}$, $m = 3.0$ and $\Delta a = 0.025$ are taken for the fatigue analysis.

Figure 5.24: Tensioned rectangular plate with two holes and an edge crack (Example 5.7.6).

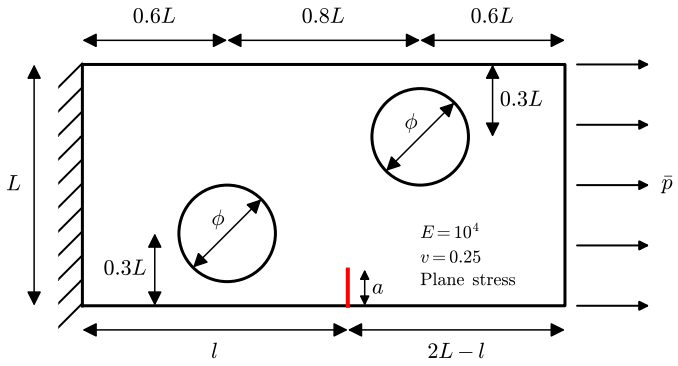

Source: Own author.

Figure 5.25: Deformed shape for configuration considering (a) $l = 0.95$, (b) $l = 1.025$, (c) $l = 1.1$, (d) $l = 1.175$ and (e) $l = 1.25$. The scale factor λ used in each figure is also indicated. The NURBS segments near the crack tip containing the enrichment term for the displacement approximation are depicted in blue (please refer to the coloured version). (f) Crack paths determined for each initial crack position (Example 5.7.6).

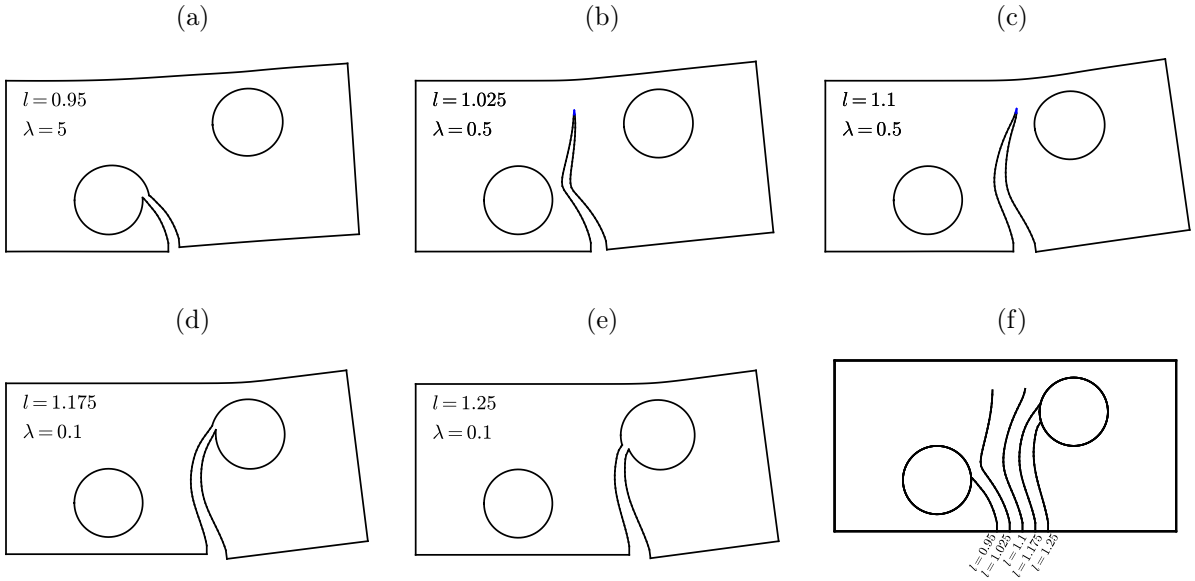

Source: Own author.

Figures 5.25a to 5.25e show the deformed shapes for different values of l obtained with XIGABEM considering the direct approach for SIF extraction. Figures 5.25a, 5.25d and

5.25e present, respectively, the cases where $l = 0.95$, $l = 1.175$ and $l = 1.25$, in which the crack is attracted to, and ends up intersecting one of the openings. The successive knot insertion to achieve C^{-1} continuity at the intersection point in the NURBS representing the hole is capable of modelling the displacement discontinuity at the crack mouth. In the cases represented by Figures 5.25b and 5.25c, where $l = 1.025$ and $l = 1.1$, respectively, the crack path tends to deviate toward the holes, but then moves away following a direction perpendicular to the applied load. The final crack paths determined in each one of these scenarios are grouped in Fig. 5.25f.

Finally, Fig. 5.26 illustrates the evolution of the crack length with load cycles, for each initial crack position, comparing the IGABEM and XIGABEM formulations. The stress concentration caused by the left hole increases the crack growth rate as the initial crack position is moved to the left (lower values of l), decreasing the fatigue life. The responses determined with the different formulations are very similar, with differences less than 1.0%. The final number of load cycles for each case, given in ascending order of l, is approximately: 0.65, 1.27, 2.07, 3.52 and 5.93 million cycles.

Figure 5.26: Crack length evolution determined by the unenriched and enriched formulations considering the different values of l (Example 5.7.6).

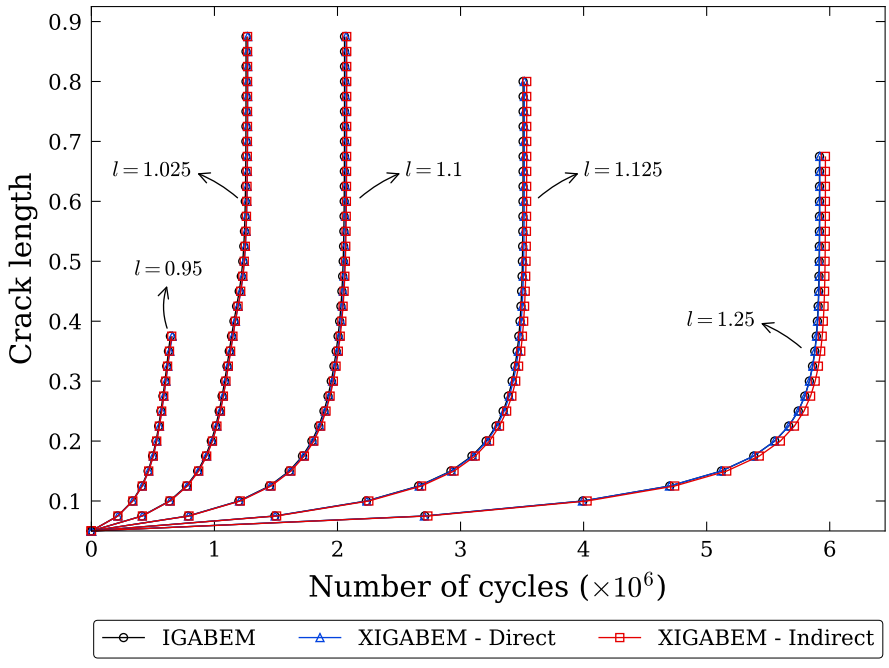

Source: Own author.

5.7.7 Perforated panel with multiple cracks

In this example, the perforated panel shown in Fig. 5.27 is analysed. The structure contains three holes of diameter $\phi = 10$ mm, with cracks of length $a = 3$ mm emanating from the top and bottom of each hole. The length in Fig. 5.27 is taken as $L = 100$ mm.

A cyclic load with components $\bar{p}_x = 9$ MPa and $\bar{p}_y = 1$ MPa is applied to the right edge of the panel, with a stress ratio of zero, while the left edge remains fixed. For the fatigue analysis, the Paris law constants are taken as $C = 10^{-13}$ and $m = 2.6$, assuming da/dN^{lc} given in mm/cycles and ΔK_{ef} in MPa $\times$ mm$^{0.5}$. During the crack growth, the crack length increment for the fastest growing tip is $\Delta a = 1$ mm, with the others growing proportionally to their respective growth rates. For the initial geometry, each crack surface is discretised with four elements, with a minimum of two elements being added to the new surfaces after propagation.

Figure 5.27: Perforated panel (Example 5.7.7).

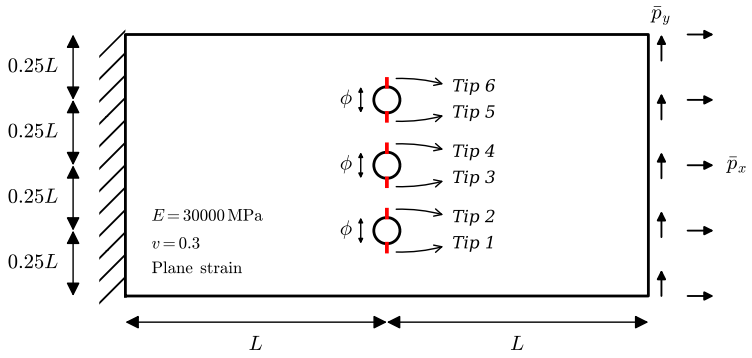

Source: Own author.

Figure 5.28a presents the evolution of ΔK_{ef} for the tips after each crack increment. The results are obtained by XIGABEM considering the direct approach for SIF computation. The curves in the figure can be interpreted in conjunction with the sequence illustrating the crack propagation in Fig. 5.29. For initial geometries (Fig. 5.29a), tip 1 has the greatest ΔK_{ef}, and consequently the highest growth rate, due to the bending effect in the plate. However, as the cracks start to grow, the stress concentration caused by the interaction between tips 2 and 3 (Fig. 5.29b) soon makes them surpass tip 1 as the most dominant, with both developing similar growth rates. However, the growth at tips 2 and 3 becomes retarded as they start to overlap each other in the classical fashion for opposing cracks (Fig. 5.29c), and tip 1 regains its dominance. At later crack increments, tips 2 and 3 develop small growth rates, whereas tips 4 and 5 move towards each other at faster rates (Fig. 5.29d). As happened for tips 2 and 3, the pair 4 and 5 also experience retardation in their crack growth rates as they overlap (Fig. 5.29d). Tip 1 continues to be the fastest growing tip and moves towards the bottom edge of the panel (Fig. 5.29e), finally intersecting the external boundary. Figure 5.29f shows the final deformed shape for the structure, in which the discontinuities in the NURBS representing the perforations and the bottom edge are clearly visible.

The history of ΔK_{ef} with crack length is shown in Fig. 5.28b. Since tip 1 is dominant for most of the analysis, it develops the largest length. For the interacting cracks - tips 2-3

and tips 4-5 - it can be noted that, as they approach each other, the behaviour for the pair is very similar, with the crack positioned towards the bottom of the plate having larger lengths due to the bending effect. The results obtained by Price and Trevelyan (2014) using BEM are also given in Fig. 5.28b. The reference considered fewer crack increments than the present study, but the solutions provided are in good agreement with the results obtained by XIGABEM.

Figure 5.28: Variation of ΔK_{ef} with (a) crack increment and (b) crack length (Example 5.7.7).

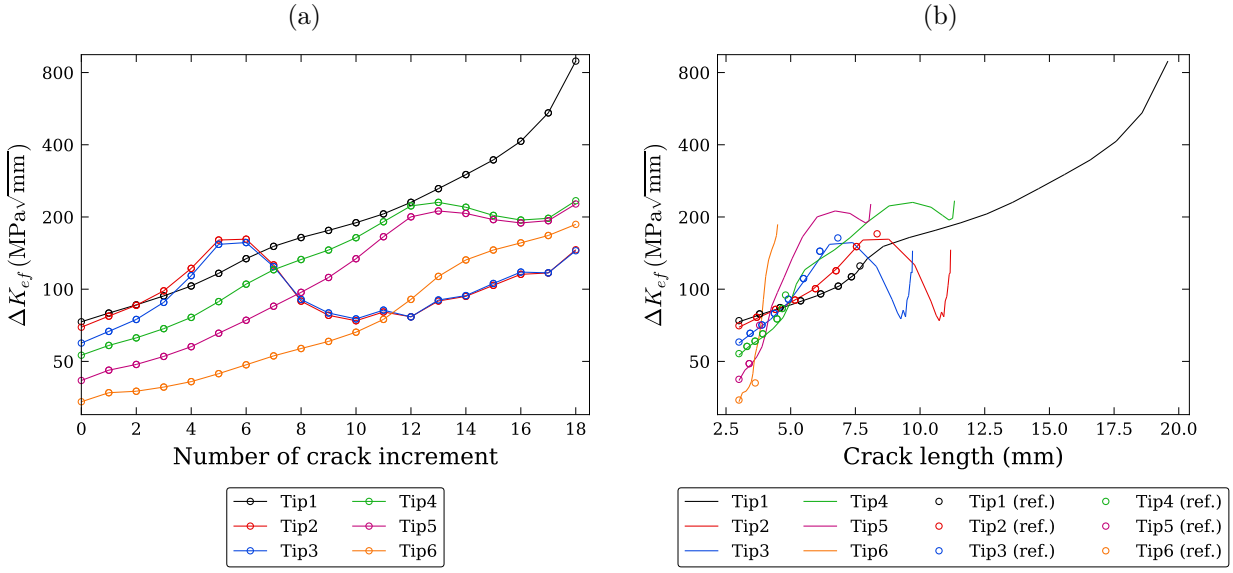

Source: Own author.

Figure 5.29: (a)-(e) Evolution of the crack paths and (f) final deformed shape obtained by the direct XIGABEM formulation. The enriched NURBS segments are depicted in blue (please refer to the coloured version) (Example 5.7.7).

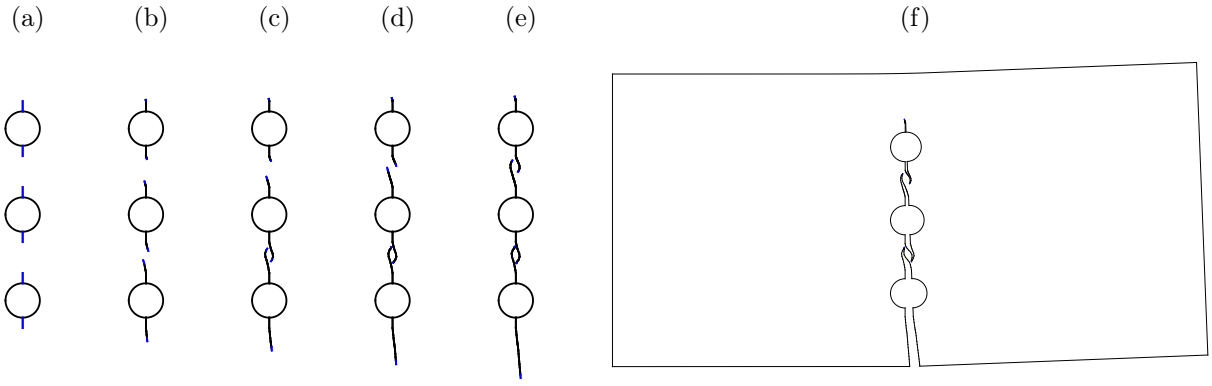

Source: Own author.

The incremental evolution of the fatigue crack growth in the perforated panel is shown in Fig. 5.30. Since this problem contains multiple cracks, with different tips dominating as the analysis progresses, the number of load cycles is related to the number of the crack

increment. The dominant tip in each geometry is also indicated. A sudden decrease in the crack growth rate can be seen between increments 6 and 7, after tip 1 regains its dominance. This occurs because the value of ΔK_{ef} in increment 6 (related to tip 2) is greater than the value of ΔK_{ef} in increment 7 (related to tip 1). The solutions obtained by IGABEM and XIGABEM considering the J-integral for SIF evaluation are also shown in Fig. 5.30 for comparison. Good agreement is observed between these results, demonstrating the accuracy of the direct method in solving problems of multiple fatigue crack propagation.

Figure 5.30: Incremental fatigue process for the perforated panel determined by the unenriched and enriched formulations (Example 5.7.7).

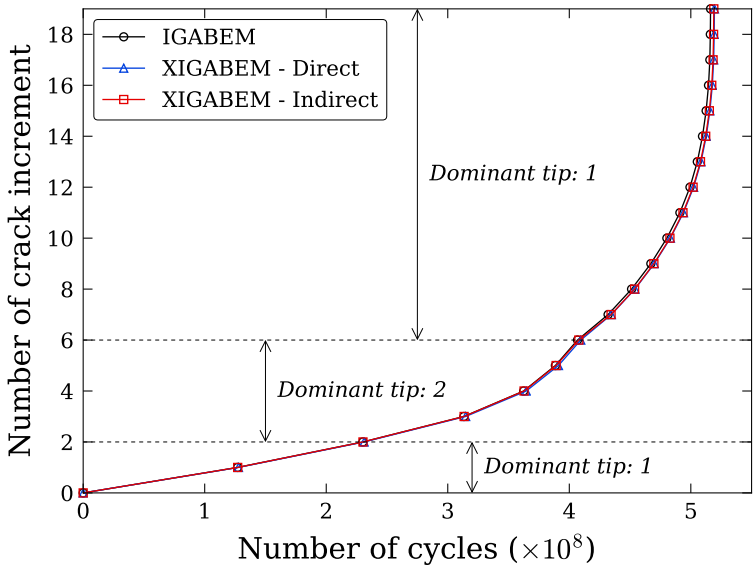

Source: Own author.

Finally, Fig. 5.31a presents the accumulated run time for the analysis of each configuration during crack growth. The results obtained by the proposed XIGABEM formulation, considering both the direct and indirect methods for SIF extraction, are compared against those determined by the conventional IGABEM. The execution time values t are normalised by t_0, which is the time for the analysis of the initial configuration considering the direct XIGABEM approach. Note that when the direct approach is considered, the run times are considerably lower than when the indirect method based on the J-integral is used for evaluation of the SIFs. Besides, the indirect XIGABEM solutions take slightly longer to obtain compared to the unenriched IGABEM due to the consideration of the enriched integral kernels in the isogeometric formulation. Nonetheless, this small increase in computational cost is accompanied by a large improvement in the accuracy of the SIF solutions, as demonstrated in previous examples.

The relative differences in execution times determined by XIGABEM (direct and indirect) compared to IGABEM are shown in Fig. 5.31b. In the case of indirect XIGABEM, the run times are 30% to 40% higher than for conventional IGABEM at the start of the

analysis; however, the absolute values of time are small, in the order of seconds. As the propagation progresses, these differences diminish and stabilise around 15% towards the end of the analysis. For direct XIGABEM, the time saving compared to the unenriched method is substantial: at the beginning of the analysis, it is around 60% and, at the end, the reduction in computational cost is approximately 50%. This demonstrates the advantage of the proposed direct XIGABEM for the crack analysis, particularly those involving large-scale problems requiring several computations for the SIFs. Such method is able to significantly decrease the computational cost while the accuracy of the results is ensured.

Figure 5.31: (a) Accumulated run time to obtain the solution for each crack configuration. The values are normalised by t_0, which is the smallest time observed for the analysis of the initial configuration and corresponds to the run time of the direct XIGABEM. (b) Relative differences between accumulated run times considering the indirect IGABEM results as reference (Example 5.7.7).

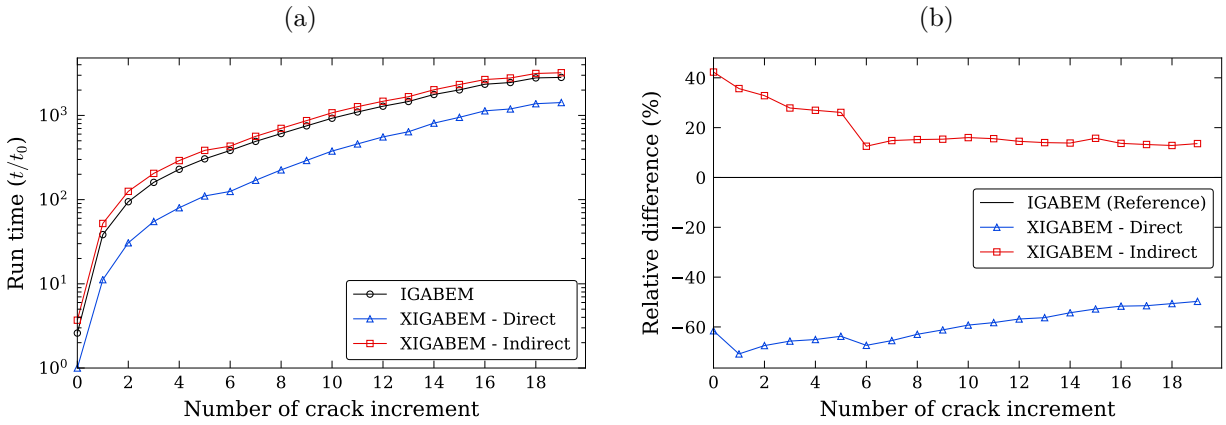

Source: Own author.

6 XIGABEM for interface cracks

6.1 Initial considerations

In the previous chapter, an XIGABEM approach is developed for simulating crack problems in homogeneous and isotropic materials. In this chapter, a novel XIGABEM formulation is proposed for the analysis of cracks between two piecewise isotropic subdomains. Therefore, the enriched approach is extended to investigate the interface fracture of bimaterial structures.

Differently from the XIGABEM strategy for homogeneous materials presented in Chapter 5, not only the crack elements are enriched, but also the elements lying on the interface between materials. Besides, in this chapter the two-term asymptotic expansion is used to define the enrichment function: the first, as in the previous chapters, is the leading order term that is related to the SIFs, while the second is the term related to the T-stress. As will be demonstrated, the SIFs and T-stress parameter can be computed directly from the system of equations when considering the proposed formulation. It is worth mentioning that the two-term enrichment can also be applied to homogeneous materials so that the T-stress can also be obtained from the solution vector.

This chapter also shows that the enrichment functions based on the straight crack solution can be applied for the direct evaluation of the crack parameters for curved cracks. In this case, the effect of the curvature can be disregarded for portions close to the tip and, consequently, the asymptotic expansion defined for a straight crack - as well as the corresponding crack parameters - are able to represent the analytical behaviour in these regions.

Several numerical applications are presented and the solutions provided by the direct XIGABEM approach are compared against analytical, semi-analytical and numerical results available in the literature.

6.2 Extended formulation

For the crack analysis of domains containing different materials, the sub-region BEM technique is adopted (see Section 2.6). Consider the inhomogeneous domain $\Omega = \Omega_1 \cup \Omega_2$ shown in Fig. 6.1. Each subdomain Ω_s is assumed as homogeneous, isotropic and linear elastic. Besides, each subregion is enclosed by its respective boundary $\Gamma_s = \partial\Omega_s$, which is given by the union of the external boundary Γ_s^B, the crack surface Γ_s^C and the interface boundary Γ_s^I, i.e., $\Gamma_s = \Gamma_s^B \cup \Gamma_s^C \cup \Gamma_s^I$. Disregarding body forces, the displacement components at each point $\mathbf{x}' \in \Gamma_s$ can be computed from the DBIE (2.31), which is rewritten in terms of the subdomain boundary Γ_s as follows:

$$c_{ij}(\mathbf{x}')u_j(\mathbf{x}') + \cancel{\int_{\Gamma_s}} P^*_{ij}(\mathbf{x}', \mathbf{x})u_j(\mathbf{x})d\Gamma_s = \int_{\Gamma_s} U^*_{ij}(\mathbf{x}', \mathbf{x})p_j(\mathbf{x})d\Gamma_s \qquad \mathbf{x}', \mathbf{x} \in \Gamma_s \tag{6.1}$$

Figure 6.1: Interface crack between two dissimilar materials.

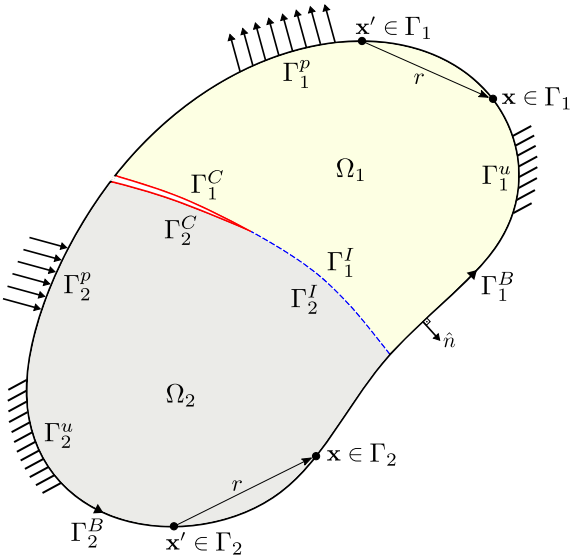

Source: Own author.

Note that, unlike Eq. (2.31), there is no jump term related to a corresponding collocation point $\bar{\mathbf{x}}'$ in Eq. (6.1) since this point belongs to a subregion different than that of $\mathbf{x}'$.

Following conventional IGABEM presented in Section 5.4, the same approximation used in the description of the geometry (Eq. (5.13)) is applied to interpolate the displacements and tractions over the element. In this case, the mechanical fields are expressed solely by the NURBS functions as follows:

$$\tilde{u}^e_j(\xi) = u^{(N)}_j(\xi) = \sum_{m=1}^{p+1} \phi^{em}(\xi) d^{em}_j \tag{6.2}$$

$$\tilde{p}^e_j(\xi) = p^{(N)}_j(\xi) = \sum_{m=1}^{p+1} \phi^{em}(\xi) t^{em}_j \tag{6.3}$$

where the superscript (N) specifies the NURBS contribution and d^{em}_j and t^{em}_jrepresent, respectively, the m-th local displacement and traction control parameter from element e.

As for homogeneous problems, the NURBS basis functions fail to accurately represent the near-tip solutions for interface cracks expressed in Eqs. (3.46) and (3.48), especially the leading-order terms. Then, to improve the numerical responses, an extended formulation is proposed, in which the two-term asymptotic expansion for stresses (Eq. (3.53)) and displacements (Eq. (3.56)) are used to augment the approximations of elements defining

the interface and crack surfaces. Hence, the displacement approximation for an element e near a crack tip λ becomes:

$$\tilde{u}_j^{e\lambda}(\xi) = u_j^{(N)}(\xi) + R_{jk}^{\lambda} u_k^{(1)}(\mathbf{x}^{\lambda}, \mathbf{x}(\xi)) + R_{jk}^{\lambda} u_k^{(2)}(\mathbf{x}^{\lambda}, \mathbf{x}(\xi)) \tag{6.4}$$

where $\mathbf{x}^{\lambda}$ denotes the position of crack tip λ and $u_k^{(1)}$ and $u_k^{(2)}$ are, respectively, the first and second term of the enrichment expressed by:

$$\left\{ \begin{array}{c} u_1^{(1)} \\ u_2^{(1)} \end{array} \right\} = \sqrt{\frac{\rho}{2\pi}} \left[\begin{array}{cc} \Delta_1^1(\theta, s) & \Theta_1^1(\theta, s) \\ \Delta_2^1(\theta, s) & \Theta_2^1(\theta, s) \end{array} \right] \left[\begin{array}{cc} \cos(\varepsilon \log \rho) & -\sin(\varepsilon \log \rho) \\ \sin(\varepsilon \log \rho) & \cos(\varepsilon \log \rho) \end{array} \right] \left\{ \begin{array}{c} \tilde{K}_1^{\lambda} \\ \tilde{K}_2^{\lambda} \end{array} \right\} \tag{6.5}$$

$$\left\{ \begin{array}{c} u_1^{(2)} \\ u_2^{(2)} \end{array} \right\} = \frac{\rho}{\sqrt{2\pi}} \left\{ \begin{array}{c} \Delta_1^2(\theta, s) \\ \Delta_2^2(\theta, s) \end{array} \right\} \tilde{K}_T^{\lambda} \tag{6.6}$$

where $\rho \coloneqq \left\| \mathbf{x} - \mathbf{x}^{\lambda} \right\|$ and $\tilde{K}_1^{\lambda}$, $\tilde{K}_2^{\lambda}$ and $\tilde{K}_T^{\lambda}$ represent the additional degrees of freedom included by the enrichment that are found as part of the BEM solution vector. It is worth mentioning that, as in the XIGABEM formulation for homogeneous materials presented in Chapter 5, the enrichment parameters become accurate approximations for the SIFs and T-stress parameter only if the additional constraints to be presented in Section 6.2.5 are enforced at the crack tip.

The components given in Eqs. (6.5) and (6.6) are related to the local crack tip coordinate system $x_1' x_2'$, as represented in Fig. 6.2a. Therefore, to express the contributions of the enrichment terms in the global coordinate system $x_1 x_2$, the components R_{jk} from the rotation matrix are included in Eq. (6.4), in which:

$$\left[\begin{array}{cc} R_{11} & R_{12} \\ R_{21} & R_{22} \end{array} \right] = \left[\begin{array}{cc} \cos\omega & -\sin\omega \\ \sin\omega & \cos\omega \end{array} \right] \tag{6.7}$$

where ω is the angle between $x_1' x_2'$ and $x_1 x_2$ (see Fig. 6.2a).

To represent the near-tip singularity, the traction approximation of interface elements is also enriched with functions based on the analytical stress expansion. The enrichment terms are obtained through Cauchy's formula $p_i = \sigma_{ij} n_j$, where the stresses σ_{ij} are defined from Eq. (3.53) and n_j represents the outward normal vector at the surface. Considering a straight crack, as depicted in Fig. 6.2a, the enrichment traction components - oriented according to the local crack tip coordinate system $x_1' x_2'$ - are: $p_1 = -\sigma_{12}$ and $p_2 = -\sigma_{22}$ for the upper interface surface ($s = 1$) and $p_1 = \sigma_{12}$ and $p_2 = \sigma_{22}$ for the lower interface surface ($s = 2$). Note that the second term of the stress component in Eq. (3.53) is related to the component σ_{11}, so there is no influence of the T-stress on the tractions along the interface. Hence, the enriched traction approximation is written as:

$$\tilde{p}_j^{e\lambda}(\xi) = p_j^{(N)}(\xi) + R_{jk}^{\lambda} p_k^{(1)}(\mathbf{x}^{\lambda}, \mathbf{x}(\xi)) \tag{6.8}$$

where the enrichment components $p_k^{(1)}$ are computed by:

$$\left\{ \begin{array}{c} p_1^{(1)} \\ p_2^{(1)} \end{array} \right\} = \frac{(\delta_{s2} - \delta_{s1})}{\sqrt{2\pi\rho}} \left[\begin{array}{cc} \Sigma_{12}^1(\theta, s) & \Upsilon_{12}^1(\theta, s) \\ \Sigma_{22}^1(\theta, s) & \Upsilon_{22}^1(\theta, s) \end{array} \right] \left[\begin{array}{cc} \cos(\varepsilon \log \rho) & -\sin(\varepsilon \log \rho) \\ \sin(\varepsilon \log \rho) & \cos(\varepsilon \log \rho) \end{array} \right] \left\{ \begin{array}{c} \tilde{K}_1^{\lambda} \\ \tilde{K}_2^{\lambda} \end{array} \right\} \tag{6.9}$$

in which the expression $(\delta_{s2} - \delta_{s1})$ is include to result in -1 for $s = 1$ and $+1$ for $s = 2$.

In the XIGABEM approximations shown in Eqs. (6.4) and (6.8), the enrichment terms are able to represent the near-tip solutions, while the NURBS bases capture the responses that deviate from the analytical fields. When analysing straight cracks, as illustrated in Fig. 6.2a, the enrichment components in Eqs. (6.5), (6.6) and (6.9) can be particularised for the crack and interface surfaces by setting $\theta = \pm\pi$ and $\theta = 0$, respectively.

In cases where curved cracks are considered, as depicted in Fig. 6.2b, the enrichment terms are still able to represent the near-tip solution at portions close to the crack tip since the curvature at this region can be disregarded. In this situation, the polar coordinate θ can be defined similarly than in Wang, Waisman, and Harari (2017), so that its value along the crack and interface surfaces are the same as for the straight crack, as represented in Fig. 6.2b. Consequently, the same enriched approximations presented above can be applied to allow the direct extraction of the tip parameters for curved cracks. While the enrichment terms capture the near-tip behaviour, the NURBS terms are responsible for representing the response that deviates from the analytical solution at portions further from the tip. The use of the direct method is particularly beneficial in this case since the application of the interaction integral (see Section 3.2.2) requires the definition of auxiliary solutions considering the curvilinear nature of cracks, which is not an easy task (GONZÁLEZ-ALBUIXECH et al., 2013; CHIARAMONTE et al., 2015).

In what follows, the displacement and traction approximations used for elements on the external boundary $\left(\Gamma_s^B\right)$, crack surface $\left(\Gamma_s^C\right)$ and interface $\left(\Gamma_s^I\right)$ are presented. Then, these approximations are included in Eq. (6.1) to define the discrete DBIE for the analysis of interface crack problems.

6.2.1 Approximations over the external boundary (Γ_s^B)

The NURBS defining the external boundary Γ_s^B are not considered enriched in the proposed XIGABEM formulation. Therefore, the displacement and tractions approximations of elements at these regions are the same used in conventional IGABEM and presented, respectively, in Eqs. (6.2) and (6.3).

Figure 6.2: Representation of (a) a straight crack and (b) a curved crack. The polar coordinates θ used in the definition of the enrichment functions over the crack and interface surfaces are equivalent in both geometries and their values are also indicated.

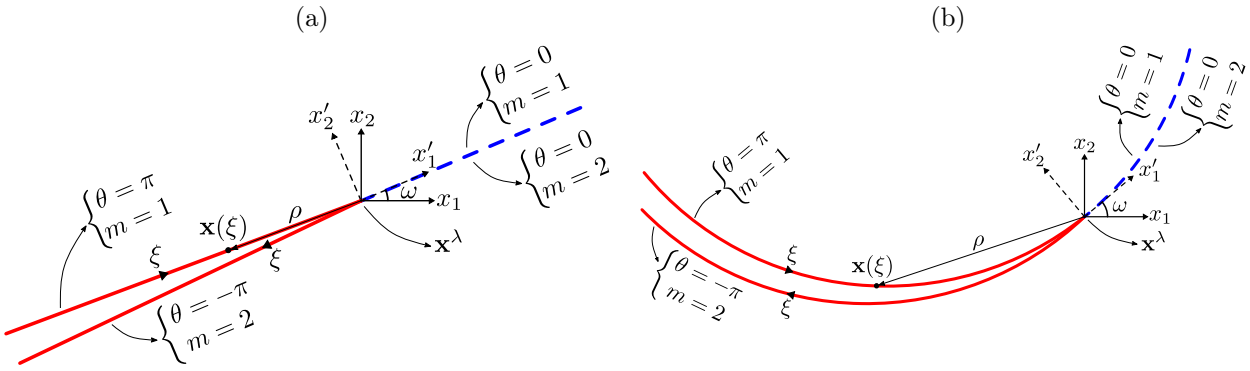

Source: Own author.

6.2.2 Approximations over the crack boundary (Γ_s^C)

For elements along the crack surfaces Γ_s^C, the enriched displacement approximation can be written as:

$$\tilde{u}_j^{e\lambda}(\xi) = \sum_{m=1}^{p+1} \phi^{em}(\xi) d_j^{em} + \sum_{M=1}^{2} \tilde{K}_M^\lambda R_{jk}^\lambda \psi_{kM}^C(\mathbf{x}^\lambda, \mathbf{x}(\xi)) + \tilde{K}_T^\lambda R_{j1}^\lambda \varphi^C(\mathbf{x}^\lambda, \mathbf{x}(\xi)) \tag{6.10}$$

where the enrichment functions ψ_{kM}^C and φ^C are determined from Eqs. (6.5) and (6.6) considering $\theta = \pm\pi$. They are expressed as follows:

$$\begin{bmatrix} \psi_{11}^C & \psi_{12}^C \\ \psi_{21}^C & \psi_{22}^C \end{bmatrix}(\rho, s) = \sqrt{\frac{\rho}{2\pi}} \frac{(\delta_{s1} - \delta_{s2})(\kappa_s + 1)}{[2\mu_s (1 + 4\varepsilon^2) \cosh(\pi\varepsilon)]} \begin{bmatrix} -2\varepsilon & 1 \\ 1 & 2\varepsilon \end{bmatrix} \begin{bmatrix} \cos(\varepsilon \log \rho) & -\sin(\varepsilon \log \rho) \\ \sin(\varepsilon \log \rho) & \cos(\varepsilon \log \rho) \end{bmatrix} \tag{6.11}$$

$$\varphi^C(\rho, s) = \frac{\rho}{2\sqrt{2\pi}} \frac{(\delta_{s1} - \delta_{s2})(1 + \kappa_1)(1 + \kappa_2)}{[(1 + \kappa_2)\mu_1 + (1 + \kappa_1)\mu_2]} \tag{6.12}$$

where $s = 1$ for the upper surface and $s = 2$ for the lower surface.

In the approximation shown in Eq. (6.10), the first enrichment term represents the analytical oscillatory square-root behaviour for displacements near the tip, while the second describes the linear contribution related to the T-stress. Although the NURBS bases are able to capture a linearly varying function, the second term of the displacement expansion is included to extract the T-stress parameter directly from the solution vector. Nevertheless, the additional constraint to accommodate $\tilde{K}_T^\lambda$ should be defined in such a way to indistinguishably specify the T-stress and NURBS contributions so that the resulting system of equations does not result singular. In other words, the definition of general supplementary equations as, e.g., by insertion of additional collocation points, is not sufficient to yield a determined algebraic system. Section 6.2.5.2 presents a constraint that

can be applied to accommodate $\tilde{K}_T^\lambda$ that leads to a non-singular system. Besides, such condition allows the direct evaluation of the T-stress parameter from the solution vector.

At the crack boundary, the enrichment traction components $p_k^{(1)}$ in Eq. (6.9) are null since traction-free surfaces are assumed in the near-tip solution. Therefore, the unenriched traction approximation given in Eq. (6.3) is considered for elements on crack surfaces.

6.2.3 Approximations for interface boundary (Γ_s^I)

For elements on the interface boundary Γ_s^I, the displacement approximation is similar to the one adopted the for crack elements, being expressed by:

$$\tilde{u}_j^{e\lambda}(\xi) = \sum_{m=1}^{p+1} \phi^{em}(\xi) d_j^{em} + \sum_{M=1}^{2} \tilde{K}_M^\lambda R_{jk}^\lambda \psi_{kM}^I(\mathbf{x}^\lambda, \mathbf{x}(\xi)) + \tilde{K}_T^\lambda R_{j1}^\lambda \varphi^I(\mathbf{x}^\lambda, \mathbf{x}(\xi)) \tag{6.13}$$

where the enrichment functions ψ_{lM}^I and φ^I are determined from Eqs. (6.5) and (6.6) considering $\theta = 0$. They are defined by:

$$\begin{bmatrix} \psi_{11}^I & \psi_{12}^I \\ \psi_{21}^I & \psi_{22}^I \end{bmatrix}(\rho) = \sqrt{\frac{\rho}{2\pi}} \frac{\kappa_1\kappa_2 - 1}{\left[(\kappa_1\mu_2 + \mu_1)(\kappa_2\mu_1 + \mu_2)\right]^{1/2}} \begin{bmatrix} 1 & 2\varepsilon \\ 2\varepsilon & -1 \end{bmatrix} \begin{bmatrix} \cos(\varepsilon \log\rho) & -\sin(\varepsilon \log\rho) \\ \sin(\varepsilon \log\rho) & \cos(\varepsilon \log\rho) \end{bmatrix} \tag{6.14}$$

$$\varphi^I(\rho) = \frac{\rho}{2\sqrt{2\pi}} \frac{(1+\kappa_1)(1+\kappa_2)}{\left[(1+\kappa_2)\mu_1 + (1+\kappa_1)\mu_2\right]} \tag{6.15}$$

Note that the displacement enrichment functions are the same regardless of whether the upper or lower material is considered, which results from the assumption of a perfectly bonded interface. Besides, the functions ψ_{kM}^I and φ^I introduce the same behaviour of the analogous enrichment functions for crack surfaces.

To represent the singular stress field at the crack tip, the enriched traction approximation over the interface elements is defined as:

$$\tilde{p}_j^{e\lambda}(\xi) = \sum_{m=1}^{p+1} \phi^{em}(\xi) t_j^{em} + \sum_{M=1}^{2} \tilde{K}_M^\lambda R_{jk}^\lambda \varpi_{kM}^I(\mathbf{x}^\lambda, \mathbf{x}(\xi)) \tag{6.16}$$

where the traction enrichment functions ϖ_{kM}^I are defined from Eq. (6.9) considering $\theta = 0$, being expressed by:

$$\begin{bmatrix} \varpi_{11}^I & \varpi_{12}^I \\ \varpi_{21}^I & \varpi_{22}^I \end{bmatrix}(\rho, s) = \frac{(\delta_{s2} - \delta_{s1})}{\sqrt{2\pi\rho}} \begin{bmatrix} \sin(\varepsilon \log\rho) & \cos(\varepsilon \log\rho) \\ \cos(\varepsilon \log\rho) & -\sin(\varepsilon \log\rho) \end{bmatrix} \tag{6.17}$$

Differently from the previous enrichments, the traction enrichment functions ϖ_{kM}^I are singular as $\rho \to 0$. Therefore, the singular analytical behaviour is introduced in the numerical model when considering the enriched approximation given in Eq. (6.16) for

interface elements.

6.2.4 Discrete DBIE

To introduce the approximations into the DBIE, the integral over Γ_s can be subdivided into integrals over the external Γ_s^B, crack Γ_s^C and interface Γ_s^I boundaries, resulting in:

$$\begin{aligned} c_{ij}(\mathbf{x}')u_j(\mathbf{x}') + \cancel{\int}_{\Gamma_s^B} P_{ij}^*(\mathbf{x}',\mathbf{x})\tilde{u}_j(\mathbf{x})d\Gamma_s^B + \cancel{\int}_{\Gamma_s^C} P_{ij}^*(\mathbf{x}',\mathbf{x})\tilde{u}_j(\mathbf{x})d\Gamma_s^C + \cancel{\int}_{\Gamma_s^I} P_{ij}^*(\mathbf{x}',\mathbf{x})\tilde{u}_j(\mathbf{x})d\Gamma_s^I = \\ = \int_{\Gamma_s^B} U_{ij}^*(\mathbf{x}',\mathbf{x})\tilde{p}_j(\mathbf{x})d\Gamma_s^B + \int_{\Gamma_s^C} U_{ij}^*(\mathbf{x}',\mathbf{x})\tilde{p}_j(\mathbf{x})d\Gamma_s^C + \int_{\Gamma_s^I} U_{ij}^*(\mathbf{x}',\mathbf{x})\tilde{p}_j(\mathbf{x})d\Gamma_s^I \end{aligned} \tag{6.18}$$

Then, introducing the displacement and tractions approximations presented in Sections 6.2.1 to 6.2.3, the discrete DBIE is obtained as:

$$\begin{aligned} c_{ij}(\mathbf{x}')\tilde{u}_j^{e'}(\xi') + \sum_{e=1}^{N_e}\sum_{m=1}^{p+1} P_{ij}^{em} d_j^{em} + \sum_{\lambda=1}^{N_t}\sum_{M=1}^{2} \tilde{K}_M^{\lambda} \left(\sum_{e=1}^{N_e^{\lambda C}} \tilde{P}_{iM}^{e\lambda C} + \sum_{e=1}^{N_e^{\lambda I}} \tilde{P}_{iM}^{e\lambda I} \right) + \\ + \sum_{\lambda=1}^{N_t} \tilde{K}_T^{\lambda} \left(\sum_{e=1}^{N_e^{\lambda C}} \bar{P}_i^{e\lambda C} + \sum_{e=1}^{N_e^{\lambda I}} \bar{P}_i^{e\lambda I} \right) = \sum_{e=1}^{N_e}\sum_{m=1}^{p+1} U_{ij}^{em} t_j^{em} + \sum_{\lambda=1}^{N_t}\sum_{M=1}^{2} \tilde{K}_M^{\lambda} \sum_{e=1}^{N_e^{\lambda I}} \tilde{U}_{iM}^{e\lambda I} \end{aligned} \tag{6.19}$$

where N_e is the number of isogeometric elements in the discretisation of Γ_s, N_t is the number of interface crack tips and $N_e^{\lambda C}$ and $N_e^{\lambda I}$ are, respectively, the number of crack and interface elements enriched by tip λ.

The integral kernels P_{ij}^{em} and U_{ij}^{em} in Eq. (6.19) are exactly the same ones determined in unenriched IGABEM and expressed in Eqs. (5.21) and (5.22), respectively. Then, they can be computed with the same strategies shown in Appendix C. The kernels $\tilde{P}_{iM}^{e\lambda C}$ and $\tilde{P}_{iM}^{e\lambda I}$ contain the first-order displacement enrichment functions for crack and interface elements, respectively, and are similar to the enriched kernel in XIGABEM for homogeneous materials (Eq. (5.35)). They can be expressed in a general form as:

$$\tilde{P}_{iM}^{e\lambda a} = \cancel{\int}_{-1}^{1} P_{ij}^*(\mathbf{x}', \mathbf{x}(\hat{\xi}))R_{jk}^{\lambda}\psi_{kM}^{a}(\mathbf{x}^{\lambda}, \mathbf{x}(\hat{\xi}))J^e(\hat{\xi})d\hat{\xi} \tag{6.20}$$

where $a = C, I$ indicates if ψ_{kM}^a is accessed at the crack or interface boundary, respectively. Despite the enrichment functions possess an oscillatory nature, this behaviour is restricted to portions very close to the crack tip. Elsewhere, these functions are well behaved, which allows the use of the same integration strategies applied for the enriched integrands in XIGABEM for homogeneous domains that are shown in Appendix D.1. Nonetheless, the precision of the Gauss-Legendre quadrature is affected when integrating the oscillatory functions, particularly over the elements containing the crack tip. The influence of the accuracy of the integration over these elements on the final numerical

solution is investigated in Example 6.3.1.

The second-order displacement enrichment functions considered in the approximations of crack and interface elements introduce the integral kernels $\bar{P}_i^{e\lambda C}$ and $\bar{P}_i^{e\lambda I}$ in Eq. (6.19), which are related to the T-stress parameter $\tilde{K}_T^{\lambda}$. They can be expressed as:

$$\bar{P}_i^{e\lambda a} = \fint_{-1}^{1} P_{ij}^{*}(\mathbf{x}', \mathbf{x}(\hat{\xi})) R_{j1}^{\lambda} \varphi^{a}(\mathbf{x}^{\lambda}, \mathbf{x}(\hat{\xi})) J^{e}(\hat{\xi}) d\hat{\xi} \tag{6.21}$$

where $a = C, I$ indicates if φ^a is accessed at the crack or interface boundary, respectively. The enrichment term φ^a is a linear function, so the integral in Eq. (6.21) can be evaluated without further difficulty with the same strategies used for other enriched kernels.

Finally, the extended traction approximation adopted for interface elements (Eq. (6.16)) introduces the integral kernel $\tilde{U}_{iM}^{e\lambda I}$ in the discrete DBIE. This integral is given by:

$$\tilde{U}_{iM}^{e\lambda I} = \int_{-1}^{1} U_{ij}^{*}(\mathbf{x}', \mathbf{x}(\hat{\xi})) R_{jk}^{\lambda} \varpi_{kM}^{I}(\mathbf{x}^{\lambda}, \mathbf{x}(\hat{\xi})) J^{e}(\hat{\xi}) d\hat{\xi} \tag{6.22}$$

Differently from the previous enrichment functions, ϖ_{lM}^{I} is singular at the $\rho = 0$. Therefore, to compute the integral in Eq. (6.22) over elements containing the crack tip using Gauss-Legendre quadrature, the singularity $\mathcal{O}(\rho^{-0.5})$ must be regularised. For this purpose, the transformation of the parent coordinate $\hat{\xi}$ presented in Appendix E is applied. It is worth mentioning that discontinuous NURBS are adopted to model the crack and interface surfaces so that no collocation point is positioned at the crack tip. Then, the singularity arising from fundamental solution U_{ij}^{*} when the tip element contains the source point $\mathbf{x}'$ does not occur at the same singular point of ϖ_{kM}^{I}.

A final remark about Eq. (6.19) is regarding the jump term. The displacement components at the source point $\tilde{u}_j^{e'}(\xi')$ must be written considering the approximation for the element e' that contains $\mathbf{x}'$, i.e., $u_j(\mathbf{x}') = \tilde{u}_j^{e'}(\xi')$. Therefore, when assembling the system of equations (Section 6.2.6), the jump term coefficients c_{ij} must be distributed over the degrees of freedom defining $\tilde{u}_j^{e'}(\xi')$, which include the enrichment parameters if e' is enriched.

6.2.5 Additional constraints

The enriched approximations used in the XIGABEM formulation contain the parameters $\tilde{K}_1^{\lambda}$, $\tilde{K}_2^{\lambda}$ and $\tilde{K}_T^{\lambda}$ that become additional degrees of freedom in the final system of equations. However, adopting only the enriched approximation in the BEM formulation is not sufficient for these additional parameters to represent the SIFs and T-stress precisely. This can only be achieved if the same analytical conditions at the crack tip are enforced in the numerical solution. In what follows, the additional constraints required to accommodate the DOF included by the enrichment are presented, which also allow the direct evaluation of the crack parameters from the solution of the algebraic system.

6.2.5.1 Crack tip tying constraint

To accommodate the additional parameters related to the SIFs, the same displacement continuity at the crack tip used for homogeneous media and shown in Section 5.5.2 is adopted for interface cracks. As in the XIGABEM approach presented in Chapter 5, distinct NURBS curves are used to describe each one of the crack surfaces (Fig. 5.4). Moreover, all elements on two NURBS defining a crack tip λ are considered enriched by the corresponding tip. Consequently, the displacement approximation over each crack element is given according to Eq. (6.10).

Note that when the tip element is considered for assessing the displacement values at the crack tip ($\rho = 0$), both enrichment terms vanish since $\lim_{\rho\to 0} \sqrt{\rho}\cos(\varepsilon \log \rho) = \lim_{\rho\to 0} \sqrt{\rho}\sin(\varepsilon \log \rho) = \lim_{\rho\to 0} \rho = 0$. In addition, as open knot vectors are employed, the NURBS contribution is reduced to the displacement control parameter at the tip. Then, the displacement components at the crack tip considering the approximations over the upper and lower crack surfaces are obtained as follows:

$$\tilde{u}_j^U(\xi_{n+p+1}) = d_j^{U_{tip}} \tag{6.23}$$

$$\tilde{u}_j^L(\xi_1) = d_j^{L_{tip}} \tag{6.24}$$

where $d_j^{U_{tip}}$ and $d_j^{L_{tip}}$ are the displacement parameters related to the control points at the crack tip of the upper and lower NURBS, respectively.

Therefore, the displacement continuity at the tip observed in the analytical solution is only satisfied in the XIGABEM responses if the equality between Eqs. (6.23) and (6.24) is met, which leads to the following relation:

$$d_j^{U_{tip}} - d_j^{L_{tip}} = 0 \tag{6.25}$$

Equation (6.25) provides a set of two equations per crack tip that accommodate the additional enrichment parameters $\tilde{K}_1^\lambda$ and $\tilde{K}_2^\lambda$.

6.2.5.2 Constraint on the normal stress parallel to the crack surface at the tip

To accommodate the enrichment T-stress parameter, a novel constraint is proposed, which is based on the relation between the normal stress components parallel to the crack surfaces that is verified at the tip in the two-term asymptotic expansion.

Similarly to displacements and tractions, the stress components over an element can also be approximated considering the NURBS and enrichment terms. Hence, the normal stress σ_{11} oriented according to the local crack tip coordinate system $x_1'x_2'$ can be approximated by:

$$\tilde{\sigma}_{11}^{e\lambda}(\xi) = \sigma_{11}^{(N)}(\xi) + \sigma_{11}^{(1)}(\mathbf{x}^{\lambda}, \mathbf{x}(\xi)) + \sigma_{11}^{(2)}(\mathbf{x}^{\lambda}, \mathbf{x}(\xi)) \tag{6.26}$$

where $\sigma_{11}^{(N)}$ is contribution obtained from the NURBS functions and $\sigma_{11}^{(1)}$ and $\sigma_{11}^{(2)}$ are, respectively, the enrichment components obtained from the first and second terms of the near-tip stress expansion shown in Eq. (3.53). For elements along the crack surfaces, the enrichment terms are expressed by:

$$\sigma_{11}^{(1)}(\rho, s) = \frac{2\left(\delta_{s2} - \delta_{s1}\right)}{\sqrt{2\pi\rho}\cosh(\pi\varepsilon)}\left[\tilde{K}_1^{\lambda}\sin\left(\varepsilon\log\rho\right) + \tilde{K}_2^{\lambda}\cos\left(\varepsilon\log\rho\right)\right] \tag{6.27}$$

$$\sigma_{11}^{(2)}(\rho, s) = C_s T = \frac{4}{\sqrt{2\pi}}\frac{\left(\kappa_1 + 1\right)\mu_2 C_s}{\left[\left(\kappa_1 + 1\right)\mu_2 + \left(\kappa_2 + 1\right)\mu_1\right]}\tilde{K}_T \tag{6.28}$$

where Eq. (3.55) was used to obtain the last equality in Eq. (6.28).

Note that along the crack, the sum of the analytical stress components of two corresponding points (same ρ) on the upper and lower surfaces results in $\left(C_1 + C_2\right)T$. However, this relation between the stress components is not ensured in the XIGABEM approximation due to the presence of the NURBS contribution. Thus, to satisfy the analytical condition at the crack tip, the sum of the NURBS terms at this point should vanish, i.e.:

$$\sigma_{11}^{(U)}(\xi_{n+p+1}) + \sigma_{11}^{(L)}(\xi_1) = 0 \tag{6.29}$$

where $\sigma_{11}^{(U)}$ and $\sigma_{11}^{(L)}$ are defined considering the approximation of the tip element on the upper and lower surfaces, respectively. These components can be obtained with the strategy shown in Section 2.5 and are related to the NURBS derivatives and displacements control parameters by:

$$\sigma_{11}^{(N)}(\xi_{tip}, s) = \frac{\left(\delta_{s1} - \delta_{s2}\right)E_s^*}{J^e(\xi_{tip})}\sum_{m=1}^{p+1}\frac{d\phi^{Nm}}{d\xi}(\xi_{tip})\left(d_1^{Nm}\cos\omega + d_2^{Nm}\sin\omega\right) \tag{6.30}$$

where $N = U, L$ indicates whether e is the tip element on the upper ($s = 1$) or lower ($s = 2$) surface, respectively, ξ_{tip} denotes the corresponding knot at the crack tip, $E_s^* = E_s$ for plane stress and $E_s^* = E_s/\left(1 - \nu_s^2\right)$ for plane strain.

Substituting Eq. (6.30) in Eq. (6.29) leads to:

$$\begin{aligned}\frac{E_1^*}{J^U(\xi_{n+p+1})}\sum_{m=1}^{p+1}\frac{d\phi^{Um}}{d\xi}(\xi_{n+p+1})\left(d_1^{Um}\cos\omega + d_2^{Um}\sin\omega\right) + \\ -\frac{E_2^*}{J^L(\xi_1)}\sum_{m=1}^{p+1}\frac{d\phi^{Lm}}{d\xi}(\xi_1)\left(d_1^{Lm}\cos\omega + d_2^{Lm}\sin\omega\right) = 0\end{aligned} \tag{6.31}$$

Equation (6.31) provides an additional relation for each crack tip that accommodates the T-stress parameter $\tilde{K}_T^{\lambda}$. This expression defines a constraint on the NURBS derivatives at the tip that is sufficient to make the linear displacement enrichment related to the T-stress independent from the NURBS contribution. Therefore, the final algebraic system becomes determined. Additionally, it is noted that normalising the terms in Eq. (6.31) by the coefficient of maximum magnitude has a beneficial effect on the conditioning of the resulting system of equations.

6.2.6 Assembly of the system of equations

Again, the collocation method is used to assemble the system of equations for interface cracks problems. The collocation points are also defined at the Greville abscissae, which are computed from Eq. (5.26). After considering each collocation point in the isogeometric boundary element mesh as the source point of the DBIE (Eq. (6.19)) and carrying out the integration over the corresponding boundary $\Gamma_s = \Gamma_s^B \cup \Gamma_s^C \cup \Gamma_s^I$, the following system of linear equation is determined:

$$\begin{bmatrix} \mathbf{H}_1^B & \mathbf{H}_1^C & \mathbf{H}_1^I & \mathbf{0} & \mathbf{0} & \mathbf{0} & \tilde{\mathbf{H}}_1^C + \tilde{\mathbf{H}}_1^I & \bar{\mathbf{H}}_1^C + \bar{\mathbf{H}}_1^I \\ \mathbf{0} & \mathbf{0} & \mathbf{0} & \mathbf{H}_2^B & \mathbf{H}_2^C & \mathbf{H}_2^I & \tilde{\mathbf{H}}_2^C + \tilde{\mathbf{H}}_2^I & \bar{\mathbf{H}}_2^C + \bar{\mathbf{H}}_2^I \end{bmatrix} \begin{Bmatrix} \mathbf{d}_1^B \\ \mathbf{d}_1^C \\ \mathbf{d}_1^I \\ \mathbf{d}_2^B \\ \mathbf{d}_2^C \\ \mathbf{d}_2^I \\ \tilde{\mathbf{K}} \\ \tilde{\mathbf{K}}_T \end{Bmatrix} = \tag{6.32}$$

$$= \begin{bmatrix} \mathbf{G}_1^B & \mathbf{G}_1^C & \mathbf{G}_1^I & \mathbf{0} & \mathbf{0} & \mathbf{0} & \tilde{\mathbf{G}}_1^I \\ \mathbf{0} & \mathbf{0} & \mathbf{0} & \mathbf{G}_2^B & \mathbf{G}_2^C & \mathbf{G}_2^I & \tilde{\mathbf{G}}_2^I \end{bmatrix} \begin{Bmatrix} \mathbf{t}_1^B \\ \mathbf{t}_1^C \\ \mathbf{t}_1^I \\ \mathbf{t}_2^B \\ \mathbf{t}_2^C \\ \mathbf{t}_2^I \\ \tilde{\mathbf{K}} \end{Bmatrix}$$

In Eq. (6.32), the subscript $s = 1, 2$ denotes the subdomain, while the superscript $a = B, C, I$ represents the external, crack and interface boundaries, respectively. The sub-matrices $\mathbf{H}_s^a$, $\tilde{\mathbf{H}}_s^a$ and $\bar{\mathbf{H}}_s^a$ are defined, respectively, from the kernels P_{ij}^{em}, $\tilde{P}_{iM}^{e\lambda a}$ and $\bar{P}_i^{e\lambda a}$ of the DBIE (6.19). These sub-matrices also contain the distribution of the jump terms c_{ij} over the degrees of freedom defining the displacement components at the source points. Additionally, the sub-matrices $\mathbf{G}_s^a$ and $\tilde{\mathbf{G}}_s^I$ collect the coefficients determined from

the integral kernels U_{ij}^{em} and $\tilde{U}_{iM}^{e\lambda I}$, respectively. Finally, the vectors $\mathbf{d}_s^a$ and $\mathbf{t}_s^a$ include the displacement and traction parameters at the control points, while the vectors $\tilde{\mathbf{K}}$ and $\tilde{\mathbf{K}}_T$ store the enrichment unknowns related to the SIFs and T-stress for all crack tips. Note that if traction-free cracks are considered, then $\mathbf{t}_1^C = \mathbf{t}_2^C = \mathbf{0}$.

In the applications considered here, the NURBS used to describe the upper and lower interface surfaces are defined by the same knot and weight vectors and by control points located at the same position. Therefore, to satisfy the conditions of a perfectly bonded interface expressed by Eq. (2.60), it is sufficient to impose the following compatibility constraints for corresponding control points:

$$\mathbf{d}_1^I = \mathbf{d}_2^I \qquad \text{and} \qquad \mathbf{t}_1^I = -\mathbf{t}_2^I \tag{6.33}$$

After imposing the external boundary conditions and the relations of Eq. (6.33) in Eq. (6.32), and then inserting the additional constraints given in Eqs. (6.25) and (6.31), the final the system of equations defined by XIGABEM is expressed as:

$$\begin{bmatrix} \mathbf{A}_1^B & \mathbf{H}_1^C & \mathbf{H}_1^I & -\mathbf{G}_1^I & \mathbf{0} & \mathbf{0} & \tilde{\mathbf{H}}_1^C + \tilde{\mathbf{H}}_1^I - \tilde{\mathbf{G}}_1^I & \bar{\mathbf{H}}_1^C + \bar{\mathbf{H}}_1^I \\ \mathbf{0} & \mathbf{0} & \mathbf{H}_2^I & \mathbf{G}_2^I & \mathbf{A}_2^B & \mathbf{H}_2^C & \tilde{\mathbf{H}}_2^C + \tilde{\mathbf{H}}_2^I - \tilde{\mathbf{G}}_2^I & \bar{\mathbf{H}}_2^C + \bar{\mathbf{H}}_2^I \\ \mathbf{0} & \hat{\mathbf{H}}_1^C & \mathbf{0} & \mathbf{0} & \mathbf{0} & \hat{\mathbf{H}}_2^C & \mathbf{0} & \mathbf{0} \end{bmatrix} \begin{Bmatrix} \mathbf{x}_1^B \\ \mathbf{d}_1^C \\ \mathbf{d}_1^I \\ \mathbf{t}_1^I \\ \mathbf{x}_2^B \\ \mathbf{d}_2^C \\ \tilde{\mathbf{K}} \\ \tilde{\mathbf{K}}_T \end{Bmatrix} = \begin{Bmatrix} \mathbf{f}_1 \\ \mathbf{f}_2 \\ \mathbf{0} \end{Bmatrix} \tag{6.34}$$

where $\mathbf{A}_s^B$ contains the coefficients from $\mathbf{H}_s^B$ and $\mathbf{G}_s^B$ that are related to the unknown control values $\mathbf{x}_s^B$ at the external boundary Γ_s^B. The vectors of constant terms $\mathbf{f}_1$ and $\mathbf{f}_2$ are given from the multiplication of the known control parameters and their corresponding influence coefficients from $\mathbf{H}_s^B$ and $\mathbf{G}_s^B$. Besides, the sub-matrices $\hat{\mathbf{H}}_s^C$ represent the additional equations introduced to accommodate the enrichment parameters, being defined by the coefficients associated with the displacement control parameters at the crack tip elements.

The solution of the linear system in Eq. (6.34) provides not only the unknown control variables but also the crack tip parameters introduced by the enriched formulation. Thus, the SIFs and T-stress parameter are defined directly from the solution vector, without the requirement of a post-processing technique.

6.3 Numerical applications

In this section, six examples are presented to illustrate the application of the proposed XIGABEM to directly evaluate the crack parameters for interface cracks. In the first two, the accuracy of the solutions is compared against the available exact responses. In addition, the convergence of the proposed numerical formulation with mesh refinement is verified. In the last four applications, the XIGABEM are compared with other numerical methods to demonstrate the efficiency of the proposed formulation against different approaches available in the literature.

For the XIGABEM modelling, all elements on the crack and interface surfaces are considered enriched by the tip that they define. Moreover, the order of the NURBS basis functions is selected as $p = 2$ for all analyses. Uniform isogeometric boundary element meshes are considered - a mesh grading scheme towards the tip or especial tip elements are not required since the enrichment terms are able to capture the analytical behaviour at this region.

In the reference solutions available in the literature, the values for the SIFs and T-stress are normalised by different terms. Where applicable, the expressions used to define the normalised values are provided.

6.3.1 Edge crack in a bimaterial plate

In this first example, consider a bimaterial plate with dimensions $L \times L$ containing an edge interface crack of length $a = 0.5L$, as depicted in Fig. 6.3a. For the analysis, the analytical two-term expansion for displacements and tractions are applied along the external boundary. The prescribed displacement components are obtained directly from Eq. (3.56), while the traction values are determined from Cauchy's formula $p_i = \sigma_{ij} n_j$, with the stresses σ_{ij} given by Eq. (3.53). Pure mode loadings are assumed to compute the analytical boundary conditions; thus, one factor among K_1, K_2 or K_T is considered to be different from zero and equal to unity, while the other two are identically null. The prescribed values for the crack parameters are the exact solution for the problem, which are used to verify the accuracy of the XIGABEM results. The application of both displacement and traction boundary conditions, although unusual, is possible with the boundary integral formulation (Eq. (6.18)), where the integration of the kernels along the outer boundary considering the analytical fields results in contributions in the vector of constant terms. This strategy leads to a precise description of the boundary conditions and allows a better assessment of the accuracy of XIGABEM in the solution of this problem with exact response.

The analyses are carried out considering the enrichment of crack and interface elements with the two-term expansion. Different Young's modulus ratios $\beta = E_1/E_2$ are considered, while the Poisson's ratios for both materials are $\nu_1 = \nu_2 = 0.3$ and plane strain condition

is assumed. The relative errors in the crack parameters obtained directly via XIGABEM for the pure mode problems are computed from:

$$e_K = \frac{\|K^{\text{ana}} - K^{\text{num}}\|}{\|K^{\text{ana}}\|} = \|1 - K^{\text{num}}\| \tag{6.35}$$

where $K^{\text{ana}} = 1$ is the crack parameter considered in the pure mode and K^{num} is the corresponding numerical solution determined by XIGABEM.

Figure 6.3: (a) Bimaterial plate containing an edge interface crack. (b) Representation of the isogeometric boundary element mesh. The red and blue lines indicate the elements enriched with the crack or interface functions, respectively (Example 6.3.1).

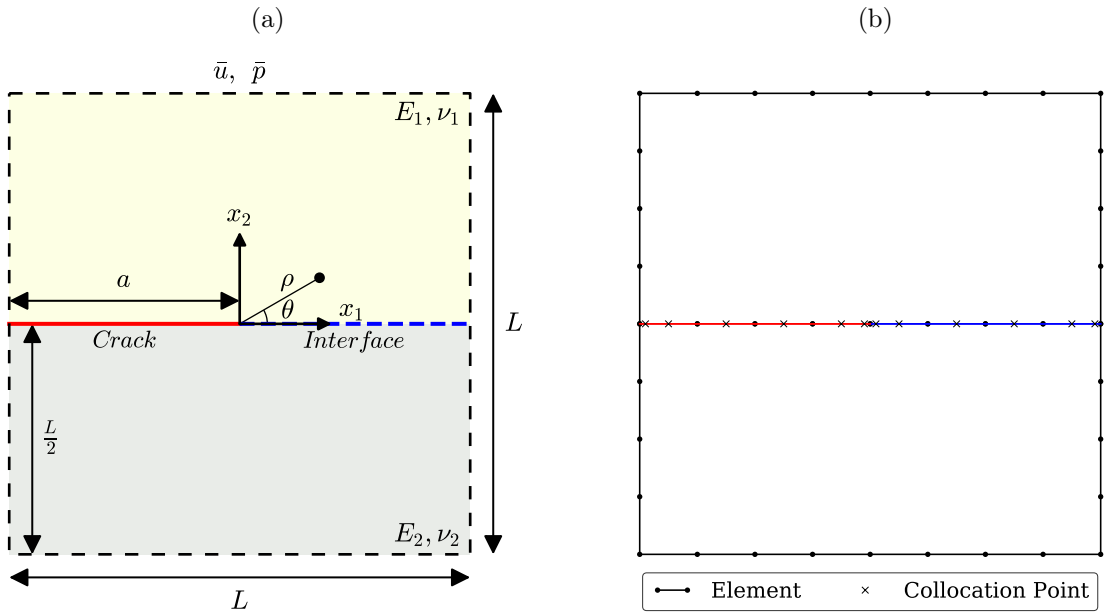

Source: Own author.

6.3.1.1 Accuracy of integration

As the enrichment terms contain the expected solution for this problem and the boundary conditions are represented with a high degree of precision, the errors in XIGABEM responses are closely related to the accuracy of the numerical integrations. Thus, the influence of the number of integration points used in the Gauss-Legendre quadrature on the results is investigated. Four material combinations are assumed: $\beta = 1, 2, 10$ and 100, corresponding to the oscillatory parameters $\varepsilon = 0, -0.030, -0.075$ and -0.092, respectively. Pure mode problems involving only K_1 ($K_1 = 1$, $K_2 = 0$, $K_T = 0$), K_2 ($K_1 = 0$, $K_2 = 1$, $K_T = 0$) or K_T ($K_1 = 0$, $K_2 = 0$, $K_T = 1$) are addressed. The XIGABEM analyses are carried out considering a uniform boundary element mesh containing forty-eight isogeometric elements and twenty-four collocation points, as illustrated in Fig. 6.3b.

Figure 6.4a presents the relative errors for the crack parameters - obtained directly by XIGABEM for the respective pure mode problems - with the number of integration

points used for the evaluation of the integrals over each element. Regarding the SIFs, the variation recovered for K_1 and K_2 are similar for every material combination since the corresponding enrichment functions and boundary conditions present the same behaviour for both parameters. As for the T-stress factor, the integrals involved in the particular pure mode problem can be computed with great accuracy when using more than 20 integration points. After this threshold, the values obtained for K_T oscillate near the computational precision, with errors remaining below 10^{-13}.

The precision of the results obtained for the SIFs shown in Fig. 6.4a is directly related to the accuracy of the numerical integration of elements containing the tip. This aspect is underlined in Figure 6.4b, which shows the relative errors for the crack parameters with the number of integration points adopted for the tip elements, while a 30-point Gaussian quadrature rule is applied for elements far from the crack tip. Comparing the results from Figs. 6.4a and 6.4b, when considering the homogeneous case ($\beta = 1$), the solutions are similar up to 30 integration points, indicating that the errors in the SIFs are defined by the accuracy of the numerical integrals over the tip elements. After that, the improvement of the SIFs responses in Fig. 6.4b becomes progressively smaller until a plateau is reached. In this situation, the reduction of the errors is only possible by increasing the quadrature points in the whole mesh, as demonstrated by the solutions shown in Fig. 6.4a.

In the inhomogeneous scenarios, practically the same SIF results are recovered by the XIGABEM for a particular β, as shown in Figs. 6.4a and 6.4b. This indicates that the errors in the numerical integration of the tip elements are dominant and control the accuracy of the solutions over the entire range of integration points. When considering material dissimilarity, the enrichment functions related to the SIFs become oscillatory. In this case, the precision of the results is strictly related to the accuracy of the quadrature used for evaluation of the integrals that contain these oscillatory terms, particularly over the tip elements. To demonstrate this, consider the integral $I = \int_0^1 \cos(\varepsilon \log z) dz$, which resembles the oscillatory enrichment terms over the elements containing the crack tip. The error in the numerical evaluation of this integral can be computed from:

$$e_{int} = \left\| 1 - \frac{I^{\text{num}}}{I^{\text{ana}}} \right\| \tag{6.36}$$

where I^{num} and I^{ana} represent, respectively, the numerical and analytical solutions for I. The error e_{int} is also presented in Fig. 6.4b when considering $\varepsilon = -0.030$, -0.075 and -0.092. Note that the convergence patterns obtained for the SIFs solutions and e_{int} are very similar, indicating that the errors in the XIGABEM are indeed determined by the accuracy of the numerical evaluation of the enriched kernels over the tip elements. Additionally, e_{int} increases with the magnitude of the oscillatory parameter ε, which is also observed in the XIGABEM responses. However, since the magnitude of ε is limited to an asymptotic value, the differences between solutions tend to reduce for increasing

values of β.

Regarding the results for the T-stress parameter presented in Figs. 6.4a and 6.4b, it is observed that the influence of the number of integration points adopted for the tip element is minimal. The enrichment functions related to K_T present linear behaviour and, therefore, the enriched integral kernels can be computed without great difficulty. Thus, when a sufficient number of quadrature points is used for assessing all other integrals over the elements on the mesh, the errors recovered for K_T remain close to the computational precision. The results show that a 30-point quadrature rule is adequate to ensure the accurate evaluation of these integrals and, therefore, this amount of integration points is adopted in the remaining examples.

Figure 6.4: Error variation of the crack parameters with the (a) number of integration points for all elements on the mesh and (b) number of integration points in the tip element while a 30-point Gaussian quadrature rule is applied for the others (Example 6.3.1).

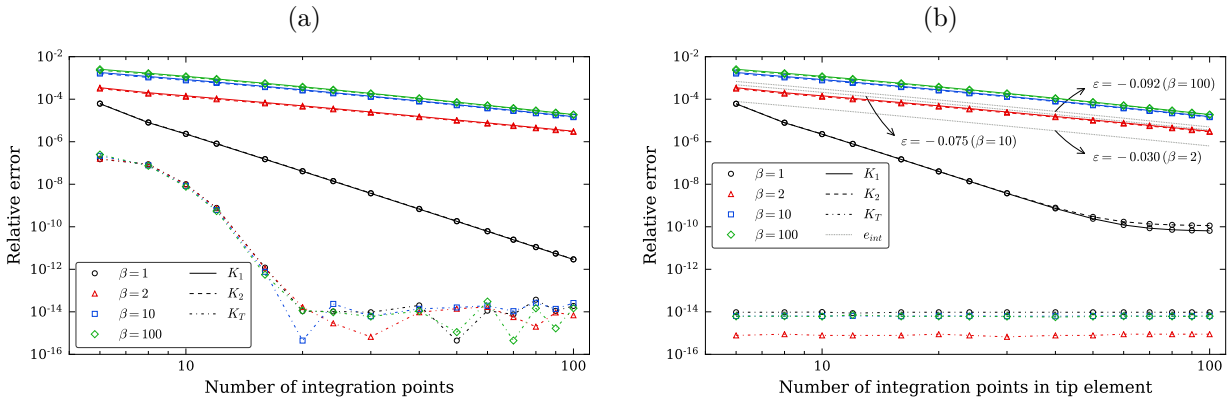

Source: Own author.

6.3.1.2 Convergence study

The convergence of XIGABEM in the analysis of this problem with exact solution is now addressed. For this purpose, the number of isogeometric elements in the uniform boundary element mesh is varied from 48 (4 elements on the crack) to 600 (50 elements on the crack), while the parameter β assumes the following values: $1, 2, 10, 100, 1000$ and 10000. Table 6.1 shows the convergence of the relative errors in the crack parameters, computed from Eq. (6.36), considering the respective pure mode problems. Comparing the SIFs results from different material combinations, note that the errors tend to increase with the magnitude of the oscillatory parameter due to the same reasons pointed in the previous analysis. For $\beta = 1000$ and $\beta = 10000$, the solutions are practically the same as a result of the similarity between the ε values. Regarding K_T, the accuracy fluctuates close to computational precision.

Table 6.1: Errors for crack parameters in pure mode problems considering different boundary element meshes (Example 6.3.1).

β	$\varepsilon\,(\times 10^{-2})$	n_{elem}	e_{K_1}	e_{K_2}	e_{K_T}	β	$\varepsilon\,(\times 10^{-2})$	n_{elem}	e_{K_1}	e_{K_2}	e_{K_T}
		48	3.7E-9	3.8E-9	9.5E-15			48	1.9E-4	1.8E-4	6.0E-15
		96	3.8E-9	3.9E-9	2.3E-14			96	1.8E-4	1.6E-4	2.6E-14
1	0.000	192	3.9E-9	4.0E-9	7.2E-14	100	-9.159	192	1.6E-4	1.5E-4	1.4E-13
		360	4.0E-9	4.0E-9	1.9E-13			360	1.5E-4	1.4E-4	2.4E-13
		600	4.0E-9	4.0E-9	5.3E-13			600	1.4E-4	1.3E-4	4.3E-14
		48	2.5E-5	2.3E-5	6.7E-15			48	1.9E-4	1.8E-4	9.5E-15
		96	2.4E-5	2.1E-5	3.8E-14			96	1.8E-4	1.7E-4	6.3E-14
2	-3.041	192	2.2E-5	2.0E-5	4.9E-14	1000	-9.335	192	1.7E-4	1.6E-4	1.1E-13
		360	2.0E-5	1.8E-5	1.1E-13			360	1.6E-4	1.5E-4	2.5E-14
		600	1.9E-5	1.7E-5	4.6E-13			600	1.5E-4	1.4E-4	9.9E-14
		48	1.4E-4	1.3E-4	6.2E-15			48	1.9E-4	1.8E-4	7.8E-15
		96	1.3E-4	1.2E-4	7.7E-14			96	1.8E-4	1.7E-4	1.5E-14
10	-7.581	192	1.2E-4	1.1E-4	1.4E-13	10000	-9.353	192	1.7E-4	1.6E-4	8.2E-14
		360	1.1E-4	1.0E-4	3.5E-13			360	1.6E-4	1.5E-4	3.0E-13
		600	1.0E-4	9.6E-5	3.0E-13			600	1.5E-4	1.4E-4	2.2E-13

Source: Own author.

Figure 6.5: (a) Deformed shape prescribed along the edges as boundary conditions and the solutions defined by the NURBS term along the crack and interface. (b) Deformed shape considering the contribution from enrichment terms for pure K_1 problem with $\beta = 10$. (c) Final deformed shape obtained by superposition of solutions (a) and (b) (Example 6.3.1).

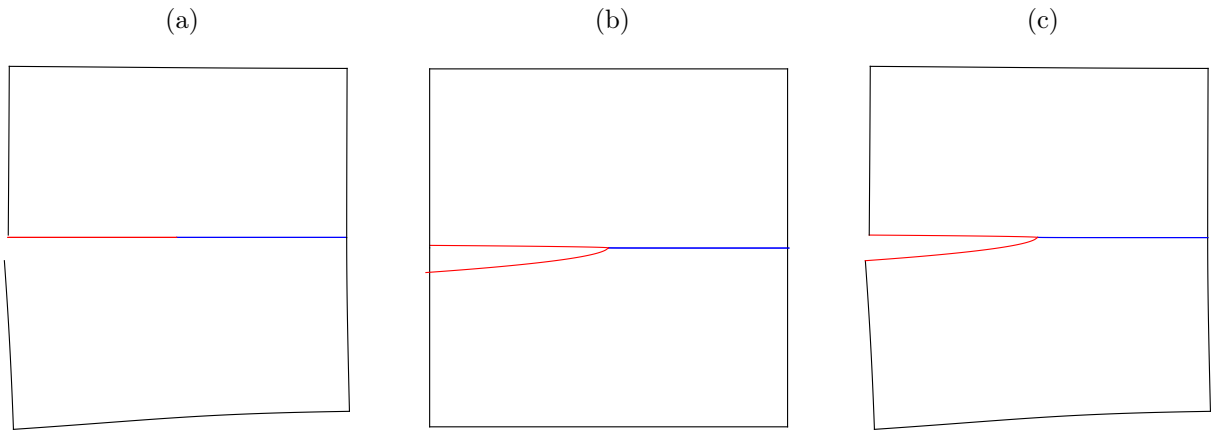

Source: Own author.

Since the enrichment functions are able to capture the response to the analytical problem, the contribution of the NURBS term to the final solution is minimal. Thus, the mesh refinement has little effect on the error improvement, except by slightly increasing the accuracy of the integration of oscillatory functions close to the tip, which ultimately leads to the small convergence verified for the SIFs in non-homogeneous scenarios. The contribution of each term of the XIGABEM approximation in the final displacement solution considering a pure K_1 problem and $\beta = 10$ is illustrated in Fig. 6.5. A 48-element mesh is used for the analysis. Figure 6.5a shows the deformed shape prescribed along the edges as boundary conditions and the solutions defined by the NURBS term along the crack and interface, while Fig. 6.5b present the deformed response recovered by the enrichment terms. When these contributions are superposed, they provide the final displacement response given in Fig. 6.5c. Note that the crack solution is defined by the enrichment term, whereas the NURBS term plays a minor role in the response. Finally, Figure 6.6 present the von Mises stress distribution determined by XIGABEM, which clearly shows the stress concentration at the crack tip and the discontinuity in the stress field occurring at the bimaterial interface.

Figure 6.6: Von Mises stress distribution determined by the XIGABEM for pure K_1 problem and $\beta = 10$ (Example 6.3.1).

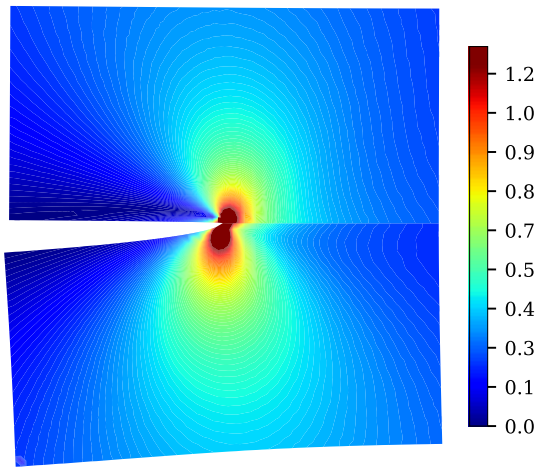

Source: Own author.

6.3.2 Curved interface crack between an inclusion and an infinite matrix

Differently from the previous example, an application in which the solution is not contained in the approximation space is now analysed. Thus, the final response is not captured solely by the enrichment terms but also by the NURBS basis functions. Consequently, the discretisation error plays an important role in the accuracy of the XIGABEM results for this problem.

Consider an infinite matrix containing a circular inclusion of radius R and subjected to a biaxial tensile loading σ_0, as illustrated in Fig. 6.7a. Besides, a curved crack with a half-crack angle θ_0 is positioned along the matrix-inclusion interface. To represent the infinite matrix, it is assumed $L = 100R$. For the numerical analysis, different Young's modulus ratios $\beta = E_2/E_1$ are considered, while the Poisson's ratios for both materials are taken as $\nu_1 = \nu_2 = 0.3$. Additionally, plane strain condition is considered.

Figure 6.7: (a) Infinite matrix containing an inclusion subjected to biaxial traction. (b) Detail of the isogeometric boundary element mesh around the inclusion. The red and blue lines indicate the elements enriched with the crack or interface functions, respectively (Example 6.3.2).

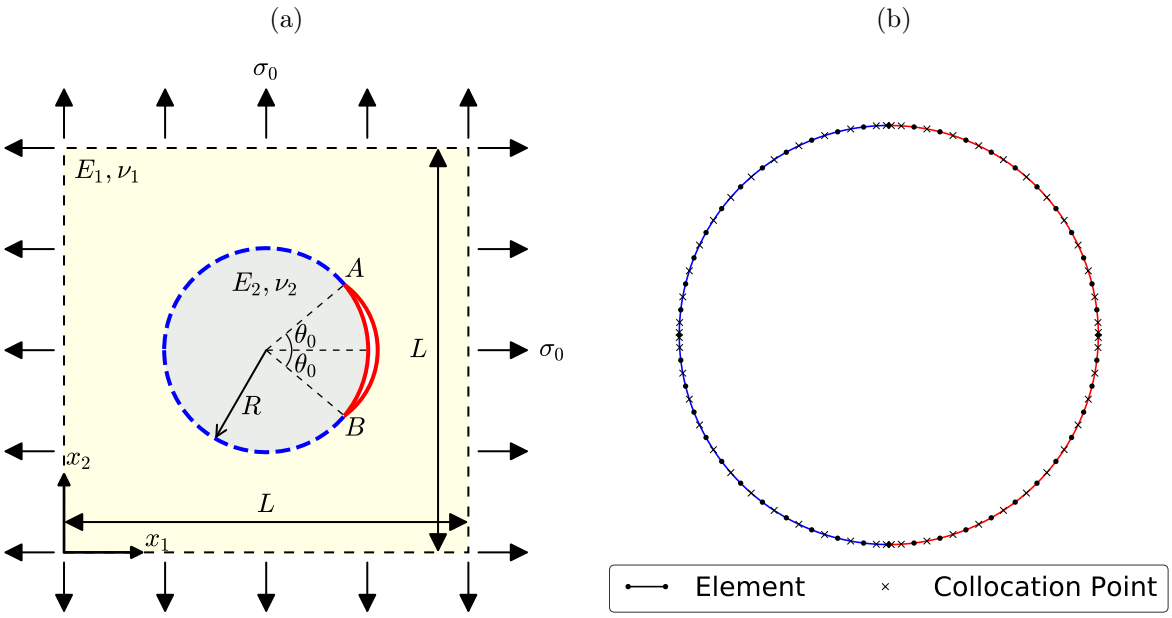

Source: Own author.

Initially, the convergence of the crack parameters at tip B is studied considering $\theta_0 = 90°$ and taking $\beta = 1, 2, 10, 100$ and 1000, which correspond to $\varepsilon = 0$, 0.030, 0.075, 0.092 and 0.093, respectively. The number of elements in the discretisation of the interface and crack surfaces is varied from 96 to 360, while the outer boundary mesh is fixed at 40 elements. Figure 6.7b shows the detail of the discretisation around the inclusion for the coarsest mesh. The SIFs are normalised by $K_1^* + \mathrm{i}K_2^* = (K_1 + \mathrm{i}K_2)\,/\left(\sigma_0\sqrt{\pi}R^{0.5-\mathrm{i}\varepsilon}\right)$, and Table 6.2 provides the analytical solutions (PERLMAN; SIH, 1967; CHEN; NAKAMICHI, 1996) used to verify the accuracy of the XIGABEM results. The convergence curves of the SIFs values are shown in Fig. 6.8. The errors in K_1^* decrease for increasing values of β (and ε), whereas the opposite behaviour is observed for K_2^*. Nevertheless, similarly to the previous example, the variations in the SIFs errors with β reduce as the oscillatory parameter ε tends to its asymptotic value. Figure 6.8 also shows the error convergence in the T-stress value at the inclusion (material 2) considering $\beta = 1$, in which the normalised reference solution is $T_2/\sigma_0 = 0.6667$ (CHEN, 2000). To the best of the author's

knowledge, no analytical response is available for the T-stress in the non-homogeneous case. Accurate solutions are obtained by the direct XIGABEM formulation for both SIFs and T-stress, with errors below 0.8% even for a coarse mesh. Besides, the convergence pattern of the solutions demonstrates the stability of the proposed method.

Table 6.2: Analytical values for the crack parameters at tip B (Example 6.3.2).

β:	1	2	10	100	1000
K_1^*:	0.4714	0.6288	0.8705	0.9566	0.9663
K_2^*:	-0.4714	-0.5808	-0.7147	-0.7543	-0.7586

Source: Own author.

Figure 6.8: Error convergence of the crack parameters solutions defined directly by XIGABEM (Example 6.3.2).

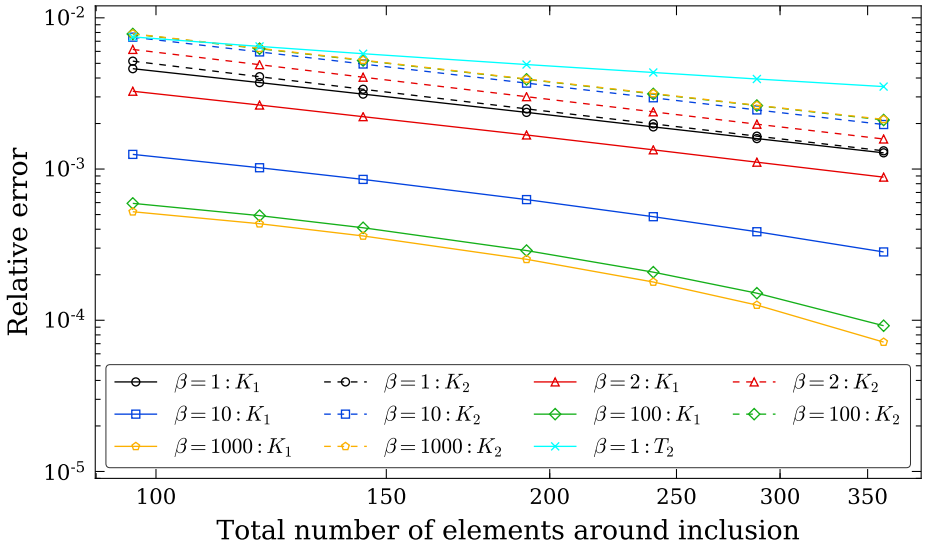

Source: Own author.

Figures 6.9a and 6.9b show, respectively, the displacement contributions of the NURBS and enrichment terms, while the superposition of these two responses provides the final solution given in Fig. 6.9c. Discontinuous NURBS are used to define each quarter of the inclusion, with those on the upper half enriched by tip A and those on the lower half enriched by tip B. Note that very close to the crack tips, the solution is mainly captured by the enrichment term. However, for points away from the tip, the NURBS have a significant contribution to the response, being responsible for correcting the enriched solution to obtain the final response. With mesh refinement, the responses from the NURBS term become more accurate, leading to the convergence of the crack parameters results shown in Fig. 6.8.

Figure 6.9: Deformed shape considering the contribution from (a) NURBS basis functions and (b) enrichment terms. (c) Final deformed shape obtained by superposition of solutions (a) and (b) (Example 6.3.2).

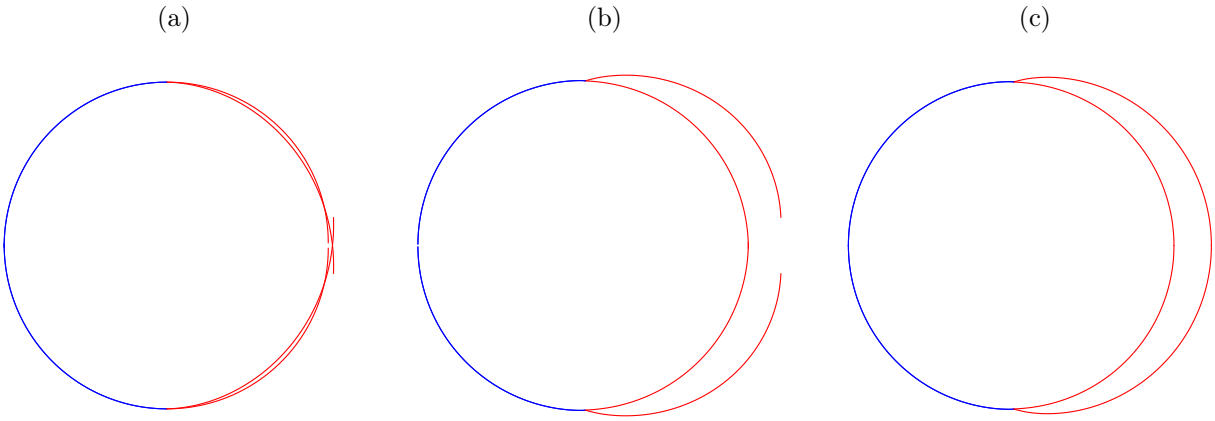

Source: Own author.

The influence of the half-crack angle on the SIFs and T-stress values is now verified. For this purpose, the parameter θ_0 is varied from 5° to 175° in steps of 5°. The analyses are carried out considering a total of 232 isogeometric elements in the boundary discretisation. Figure 6.10a present the discrete results for the SIFs determined directly by XIGABEM. The analytical solutions for K_1^* and K_2^* are also given and are represented in solid or dashed lines, respectively. Excellent agreement is observed between the numerical and reference results in the whole range of θ_0. The responses for the T-stress are also determined and are shown in Fig. 6.10b. Note that both the SIFs and T-stresses tend to be limited as ε approaches its asymptotic value. Figure 6.10b also present the analytical solutions of the T-stress for the homogeneous case, which, again, have excellent correspondence with the XIGABEM results.

6.3.3 Edge interface crack in a bimaterial strip

Consider a bimaterial strip composed of two layers of thickness h and containing an edge crack of length a. The strip is constrained at the right end, while a load of magnitude σ_0 is applied at the left end of the layers, as indicated in Fig. 6.11. The dimensions are taken as $L = 10h$, $a = 0.5L$ and plane strain condition is assumed in the analyses. Four different material combinations are considered for the strip, and the parameters adopted for each case are shown in Table 6.3.

Initially, it is investigated the convergence of the SIFs and T-stress obtained by the proposed XIGABEM formulation for each material combination. Figures 6.12a and 6.12b show, respectively, the variation of the normalised SIFs K_1^* and K_2^* with the number of boundary elements (knot spans) considered in the discretisation. The normalised SIFs

Figure 6.10: Variation of normalised (a) SIFs and (b) T-stress with the half-crack angle (Example 6.3.2).

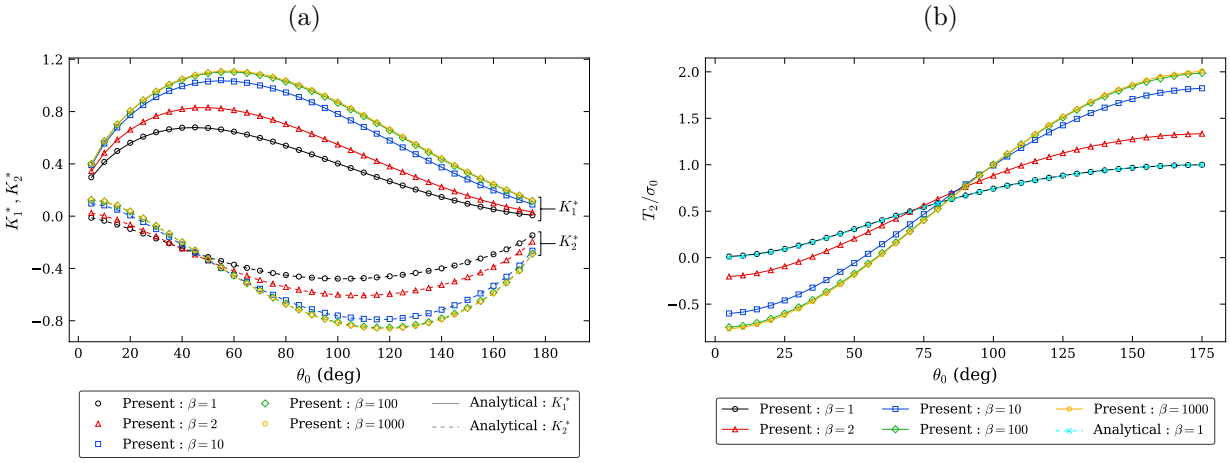

Source: Own author.

Figure 6.11: Bimaterial strip with an edge interface crack (Example 6.3.3).

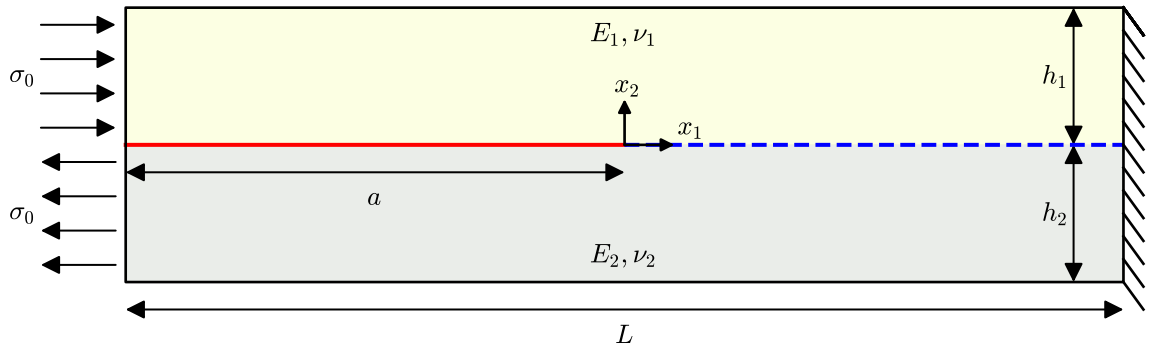

Source: Own author.

values are determined by $K_1^* + \mathrm{i}K_2^* = (K_1 + \mathrm{i}K_2)\,/\left(\sigma_0\sqrt{\pi}h^{0.5-\mathrm{i}\varepsilon}\right)$. Additionally, Fig. 6.12c presents the variation of the T-stress in material 1 (T_1) normalised by the magnitude of the load σ_0. The number of elements in the numerical simulations ranges from 44 (5 elements on each crack surface) to 264 (30 elements on each crack surface). At the finest mesh, the variations in the normalised SIFs and T-stress values with respect to the previous discretisation are below 0.5% for all cases. At this point, convergence of the XIGABEM results is assumed and the solutions are compared with reference responses.

Table 6.3 shows the SIFs and T-stress values computed directly by XIGABEM. Other solutions available in the literature are also presented. The results given by Suo and Hutchinson (1990) for SIFs and Kim and Vlassak (2007) for T-Stress are determined from semi-analytical (S-Analy) expressions considering a bimaterial strip with infinite length. On the other hand, the numerical solutions for the T-stress obtained by Yu, Wu, and Li (2012) (XFEM) and Muthu et al. (2016) (EFG) are also obtained considering a finite strip of length $L = 10h$. Excellent agreement is found between the solution determined

Figure 6.12: Convergence of (a) K_1^*, (b) K_2^* and (c) T_1/σ_0 with the number of elements (knot spans) in the isogeometric boundary mesh (Example 6.3.3).

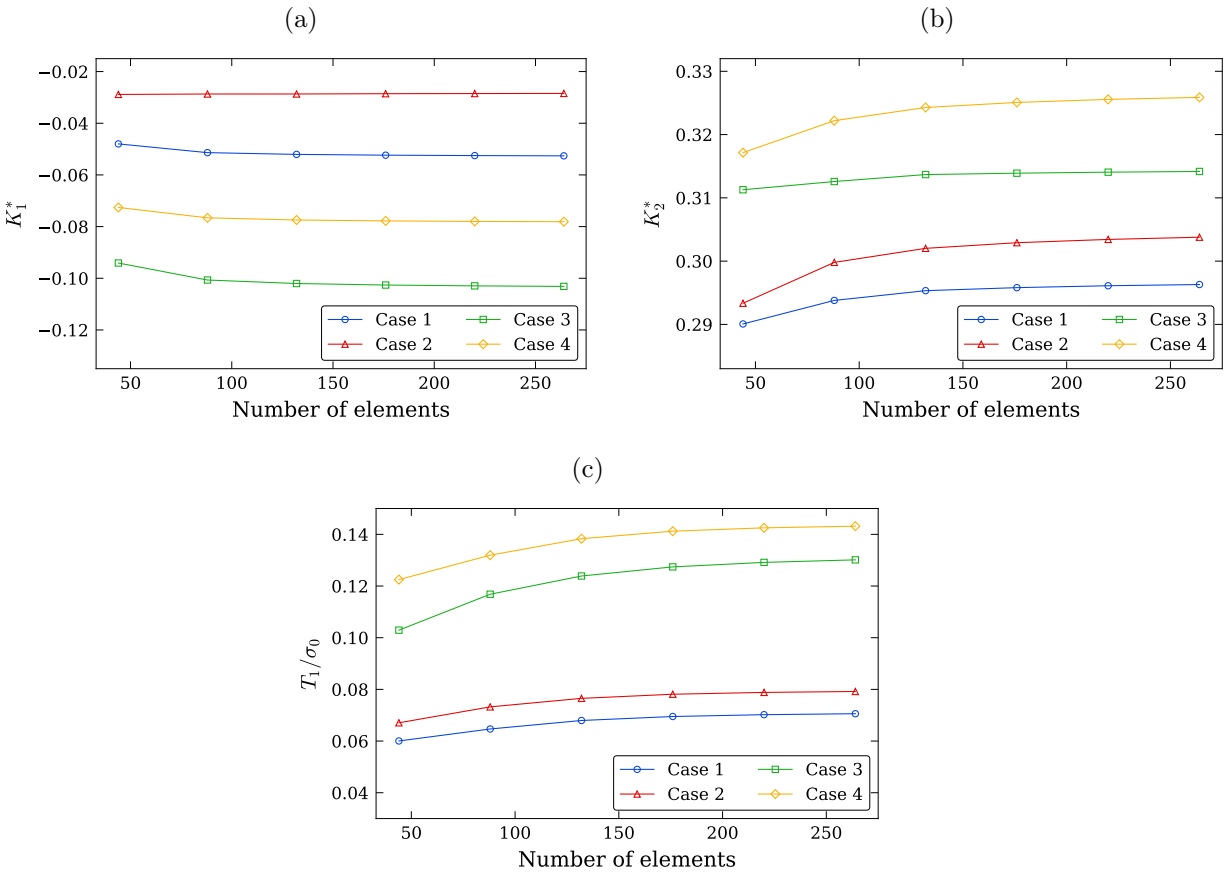

Source: Own author.

by the proposed direct method and the reference results. Particularly, when compared to the semi-analytical responses provided by Suo and Hutchinson (1990) and Kim and Vlassak (2007), the errors obtained by the XIGABEM are inferior to 1%, demonstrating the accuracy of the proposed direct method in evaluating the crack parameters.

Table 6.3: Normalised SIFs and T-stress in material 1 for bimaterial strip with edge crack (Example 6.3.3).

Case	$\frac{E_1}{E_2}$	ν_1	ν_2	K_1^*		K_2^*		T_1/σ_0			
				S-Analy	Present	S-Analy	Present	S-Analy	XFEM	EFG	Present
1	7/3	1/3	1/3	-0.0528	-0.0526	0.2976	0.2963	0.0709	0.0702	0.0709	0.0706
2	20/9	1/4	1/8	-0.0282	-0.0285	0.3056	0.3038	0.0784	0.0773	0.0778	0.0792
3	4	2/5	2/5	-0.1033	-0.1032	0.3153	0.3142	0.1310	0.1317	0.1301	0.1301
4	4	1/4	1/4	-0.0783	-0.0781	0.3277	0.3259	0.1424	0.1410	0.1419	0.1432

Source: Own author.

6.3.4 Curved interface crack between the inclusion and matrix

In this example, consider a square plate of unit length ($L = 1$) composed of a matrix of material 1 and an inclusion of material 2. In the interface between the inclusion and the matrix, there is a circular crack with a half-crack angle θ_0, as illustrated in Fig. 6.13. The volume fraction of the inclusion is 20%, so its radius is given by $R = \sqrt{0.2/\pi}$. The displacements in the x_1 direction are constrained along the left edge, while a constant displacement $u_1 = \delta = 0.01$ is prescribed at the right edge. Two cases are analysed: in the first one (6.3.4.1), the SIFs determined by the XIGABEM are compared with reference results, while in the second (6.3.4.2), the accuracy of the T-stress solutions is assessed. For all analyses, plane strain condition is considered. Additionally, 184 elements are used in the boundary element discretisation (10 at each side of the plate and 72 along the perimeter of the inclusion).

Figure 6.13: Circular crack around an inclusion in a square plate (Example 6.3.4).

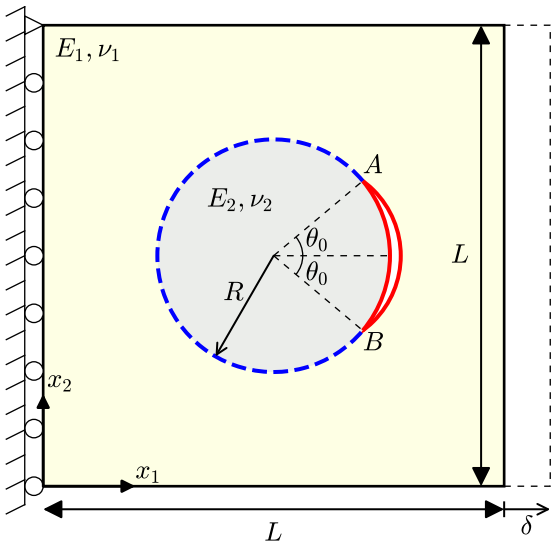

Source: Own author.

6.3.4.1 Stress intensity factors

In this scenario, the following material properties are considered for the numerical analysis: $E_1 = 72.4 \times 10^3$, $\nu_1 = 0.22$, $E_2 = 3.45 \times 10^3$ and $\nu_2 = 0.35$. Additionally, the half-crack length θ_0 varies from 10° to 60°.

Figure 6.14 shows the results obtained for the SIFs normalised by $\sigma_{\text{ave}}\sqrt{\pi R\theta_0}$, where σ_{ave} is the average normal stress on the right edge of the plate. The solutions determined by Liu and Xu (2000) using BEM and by Wu et al. (2011) using XFEM are also provided for comparison. Good correspondence is observed between the XIGABEM responses and the reference results, especially with those given by Wu et al. (2011). Similarly to the XFEM solutions, the curves determined by XIGABEM vary more smoothly than those

obtained by conventional BEM, which indicates that the enriched formulation contributes to the stability of the results.

Figure 6.14: Variation of the normalised SIFs at tip A with the half-crack angle θ_0 (Example 6.3.4).

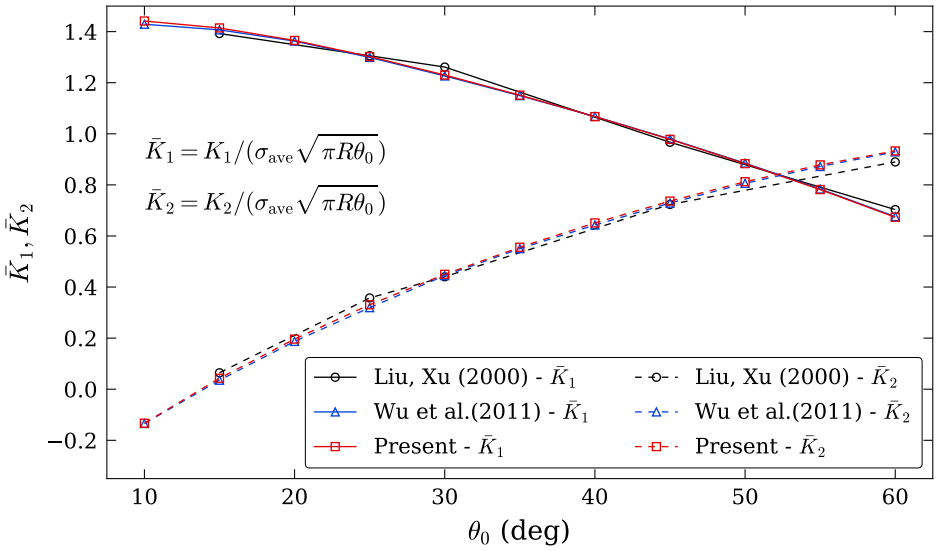

Source: Own author.

6.3.4.2 T-stress

For the T-stress analysis of the problem illustrated in Fig. 6.13, different ratios between the Young's modulus of the inclusion and matrix, defined as $\beta = E_2/E_1$, are considered. The ratio β is taken as 0.25 (soft inclusion), 1.0 (homogeneous) and 4.0 (hard inclusion), while the Poisson's ratios for the materials are $\nu_1 = \nu_2 = 0.3$. Additionally, the half-crack angle range is $\theta_0 = 10° - 90°$.

The results for the normalised T-stress in material 1 obtained directly by XIGABEM are presented in Fig. 6.15. Due to symmetry, the T-stress values in the matrix for both tips are the same. For small cracks, T_1 tends to be a compressive stress, but as the crack length increases, T_1 becomes a tensile stress. Moreover, apart from the values of θ_0 around 40° where T_1 switch from compressive to tensile stress, the magnitude of T_1 is greater the stiffer the matrix is to the inclusion. Yu, Wu, and Li (2012) also analysed this problem using the XFEM, and their solutions are shown in Fig. 6.15. Good agreement is attained between the XIGABEM and XFEM results for different material combinations. The difference between the solutions is in the same order of magnitude as in the previous example, in which the solutions given by Yu, Wu, and Li (2012) were also taken for comparison.

Figure 6.15: Variation of the normalised T-stress in material 1 with the half-crack angle θ_0(Example 6.3.4).

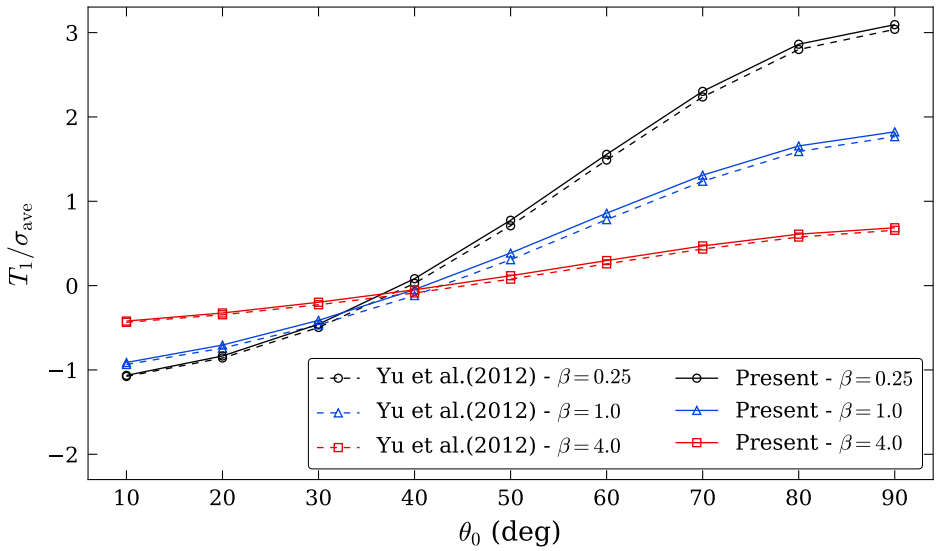

Source: Own author.

6.3.5 Bimaterial plate with a centre interface crack

Consider the bimaterial plate containing a centre crack lying along a slanted interface, as illustrated in Fig. 6.16. The plate has dimensions $2w \times 2h$ and is tensioned by a uniform load σ_0. Besides, the crack length is such that $a/w = 0.5$. In this example, two analyses are undertaken: firstly, it is assumed a horizontal interface ($\alpha = 0°$) and the variation of the SIFs and T-stress is investigated for different material properties. Secondly, the influence of the interface slope α and the ratio E_1/E_2 in the values of the crack parameters is assessed. The SIFs solutions are given in normalised form given by $K_1^* + \mathrm{i}K_2^* = (K_1 + \mathrm{i}K_2) \,/\, \left[(2a)^{-\mathrm{i}\varepsilon}\sigma_0\sqrt{\pi a}\right]$, while the normalised T-stress is obtained by $T^* = T\sqrt{\pi a}/K_0$, with $K_0 = \sqrt{K_1^2 + K_2^2}$. All analyses are carried out considering 200 isogeometric elements in the boundary discretisation, with 20 elements on each crack surface.

6.3.5.1 Horizontal interface ($\alpha = 0°$)

For the configuration of a horizontal interface ($\alpha = 0°$), the SIFs and T-stress are computed for the ratio between Young's moduli $E_1/E_2 = 1, 2, 5$ and 10. The Poisson's ratios for both materials are $\nu_1 = \nu_2 = 0.3$ and plane strain condition is assumed.

Table 6.4 presents the normalised valued obtained for the SIFs and T-stress in material 2. The XIGABEM solutions are compared with the results determined with SBFEM (SONG, 2005) and with xSBFEM (NATARAJAN; SONG; BELOUETTAR, 2014), which are also presented in Table 6.4. Excellent agreement is observed between the responses for all considered combinations of material properties. This demonstrates the accuracy of the

Figure 6.16: Tensioned bimaterial plate containing a centre interface crack (Example 6.3.5).

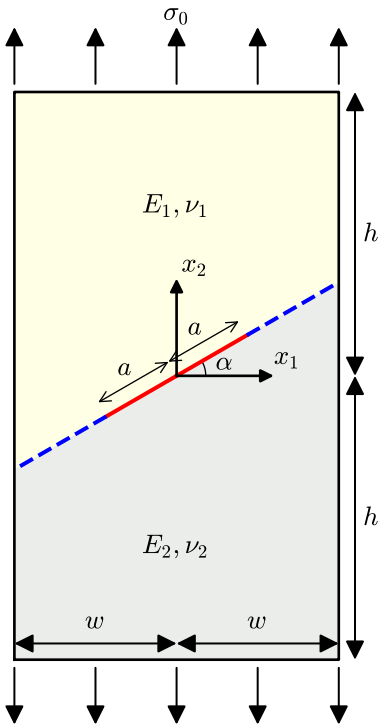

Source: Own author.

proposed direct approach for computing the interface crack parameters, especially as it performs well in face of the SBFEM formulation, which is acknowledged to be efficient in the analysis of fracture problems due to the feature of naturally capturing the asymptotic fields near the tip.

Table 6.4: Normalised SIFs and T-stress in material 2 for bimaterial plate with a horizontal centre crack (Example 6.3.5).

$\frac{E_1}{E_2}$	K_1^*			K_2^*			T_2^*		
	SBFEM	xSBFEM	Present	SBFEM	xSBFEM	Present	SBFEM	xSBFEM	Present
1	1.1890	1.1893	1.1901	0.0000	0.0000	0.0000	-1.0600	-1.0552	-1.0531
2	1.1790	1.1798	1.1807	-0.0550	-0.0566	-0.0543	-0.7180	-0.7144	-0.7131
5	1.1480	1.1483	1.1494	-0.1040	-0.1053	-0.1041	-0.3790	-0.3770	-0.3760
10	1.1230	1.1237	1.1249	-0.1230	-0.1240	-0.1234	-0.2160	-0.2147	-0.2139

Source: Own author.

6.3.5.2 Slanted interface ($\alpha = 0° - 60°$)

The inclination angle α of the interface in the bimaterial plate shown in Fig. 6.16 is now varied from 0° to 60°, while the ratio between Young's modulus is considered fixed, with $E_1/E_2 = 10$. Again, the Poisson's ratios are assumed constant and given by $\nu_1 = \nu_2 = 0.3$. The analyses are carried out considering plane stress condition.

Figures 6.17a and 6.17b show the results for the normalised SIFs and T-stress in material 2 determined for the right and left tips, respectively. Differently from the homogeneous case (see Portela, Aliabadi, and Rooke (1992)) the crack parameters computed for both tips are distinct because of the material dissimilarity. The figures also present the variation of the SIFs obtained by Wang et al. (2017) using XFEM and the BEM solutions provided by Miyazaki et al. (1993) and Gu and Zhang (2020) considering $\alpha = 15°, 30°, 45°$ and $60°$. To compute the SIFs, Wang et al. (2017) used Irwin's crack closure integral, Gu and Zhang (2020) adopted the displacement extrapolation method combined with a crack-tip element strategy and Miyazaki et al. (1993) applied a conservation integral. In these references, the K_2^* responses appear with the opposite sign than shown here due to the convention adopted in the definition of this factor. Again, the XIGABEM results are in good agreement with the solutions found in the literature, demonstrating the accuracy of the proposed direct method. Particularly, when compared to the XFEM (WANG et al., 2017), the SIFs values obtained here better approximate the BEM solutions given by Miyazaki et al. (1993) and Gu and Zhang (2020). Regarding the T-stress, it can be noted that for both tips this stress term changes from compression to tension as the inclination of the interface increases.

Figure 6.17: Variation of the normalised SIFs and T-stress in material 2 with the interface orientation α for the (a) right tip and (b) left tip. The XIGABEM results are compared against the numerical solutions provided by Miyazaki et al. (1993), Wang et al. (2017) and Gu and Zhang (2020) (Example 6.3.5).

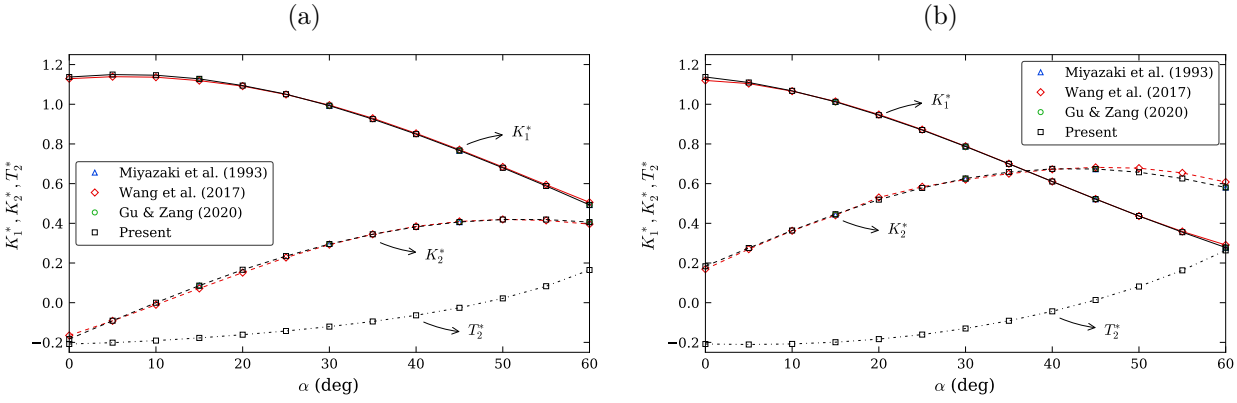

Source: Own author.

Considering the inclination angle of the interface as $\alpha = 15°, 30°, 45°$ and $60°$, the scenarios in which $E_1/E_2 = 100$ and $E_1/E_2 = 1000$ are also addressed. Table 6.5 shows the results obtained by the XIGABEM model and the BEM responses provided by Gu and Zhang (2020), including the case $E_1/E_2 = 10$ plotted in Figs. 6.17a and 6.17b. Again, the XIGABEM solutions are in excellent agreement with those provided by the reference, with average difference between the solutions around 0.4%. Notwithstanding, the results shown here are obtained with a coarser mesh than in Gu and Zhang (2020). While

272 quadratic Lagrange elements were used in the reference, including 40 discontinuous elements along each crack surface, 200 quadratic isogeometric elements are applied here, which represents a substantial reduction in the number of degrees of freedom. The results for the T-stress in material 2 are also shown in Table 6.5 for completeness. It can be observed that the magnitude of T_2^* reduces as material 1 becomes relatively stiffer.

Table 6.5: Normalised SIFs and T-stress in material 1 for bimaterial plate with a horizontal centre crack (Example 6.3.5).

$\frac{E_1}{E_2}$	α (°)	Right tip					Left tip				
		Gu and Zhang (2020)		Present			Gu and Zhang (2020)		Present		
		K_1^*	K_2^*	K_1^*	K_2^*	T_2^*	K_1^*	K_2^*	K_1^*	K_2^*	T_2^*
10	15	1.1269	0.0852	1.1280	0.0860	-0.1775	1.0096	0.4440	1.0123	0.4458	-0.1991
	30	0.9924	0.2949	0.9928	0.2955	-0.1205	0.7843	0.6246	0.7871	0.6260	-0.1300
	45	0.7656	0.4061	0.7671	0.4068	-0.0257	0.5217	0.6730	0.5222	0.6739	0.0136
	60	0.4919	0.4059	0.4928	0.4060	0.1647	0.2772	0.5810	0.2779	0.5808	0.2636
100	15	1.1155	0.0590	1.1189	0.0611	-0.0198	0.9680	0.4768	0.9672	0.4799	-0.0233
	30	1.0048	0.2619	1.0079	0.2635	-0.0131	0.7543	0.6540	0.7542	0.6563	-0.0146
	45	0.8029	0.3556	0.8051	0.3563	-0.0020	0.5389	0.6957	0.5399	0.6967	0.0058
	60	0.5284	0.3290	0.5312	0.3304	0.0255	0.3498	0.5879	0.3520	0.5898	0.0483
1000	15	1.1164	0.0574	1.1176	0.0590	-0.0020	0.9597	0.4811	0.9610	0.4836	-0.0024
	30	1.0075	0.2596	1.0095	0.2601	-0.0013	0.7493	0.6583	0.7502	0.6596	-0.0015
	45	0.8065	0.3471	0.8090	0.3480	-0.0002	0.5454	0.6965	0.5466	0.6976	0.0007
	60	0.5221	0.3055	0.5271	0.3086	0.0029	0.3691	0.5749	0.3727	0.5792	0.0056

Source: Own author.

6.3.6 Asymmetric interface cracks between a circular inclusion and the matrix

For this last example, consider the problem of two asymmetrical circular cracks along the matrix-inclusion interface under uniform traction σ_0 at infinity, as depicted in Fig. 6.18. The half-crack angle of the right and left cracks are β_1 and β_2, respectively. It is assumed a fixed $\beta_2 = 30°$, while β_1 varies in the range $5° - 55°$. To simulate the infinite matrix condition and reduce the finite length effect in the numerical solutions, it is adopted $L = 40R$. For each crack geometry, two material combinations are considered: the first contains a hard inclusion ($E_2 = 10E_1$, $\nu_1 = 0.3$ and $\nu_2 = 0.2$), while the second has a soft inclusion ($E_1 = 10E_2$, $\nu_1 = 0.3$ and $\nu_2 = 0.2$). Le, Brisard, and Pouya (2019) derived semi-analytical expressions of the SIFs for this problem, which are used for comparison against the direct XIGABEM solutions. The isogeometric boundary element mesh considered in the numerical analysis is composed of 184 elements: 10 at each side of the plate and 72 along the perimeter of the inclusion.

Figure 6.18: Asymmetrical cracks around a circular inclusion (Example 6.3.6).

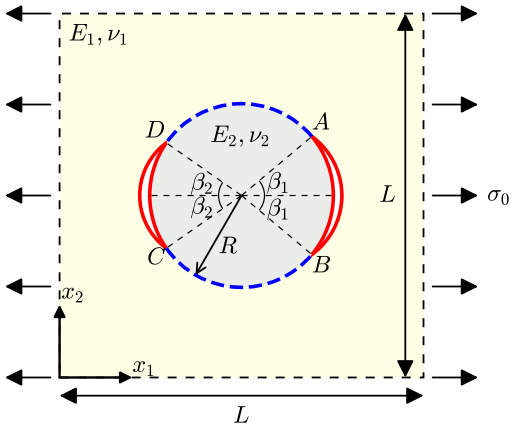

Source: Own author.

The results obtained by XIGABEM for the normalised SIFs of tips A and C with the variation of β_1 are shown in Figs 6.19a and 6.19b for the cases of hard inclusion and soft inclusion, respectively. For comparisons with the solutions given by Le, Brisard, and Pouya (2019), the normalised SIFs are computed by $K_1^* + \mathrm{i}K_2^* = (K_1 + \mathrm{i}K_2) / \left(\sigma_0\sqrt{2}R^{0.5+\mathrm{i}\varepsilon}\right)$. For tip A, in both material combinations, the value of K_1^* increases for small values of β_1, reaches a maximum and then decreases with the growth of the right crack. On the other hand, K_2^* monotonically grows with increments in β_1. For tip C, located in the crack that remains with a fixed length, the values of the SIFs are reduced as the right crack increases and becomes dominant. Additionally, when $\beta_1 = 30°$, both cracks have the same size and, due to the symmetry of the problem, the SIFs recovered for tips A and C are the same. Apart from the signal of K_2^*, the solutions for tips B and D (not shown) are equivalent to tips A and C, respectively.

Figures 6.19a and 6.19b also present the semi-analytical and numerical SIFs solutions provided by Le, Brisard, and Pouya (2019). In general, when compared to the FEM solutions given by the reference, the present results better approximate the semi-analytical responses, which demonstrates the efficiency of the proposed direct XIGABEM model to determine the SIFs for interface cracks.

Finally, for sake of completeness, the T-stress results in the inclusion determined by the direct XIGABEM are also provided for the cases of hard inclusion (Fig. 6.21a) and soft inclusion (Fig. 6.21b). Like the SIFs, the T-stress magnitude also reduces for the soft inclusion case since the stress level near the interface cracks decreases when the matrix is stiffer. Moreover, for hard and soft inclusion scenarios, the T-stress in material 2 for the right crack passes from compressive to tension as β_1 increases. For the fixed-length crack, the T-stress varies less than for the right crack and remains as a compressive stress throughout the range considered for β_1. Again, due to the symmetry at $\beta_1 = \beta_2 = 30°$, the results of the T-stress parameter for both cracks are the same at this point.

Figure 6.19: Variation of the normalised SIFs with β_1 considering the cases of (a) hard inclusion and (b) soft inclusion. The normalised SIF values are evaluated by $K_1^* + \mathrm{i}K_2^* = (K_1 + \mathrm{i}K_2) / \left(\sigma_0\sqrt{2}R^{0.5+\mathrm{i}\varepsilon}\right)$. The solutions for tip A are compared with the semi-analytical (Ana) and numerical (Num) responses provided by Le, Brisard, and Pouya (2019) (Example 6.3.6).

(a) (b)

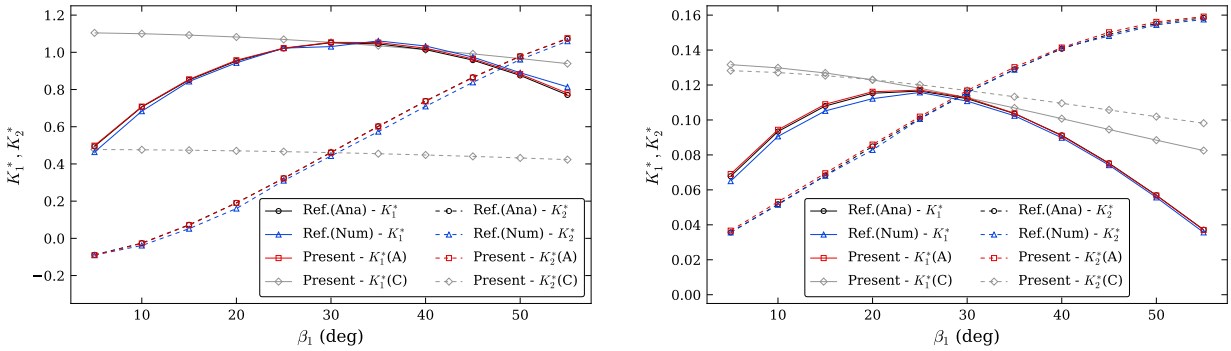

Source: Own author.

Figure 6.20: Variation of the normalised T-stress in material 2 for right crack (tips A and B) and left crack (tips C and D) considering a (a) hard inclusion and a (b) soft inclusion (Example 6.3.6).

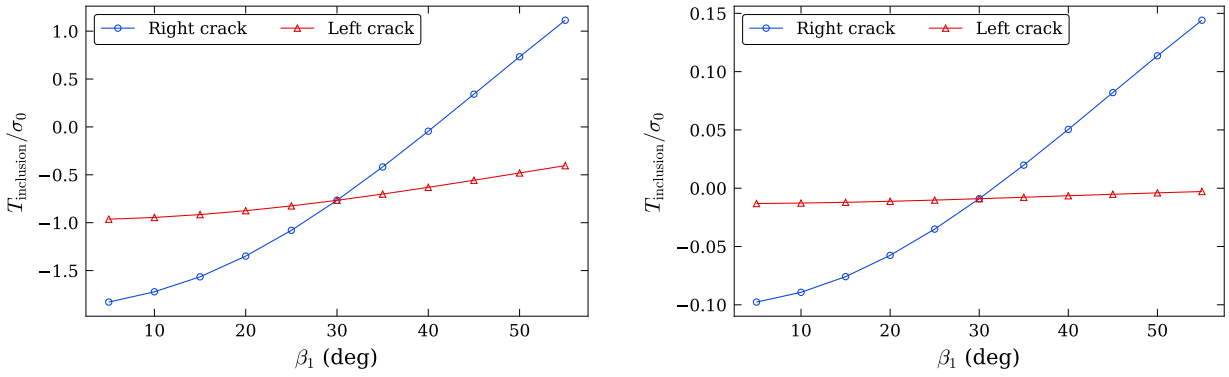

(a) (b)

Source: Own author.

7 Concluding remarks

In this thesis, several enriched BEM formulations have been developed for the analysis of fracture problems in two-dimensional domains. Emphasis was given to the direct approach, in which the crack parameters are found as part of the solution of the system of equations. The proposed extended formulations allow the computation of accurate solutions with reduced computational effort and using coarse meshes. These accurate results are found without the further expense of post-processing techniques such as the ones based on the J-integral. Additionally, it was shown that if we choose to incur the extra cost of such post-processing when employing the enriched formulations, results of very high accuracy can be recovered.

The extended approaches presented here introduces few modifications to the unenriched formulation, which facilitates their implementation into existing codes. The components of the original BEM/IGABEM matrices are kept unaltered, while just new coefficients related to the enrichment parameters are introduced in the system. Besides, the enriched integral kernels are very similar to the unenriched ones, the only difference being the replacement of the shape functions by the enrichment functions. Therefore, since the singularity order is not modified - or can even be reduced when considering shifted enrichment functions -, the usual BEM numerical integration schemes can be applied to assess the enriched integrals.

In Chapter 4, a fully enriched boundary element formulation for modelling the linear crack growth in isotropic and anisotropic domains has been proposed. Two displacement enrichments were presented: the crack tip enrichment, based on the first-order asymptotic expansion, and the discontinuous enrichment, based on the Heaviside sign step function. The first, associated with the crack tip tying constraint to accommodate the additional DOF, improves the near-tip response and enables the direct computation of the SIFs. Thus, the extended formulation has the advantage of saving computational cost by dismissing the use of post-processing techniques to compute these factors. However, where high accuracy is required in the SIFs evaluation, it was shown that the combination of the XBEM scheme with the J-integral is highly effective. The second displacement enrichment is capable of representing the discontinuity occurring at elements intercepted by cracks. This enrichment prevents the remeshing and, consequently, the corresponding modifications that would occur in the BEM matrices. The continuity conditions between the crossed element and the crack surfaces at the intersection point are applied to contemplate the four additional parameters introduced by the Heaviside enrichment. Both displacement enrichments are composed of shifted functions, preserving the physical meaning of the nodal parameters. This strategy also kept the jump term unaltered and

reduced the singularity orders from the enriched kernels in the XBEM formulation.

Additionally, an enriched traction approximation has also been shown in Chapter 4, which allows the application of concentrated forces or support points along the boundary. In the latter case, additional parameters corresponding to the support reactions are introduced in the analysis. To accommodate them, the essential boundary conditions at the point are used as supplementary equations.

The numerical examples presented in Chapter 4 demonstrated the accuracy and stability of the proposed XBEM formulation to simulate crack growth problems in isotropic and anisotropic domains. Good agreement was achieved between the results obtained by the enriched method and the solutions found in the literature.

In Chapter 5, the enriched formulation was combined with an isogeometric BEM formulation, which allowed a straightforward integration between CAD and numerical analysis. The resulting XIGABEM approach was then applied for simulating fatigue crack growth in isotropic materials. In the extended approach, the leading-order term from Williams expansion was embedded directly in the displacement approximation. As in XBEM, the crack tip tying constraint was used to accommodate the additional degrees of freedom introduced by the enrichment, and the SIFs could be defined directly from the solution vector. In most of the applications considered in Chapter 5, the direct approach was able to provide SIF values with errors lower than those from an unenriched IGABEM formulation, in which the J-integral was applied for SIF extraction. Even when the unenriched IGABEM outperformed the direct XIGABEM approach (internal crack problem), the errors obtained by the direct method were satisfactory, being less than 1%. Alternatively, for cases in which very high accuracy is required, a J-integral calculation based on the XIGABEM results was able to improve considerably the accuracy and convergence rate for SIF calculations.

The first set of examples presented in Chapter 5 clearly demonstrate the accuracy and convergence benefits of the XIGABEM formulation. Regarding fatigue crack propagation applications, the direct method provided propagation paths, SIF history and fatigue lives in good agreement with experimental and numerical results available in the literature. In general, the solutions given by the direct approach better approximated those found by combining the enriched XIGABEM formulation and the J-integral - which is the most accurate model - when compared to unenriched IGABEM. Furthermore, as demonstrated by the last example of the Chapter, the run times when the direct approach is considered are significantly lower than those determined when using the indirect J-integral for SIF extraction.

The continuity properties of NURBS, related to the multiplicity of repeated knots in the knot vector, was also exploited Chapter 5 for the development of a C^{-1} continuity strategy that was able to model discontinuities at boundaries intersected by cracks with a trivial modification of the NURBS definition. This strategy was also employed to ensure

independence between the basis functions over the new and existing crack surfaces during crack propagation, thus restricting the enriched elements to the NURBS portion defining the crack tip. The independence along the newly created surfaces also facilitated the remeshing process and the corresponding modifications in the system of equations during crack growth.

In Chapter 6, a novel XIGABEM formulation was developed for the direct evaluation of the SIFs and T-stress of interface cracks. For this purpose, the two-term asymptotic expansion was used to augment the displacement and traction approximations of boundary elements on the crack surfaces and interfaces. As in the previous enrichment strategies, the crack tip tying constraint was used to directly evaluate the SIFs. Furthermore, an expression involving the NURBS derivatives at the crack tip was proposed to obtain the T-stress parameter directly from the solution vector.

Additionally, in Chapter 6, the direct XIGABEM formulation, which is based on the analytical responses of a straight crack, was also successfully employed for the analysis of curved cracks for the first time. The use of the direct method is particularly beneficial in this case since the application of interaction integrals for the definition of the crack parameters requires auxiliary solutions accounting for the curvilinear nature of cracks, which is not straightforward. Besides, the use of NURBS approximations in the XIGABEM formulation allows the proper description of curved geometries, including cracks and interfaces.

The numerical applications presented in Chapter 6 demonstrates the stability and accuracy of the direct XIGABEM for the analysis of interface cracks. A careful study of the influence of the oscillatory enrichment functions on the precision of numerical integration was also considered. Besides, the convergence of the method was investigated for different material combinations. Excellent agreement was attained between the XIGABEM responses and the reference results available in the literature. When compared to other numerical methods - in which different techniques were used for extraction of the crack parameters - the XIGABEM proved to be an efficient approach. Moreover, the proposed method has the advantage of defining accurate solutions without the requirement of post-processing strategies, which can be computationally expensive within the BEM framework.

7.1 Recommendations for future work

Perhaps the most appealing extension of the work reported in this thesis is the application of the enriched formulations to three-dimensional domains. In this case, each crack possesses several fronts, for which the tip parameters must be assessed to verify stability. Therefore, the prospect of accurate SIF predictions in 3D without the expense of multiple J-integral evaluations is highly attractive. In addition, the isogeometric approach is also

recommended for these applications since the direct link between CAD and analysis is especially useful when dealing with 3D models, where a considerable amount of time can be saved from the mesh generation process.

Still regarding three-dimensional applications, the discontinuous enrichment strategy presented in Chapter 4 can also be employed to model the intersection between the crack and the boundary when considering propagation problems. Such an approach would be similar to the XFEM formulations for plane problems. Alternatively, the use of discontinuous and/or trimmed NURBS could also be appraised for this purpose.

Concerning studies in two-dimensional media, the fracture process of inhomogeneous materials could be further investigated. For these types of materials, the degradation process involving simultaneously the matrix and the interface can be analysed by a general extended formulation. To this end, besides enrichment functions presented here for cracks on the interface and homogeneous materials, new enrichment functions related to a crack tip terminating at a bimaterial interface could be considered (CHANG; XU, 2007). Hence, cracks emanating and arriving at the interface could be modelled, allowing the proper simulation of the crack percolation throughout the inhomogeneous medium. Additionally, fracture in anisotropic bimaterial, which application has been intensified with the increasing use of composites, could also be studied. In this case, the analytical solutions provided by Gao, Abbudi, and Barnett (1992), for example, could be applied for the enrichment of crack and interface elements.

References

AGATHOS, K.; BORDAS, S.; CHATZI, E. Improving the conditioning of XFEM/GFEM for fracture mechanics problems through enrichment quasi-orthogonalization. **Computer Methods in Applied Mechanics and Engineering**, Elsevier BV, v. 346, p. 1051–1073, Apr. 2019. DOI: 10.1016/j.cma.2018.08.007.

AGATHOS, K.; CHATZI, E.; BORDAS, S. Multiple crack detection in 3D using a stable XFEM and global optimization. **Computational Mechanics**, Springer Nature, v. 62, n. 4, p. 835–852, Feb. 2018. DOI: 10.1007/s00466-017-1532-y.

_____. Stable 3D extended finite elements with higher order enrichment for accurate non planar fracture. **Computer Methods in Applied Mechanics and Engineering**, Elsevier BV, v. 306, p. 19–46, July 2016. DOI: 10.1016/j.cma.2016.03.023.

AGATHOS, K.; CHATZI, E.; BORDAS, S.; TALASLIDIS, D. A well-conditioned and optimally convergent XFEM for 3D linear elastic fracture. **International Journal for Numerical Methods in Engineering**, Wiley, v. 105, n. 9, p. 643–677, Aug. 2015. DOI: 10.1002/nme.4982.

AGATHOS, K.; VENTURA, G., et al. Stable 3D XFEM/vector level sets for non-planar 3D crack propagation and comparison of enrichment schemes. **International Journal for Numerical Methods in Engineering**, Wiley, v. 113, n. 2, p. 252–276, Sept. 2017. DOI: 10.1002/nme.5611.

AKHRAS, H. Al et al. Towards an automatic isogeometric analysis suitable trivariate models generation—Application to geometric parametric analysis. **Computer Methods in Applied Mechanics and Engineering**, Elsevier BV, v. 316, p. 623–645, Apr. 2017. DOI: 10.1016/j.cma.2016.09.030.

AKIN, J. E. The generation of elements with singularities. **International Journal for Numerical Methods in Engineering**, Wiley, v. 10, n. 6, p. 1249–1259, 1976. DOI: 10.1002/nme.1620100605.

ALATAWI, I.A.; TREVELYAN, J. A direct evaluation of stress intensity factors using the Extended Dual Boundary Element Method. **Engineering Analysis with Boundary Elements**, Elsevier BV, v. 52, p. 56–63, Mar. 2015. DOI: 10.1016/j.enganabound.2014.11.022.

ALBUQUERQUE, E. L.; SOLLERO, P.; ALIABADI, M. H. Dual boundary element method for anisotropic dynamic fracture mechanics. **International Journal for Numerical Methods in Engineering**, Wiley, v. 59, n. 9, p. 1187–1205, Feb. 2004. DOI: 10.1002/nme.912.

ALIABADI, Mohammad H. **The boundary element method, volume 2: applications in solids and structures**. [S.l.]: John Wiley & Sons, 2002. v. 2.

ALIABADI, Mohammad H; ROOKE, David P. **Numerical fracture mechanics**. [S.l.]: Springer Science & Business Media, 1991. v. 8.

AN, Zhilin et al. Implementation of isogeometric boundary element method for 2-D steady heat transfer analysis. **Advances in Engineering Software**, Elsevier BV, v. 116, p. 36–49, Feb. 2018. DOI: 10.1016/j.advengsoft.2017.11.008.

ANDRADE, H.C.; LEONEL, E.D. An enriched dual boundary element method formulation for linear elastic crack propagation. **Engineering Analysis with Boundary Elements**, Elsevier BV, v. 121, p. 158–179, Dec. 2020. DOI: 10.1016/j.enganabound.2020.09.007.

_____. The multiple fatigue crack propagation modelling in nonhomogeneous structures using the DBEM. **Engineering Analysis with Boundary Elements**, Elsevier BV, v. 98, p. 296–309, Jan. 2019. DOI: 10.1016/j.enganabound.2018.10.026.

ANDRADE, Heider. **Análise da propagação de fissuras em estruturas bidimensionais não-homogêneas via Método dos Elementos de Contorno**. 2017. MA thesis – Universidade de Sao Paulo. DOI: 10.11606/d.18.2017.tde-27042017-093540.

ASADPOURE, A; MOHAMMADI, S. Developing new enrichment functions for crack simulation in orthotropic media by the extended finite element method. **International Journal for Numerical Methods in Engineering**, Wiley Online Library, v. 69, n. 10, p. 2150–2172, 2007. DOI: 10.1002/nme.1839.

AZADI, H.; KHOEI, A. R. Numerical simulation of multiple crack growth in brittle materials with adaptive remeshing. **International Journal for Numerical Methods in Engineering**, Wiley, v. 85, n. 8, p. 1017–1048, Aug. 2010. DOI: 10.1002/nme.3002.

BABUSKA, I.; MELENK, J. M. THE PARTITION OF UNITY METHOD. **International Journal for Numerical Methods in Engineering**, Wiley, v. 40, n. 4, p. 727–758, Feb. 1997. DOI: 10.1002/(sici)1097-0207(19970228)40:4<727::aid-nme86>3.0.co;2-n.

BABUŠKA, Ivo; BANERJEE, Uday. Stable generalized finite element method (SGFEM). **Computer Methods in Applied Mechanics and Engineering**, Elsevier, v. 201, p. 91–111, 2012. DOI: 10.1016/j.cma.2011.09.012.

BANERJEE, P.K. Integral equation methods for analysis of piece-wise non-homogeneous three-dimensional elastic solids of arbitrary shape. **International Journal of Mechanical Sciences**, Elsevier BV, v. 18, n. 6, p. 293–303, June 1976. DOI: 10.1016/0020-7403(76)90031-x.

BANKS-SILLS, Leslie. **Interface Fracture and Delaminations in Composite Materials**. [S.l.]: Springer, 2018.

BARSOUM, Roshdy S. On the use of isoparametric finite elements in linear fracture mechanics. **International Journal for Numerical Methods in Engineering**, Wiley, v. 10, n. 1, p. 25–37, 1976. DOI: 10.1002/nme.1620100103.

BAZILEVS, Y. et al. Isogeometric analysis using T-splines. **Computer Methods in Applied Mechanics and Engineering**, Elsevier BV, v. 199, n. 5-8, p. 229–263, Jan. 2010. DOI: 10.1016/j.cma.2009.02.036.

BÉCHET, E. et al. Improved implementation and robustness study of the X-FEM for stress analysis around cracks. **International Journal for Numerical Methods in Engineering**, Wiley, v. 64, n. 8, p. 1033–1056, 2005. DOI: 10.1002/nme.1386.

BEER, G.; MARUSSIG, B.; DUENSER, C. Isogeometric boundary element method for the simulation of underground excavations. **Géotechnique Letters**, Thomas Telford Ltd., v. 3, n. 3, p. 108–111, Sept. 2013. DOI: 10.1680/geolett.13.00009.

BEER, Gernot; DUENSER, Christian. Advanced 3-D Boundary Element analysis of underground excavations. **Computers and Geotechnics**, Elsevier BV, v. 101, p. 196–207, Sept. 2018. DOI: 10.1016/j.compgeo.2018.05.005.

BELINHA, J. et al. The Natural Neighbor Radial Point Interpolation Method Extended to the Crack Growth Simulation. **International Journal of Applied Mechanics**, World Scientific Pub Co Pte Lt, v. 08, n. 01, p. 1650006, Feb. 2016. DOI: 10.1142/s175882511650006x.

BELYTSCHKO, T.; BLACK, T. Elastic crack growth in finite elements with minimal remeshing. **International Journal for Numerical Methods in Engineering**, Wiley, v. 45, n. 5, p. 601–620, June 1999. DOI: 10.1002/(sici)1097-0207(19990620)45:5<601::aid-nme598>3.0.co;2-s.

BELYTSCHKO, T.; KRONGAUZ, Y., et al. Meshless methods: An overview and recent developments. **Computer Methods in Applied Mechanics and Engineering**, Elsevier BV, v. 139, n. 1-4, p. 3–47, Dec. 1996. DOI: 10.1016/s0045-7825(96)01078-x.

BENEDETTI, I.; ALIABADI, M. H. A fast hierarchical dual boundary element method for three-dimensional elastodynamic crack problems. **International Journal for Numerical Methods in Engineering**, Wiley, v. 84, n. 9, p. 1038–1067, Oct. 2010. DOI: 10.1002/nme.2929.

BENEDETTI, I.; ALIABADI, M.H.; DAVÌ, G. A fast 3D dual boundary element method based on hierarchical matrices. **International Journal of Solids and Structures**, Elsevier BV, v. 45, n. 7-8, p. 2355–2376, Apr. 2008. DOI: 10.1016/j.ijsolstr.2007.11.018.

BENEDETTI, I.; MILAZZO, A.; ALIABADI, M. H. A fast dual boundary element method for 3D anisotropic crack problems. **International Journal for Numerical Methods in Engineering**, Wiley, v. 80, n. 10, p. 1356–1378, June 2009. DOI: 10.1002/nme.2666.

BENSON, D.J.; BAZILEVS, Y.; HSU, M.C., et al. Isogeometric shell analysis: The Reissner–Mindlin shell. **Computer Methods in Applied Mechanics and Engineering**, Elsevier BV, v. 199, n. 5-8, p. 276–289, Jan. 2010. DOI: 10.1016/j.cma.2009.05.011.

BENSON, D.J.; BAZILEVS, Y.; LUYCKER, E. De, et al. A generalized finite element formulation for arbitrary basis functions: From isogeometric analysis to XFEM. **International Journal for Numerical Methods in Engineering**, Wiley, p. 765–785, 2010. DOI: 10.1002/nme.2864.

BENZLEY, S. E. Representation of singularities with isoparametric finite elements. **International Journal for Numerical Methods in Engineering**, Wiley, v. 8, n. 3, p. 537–545, 1974. DOI: 10.1002/nme.1620080310.

BINGOL, Onur Rauf; KRISHNAMURTHY, Adarsh. NURBS-Python: An open-source object-oriented NURBS modeling framework in Python. **SoftwareX**, Elsevier, v. 9, p. 85–94, 2019. DOI: 10.1016/j.softx.2018.12.005.

BITTENCOURT, T.N. et al. Quasi-automatic simulation of crack propagation for 2D LEFM problems. **Engineering Fracture Mechanics**, Elsevier BV, v. 55, n. 2, p. 321–334, Sept. 1996. DOI: 10.1016/0013-7944(95)00247-2.

BLANDFORD, George E.; INGRAFFEA, Anthony R.; LIGGETT, James A. Two-dimensional stress intensity factor computations using the boundary element method. **International Journal for Numerical Methods in Engineering**, Wiley, v. 17, n. 3, p. 387–404, Mar. 1981. DOI: 10.1002/nme.1620170308.

BORDAS, S.; DUFLOT, M.; LE, P. A simple error estimator for extended finite elements. **Communications in Numerical Methods in Engineering**, Wiley, v. 24, n. 11, p. 961–971, Mar. 2007. DOI: 10.1002/cnm.1001.

BORDAS, S.; RABCZUK, T.; ZI, G. Three-dimensional crack initiation, propagation, branching and junction in non-linear materials by an extended meshfree method without asymptotic enrichment. **Engineering Fracture Mechanics**, Elsevier BV, v. 75, n. 5, p. 943–960, Mar. 2008. DOI: 10.1016/j.engfracmech.2007.05.010.

BORDEN, Michael J. et al. Isogeometric finite element data structures based on Bézier extraction of NURBS. **International Journal for Numerical Methods in Engineering**, Wiley, v. 87, n. 1-5, p. 15–47, Aug. 2010. DOI: 10.1002/nme.2968.

BOUCHARD, P.O.; BAY, F.; CHASTEL, Y. Numerical modelling of crack propagation: automatic remeshing and comparison of different criteria. **Computer Methods in Applied Mechanics and Engineering**, Elsevier BV, v. 192, n. 35-36, p. 3887–3908, Aug. 2003. DOI: 10.1016/s0045-7825(03)00391-8.

BREBBIA, Carlos Alberto; DOMINGUEZ, Jose. **Boundary elements: an introductory course**. [S.l.]: WIT press, 1994.

BUDYN, É et al. A method for multiple crack growth in brittle materials without remeshing. **International Journal for Numerical Methods in Engineering**, v. 61, n. 10, p. 1741–1770, 2004. ISSN 00295981. DOI: 10.1002/nme.1130.

CAMPOS, Lucas Silveira; ALBUQUERQUE, Éder Lima de; WROBEL, Luiz Carlos. An ACA accelerated isogeometric boundary element analysis of potential problems with non-uniform boundary conditions. **Engineering Analysis with Boundary Elements**, Elsevier BV, v. 80, p. 108–115, July 2017. DOI: 10.1016/j.enganabound.2017.04.004.

CARPINTERI, Alberto; MONETTO, Ilaria. Snap-back analysis of fracture evolution in multi-cracked solids using Boundary Element Method. **International Journal of Fracture**, Springer Nature, v. 98, n. 3/4, p. 225–241, 1999. DOI: 10.1023/a:1018660600546.

CHANG, Jun; XU, Jin-Quan. The singular stress field and stress intensity factors of a crack terminating at a bimaterial interface. **International Journal of Mechanical Sciences**, Elsevier BV, v. 49, n. 7, p. 888–897, Sept. 2007. DOI: 10.1016/j.ijmecsci.2006.11.009.

CHEN, Chao-Shi; PAN, Ernian; AMADEI, Bernard. Fracture mechanics analysis of cracked discs of anisotropic rock using the boundary element method. **International Journal of Rock Mechanics and Mining Sciences**, Elsevier BV, v. 35, n. 2, p. 195–218, Mar. 1998. DOI: 10.1016/s0148-9062(97)00330-6.

CHEN, Dai-Heng; NAKAMICHI, Seiji. Stress intensity factors for an interface crack along an elliptical inclusion. **International Journal of Fracture**, Springer Science and Business Media LLC, v. 82, n. 2, p. 131–152, Apr. 1996. DOI: 10.1007/bf00034660.

CHEN, Francis H. K.; SHIELD, Richard T. Conservation laws in elasticity of the J-integral type. **Zeitschrift für angewandte Mathematik und Physik**, Springer Nature America, Inc, v. 28, n. 1, p. 1–22, Jan. 1977. DOI: 10.1007/bf01590704.

CHEN, L.; RABCZUK, T., et al. Extended finite element method with edge-based strain smoothing (ESm-XFEM) for linear elastic crack growth. **Computer Methods in Applied Mechanics and Engineering**, Elsevier BV, v. 209-212, p. 250–265, Feb. 2012. DOI: 10.1016/j.cma.2011.08.013.

CHEN, Y.Z. Closed form solutions of T-stress in plane elasticity crack problems. **International Journal of Solids and Structures**, Elsevier BV, v. 37, n. 11, p. 1629–1637, Mar. 2000. DOI: 10.1016/s0020-7683(98)00312-6.

CHESSA, Jack; WANG, Hongwu; BELYTSCHKO, Ted. On the construction of blending elements for local partition of unity enriched finite elements. **International Journal for Numerical Methods in Engineering**, Wiley, v. 57, n. 7, p. 1015–1038, 2003. DOI: 10.1002/nme.777.

CHIARAMONTE, Maurizio M. et al. Computing stress intensity factors for curvilinear cracks. **International Journal for Numerical Methods in Engineering**, Wiley, v. 104, n. 4, p. 260–296, May 2015. DOI: 10.1002/nme.4938.

CHO, Seonho; HA, Seung-Hyun. Isogeometric shape design optimization: exact geometry and enhanced sensitivity. **Structural and Multidisciplinary Optimization**, Springer Nature, v. 38, n. 1, p. 53–70, May 2008. DOI: 10.1007/s00158-008-0266-z.

CIVELEK, M. B.; ERDOGAN, F. Crack problems for a rectangular plate and an infinite strip. **International Journal of Fracture**, v. 19, n. 2, p. 139–159, 1982. ISSN 03769429. DOI: 10.1007/BF00016570.

COMNINOU, Maria. An overview of interface cracks. **Engineering Fracture Mechanics**, Elsevier BV, v. 37, n. 1, p. 197–208, Jan. 1990. DOI: 10.1016/0013-7944(90)90343-f.

COOX, Laurens et al. An isogeometric indirect boundary element method for solving acoustic problems in open-boundary domains. **Computer Methods in Applied Mechanics and Engineering**, Elsevier BV, v. 316, p. 186–208, Apr. 2017. DOI: 10.1016/j.cma.2016.05.039.

CORDEIRO, Sergio Gustavo Ferreira; LEONEL, Edson Denner. Mechanical modelling of three-dimensional cracked structural components using the isogeometric dual boundary element method. **Applied Mathematical Modelling**, Elsevier BV, v. 63, p. 415–444, Nov. 2018. DOI: 10.1016/j.apm.2018.06.042.

COTTRELL, J.A.; HUGHES, T.J.R.; BAZILEVS, Y. **Isogeometric analysis: toward integration of CAD and FEA**. [S.l.]: John Wiley & Sons, 2009.

COTTRELL, J.A.; REALI, A., et al. Isogeometric analysis of structural vibrations. **Computer Methods in Applied Mechanics and Engineering**, Elsevier BV, v. 195, n. 41-43, p. 5257–5296, Aug. 2006. DOI: 10.1016/j.cma.2005.09.027.

COX, Maurice G. The numerical evaluation of B-splines. **IMA Journal of Applied Mathematics**, Oxford University Press, v. 10, n. 2, p. 134–149, 1972. DOI: 10.1093/imamat/10.2.134.

CRUSE, TA. **Numerical evaluation of elastic stress intensity factors by the boundary-integral equation method**. [S.l.], 1972.

CRUSE, Thomas A; SWEDLOW, JL. **Interactive program for analysis and design problems in advanced composites technology**. [S.l.], 1971.

DE BOOR, Carl. On calculating with B-splines. **Journal of Approximation theory**, Academic Press, v. 6, n. 1, p. 50–62, 1972. DOI: 10.1016/0021-9045(72)90080-9.

DENG, Jiansong et al. Polynomial splines over hierarchical T-meshes. **Graphical Models**, Elsevier BV, v. 70, n. 4, p. 76–86, July 2008. DOI: 10.1016/j.gmod.2008.03.001.

DENG, X. General crack-tip fields for stationary and steadily growing interface cracks in anisotropic bimaterials. **Journal of Applied Mechanics**, American Society of Mechanical Engineers, v. 60, n. 1, p. 183–189, 1993. DOI: 10.1115/1.2900743.

DOKKEN, Tor; LYCHE, Tom; PETTERSEN, Kjell Fredrik. Polynomial splines over locally refined box-partitions. **Computer Aided Geometric Design**, Elsevier BV, v. 30, n. 3, p. 331–356, Mar. 2013. DOI: 10.1016/j.cagd.2012.12.005.

DUFLOT, M.; BORDAS, S. A posteriorierror estimation for extended finite elements by an extended global recovery. **International Journal for Numerical Methods in Engineering**, Wiley, v. 76, n. 8, p. 1123–1138, Nov. 2008. DOI: 10.1002/nme.2332.

DUFLOT, Marc; NGUYEN-DANG, Hung. A meshless method with enriched weight functions for fatigue crack growth. **International Journal for Numerical Methods in Engineering**, Wiley, v. 59, n. 14, p. 1945–1961, Apr. 2004. DOI: 10.1002/nme.948.

ENGLAND, AH. A crack between dissimilar media. **J. appl. Mech**, v. 32, n. 2, p. 400–402, 1965. DOI: 10.1115/1.3625813.

ERDOGAN, F. Stress Distribution in Bonded Dissimilar Materials With Cracks. **Journal of Applied Mechanics**, ASME International, v. 32, n. 2, p. 403–410, June 1965. DOI: 10.1115/1.3625814.

ERDOGAN, F.; SIH, G. C. On the Crack Extension in Plates Under Plane Loading and Transverse Shear. **Journal of Basic Engineering**, ASME International, v. 85, n. 4, p. 519, 1963. DOI: 10.1115/1.3656897.

FALLAH, N; NIKRAFTAR, N. Meshless finite volume method for the analysis of fracture problems in orthotropic media. **Engineering Fracture Mechanics**, Elsevier, v. 204, p. 46–62, 2018. DOI: 10.1016/j.engfracmech.2018.09.029.

FEDELINSKI, P.; ALIABADI, M.H.; ROOKE, D.P. The dual boundary element method in dynamic fracture mechanics. **Engineering Analysis with Boundary Elements**, Elsevier BV, v. 12, n. 3, p. 203–210, Jan. 1993. DOI: 10.1016/0955-7997(93)90016-e.

FETT, Theo. **Stress Intensity Factors - T-Stresses - Weight Functions**. v. 50. [S.l.], 2008. 362 pp. (Schriftenreihe des Instituts für Keramik im Maschinenbau - IKM). ISBN 978-3-86644-235-1. DOI: 10.5445/KSP/1000007996.

FIX, G.J; GULATI, S; WAKOFF, G.I. On the use of singular functions with finite element approximations. **Journal of Computational Physics**, Elsevier BV, v. 13, n. 2, p. 209–228, Oct. 1973. DOI: 10.1016/0021-9991(73)90023-5.

FLEMING, M. et al. Enriched Element-Free Galerkin methods for crack tip fields. **International Journal for Numerical Methods in Engineering**, Wiley, v. 40, n. 8, p. 1483–1504, Apr. 1997. DOI: 10.1002/(sici)1097-0207(19970430)40:8<1483::aid-nme123>3.0.co;2-6.

FRIES, Thomas-Peter. A corrected XFEM approximation without problems in blending elements. **International Journal for Numerical Methods in Engineering**, Wiley, v. 75, n. 5, p. 503–532, July 2008. DOI: 10.1002/nme.2259.

GAO, H.; ABBUDI, M.; BARNETT, D.M. Interfacial crack-tip field in anisotropic elastic solids. **Journal of the Mechanics and Physics of Solids**, Elsevier BV, v. 40, n. 2, p. 393–416, Jan. 1992. DOI: 10.1016/s0022-5096(05)80018-3.

GARCÍA, F; SÁEZ, A; DOMÍNGUEZ, J. Traction boundary elements for cracks in anisotropic solids. **Engineering Analysis with Boundary Elements**, Elsevier BV, v. 28, n. 6, p. 667–676, June 2004. DOI: 10.1016/j.enganabound.2003.08.005.

GHORASHI, S.Sh.; VALIZADEH, N.; MOHAMMADI, S.; RABCZUK, T. T-spline based XIGA for fracture analysis of orthotropic media. **Computers & Structures**, Elsevier BV, v. 147, p. 138–146, Jan. 2015. DOI: 10.1016/j.compstruc.2014.09.017.

GHORASHI, Seyed Shahram; VALIZADEH, Navid; MOHAMMADI, Soheil. Extended isogeometric analysis for simulation of stationary and propagating cracks. **International Journal for Numerical Methods in Engineering**, Wiley, v. 89, n. 9, p. 1069–1101, Sept. 2011. DOI: 10.1002/nme.3277.

GONG, Y.P.; DONG, C.Y.; QIN, X.C. An isogeometric boundary element method for three dimensional potential problems. **Journal of Computational and Applied Mathematics**, Elsevier BV, v. 313, p. 454–468, Mar. 2017. DOI: 10.1016/j.cam.2016.10.003.

GONG, Yanpeng; TREVELYAN, Jon, et al. Hybrid nearly singular integration for isogeometric boundary element analysis of coatings and other thin 2D structures. **Computer Methods in Applied Mechanics and Engineering**, Elsevier BV, v. 346, p. 642–673, Apr. 2019. DOI: 10.1016/j.cma.2018.12.019.

GONZÁLEZ-ALBUIXECH, V.F. et al. Convergence of domain integrals for stress intensity factor extraction in 2-D curved cracks problems with the extended finite element method. **International Journal for Numerical Methods in Engineering**, Wiley, v. 94, n. 8, p. 740–757, Apr. 2013. DOI: 10.1002/nme.4478.

GRACIE, Robert; WANG, Hongwu; BELYTSCHKO, Ted. Blending in the extended finite element method by discontinuous Galerkin and assumed strain methods. **International Journal for Numerical Methods in Engineering**, Wiley, v. 74, n. 11, p. 1645–1669, 2008. DOI: 10.1002/nme.2217.

GREVILLE, TNE. Numerical procedures for interpolation by spline functions. **Journal of the Society for Industrial and Applied Mathematics, Series B: Numerical Analysis**, SIAM, v. 1, n. 1, p. 53–68, 1964. DOI: 10.1137/0701005.

GRIFFITH, A. A. The Phenomena of Rupture and Flow in Solids. **Philosophical Transactions of the Royal Society A: Mathematical, Physical and Engineering Sciences**, The Royal Society, v. 221, n. 582-593, p. 163–198, Jan. 1921. DOI: 10.1098/rsta.1921.0006.

GU, Yan; ZHANG, Chuanzeng. Novel special crack-tip elements for interface crack analysis by an efficient boundary element method. **Engineering Fracture Mechanics**, Elsevier BV, v. 239, p. 107302, Nov. 2020. DOI: 10.1016/j.engfracmech.2020.107302.

GUIGGIANI, Massimo; CASALINI, Paolo. Direct computation of Cauchy principal value integrals in advanced boundary elements. **International Journal for Numerical Methods in Engineering**, Wiley, v. 24, n. 9, p. 1711–1720, Sept. 1987. DOI: 10.1002/nme.1620240908.

HARROP, L. P. The optimum size of quarter-point crack tip elements. **International Journal for Numerical Methods in Engineering**, Wiley, v. 18, n. 7, p. 1101–1103, July 1982. DOI: 10.1002/nme.1620180713.

HATTORI, G.; ALATAWI, I. A.; TREVELYAN, J. An extended boundary element method formulation for the direct calculation of the stress intensity factors in fully anisotropic materials. **International Journal for Numerical Methods in Engineering**, Wiley, v. 109, n. 7, p. 965–981, July 2016. DOI: 10.1002/nme.5311.

HE, Ming-Yuan et al. Kinking of a Crack out of an Interface: Role of In-Plane Stress. **Journal of the American Ceramic Society**, Wiley, v. 74, n. 4, p. 767–771, Apr. 1991. DOI: 10.1111/j.1151-2916.1991.tb06922.x.

HENSHELL, R. D.; SHAW, K. G. Crack tip finite elements are unnecessary. **International Journal for Numerical Methods in Engineering**, Wiley, v. 9, n. 3, p. 495–507, 1975. DOI: 10.1002/nme.1620090302.

HONG, Hong-Ki; CHEN, Jeng-Tzong. Derivations of Integral Equations of Elasticity. **Journal of Engineering Mechanics**, American Society of Civil Engineers (ASCE), v. 114, n. 6, p. 1028–1044, June 1988. DOI: 10.1061/(asce)0733-9399(1988)114:6(1028).

HONNOR, M.E.; TREVELYAN, J.; HUYBRECHS, D. Numerical evaluation of the two-dimensional partition of unity boundary integrals for Helmholtz problems. **Journal of Computational and Applied Mathematics**, Elsevier BV, v. 234, n. 6, p. 1656–1662, July 2010. DOI: 10.1016/j.cam.2009.08.012.

HUGHES, T.J.R.; COTTRELL, J.A.; BAZILEVS, Y. Isogeometric analysis: CAD, finite elements, NURBS, exact geometry and mesh refinement. **Computer Methods in Applied Mechanics and Engineering**, Elsevier BV, v. 194, n. 39-41, p. 4135–4195, Oct. 2005. DOI: 10.1016/j.cma.2004.10.008.

HUTCHINSON, J. W.; MEAR, M. E.; RICE, J. R. Crack Paralleling an Interface Between Dissimilar Materials. **Journal of Applied Mechanics**, ASME International, v. 54, n. 4, p. 828–832, Dec. 1987. DOI: 10.1115/1.3173124.

HUTCHINSON, J.W.; SUO, Z. Mixed Mode Cracking in Layered Materials. In: ADVANCES in Applied Mechanics. [S.l.]: Elsevier, 1991. p. 63–191. DOI: 10.1016/s0065-2156(08)70164-9.

INGRAFFEA, Anthony R.; MANU, Corneliu. Stress-intensity factor computation in three dimensions with quarter-point elements. **International Journal for Numerical Methods in Engineering**, Wiley, v. 15, n. 10, p. 1427–1445, Oct. 1980. DOI: 10.1002/nme.1620151002.

INGRAFFEA, Anthony R; GRIGORIU, Mircea. **Probabilistic fracture mechanics: A validation of predictive capability**. [S.l.], 1990.

IRWIN, George R. Analysis of stresses and strains near the end of a crack traversing a plate. **J. appl. Mech.**, 1957.

JIN, Y. et al. Error-controlled adaptive extended finite element method for 3D linear elastic crack propagation. **Computer Methods in Applied Mechanics and Engineering**, Elsevier BV, v. 318, p. 319–348, May 2017. DOI: 10.1016/j.cma.2016.12.016.

JOHNSON, Richard W. Higher order B-spline collocation at the Greville abscissae. **Applied Numerical Mathematics**, Elsevier BV, v. 52, n. 1, p. 63–75, Jan. 2005. DOI: 10.1016/j.apnum.2004.04.002.

KANG, Ki Ju. Criteria for kinking out of interface crack. **Engineering Fracture Mechanics**, Elsevier BV, v. 49, n. 4, p. 587–598, Nov. 1994. DOI: 10.1016/0013-7944(94)90051-5.

KHOEI, A.R.; VAHAB, M.; HIRMAND, M. An enriched–FEM technique for numerical simulation of interacting discontinuities in naturally fractured porous media. **Computer Methods in Applied Mechanics and Engineering**, Elsevier BV, v. 331, p. 197–231, Apr. 2018. DOI: 10.1016/j.cma.2017.11.016.

KHOSRAVIFARD, A. et al. Accurate and efficient analysis of stationary and propagating crack problems by meshless methods. **Theoretical and Applied Fracture Mechanics**, Elsevier BV, v. 87, p. 21–34, Feb. 2017. DOI: 10.1016/j.tafmec.2016.10.004.

KIM, Hyun-Jung; SEO, Yu-Deok; YOUN, Sung-Kie. Isogeometric analysis for trimmed CAD surfaces. **Computer Methods in Applied Mechanics and Engineering**, Elsevier BV, v. 198, n. 37-40, p. 2982–2995, Aug. 2009. DOI: 10.1016/j.cma.2009.05.004.

_____. Isogeometric analysis with trimming technique for problems of arbitrary complex topology. **Computer Methods in Applied Mechanics and Engineering**, Elsevier BV, v. 199, n. 45-48, p. 2796–2812, Nov. 2010. DOI: 10.1016/j.cma.2010.04.015.

KIM, J.H.; MOON, H.J.; EARMME, Y.Y. Inplane and antiplane T-stresses for an interface crack in anisotropic bimaterial. **Mechanics of Materials**, Elsevier BV, v. 33, n. 1, p. 21–32, Jan. 2001. DOI: 10.1016/s0167-6636(00)00034-x.

KIM, Jae-Hyun; VLASSAK, Joost J. T-Stress of a Bi-Material Strip Under Generalized Edge Loads. **International Journal of Fracture**, Springer Science and Business Media LLC, v. 142, n. 3-4, p. 315–322, Jan. 2007. DOI: 10.1007/s10704-006-9033-6.

KUMAR, Sachin; SINGH, I.V.; MISHRA, B.K. A homogenized XFEM approach to simulate fatigue crack growth problems. **Computers & Structures**, Elsevier BV, v. 150, p. 1–22, Apr. 2015. DOI: 10.1016/j.compstruc.2014.12.008.

LE, V.H.T.; BRISARD, S.; POUYA, A. Debonding of a circular inclusion: Asymmetric propagation of a pair of cracks. **International Journal of Solids and Structures**, Elsevier BV, v. 167, p. 71–78, Aug. 2019. DOI: 10.1016/j.ijsolstr.2019.03.004.

LEGAY, A.; WANG, H. W.; BELYTSCHKO, T. Strong and weak arbitrary discontinuities in spectral finite elements. **International Journal for Numerical Methods in Engineering**, Wiley, v. 64, n. 8, p. 991–1008, 2005. DOI: 10.1002/nme.1388.

LEITÃO, V.; ALIABADI, M.H.; ROOKE, D.P. Elastoplastic dual boundary elements: Application to crack-face contact. **Computers & Structures**, Elsevier BV, v. 54, n. 3, p. 443–454, Feb. 1995. DOI: 10.1016/0045-7949(94)00340-9.

LEKHNITSKII, Sergei Georgievich. **Anisotropic plates**. [S.l.], 1968.

LEONEL, Edson Denner; VENTURINI, Wilson Sergio. Dual boundary element formulation applied to analysis of multi-fractured domains. **Engineering Analysis with Boundary Elements**, Elsevier BV, v. 34, n. 12, p. 1092–1099, Dec. 2010. DOI: 10.1016/j.enganabound.2010.06.014.

_____. Non-linear boundary element formulation applied to contact analysis using tangent operator. **Engineering Analysis with Boundary Elements**, Elsevier BV, v. 35, n. 12, p. 1237–1247, Dec. 2011. DOI: 10.1016/j.enganabound.2011.06.005.

LI, S.C.; LI, S.C.; CHENG, Y.M. Enriched meshless manifold method for two-dimensional crack modeling. **Theoretical and Applied Fracture Mechanics**, Elsevier BV, v. 44, n. 3, p. 234–248, Dec. 2005. DOI: 10.1016/j.tafmec.2005.09.002.

LIAN, H.; KERFRIDEN, P.; BORDAS, S. Shape optimization directly from CAD: An isogeometric boundary element approach using T-splines. **Computer Methods in Applied Mechanics and Engineering**, Elsevier BV, v. 317, p. 1–41, Apr. 2017. DOI: 10.1016/j.cma.2016.11.012.

LIEW, K.M.; CHENG, Yumin; KITIPORNCHAI, S. Analyzing the 2D fracture problems via the enriched boundary element-free method. **International Journal of Solids and Structures**, Elsevier BV, v. 44, n. 11-12, p. 4220–4233, June 2007. DOI: 10.1016/j.ijsolstr.2006.11.018.

LINS, R. M. et al. An a-posteriori error estimator for linear elastic fracture mechanics using the stable generalized/extended finite element method. **Computational Mechanics**, Springer Science and Business Media LLC, v. 56, n. 6, p. 947–965, Oct. 2015. DOI: 10.1007/s00466-015-1212-8.

LIU, X. Y.; XIAO, Q. Z.; KARIHALOO, B. L. XFEM for direct evaluation of mixed mode SIFs in homogeneous and bi-materials. **International Journal for Numerical Methods in Engineering**, Wiley, v. 59, n. 8, p. 1103–1118, Jan. 2004. DOI: 10.1002/nme.906.

LIU, Y.J.; LI, Y.X.; XIE, W. Modeling of multiple crack propagation in 2-D elastic solids by the fast multipole boundary element method. **Engineering Fracture Mechanics**, Elsevier BV, v. 172, p. 1–16, Mar. 2017. DOI: 10.1016/j.engfracmech.2017.01.010.

LIU, Yijun. **Fast multipole boundary element method: theory and applications in engineering**. [S.l.]: Cambridge university press, 2009.

LIU, Yijun J; XU, Nan. Modeling of interface cracks in fiber-reinforced composites with the presence of interphases using the boundary element method. **Mechanics of Materials**, Elsevier BV, v. 32, n. 12, p. 769–783, Dec. 2000. DOI: 10.1016/s0167-6636(00)00045-4.

LOEHNERT, S.; PRANGE, C.; WRIGGERS, P. Error controlled adaptive multiscale XFEM simulation of cracks. **International Journal of Fracture**, Springer Science and Business Media LLC, v. 178, n. 1-2, p. 147–156, Nov. 2012. DOI: 10.1007/s10704-012-9777-0.

LUYCKER, E. De et al. X-FEM in isogeometric analysis for linear fracture mechanics. **International Journal for Numerical Methods in Engineering**, Wiley, v. 87, n. 6, p. 541–565, Jan. 2011. DOI: 10.1002/nme.3121.

MARTÍNEZ, José; DOMÍNGUEZ, José. On the use of quarter-point boundary elements for stress intensity factor computations. **International Journal for Numerical Methods in Engineering**, Wiley, v. 20, n. 10, p. 1941–1950, Oct. 1984. DOI: 10.1002/nme.1620201013.

MELENK, J.M.; BABUSKA, I. The partition of unity finite element method: Basic theory and applications. **Computer Methods in Applied Mechanics and Engineering**, Elsevier BV, v. 139, n. 1-4, p. 289–314, Dec. 1996. DOI: 10.1016/s0045-7825(96)01087-0.

MENK, A.; BORDAS, S. A robust preconditioning technique for the extended finite element method. **International Journal for Numerical Methods in Engineering**, Wiley, v. 85, n. 13, p. 1609–1632, Oct. 2010. DOI: 10.1002/nme.3032.

MI, Y.; ALIABADI, M.H. Dual boundary element method for three-dimensional fracture mechanics analysis. **Engineering Analysis with Boundary Elements**, Elsevier BV, v. 10, n. 2, p. 161–171, 1992. DOI: 10.1016/0955-7997(92)90047-b.

MIYAZAKI, N. et al. Stress intensity factor analysis of interface crack using boundary element method—Application of contour-integral method. **Engineering Fracture Mechanics**, Elsevier BV, v. 45, n. 5, p. 599–610, July 1993. DOI: 10.1016/0013-7944(93)90266-u.

MOËS, Nicolas; DOLBOW, John; BELYTSCHKO, Ted. A finite element method for crack growth without remeshing. **International Journal for Numerical Methods in Engineering**, Wiley, v. 46, n. 1, p. 131–150, Sept. 1999. DOI: 10.1002/(sici)1097-0207(19990910)46:1<131::aid-nme726>3.0.co;2-j.

MURAKAMI, Yu et al. Handbook of stress intensity factors. In: PERGAMON Press, Oxford (UK). [S.l.: s.n.], 1987. p. 1011.

MUTHU, N et al. Crack propagation in non-homogenous materials: Evaluation of mixed-mode SIFs, T-stress and kinking angle using a variant of EFG Method. **Engineering Analysis with Boundary Elements**, Elsevier, v. 72, p. 11–26, 2016. DOI: 10.1016/j.enganabound.2016.07.017.

NATARAJAN, Sundararajan; SONG, Chongmin; BELOUETTAR, Salim. Numerical evaluation of stress intensity factors and T-stress for interfacial cracks and cracks terminating at the interface without asymptotic enrichment. **Computer Methods in Applied Mechanics and Engineering**, Elsevier BV, v. 279, p. 86–112, Sept. 2014. DOI: 10.1016/j.cma.2014.06.024. Available from: <https://doi.org/10.1016/j.cma.2014.06.024>.

NGUYEN, B.H. et al. An isogeometric symmetric Galerkin boundary element method for two-dimensional crack problems. **Computer Methods in Applied Mechanics and Engineering**, Elsevier BV, v. 306, p. 252–275, July 2016. DOI: 10.1016/j.cma.2016.04.002.

NGUYEN, V. et al. Isogeometric analysis: An overview and computer implementation aspects. **Mathematics and Computers in Simulation**, Elsevier BV, v. 117, p. 89–116, Nov. 2015. DOI: 10.1016/j.matcom.2015.05.008.

NISHIMURA, Naoshi; YOSHIDA, Ken-ichi; KOBAYASHI, Shoichi. A fast multipole boundary integral equation method for crack problems in 3D. **Engineering Analysis with Boundary Elements**, Elsevier BV, v. 23, n. 1, p. 97–105, Jan. 1999. DOI: 10.1016/s0955-7997(98)00065-4.

OLIVEIRA, Hugo Luiz; ANDRADE, Heider Castro; LEONEL, Edson Denner. An isogeometric boundary element approach for topology optimization using the level set method. **Applied Mathematical Modelling**, Elsevier BV, v. 84, p. 536–553, Aug. 2020. DOI: 10.1016/j.apm.2020.03.047.

OLIVEIRA, T.; PORTELA, A. A local mesh free method with the singularity subtraction technique. **Engineering Analysis with Boundary Elements**, Elsevier BV, v. 104, p. 148–159, July 2019. DOI: 10.1016/j.enganabound.2019.03.031.

PARIS, Paul C. A rational analytic theory of fatigue. **The trend in engineering**, v. 13, p. 9, 1961.

PARIS, Paul C; SIH, George C. Stress analysis of cracks. In: FRACTURE toughness testing and its applications. [S.l.]: ASTM International, 1965.

PASTERNAK, Iaroslav. Boundary integral equations and the boundary element method for fracture mechanics analysis in 2D anisotropic thermoelasticity. **Engineering Analysis with Boundary Elements**, Elsevier BV, v. 36, n. 12, p. 1931–1941, Dec. 2012. DOI: 10.1016/j.enganabound.2012.07.007.

PEAKE, M.J.; TREVELYAN, J.; COATES, G. Extended isogeometric boundary element method (XIBEM) for three-dimensional medium-wave acoustic scattering problems. **Computer Methods in Applied Mechanics and Engineering**, Elsevier BV, v. 284, p. 762–780, Feb. 2015. DOI: 10.1016/j.cma.2014.10.039.

_____. Extended isogeometric boundary element method (XIBEM) for two-dimensional Helmholtz problems. **Computer Methods in Applied Mechanics and Engineering**, Elsevier BV, v. 259, p. 93–102, June 2013. DOI: 10.1016/j.cma.2013.03.016.

PENG, X.; ATROSHCHENKO, E., et al. Isogeometric boundary element methods for three dimensional static fracture and fatigue crack growth. **Computer Methods in Applied Mechanics and Engineering**, Elsevier BV, v. 316, p. 151–185, Apr. 2017. DOI: 10.1016/j.cma.2016.05.038.

_____. Linear elastic fracture simulation directly from CAD: 2D NURBS-based implementation and role of tip enrichment. **International Journal of Fracture**, Springer Nature, v. 204, n. 1, p. 55–78, Sept. 2016. DOI: 10.1007/s10704-016-0153-3.

PENG, X.; KULASEGARAM, S., et al. An extended finite element method (XFEM) for linear elastic fracture with smooth nodal stress. **Computers & Structures**, Elsevier BV, v. 179, p. 48–63, Jan. 2017. DOI: 10.1016/j.compstruc.2016.10.014.

PEREIRA, J. P.; DUARTE, C. A.; JIAO, X. Three-dimensional crack growth with hp-generalized finite element and face offsetting methods. **Computational Mechanics**, Springer Science and Business Media LLC, v. 46, n. 3, p. 431–453, Mar. 2010. DOI: 10.1007/s00466-010-0491-3.

PERLMAN, A.B.; SIH, G.C. Elastostatic problems of curvilinear cracks in bonded dissimilar materials. **International Journal of Engineering Science**, Elsevier BV, v. 5, n. 11, p. 845–867, Nov. 1967. DOI: 10.1016/0020-7225(67)90009-2.

PERREY-DEBAIN, E.; LAGHROUCHE, O., et al. Plane-wave basis finite elements and boundary elements for three-dimensional wave scattering. Ed. by P. Bettess, O. Laghrouche and E. Perrey-Debain. **Philosophical Transactions of the Royal Society of London. Series A: Mathematical, Physical and Engineering Sciences**, The Royal Society, v. 362, n. 1816, p. 561–577, Mar. 2004. DOI: 10.1098/rsta.2003.1335.

PERREY-DEBAIN, E.; TREVELYAN, J.; BETTESS, P. New special wave boundary elements for short wave problems. **Communications in Numerical Methods in Engineering**, Wiley, v. 18, n. 4, p. 259–268, Feb. 2002. DOI: 10.1002/cnm.492.

_____. Plane wave interpolation in direct collocation boundary element method for radiation and wave scattering: numerical aspects and applications. **Journal of Sound and Vibration**, Elsevier BV, v. 261, n. 5, p. 839–858, Apr. 2003. DOI: 10.1016/s0022-460x(02)01006-4.

_____. Use of Wave Boundary Elements for Acoustic Computations. **Journal of Computational Acoustics**, World Scientific Pub Co Pte Lt, v. 11, n. 02, p. 305–321, June 2003. DOI: 10.1142/s0218396x03001924.

PIEGL, Les; TILLER, Wayne. **The NURBS Book**. [S.l.]: Springer Berlin Heidelberg, 1995. DOI: 10.1007/978-3-642-97385-7.

POLITIS, Costas et al. An isogeometric BEM for exterior potential-flow problems in the plane. In: 2009 SIAM/ACM Joint Conference on Geometric and Physical Modeling on - SPM 09. [S.l.]: ACM Press, 2009. DOI: 10.1145/1629255.1629302.

PORTELA, A.; ALIABADI, M.H.; ROOKE, D.P. Dual boundary element incremental analysis of crack propagation. **Computers & Structures**, Elsevier BV, v. 46, n. 2, p. 237–247, Jan. 1993. DOI: 10.1016/0045-7949(93)90189-k.

_____. The dual boundary element method: Effective implementation for crack problems. **International Journal for Numerical Methods in Engineering**, Wiley, v. 33, n. 6, p. 1269–1287, Apr. 1992. DOI: 10.1002/nme.1620330611.

PRANGE, C.; LOEHNERT, S.; WRIGGERS, P. Error estimation for crack simulations using the XFEM. **International Journal for Numerical Methods in Engineering**, Wiley, v. 91, n. 13, p. 1459–1474, Aug. 2012. DOI: 10.1002/nme.4331.

PRASAD, N. N. V.; ALIABADI, M. H.; ROOKE, D. P. The dual boundary element method for thermoelastic crack problems. **International Journal of Fracture**, Springer Science and Business Media LLC, v. 66, n. 3, p. 255–272, Apr. 1994. DOI: 10.1007/bf00042588.

PRICE, R.J.; TREVELYAN, J. Boundary element simulation of fatigue crack growth in multi-site damage. **Engineering Analysis with Boundary Elements**, Elsevier BV, v. 43, p. 67–75, June 2014. DOI: 10.1016/j.enganabound.2014.03.002.

PUSTEJOVSKY, Michael A. Fatigue crack propagation in titanium under general in-plane loading—I: Experiments. **Engineering Fracture Mechanics**, Elsevier BV, v. 11, n. 1, p. 9–15, Jan. 1979. DOI: 10.1016/0013-7944(79)90025-0.

RABCZUK, T.; BELYTSCHKO, T. Cracking particles: a simplified meshfree method for arbitrary evolving cracks. **International Journal for Numerical Methods in Engineering**, Wiley, v. 61, n. 13, p. 2316–2343, 2004. DOI: 10.1002/nme.1151.

RABCZUK, T.; BORDAS, S.; ZI, G. A three-dimensional meshfree method for continuous multiple-crack initiation, propagation and junction in statics and dynamics. **Computational Mechanics**, Springer Science and Business Media LLC, v. 40, n. 3, p. 473–495, Mar. 2007. DOI: 10.1007/s00466-006-0122-1.

RABCZUK, T.; ZI, G., et al. A simple and robust three-dimensional cracking-particle method without enrichment. **Computer Methods in Applied Mechanics and Engineering**, Elsevier BV, v. 199, n. 37-40, p. 2437–2455, Aug. 2010. DOI: 10.1016/j.cma.2010.03.031.

RICE, J. R. A Path Independent Integral and the Approximate Analysis of Strain Concentration by Notches and Cracks. **Journal of Applied Mechanics**, ASME International, v. 35, n. 2, p. 379, 1968. DOI: 10.1115/1.3601206.

_____. Elastic Fracture Mechanics Concepts for Interfacial Cracks. **Journal of Applied Mechanics**, ASME International, v. 55, n. 1, p. 98–103, Mar. 1988. DOI: 10.1115/1.3173668.

RICE, J. R.; SIH, G. C. Plane Problems of Cracks in Dissimilar Media. **Journal of Applied Mechanics**, ASME International, v. 32, n. 2, p. 418–423, June 1965. DOI: 10.1115/1.3625816.

RICE, James R; SUO, Zhigang; WANG, Jian-Sheng. Mechanics and thermodynamics of brittle interfacial failure in bimaterial systems. **Acta-Scripta Metallurgica Proceedings Series**, Pergamon Press, London, v. 4, p. 269–294, 1990. DOI: 10.1016/B978-0-08-040505-6.50036-2.

RÓDENAS, J.J. et al. Accurate recovery-based upper error bounds for the extended finite element framework. **Computer Methods in Applied Mechanics and Engineering**, Elsevier BV, v. 199, n. 37-40, p. 2607–2621, Aug. 2010. DOI: 10.1016/j.cma.2010.04.010.

ROOKE, David Percy; CARTWRIGHT, David John. Compendium of stress intensity factors. **Procurement Executive, Ministry of Defence. H. M. S. O. 1976, 330 p(Book).**, 1976.

RYBICKI, E.F.; KANNINEN, M.F. A finite element calculation of stress intensity factors by a modified crack closure integral. **Engineering Fracture Mechanics**, Elsevier BV, v. 9, n. 4, p. 931–938, Jan. 1977. DOI: 10.1016/0013-7944(77)90013-3.

RYOJI, Yuuki; SANG-BONG, Cho. Efficient boundary element analysis of stress intensity factors for interface cracks in dissimilar materials. **Engineering Fracture Mechanics**, Elsevier BV, v. 34, n. 1, p. 179–188, Jan. 1989. DOI: 10.1016/0013-7944(89)90251-8.

SALEH, A.L.; ALIABADI, M.H. Crack growth analysis in concrete using boundary element method. **Engineering Fracture Mechanics**, Elsevier BV, v. 51, n. 4, p. 533–545, July 1995. DOI: 10.1016/0013-7944(94)00301-w.

SAOUMA, Victor E; AYARI, Mohamed L; LEAVELL, Daniel A. Mixed mode crack propagation in homogeneous anisotropic solids. **Engineering Fracture Mechanics**, Elsevier, v. 27, n. 2, p. 171–184, 1987. DOI: 10.1016/0013-7944(87)90166-4.

SCHMIDT, Robert; WÜCHNER, Roland; BLETZINGER, Kai-Uwe. Isogeometric analysis of trimmed NURBS geometries. **Computer Methods in Applied Mechanics and Engineering**, Elsevier BV, v. 241-244, p. 93–111, Oct. 2012. DOI: 10.1016/j.cma.2012.05.021.

SCOTT, Michael A. et al. Isogeometric finite element data structures based on Bézier extraction of T-splines. **International Journal for Numerical Methods in Engineering**, Wiley, v. 88, n. 2, p. 126–156, Mar. 2011. DOI: 10.1002/nme.3167.

SIH, G.C.; PARIS, P.C.; IRWIN, G.R. On cracks in rectilinearly anisotropic bodies. **International Journal of Fracture Mechanics**, Springer Nature, v. 1, n. 3, Sept. 1965. DOI: 10.1007/bf00186854.

SIMPSON, R.; BORDAS, S.; LIAN, H., et al. An isogeometric boundary element method for elastostatic analysis: 2D implementation aspects. **Computers & Structures**, Elsevier BV, v. 118, p. 2–12, Mar. 2013. DOI: 10.1016/j.compstruc.2012.12.021.

SIMPSON, R.; BORDAS, S.; TREVELYAN, J., et al. A two-dimensional Isogeometric Boundary Element Method for elastostatic analysis. **Computer Methods in Applied Mechanics and Engineering**, Elsevier BV, v. 209-212, p. 87–100, Feb. 2012. DOI: 10.1016/j.cma.2011.08.008.

SIMPSON, R.; TREVELYAN, J. A partition of unity enriched dual boundary element method for accurate computations in fracture mechanics. **Computer Methods in Applied Mechanics and Engineering**, Elsevier BV, v. 200, n. 1-4, p. 1–10, Jan. 2011. DOI: 10.1016/j.cma.2010.06.015.

_____. Evaluation of J1 and J2 integrals for curved cracks using an enriched boundary element method. **Engineering Fracture Mechanics**, Elsevier BV, v. 78, n. 4, p. 623–637, Mar. 2011. DOI: 10.1016/j.engfracmech.2010.12.006.

SIMPSON, R.N.; SCOTT, M.A., et al. Acoustic isogeometric boundary element analysis. **Computer Methods in Applied Mechanics and Engineering**, Elsevier BV, v. 269, p. 265–290, Feb. 2014. DOI: 10.1016/j.cma.2013.10.026.

SIMPSON, Robert. **Enrichment of the boundary element method through the partition of unity method for fracture analysis using local and global formulations**. 2010. PhD thesis – Durham University.

SINGH, S.K. et al. A simple, efficient and accurate Bézier extraction based T-spline XIGA for crack simulations. **Theoretical and Applied Fracture Mechanics**, Elsevier BV, v. 88, p. 74–96, Apr. 2017. DOI: 10.1016/j.tafmec.2016.12.002.

SLADEK, J.; SLADEK, V. Evaluations of the T-stress for interface cracks by the boundary element method. **Engineering Fracture Mechanics**, Elsevier BV, v. 56, n. 6, p. 813–825, Apr. 1997. DOI: 10.1016/s0013-7944(96)00131-2.

SNYDER, M. D.; CRUSE, T. A. Boundary-integral equation analysis of cracked anisotropic plates. **International Journal of Fracture**, Springer Science and Business Media LLC, v. 11, n. 2, p. 315–328, Apr. 1975. DOI: 10.1007/bf00038898.

SOLLERO, P.; ALIABADI, M.H. Anisotropic analysis of cracks in composite laminates using the dual boundary element method. **Composite Structures**, Elsevier BV, v. 31, n. 3, p. 229–233, Jan. 1995. DOI: 10.1016/0263-8223(95)00105-0.

SONG, Chongmin. Evaluation of power-logarithmic singularities, T-stresses and higher order terms of in-plane singular stress fields at cracks and multi-material corners. **Engineering Fracture Mechanics**, Elsevier BV, v. 72, n. 10, p. 1498–1530, July 2005. DOI: 10.1016/j.engfracmech.2004.11.002.

STROUBOULIS, T.; BABUŠKA, I.; COPPS, K. The design and analysis of the Generalized Finite Element Method. **Computer Methods in Applied Mechanics and Engineering**, Elsevier BV, v. 181, n. 1-3, p. 43–69, Jan. 2000. DOI: 10.1016/s0045-7825(99)00072-9.

SUKUMAR, N. et al. Partition of unity enrichment for bimaterial interface cracks. **International Journal for Numerical Methods in Engineering**, Wiley, v. 59, n. 8, p. 1075–1102, Jan. 2004. DOI: 10.1002/nme.902.

SUN, F.L.; DONG, C.Y.; YANG, H.S. Isogeometric boundary element method for crack propagation based on Bézier extraction of NURBS. **Engineering Analysis with Boundary Elements**, Elsevier BV, v. 99, p. 76–88, Feb. 2019. DOI: 10.1016/j.enganabound.2018.11.010.

SUN, S.H. et al. Structural shape optimization by IGABEM and particle swarm optimization algorithm. **Engineering Analysis with Boundary Elements**, Elsevier BV, v. 88, p. 26–40, Mar. 2018. DOI: 10.1016/j.enganabound.2017.12.007.

SUN, Yi et al. Discontinuous isogeometric boundary element (IGABEM) formulations in 3D automotive acoustics. **Engineering Analysis with Boundary Elements**, Elsevier BV, v. 105, p. 303–311, Aug. 2019. DOI: 10.1016/j.enganabound.2019.04.011.

SUO, Zhigang; HUTCHINSON, John W. Interface crack between two elastic layers. **International Journal of Fracture**, Springer Science and Business Media LLC, v. 43, n. 1, p. 1–18, May 1990. DOI: 10.1007/bf00018123.

SUTULA, D. et al. Minimum energy multiple crack propagation. Part I: Theory and state of the art review. **Engineering Fracture Mechanics**, Elsevier BV, v. 191, p. 205–224, Mar. 2018. DOI: 10.1016/j.engfracmech.2017.07.028.

_____. Minimum energy multiple crack propagation. Part III: XFEM computer implementation and applications. **Engineering Fracture Mechanics**, Elsevier BV, v. 191, p. 257–276, Mar. 2018. DOI: 10.1016/j.engfracmech.2017.08.004.

_____. Minimum energy multiple crack propagation. Part-II: Discrete solution with XFEM. **Engineering Fracture Mechanics**, Elsevier BV, v. 191, p. 225–256, Mar. 2018. DOI: 10.1016/j.engfracmech.2017.07.029.

TADA, Hiroshi; PARIS, Paul C.; IRWIN, George R. **The Stress Analysis of Cracks Handbook, Third Edition**. [S.l.]: ASME, Jan. 2000. DOI: 10.1115/1.801535.

TANAKA, Keisuke. Fatigue crack propagation from a crack inclined to the cyclic tensile axis. **Engineering Fracture Mechanics**, Elsevier BV, v. 6, n. 3, p. 493–507, Oct. 1974. DOI: 10.1016/0013-7944(74)90007-1.

TANAKA, Masataka; ITOH, Hidekazu. New crack elements for boundary element analysis of elastostatics considering arbitrary stress singularities. **Applied Mathematical Modelling**, Elsevier BV, v. 11, n. 5, p. 357–363, Oct. 1987. DOI: 10.1016/0307-904x(87)90030-8.

TAUS, Matthias; RODIN, Gregory J.; HUGHES, Thomas J. R. Isogeometric analysis of boundary integral equations: High-order collocation methods for the singular and hyper-singular equations. **Mathematical Models and Methods in Applied Sciences**, World Scientific Pub Co Pte Lt, v. 26, n. 08, p. 1447–1480, June 2016. DOI: 10.1142/s0218202516500354.

TAUS, Matthias; RODIN, Gregory J.; HUGHES, Thomas J.R.; SCOTT, Michael A. Isogeometric boundary element methods and patch tests for linear elastic problems: Formulation, numerical integration, and applications. **Computer Methods in Applied Mechanics and Engineering**, Elsevier BV, v. 357, p. 112591, Dec. 2019. DOI: 10.1016/j.cma.2019.112591.

TELLES, J. C. F. A self-adaptive co-ordinate transformation for efficient numerical evaluation of general boundary element integrals. **International Journal for Numerical Methods in Engineering**, Wiley, v. 24, n. 5, p. 959–973, May 1987. DOI: 10.1002/nme.1620240509.

TELLES, J.C.F.; MANSUR, W.J.; WROBEL, L.C. On boundary elements for external potential problems. **Mechanics Research Communications**, Elsevier BV, v. 11, n. 6, p. 373–377, Nov. 1984. DOI: 10.1016/0093-6413(84)90044-2.

TELLES, JCF; OLIVEIRA, RF. Third degree polynomial transformation for boundary element integrals: further improvements. **Engineering analysis with boundary elements**, Elsevier, v. 13, n. 2, p. 135–141, 1994. DOI: 10.1016/0955-7997(94)90016-7.

TEMIZER, İ.; WRIGGERS, P.; HUGHES, T.J.R. Contact treatment in isogeometric analysis with NURBS. **Computer Methods in Applied Mechanics and Engineering**, Elsevier BV, v. 200, n. 9-12, p. 1100–1112, Feb. 2011. DOI: 10.1016/j.cma.2010.11.020.

TIAN, Rong; WEN, Longfei; WANG, Lixiang. Three-dimensional improved XFEM (IXFEM) for static crack problems. **Computer Methods in Applied Mechanics and Engineering**, Elsevier BV, v. 343, p. 339–367, Jan. 2019. DOI: 10.1016/j.cma.2018.08.029.

TRACEY, Dennis M. Finite elements for determination of crack tip elastic stress intensity factors. **Engineering Fracture Mechanics**, Elsevier BV, v. 3, n. 3, p. 255–265, Oct. 1971. DOI: 10.1016/0013-7944(71)90036-1.

TREVELYAN, J.; COATES, G. On adaptive definition of the plane wave basis for wave boundary elements in acoustic scattering: the 2D case. **Computer modeling in engineering and sciences.**, Tech Science Press, v. 55, n. 2, p. 147–170, 2010. DOI: 10.3970/cmes.2010.055.147.

VENTURA, G.; XU, J. X.; BELYTSCHKO, T. A vector level set method and new discontinuity approximations for crack growth by EFG. **International Journal for Numerical Methods in Engineering**, Wiley, v. 54, n. 6, p. 923–944, 2002. DOI: 10.1002/nme.471.

VERHOOSEL, Clemens V. et al. An isogeometric approach to cohesive zone modeling. **International Journal for Numerical Methods in Engineering**, Wiley, v. 87, n. 1-5, p. 336–360, Dec. 2010. DOI: 10.1002/nme.3061.

WANG, S. S.; YAU, J. F.; CORTEN, H. T. A mixed-mode crack analysis of rectilinear anisotropic solids using conservation laws of elasticity. **International Journal of Fracture**, Springer Nature, v. 16, n. 3, p. 247–259, June 1980. DOI: 10.1007/bf00013381.

WANG, Yongxiang; CERIGATO, Chiara, et al. XFEM with high-order material-dependent enrichment functions for stress intensity factors calculation of interface cracks using Irwin's crack closure integral. **Engineering Fracture Mechanics**, Elsevier BV, v. 178, p. 148–168, June 2017. DOI: 10.1016/j.engfracmech.2017.04.021.

WANG, Yongxiang; WAISMAN, Haim; HARARI, Isaac. Direct evaluation of stress intensity factors for curved cracks using Irwin's integral and XFEM with high-order enrichment functions. **International Journal for Numerical Methods in Engineering**, Wiley, v. 112, n. 7, p. 629–654, Feb. 2017. DOI: 10.1002/nme.5517.

WAWRZYNEK, Paul; INGRAFFEA, Anthony. FRANC2D: A two-dimensional crack propagation simulator. Version 2.7: User's guide, 1994.

WILLIAMS, M.L. On the Stress Distribution at the Base of a Stationary Crack. **Journal of Applied Mechanics**, v. 24, p. 109–114, Jan. 1957.

WILLIAMS, M.L. The stresses around a fault or crack in dissimilar media. **Bulletin of the seismological society of America**, The Seismological Society of America, v. 49, n. 2, p. 199–204, 1959.

WU, Linzhi et al. Investigation of Stress Intensity Factors for an Interface Crack in Multi-Interface Materials Using an Interaction Integral Method. **Journal of Applied Mechanics**, ASME International, v. 78, n. 6, Aug. 2011. DOI: 10.1115/1.4003906.

YAMADA, Y. et al. Reconsiderations on singularity or crack tip elements. **International Journal for Numerical Methods in Engineering**, Wiley, v. 14, n. 10, p. 1525–1544, 1979. DOI: 10.1002/nme.1620141008.

YEHIA, Nabil A. B.; SHEPHARD, Mark S. On the effect of quarter-point element size on fracture criteria. **International Journal for Numerical Methods in Engineering**, Wiley, v. 21, n. 10, p. 1911–1924, Oct. 1985. DOI: 10.1002/nme.1620211014.

YU, Hongjun; WU, Linzhi; GUO, Licheng, et al. Investigation of mixed-mode stress intensity factors for nonhomogeneous materials using an interaction integral method. **International Journal of Solids and Structures**, Elsevier BV, v. 46, n. 20, p. 3710–3724, Oct. 2009. DOI: 10.1016/j.ijsolstr.2009.06.019.

YU, Hongjun; WU, Linzhi; LI, Hui. T-stress evaluations of an interface crack in the materials with complex interfaces. **International Journal of Fracture**, Springer Science and Business Media LLC, v. 177, n. 1, p. 25–37, July 2012. DOI: 10.1007/s10704-012-9747-6.

ZHOU, Wei et al. The boundary element method for elasticity problems with concentrated loads based on displacement singular elements. **Engineering Analysis with Boundary Elements**, Elsevier BV, v. 99, p. 195–205, Feb. 2019. DOI: 10.1016/j.enganabound.2018.11.016.

ZHUANG, X.; AUGARDE, C.E.; MATHISEN, K.M. Fracture modeling using meshless methods and level sets in 3D: Framework and modeling. **International Journal for Numerical Methods in Engineering**, Wiley, v. 92, n. 11, p. 969–998, June 2012. DOI: 10.1002/nme.4365.

A Stress and displacement functions for interface cracks

When n is odd, the stress functions $\Sigma_{ij}^n(\theta,s)$ and $\Upsilon_{ij}^n(\theta,s)$ in Eq. (3.46) can be written as follows:

$$\Sigma_{11}^n(\theta,s)=\frac{1}{\cosh\pi\varepsilon}\left\{-\left[\sinh\left(\varepsilon(\Pi_s-\theta)\right)-e^{-\varepsilon(\Pi_s-\theta)}\right]\cos\frac{n-2}{2}\theta-\frac{1}{2}e^{-\varepsilon(\Pi_s-\theta)}\sin\theta\left[(n-2)\sin\frac{n-4}{2}\theta-2\varepsilon\cos\frac{n-4}{2}\theta\right]\right\}$$

$$\Sigma_{12}^n(\theta,s)=\frac{1}{\cosh\pi\varepsilon}\left\{\sinh\left(\varepsilon(\Pi_s-\theta)\right)\sin\frac{n-2}{2}\theta-\frac{1}{2}e^{-\varepsilon(\Pi_s-\theta)}\sin\theta\left[(n-2)\cos\frac{n-4}{2}\theta+2\varepsilon\sin\frac{n-4}{2}\theta\right]\right\}$$

$$\Sigma_{22}^n(\theta,s)=\frac{1}{\cosh\pi\varepsilon}\left\{\left[\sinh\left(\varepsilon(\Pi_s-\theta)\right)+e^{-\varepsilon(\Pi_s-\theta)}\right]\cos\frac{n-2}{2}\theta+\frac{1}{2}e^{-\varepsilon(\Pi_s-\theta)}\sin\theta\left[(n-2)\sin\frac{n-4}{2}\theta-2\varepsilon\cos\frac{n-4}{2}\theta\right]\right\}$$

$$\Upsilon_{11}^n(\theta,s)=\frac{1}{\cosh\pi\varepsilon}\left\{\left[\cosh\left(\varepsilon(\Pi_s-\theta)\right)+e^{-\varepsilon(\Pi_s-\theta)}\right]\sin\frac{n-2}{2}\theta+\frac{1}{2}e^{-\varepsilon(\Pi_s-\theta)}\sin\theta\left[(n-2)\cos\frac{n-4}{2}\theta+2\varepsilon\sin\frac{n-4}{2}\theta\right]\right\}$$

$$\Upsilon_{12}^n(\theta,s)=\frac{1}{\cosh\pi\varepsilon}\left\{\cosh\left(\varepsilon(\Pi_s-\theta)\right)\cos\frac{n-2}{2}\theta-\frac{1}{2}e^{-\varepsilon(\Pi_s-\theta)}\sin\theta\left[(n-2)\sin\frac{n-4}{2}\theta-2\varepsilon\cos\frac{n-4}{2}\theta\right]\right\}$$

$$\Upsilon_{22}^n(\theta,s)=\frac{1}{\cosh\pi\varepsilon}\left\{-\left[\cosh\left(\varepsilon(\Pi_s-\theta)\right)-e^{-\varepsilon(\Pi_s-\theta)}\right]\sin\frac{n-2}{2}\theta-\frac{1}{2}e^{-\varepsilon(\Pi_s-\theta)}\sin\theta\left[(n-2)\cos\frac{n-4}{2}\theta+2\varepsilon\sin\frac{n-4}{2}\theta\right]\right\}$$

where $s=1,2$ indicates the upper and lower materials, respectively, and $\Pi_1=\pi$ and $\Pi_2=-\pi$:

When n is even, the stress functions are obtained by:

$$\Sigma_{11}^n(\theta,s)=\frac{1}{1+\omega_s}\left\{4\cos\frac{n-2}{2}\theta-(n-2)\sin\theta\sin\frac{n-4}{2}\theta\right\}$$

$$\Sigma_{12}^n(\theta,s)=\frac{1}{1+\omega_s}\left\{-2\sin\frac{n-2}{2}\theta-(n-2)\sin\theta\cos\frac{n-4}{2}\theta\right\}$$

$$\Sigma_{22}^n(\theta,s)=\frac{1}{1+\omega_s}\left\{(n-2)\sin\theta\sin\frac{n-4}{2}\theta\right\}$$

$$\Upsilon_{11}^n(\theta,s)=\frac{1}{1+\omega_s}\left\{2\sin\frac{n-2}{2}\theta+(n-2)\sin\theta\cos\frac{n-4}{2}\theta\right\}$$

$$\Upsilon_{12}^n(\theta,s)=\frac{1}{1+\omega_s}\left\{-(n-2)\sin\theta\sin\frac{n-4}{2}\theta\right\}$$

$$\Upsilon_{22}^n(\theta,s)=\frac{1}{1+\omega_s}\left\{2\sin\frac{n-2}{2}\theta-(n-2)\sin\theta\cos\frac{n-4}{2}\theta\right\}$$

where $\omega_1 = [(\kappa_1+1)\,\mu_2]\,/\,[(\kappa_2+1)\,\mu_1]$ and $\omega_2 = [(\kappa_2+1)\,\mu_1]\,/\,[(\kappa_1+1)\,\mu_2]$.

When n is odd, the displacement functions $\Delta_j^n(\theta,s)$ and $\Theta_j^n(\theta,s)$ in Eq. (3.48) are given by:

$$\Delta_1^n(\theta,s) = -\frac{1}{\mu_s\,(n^2+4\varepsilon^2)\cosh(\pi\varepsilon)}\left\{n\left[\sinh(\varepsilon(\Pi_s-\theta)) - \frac{\kappa_s-1}{2}e^{-\varepsilon(\Pi_s-\theta)}\right]\cos\frac{n\theta}{2} + \right.$$
$$\left. +\frac{1}{2}\left(n^2+4\varepsilon^2\right)e^{-\varepsilon(\Pi_s-\theta)}\sin\theta\sin\frac{n-2}{2}\theta + 2\varepsilon\left[\cosh(\varepsilon(\Pi_s-\theta)) + \frac{\kappa_s-1}{2}e^{-\varepsilon(\Pi_s-\theta)}\right]\sin\frac{n\theta}{2}\right\}$$

$$\Delta_2^n(\theta,s) = \frac{1}{\mu_s\,(n^2+4\varepsilon^2)\cosh(\pi\varepsilon)}\left\{n\left[\cosh(\varepsilon(\Pi_s-\theta)) + \frac{\kappa_s-1}{2}e^{-\varepsilon(\Pi_s-\theta)}\right]\sin\frac{n\theta}{2} + \right.$$
$$\left. -\frac{1}{2}\left(n^2+4\varepsilon^2\right)e^{-\varepsilon(\Pi_s-\theta)}\sin\theta\cos\frac{n-2}{2}\theta - 2\varepsilon\left[\sinh(\varepsilon(\Pi_s-\theta)) - \frac{\kappa_s-1}{2}e^{-\varepsilon(\Pi_s-\theta)}\right]\cos\frac{n\theta}{2}\right\}$$

$$\Theta_1^n(\theta,s) = \frac{1}{\mu_s\,(n^2+4\varepsilon^2)\cosh(\pi\varepsilon)}\left\{n\left[\cosh(\varepsilon(\Pi_s-\theta)) + \frac{\kappa_s-1}{2}e^{-\varepsilon(\Pi_s-\theta)}\right]\sin\frac{n\theta}{2} + \right.$$
$$\left. +\frac{1}{2}\left(n^2+4\varepsilon^2\right)e^{-\varepsilon(\Pi_s-\theta)}\sin\theta\cos\frac{n-2}{2}\theta - 2\varepsilon\left[\sinh(\varepsilon(\Pi_s-\theta)) - \frac{\kappa_s-1}{2}e^{-\varepsilon(\Pi_s-\theta)}\right]\cos\frac{n\theta}{2}\right\}$$

$$\Theta_2^n(\theta,s) = \frac{1}{\mu_s\,(n^2+4\varepsilon^2)\cosh(\pi\varepsilon)}\left\{n\left[\sinh(\varepsilon(\Pi_s-\theta)) - \frac{\kappa_s-1}{2}e^{-\varepsilon(\Pi_s-\theta)}\right]\cos\frac{n\theta}{2} + \right.$$
$$\left. -\frac{1}{2}\left(n^2+4\varepsilon^2\right)e^{-\varepsilon(\Pi_s-\theta)}\sin\theta\sin\frac{n-2}{2}\theta + 2\varepsilon\left[\cosh(\varepsilon(\Pi_s-\theta)) + \frac{\kappa_s-1}{2}e^{-\varepsilon(\Pi_s-\theta)}\right]\sin\frac{n\theta}{2}\right\}$$

For n even, the displacement functions are expressed by:

$$\Delta_1^n(\theta,s) = \frac{1}{\mu_s n\,(1+\omega_s)}\left[(\kappa_s+1)\cos\frac{n\theta}{2} - n\sin\theta\sin\frac{n-2}{2}\theta\right]$$

$$\Delta_2^n(\theta,s) = \frac{1}{\mu_s n\,(1+\omega_s)}\left[(\kappa_s-1)\sin\frac{n\theta}{2} - n\sin\theta\cos\frac{n-2}{2}\theta\right]$$

$$\Theta_1^n(\theta,s) = \frac{1}{\mu_s n\,(1+\omega_s)}\left[(\kappa_s-1)\sin\frac{n\theta}{2} + n\sin\theta\cos\frac{n-2}{2}\theta\right]$$

$$\Theta_2^n(\theta,s) = \frac{1}{\mu_s n\,(1+\omega_s)}\left[-(\kappa_s+1)\cos\frac{n\theta}{2} - n\sin\theta\sin\frac{n-2}{2}\theta\right]$$

B Fundamental solutions

B.1 Isotropic

Equations (2.1), (2.2) and (2.8) can be grouped to obtain Navier's equation as follows:

$$\frac{1}{1-2\nu}u_{j,ji} + u_{i,jj} + \frac{b_i}{\mu} = 0 \tag{B.1}$$

For a point-force problem ($b_i^* = \Delta(\mathbf{x}', \mathbf{x})e_i$), a displacement solution field that satisfies Eq. (B.1) is $u_i^* = U_{ij}^*(\mathbf{x}', \mathbf{x})e_i$, in which:

$$U_{ij}^*(\mathbf{x}', \mathbf{x}) = \frac{1}{8\pi\mu\,(1-\nu)}\left[(3-4\nu)\ln\left(\frac{1}{r}\right)\delta_{ij} + r_{,i}r_{,j}\right] \tag{B.2}$$

represents the displacement fundamental solution, with $r \coloneqq \|\mathbf{x} - \mathbf{x}'\|$ being the distance between the field point and the source point. Besides, the distance derivatives in Eq. B.2 are evaluated as:

$$r_{,i} = \frac{\partial r}{\partial x_i} = \frac{x_i - x_i'}{r} \tag{B.3}$$

The traction fundamental solution is determined from the U_{ij}^* derivatives by means of Eqs. (2.2), (2.8) and (2.12):

$$P_{ij}^*(\mathbf{x}', \mathbf{x}) = -\frac{1}{4\pi\,(1-\nu)\,r}\left\{(1-2\nu)\,(r_{,j}n_i - r_{,i}n_j) + r_{,n}\left[(1-2\nu)\,\delta_{ij} + 2r_{,i}r_{,j}\right]\right\} \tag{B.4}$$

where:

$$r_{,n} = \frac{\partial r}{\partial n} = r_{,m}n_m \tag{B.5}$$

Finally, the fundamental solutions presented in the TBIE are obtained from the derivatives of U_{ij}^* and P_{ij}^*, and they are given by:

$$D_{kij}^*(\mathbf{x}', \mathbf{x}) = \frac{1}{4\pi\,(1-\nu)\,r}\left[(1-2\nu)\,(r_{,i}\delta_{jk} + r_{,j}\delta_{ik} - r_{,k}\delta_{ij}) + 2r_{,i}r_{,j}r_{,k}\right] \tag{B.6}$$

$$\begin{aligned} S_{kij}^*(\mathbf{x}', \mathbf{x}) = \frac{\mu}{2\pi\,(1-\nu)\,r^2}\Bigg\{2\frac{\partial r}{\partial n}\left[(1-2\nu)\,r_{,k}\delta_{ij} + \nu\,(r_{,i}\delta_{jk} + r_{,j}\delta_{ik}) - 4r_{,i}r_{,j}r_{,k}\right] + \\ +2\nu\,(n_i r_{,j}r_{,k} + n_j r_{,i}r_{,k}) + (1-2\nu)\,(2n_k r_{,i}r_{,j} + n_i\delta_{jk} + n_j\delta_{ik}) - (1-4\nu)\,n_k\delta_{ij}\Bigg\} \end{aligned} \tag{B.7}$$

The above fundamental solutions are valid for plane strain conditions. For plane stress problems, these solutions may be used with the modified Young's modulus and Poisson's ratio:

$$\bar{E} = E\left[1 - \left(\frac{\nu}{1+\nu}\right)^2\right] \tag{B.8}$$

$$\bar{\nu} = \frac{\nu}{1+\nu} \tag{B.9}$$

B.2 Anisotropic

For anisotropic materials, the fundamental solutions are expressed in terms of the difference between the positions of source point and the field point in a complex plane, which are defined as:

$$z_i = x_1 + \mu_i x_2 \tag{B.10}$$

where μ_i represents the material complex parameters with positive imaginary part given by the roots of the following characteristic equation:

$$c_{11}\mu^4 - 2c_{16}\mu^3 + (2c_{12} + c_{66})\,\mu^2 - 2c_{26}\mu + c_{22} = 0 \tag{B.11}$$

The coefficients c_{ij} in Eq. (B.11) are the values of the elastic compliance tensor presented in Eq. (2.13).

Based on the Lekhnitskii formalism (LEKHNITSKII, 1968), Cruse and Swedlow (1971) obtained the fundamental solutions for the point force problem considering anisotropic materials. These solutions are expressed by:

$$U^*_{ij}(\mathbf{x}', \mathbf{x}) = 2\Re\left[q_{jl} b_{il} \ln \hat{r}\right] \tag{B.12}$$

$$P^*_{ij}(\mathbf{x}', \mathbf{x}) = 2\Re\left[g_{jl} b_{il} \frac{\mu_l n_1 - n_2}{\hat{r}}\right] \tag{B.13}$$

where:

$$\hat{r} := z_l - z'_l, \tag{B.14}$$

$\Re$ denotes the real part operator, q_{jl} and g_{jl} are defined as:

$$q_{jl} = c_{j1}\mu_l^{3-j} - c_{j6}\mu_l^{2-j} + c_{j2}\mu_l^{1-j} \tag{B.15}$$

$$g_{jl} = \delta_{1j}\mu_l - \delta_{2j} \tag{B.16}$$

and b_{il} are given by the solution of the following system of linear equations with complex coefficients:

$$\begin{bmatrix} 1 & -1 & 1 & -1 \\ \mu_1 & -\bar{\mu}_1 & \mu_2 & -\bar{\mu}_2 \\ q_{11} & -\bar{q}_{11} & q_{12} & -\bar{q}_{12} \\ q_{21} & -\bar{q}_{21} & q_{22} & -\bar{q}_{22} \end{bmatrix} \begin{Bmatrix} b_{i1} \\ \bar{b}_{i1} \\ b_{i2} \\ \bar{b}_{i2} \end{Bmatrix} = \begin{Bmatrix} \frac{\delta_{i2}}{2\pi\mathrm{i}} \\ -\frac{\delta_{i1}}{2\pi\mathrm{i}} \\ 0 \\ 0 \end{Bmatrix} \tag{B.17}$$

in which the over-bar indicates the complex conjugate and $\mathrm{i} = \sqrt{-1}$ is the imaginary unit.

Regarding the TBIE, the components of fundamental solution D^*_{kij} for anisotropic materials are defined by:

$$\begin{Bmatrix} D^*_{k1} \\ D^*_{k2} \\ D^*_{k6} \end{Bmatrix} = \begin{bmatrix} a_{11} & a_{12} & a_{16} \\ a_{21} & a_{22} & a_{26} \\ a_{61} & a_{62} & a_{66} \end{bmatrix} \begin{Bmatrix} \varepsilon^*_{k1} \\ \varepsilon^*_{k2} \\ \varepsilon^*_{k6} \end{Bmatrix} \tag{B.18}$$

where the index transformation $\alpha \leftrightarrow ij$ (2.7) was used, with $\alpha = 1, 2, 6$. The coefficients a_{ij} represent the components of the elastic stiffness tensor, and $\varepsilon^*_{k\alpha}$ is obtained from the derivatives of U^*_{ij} as:

$$\varepsilon_{k\alpha} = \varepsilon_{kij} = -\Re\left\{\frac{q_{kl}}{\hat{r}}\left[b_{il}\left(\delta_{1j} + \mu_l\delta_{2j}\right) + b_{jl}\left(\delta_{1i} + \mu_l\delta_{2i}\right)\right]\right\} \tag{B.19}$$

Analogously, the fundamental solution S^*_{kij} can be determined. In this case, the derivatives of P^*_{ij} are used, resulting in:

$$\begin{Bmatrix} S^*_{k1} \\ S^*_{k2} \\ S^*_{k6} \end{Bmatrix} = \begin{bmatrix} a_{11} & a_{12} & a_{16} \\ a_{21} & a_{22} & a_{26} \\ a_{61} & a_{62} & a_{66} \end{bmatrix} \begin{Bmatrix} \rho^*_{k1} \\ \rho^*_{k2} \\ \rho^*_{k6} \end{Bmatrix} \tag{B.20}$$

with:

$$\rho_{k\alpha} = \rho_{kij} = -\Re\left\{g_{kl}\frac{\mu_l n_1 - n_2}{\hat{r}^2}\left[b_{il}\left(\delta_{1j} + \mu_l\delta_{2j}\right) + b_{jl}\left(\delta_{1i} + \mu_l\delta_{2i}\right)\right]\right\} \tag{B.21}$$

C Evaluation of BEM integrals

The strategy used to evaluate the integrals in the DBEM and IGABEM formulations depends on the distance between the source point and the integrated element since the fundamental solutions become singular as this distance approaches zero. Three different procedures are adopted in this work and their fundamentals, as well as their scope of application, are presented in what follows.

Before proceeding, the expressions presented in integral kernels can be rewritten in a general form as follows:

$$I^{em} = \int_{-1}^{1} F^{em}(\mathbf{x}', \mathbf{x}(\xi)) d\xi \tag{C.1}$$

in which F^{em} contains the product between the respective fundamental solution, the shape functions and the Jacobian of transformation.

Note that for the isogeometric approach, the parameter ξ in the following equations is simply substituted by $\hat{\xi}$.

C.1 Regular integrands

When the source point is far from the integrated element, the integrands represented by Eq. (C.1) are regular. In this case, the standard Gauss-Legendre quadrature is applied for numerical integration as follows:

$$I^{em} \approx \sum_{n=1}^{N_g} F^{em}(\mathbf{x}', \mathbf{x}(\xi_n)) \omega_n \tag{C.2}$$

where ξ_n and ω_n are, respectively, the non-dimensional coordinate and weight associated with the n-th integration point, and N_g is the number of integration points.

C.2 Quasi-singular integrands

When the integrated element is near the source point, the kernels represented by Eq. (C.1) become quasi-singular because of the dominant effect of the fundamental solutions. In this situation, the accuracy of the numerical integration is compromised when the standard Gauss-Legendre quadrature is applied. To overcome this deficiency, Telles (1987) and Telles and Oliveira (1994) proposed a third-degree polynomial transformation for the integration points coordinates. In this transformation, the integration points along the element are lumped toward the source point, improving the accuracy of the numerical evaluation of quasi-singular integrals. The new integration points coordinates ς are ob-

tained from the non-dimensional coordinates ξ of the integration points by the following expression:

$$\varsigma(\xi) = a_0 + a_1\xi + a_2\xi^2 + a_3\xi^3 \tag{C.3}$$

with a_i representing the transformation coefficients. To obtain the values of a_i, the minimum distance R_{min} between the source point and the integrated element is first determined. The non-dimensional coordinate associated to the point of minimum distance along the element is defined as $\bar{\varsigma}$. Then, a non-dimensional distance D is computed as follows:

$$D = \frac{2R_{min}}{L} \tag{C.4}$$

where L is the length of the integrated element. With D, the parameter $\bar{r}$ that is associated with the Jacobian of the transformation of Eq. (C.3) at $\bar{\varsigma}$ is obtained from the following relations:

$$\bar{r} = \begin{cases} 2.620D, & 0 < D \leq 0.05 \\ 0.85 + 0.24\ln D, & 0.05 < D \leq 1.3 \\ 0.893 + 0.0832\ln D, & 1.3 < D \leq 3.618 \\ 1, & D > 3.618 \end{cases} \tag{C.5}$$

Finally, the coefficients a_i are given by the solution of the following system of equations:

$$\begin{bmatrix} 1 & 1 & 1 & 1 \\ 1 & -1 & 1 & -1 \\ 0 & 1 & 2\bar{\xi} & 3\bar{\xi}^2 \\ 0 & 0 & 2 & 6\bar{\xi} \end{bmatrix} \begin{Bmatrix} a_0 \\ a_1 \\ a_2 \\ a_3 \end{Bmatrix} = \begin{Bmatrix} 1 \\ -1 \\ \bar{r} \\ 0 \end{Bmatrix} \tag{C.6}$$

in which $\bar{\xi}$ is the non-dimension coordinate corresponding to $\bar{\varsigma}$ in the third-degree transformation. This coordinate can be computed by:

$$\bar{\xi} = \sqrt[3]{-q + \sqrt{(q^2 + p^3)}} + \sqrt[3]{-q - \sqrt{(q^2 + p^3)}} + \frac{\bar{\varsigma}}{1 + 2\bar{r}} \tag{C.7}$$

where:

$$q = \frac{\bar{\varsigma}}{2\left(1 + 2\bar{r}\right)} \left\{ \frac{1}{1 + 2\bar{r}} \left[(3 - 2\bar{r}) - \frac{2\bar{\varsigma}^2}{1 + 2\bar{r}} \right] - 1 \right\} \tag{C.8}$$

$$p = \frac{1}{3\left(1 + 2\bar{r}\right)^2} \left[4\bar{r}\left(1 - \bar{r}\right) + 3\left(1 - \bar{\varsigma}^2\right) \right] \tag{C.9}$$

The solution of Eq. (C.6) gives:

$$\begin{aligned} a_0 &= 3k\left(1-\bar{r}\right)\bar{\xi} \\ a_1 &= k\left(\bar{r}+3\bar{\xi}^2\right) \\ a_2 &= -a_0 \\ a_3 &= k\left(1-\bar{r}\right) \end{aligned} \tag{C.10}$$

where $k = 1/\left(1+3\bar{\xi}^2\right)$:

Hence, the integrals expressed by Eq. (C.1) can be evaluated as follows:

$$I^{em} \approx \sum_{n=1}^{N_g} F^{em}(\mathbf{x}', \mathbf{x}(\varsigma(\xi_n)) J^t(\xi_n)\omega_n \tag{C.11}$$

in which J^t is the Jacobian of the third-degree polynomial transformation given by:

$$J^t(\xi) = a_1 + 2a_2\xi + 3a_3\xi^2 \tag{C.12}$$

From the above expressions, it can be noted that if $\bar{r} = 1$ the third-degree polynomial transformation degenerates into $\varsigma = \xi$ with $J^t(\xi) = 1$, i.e., the standard Gauss-Legendre quadrature is recovered. This values of $\bar{r}$ is obtained for $D > 3.618$, as shown by Eq. (C.5). Therefore, $D = 3.618$ can be defined as a threshold value to state if an element is far or near the source point, for which the standard Gauss-Legendre quadrature or the third-degree transformation are used, respectively.

C.3 Singular integrands

When integrating an element that contains the source point, the integrand in Eq. (C.1) must be firstly regularised. For the weakly singular kernel U_{ij}^{em}, Telles' transformation can be used for regularisation. For the strongly singular and hypersingular integrals, a special integration scheme should be considered. For this purpose, the singularity subtraction method (SSM) may be used. In what follows, the expressions implemented for isotropic materials are presented. For anisotropic materials, it is only necessary to substitute r by $\hat{r}$ in the expressions (see Appendix B for more details).

To proceed with the SSM, the following auxiliary coordinate is defined:

$$\eta(\xi', \xi) = J^e(\xi')\left(\xi - \xi'\right) \tag{C.13}$$

where ξ' and $J^e(\xi')$ are, respectively, the parametric coordinate and the Jacobian at the source point. The value of η can be interpreted as a signed distance along a supporting line tangent to the boundary at the source point.

The kernel P_{ij}^{em} (2.40) from the DBIE can be rewritten as:

$$P_{ij}^{em} = \int_{-1}^{1} \frac{\bar{P}_{ij}^{*}(\xi', \xi)}{r(\xi', \xi)} \phi^{em}(\xi) J^{e}(\xi) d\xi \tag{C.14}$$

where $\bar{P}_{ij}^{*} = rP_{ij}^{*}$ is the regular part of the traction fundamental solution.

The SSM can be applied in Eq. (C.14) to remove the singularity from P_{ij}^{em}. For this purpose, a kernel with the same order of singularity, now expressed in terms of the auxiliary coordinate η, is added and subtracted from the integrand as follows:

$$P_{ij}^{em} = \int_{-1}^{1} \frac{\bar{P}_{ij}^{*}(\xi', \xi)}{r(\xi', \xi)} \phi^{em}(\xi) J^{e}(\xi) - \frac{\bar{P}_{ij}^{*}(\xi')}{\eta(\xi', \xi)} \phi^{em}(\xi') J^{e}(\xi') d\xi + \int_{-1}^{1} \frac{\bar{P}_{ij}^{*}(\xi')}{\eta(\xi', \xi)} \phi^{em}(\xi') J^{e}(\xi') d\xi \tag{C.15}$$

where $\bar{P}_{ij}^{*}(\xi')$ is determined from $\bar{P}_{ij}^{*}(\xi', \xi)$ when $\xi \to \xi'$ and expressed by:

$$\bar{P}_{ij}^{*}(\xi') = -\frac{1 - 2\nu}{4\pi(1 - \nu)} \left(n_i' r_{,j}' - n_j' r_{,i}' \right) \tag{C.16}$$

in which n_i' and $r_{,i}'$ denote, respectively, the components of outward normal vector and the distance derivatives at the source point, with $r_{,1}' = -n_2'$ and $r_{,2}' = n_1'$.

Substituting the definition of η (Eq. (C.13)) in Eq. (C.15) leads to:

$$P_{ij}^{em} = \int_{-1}^{1} \frac{\bar{P}_{ij}^{*}(\xi', \xi)}{r(\xi', \xi)} \phi^{em}(\xi) J^{e}(\xi) - \frac{\bar{P}_{ij}^{*}(\xi')}{\xi - \xi'} \phi^{em}(\xi') d\xi + \bar{P}_{ij}^{*}(\xi') \phi^{em}(\xi') \int_{-1}^{1} \frac{1}{\xi - \xi'} d\xi \tag{C.17}$$

The first integral on the right-hand side of Eq. (C.15) is regular and can be computed with standard Gauss-Legendre quadrature. The second integral can be evaluated analytically to give the Cauchy principal value, CPV, as follows:

$$CPV = \int_{-1}^{1} \frac{1}{\xi - \xi'} d\xi = \ln \left| \frac{1 - \xi'}{1 + \xi'} \right| \tag{C.18}$$

The expression in Eq. (C.18) is valid for $|\xi'| \neq 1$, i.e., when the source point is not between continuous elements. Otherwise, the Cauchy principal value is given by (GUIGGIANI; CASALINI, 1987):

$$CPV = -\text{sign}(\xi') \ln \left(2J^{e}(\xi') \right) \tag{C.19}$$

Regarding the TBIE, the kernel D_{kij}^{em} (2.44) can be evaluated in a similarly to P_{ij}^{em} since both have the same order of singularity $\mathcal{O}(r^{-1})$. For S_{kij}^{em} (2.43), it can be firstly rewritten as:

$$S_{kij}^{em} = \int_{-1}^{1} \frac{\bar{S}_{kij}^{*}(\xi', \xi)}{r^2(\xi', \xi)} \phi^{em}(\xi) J^{e}(\xi) d\xi \tag{C.20}$$

where $\bar{S}^*_{kij} = r^2 S^*_{kij}$ is the regular part of the fundamental solution.

The integrand in Eq. (C.20) can be regularised by the SSM considering the first-order Taylor expansion around ξ' for the shape functions, resulting in:

$$S^{em}_{kij} = \int_{-1}^{1} \frac{\bar{S}^*_{kij}(\xi',\xi)}{r^2(\xi',\xi)}\phi^{em}(\xi)J^e(\xi) - \frac{\bar{S}^*_{kij}(\xi')}{\eta^2(\xi',\xi)}\left[\phi^{em}(\xi') + \frac{d\phi^{em}}{d\xi}(\xi')\,(\xi-\xi')\right]J^e(\xi')d\xi + \\ + \oint_{-1}^{1} \frac{\bar{S}^*_{kij}(\xi')}{\eta^2(\xi',\xi)}\left[\phi^{em}(\xi') + \frac{d\phi^{em}}{d\xi}(\xi')\,(\xi-\xi')\right]J^e(\xi')d\xi \tag{C.21}$$

where $\bar{S}^*_{kij}(\xi')$ is obtained from $\bar{S}^*_{kij}(\xi',\xi)$ when $\xi \to \xi'$ as:

$$\bar{S}^*_{kij}(\xi') = \frac{\mu}{2\pi\,(1-\nu)\,r^2}\left[2\nu\,(n_i r_{,j} r_{,k} + n_j r_{,i} r_{,k}) + (1-2\nu)\,(2n_k r_{,i} r_{,j} + n_i\delta_{jk} + n_j\delta_{ik}) + \right. \\ \left. - (1-4\nu)\,n_k\delta_{ij}\right] \tag{C.22}$$

Substituting Eq. (C.13) in Eq. (C.21) results in:

$$S^{em}_{kij} = \int_{-1}^{1} \frac{\bar{S}^*_{kij}(\xi',\xi)}{r^2(\xi',\xi)}\phi^{em}(\xi)J^e(\xi) - \frac{\bar{S}^*_{kij}(\xi')}{J^e(\xi')\,(\xi-\xi')}\left[\frac{\phi^{em}(\xi')}{(\xi-\xi')} + \frac{d\phi^{em}}{d\xi}(\xi')\right]d\xi + \\ + \frac{\bar{S}^*_{kij}(\xi')}{J^e(\xi')}\left[\phi^{em}(\xi')\oint_{-1}^{1}\frac{1}{(\xi-\xi')^2}d\xi + \frac{d\phi^{em}}{d\xi}(\xi')\int_{-1}^{1}\frac{1}{\xi-\xi'}d\xi\right] \tag{C.23}$$

Again, the first integral on the right-hand side of Eq. (C.23) can be evaluated numerically with Gauss-Legendre quadrature. The last integral corresponds to the Cauchy principal value presented in Eq. (C.18), while the second represents the Hadamard finite-part given by:

$$HFP = \oint_{-1}^{1}\frac{1}{(\xi-\xi')^2}d\xi = -\frac{1}{1-\xi'} - \frac{1}{1+\xi'} \tag{C.24}$$

D Evaluation of enriched singular integrands

D.1 Crack tip enrichment

The SSM can also be used to evaluate the kernels $\tilde{P}_{iM}^{e\lambda}$ and $\tilde{S}_{ijM}^{em}$ to singular elements. In this case, the equations obtained are similar to Eqs. (C.17) and (C.23), in which the shape functions ϕ^{em} are replaced by the shifted enrichment functions $Z_{jM}^{e\lambda}$ given by:

$$Z_{jM}^{e\lambda}\left(\mathbf{x}^{\lambda},\mathbf{x}(\xi)\right)=R_{jk}^{\lambda}\sum_{m=1}^{n_e}\phi^{em}(\xi)\left[\psi_{kM}\left(\mathbf{x}^{\lambda},\mathbf{x}(\xi)\right)-\psi_{kM}\left(\mathbf{x}^{\lambda},\mathbf{x}(\xi^{m})\right)\right] \tag{D.1}$$

when considering the shifted enrichment function in Eq. (4.5), or by

$$Z_{jM}^{e\lambda}\left(\mathbf{x}^{\lambda},\mathbf{x}(\xi)\right)=R_{jk}^{\lambda}\psi_{kM}\left(\mathbf{x}^{\lambda},\mathbf{x}(\xi)\right) \tag{D.2}$$

when considering the enriched approximation in Eq. (5.31).

Therefore, $\tilde{P}_{iM}^{e\lambda}$ becomes:

$$\begin{aligned}\tilde{P}_{iM}^{e\lambda}=&\int_{-1}^{1}\frac{\bar{P}_{ij}^{*}(\xi',\xi)}{r(\xi',\xi)}Z_{jM}^{e\lambda}\left(\mathbf{x}^{\lambda},\mathbf{x}(\xi)\right)J^{e}(\xi)-\frac{\bar{P}_{ij}^{*}(\xi')}{\xi-\xi'}Z_{jM}^{e\lambda}\left(\mathbf{x}^{\lambda},\mathbf{x}(\xi')\right)d\xi+\\&+\bar{P}_{ij}^{*}(\xi')Z_{jM}^{e\lambda}\left(\mathbf{x}^{\lambda},\mathbf{x}(\xi')\right)CPV\end{aligned} \tag{D.3}$$

Equation (D.3) can be used to evaluate the strongly singular kernel when the enrichments used in the XIGABEM are considered. On the other hand, when considering the shifted enrichment functions in the proposed XBEM formulations, $Z_{jM}^{e\lambda}\left(\mathbf{x}^{\lambda},\mathbf{x}(\xi')\right)=0$ since the enrichment function is null at the source points. Hence, $\tilde{P}_{iM}^{e\lambda}$ is simplified to:

$$\tilde{P}_{iM}^{e\lambda}=\fint_{-1}^{1}\frac{\bar{P}_{ij}^{*}(\xi',\xi)}{r(\xi',\xi)}Z_{jM}^{e\lambda}\left(\mathbf{x}^{\lambda},\mathbf{x}(\xi)\right)J^{e}(\xi)d\xi \tag{D.4}$$

The adopted shifted enrichment in XBEM makes $\tilde{P}_{iM}^{e\lambda}$ regular and, therefore, this kernel can be evaluated with the Gauss-Legendre quadrature even for elements containing the source point.

Proceeding in a similar fashion to obtain $\tilde{S}_{ijM}^{em}$, the following expression is derived:

$$\hat{S}^{e\lambda}_{ijM} = \int_{-1}^{1} \frac{\bar{S}^{*}_{kij}(\xi',\xi)}{r^2(\xi',\xi)} Z^{e\lambda}_{kM}\left(\mathbf{x}^{\lambda},\mathbf{x}(\xi)\right) J^{e}(\xi) - \frac{\bar{S}^{*}_{kij}(\xi')}{J^{e}(\xi')\,(\xi-\xi')}\left[\frac{Z^{e\lambda}_{kM}\left(\mathbf{x}^{\lambda},\mathbf{x}(\xi')\right)}{(\xi-\xi')} + Z^{e\lambda}_{kM,\xi}\left(\mathbf{x}^{\lambda},\mathbf{x}(\xi')\right)\right] d\hat{\xi} + \tag{D.5}$$

$$+ \frac{\bar{S}^{*}_{kij}(\hat{\xi}')}{J^{e}(\hat{\xi}')}\left[Z^{e\lambda}_{kM}\left(\mathbf{x}^{\lambda},\mathbf{x}(\xi')\right) HFP + Z^{e\lambda}_{kM,\xi}\left(\mathbf{x}^{\lambda},\mathbf{x}(\xi')\right) CPV\right]$$

which can be used for evaluation of the enriched hypersingular kernel in XIGABEM. The derivatives $Z^{e\lambda}_{kM,\xi}$ in this case are computed from:

$$Z^{e\lambda}_{jM,\xi} = \frac{dZ^{e\lambda}_{jM}}{d\xi} = R^{\lambda}_{jk}\left(\frac{\partial\psi_{kM}}{\partial\rho}\frac{d\rho}{d\xi} + \frac{\partial\psi_{kM}}{\partial\theta}\frac{d\theta}{d\xi}\right) \tag{D.6}$$

When the shifted enrichment is considered, Eq. (D.5) reduces to:

$$\tilde{S}^{e\lambda}_{ijM} = \int_{-1}^{1} \frac{\bar{S}^{*}_{kij}(\xi',\xi)}{r^2(\xi',\xi)} Z^{e\lambda}_{kM}\left(\mathbf{x}^{\lambda},\mathbf{x}(\xi)\right) J^{e}(\xi) - \frac{\bar{S}^{*}_{kij}(\xi')}{J^{e}(\xi')\,(\xi-\xi')} Z^{e\lambda}_{kM,\xi}\left(\mathbf{x}^{\lambda},\mathbf{x}(\xi')\right) d\xi + \tag{D.7}$$

$$+ \frac{\bar{S}^{*}_{kij}(\xi')}{J^{e}(\xi')} Z^{e\lambda}_{kM,\xi}\left(\mathbf{x}^{\lambda},\mathbf{x}(\xi')\right) \int_{-1}^{1} \frac{1}{\xi-\xi'} d\xi$$

in which the derivative $Z^{e\lambda}_{kM,\xi}$ can be determined by using the chain rule as follows:

$$Z^{e\lambda}_{jM,\xi} = \frac{dZ^{e\lambda}_{jM}}{d\xi} = R^{\lambda}_{jk}\sum_{m=1}^{n_e}\left[\frac{d\phi^{em}}{d\xi}\left(\psi^{\lambda}_{Mk} - \psi^{\lambda m}_{Mk}\right) + \phi^{em}\left(\frac{\partial\psi^{\lambda}_{Mk}}{\partial\rho}\frac{d\rho}{d\xi} + \frac{\partial\psi^{\lambda}_{Mk}}{\partial\theta}\frac{d\theta}{d\xi}\right)\right] \tag{D.8}$$

Note that if the parameter θ does not vary along the elements, as considered in the present study even for curved cracks, Eqs. (D.6) and (D.8) are simplified since $\frac{d\theta}{d\xi} = 0$.

D.2 Heaviside enrichment

To apply the SSM to evaluate $\hat{S}^{\bar{e}l}_{kij}$, we first rewrite the kernel as:

$$\hat{S}^{\bar{e}l}_{kij} = \neq\!\!\!\!\int_{-1}^{1} S^{*}_{kij}(\xi',\xi) J^{\bar{e}}(\xi) Y^{\bar{e}l}\left(\xi^{\bar{e}}_{P},\xi\right) d\xi \tag{D.9}$$

where $Y^{\bar{e}l}(\xi^{\bar{e}}_{P},\xi)$ is the discontinuous enrichment function given by:

$$Y^{\bar{e}l}(\xi^{\bar{e}}_{P},\xi) = g^{l}(\xi^{\bar{e}}_{P},\xi)\sum_{m=1}^{n_{\bar{e}}}\phi^{\bar{e}m}(\xi)\left[H(\xi^{\bar{e}}_{P},\xi) - H(\xi^{\bar{e}}_{P},\xi^{m})\right] \tag{D.10}$$

If the source point does not belong to the portion l, the integrand in Eq. (D.9) is regular and can be assessed with Eq. (4.24) or Eq. (4.25) if $\xi' \notin [\xi^{\bar{e}}_{P}, 1]$ or $\xi' \notin [-1, \xi^{\bar{e}}_{P}]$, respectively. Otherwise, the integration over the portion l is singular and singularity-

subtraction must be performed over Eq. (D.9) to give:

$$\hat{S}^{\bar{e}l}_{kij} = \int_{-1}^{1} \frac{\bar{S}^{*}_{kij}(\xi',\xi)}{r^2(\xi',\xi)} Y^{\bar{e}l}(\xi^{\bar{e}}_P,\xi) J^{\bar{e}}(\xi) - \frac{\bar{S}^{*}_{kij}(\xi')}{J^{\bar{e}}(\xi')\,(\xi-\xi')} Y^{\bar{e}l}_{,\xi}(\xi^{\bar{e}}_P,\xi') d\xi + \\ + \frac{\bar{S}^{*}_{kij}(\xi')}{J^{\bar{e}}(\xi')} Y^{\bar{e}l}_{,\xi}(\xi^{\bar{e}}_P,\xi') \fint_{-1}^{1} \frac{1}{\xi-\xi'} d\xi \tag{D.11}$$

in which the enrichment function derivative is determined as follows:

$$Y^{\bar{e}l}_{,\xi}(\xi^{\bar{e}}_P,\xi') = \frac{dY^{\bar{e}l}}{d\xi}(\xi^{\bar{e}}_P,\xi') = g^{l}(\xi^{\bar{e}}_P,\xi') \sum_{m=1}^{n_{\bar{e}}} \frac{d\phi^{\bar{e}m}}{d\xi} \left[H(\xi^{\bar{e}}_P,\xi') - H(\xi^{\bar{e}}_P,\xi^{m})\right] \tag{D.12}$$

Using the definition of $g^{l}(\xi^{\bar{e}}_P,\xi)$ (Eq. (4.17)) and observing that $g^{l}(\xi^{\bar{e}}_P,\xi') = 1$ for the singular portion, from Eq. (D.11) we obtain:

$$\hat{S}^{\bar{e}l}_{kij} = \int_{-1}^{1} \left[\frac{\bar{S}^{*}_{kij}(\xi',\xi(\eta))}{r^2(\xi',\xi(\eta))} Y^{\bar{e}l}(\xi^{\bar{e}}_P,\xi(\eta)) J^{\bar{e}}(\xi(\eta)) - \frac{\bar{S}^{*}_{kij}(\xi')}{J^{\bar{e}}(\xi')\,(\xi(\eta)-\xi')} Y^{\bar{e}l}_{,\xi}(\xi^{\bar{e}}_P,\xi') \right] J^{l}(\eta) d\eta + \tag{D.13}$$

$$+ \frac{\bar{S}^{*}_{kij}(\xi')}{J^{\bar{e}}(\xi')} Y^{\bar{e}l}_{,\xi}(\xi^{\bar{e}}_P,\xi') \left[\fint_{-1}^{1} \frac{1}{\xi-\xi'} d\xi - \fint_{-1}^{1} \frac{J^{\bar{l}}(\eta)}{\xi(\eta)-\xi'} d\eta \right]$$

where $\bar{l}$ represents the complementary non-singular part of the element, i.e., $\bar{l} = a$ if $l = b$ or $\bar{l} = b$ if $l = a$.

E Regularisation of kernel with singular traction enrichment

The integral kernels containing only non-singular terms can be computed using Gauss-Legendre quadrature, with the accuracy of the integration depending on the number of gauss points used in the quadrature. However, the integral over tip elements on the interface, which contains the traction enrichment in Eq. (6.16), must be firstly regularised since the enrichment function is singular at the $\rho = 0$. Without loss of generality, considering a tip element at the upper material, the integral is written as:

$$\tilde{U}_{iM}^{e\lambda I} = \int_{-1}^{1} U_{ij}^{*}(\mathbf{x}', \mathbf{x}(\hat{\xi})) R_{jk}^{\lambda} \varpi_{kM}^{I}(\mathbf{x}^{\lambda}, \mathbf{x}(\hat{\xi})) J^{e}(\hat{\xi}) d\hat{\xi} \tag{E.1}$$

To remove the singularity at the crack tip ($\hat{\xi} = -1$), the following variable $\eta \in [-1, 1]$ can be defined:

$$\hat{\xi}(\eta) = \frac{1}{2}\left(\eta^2 + 2\eta - 1\right) \tag{E.2}$$

Then, the integral kernel in Eq. (E.1) can be rewritten as:

$$\tilde{U}_{iM}^{e\lambda I} = \int_{-1}^{+1} U_{ij}^{*}(\mathbf{x}', \mathbf{x}(\eta) R_{jk}^{\lambda} \varpi_{kM}^{I}(\mathbf{x}^{\lambda}, \mathbf{x}(\eta)) J^{e}(\eta) \left(\eta + 1\right) d\eta \tag{E.3}$$

The above expression can be computed following the steps below:

1. Take an integration point to be η
2. Compute the coordinate $\hat{\xi}$ with Eq. (E.2)
3. Define the coordinates $\mathbf{x}(\hat{\xi})$, the Jacobian $J^{e}(\hat{\xi})$ and the fundamental solution $U_{ij}^{*}(\mathbf{x}', \mathbf{x}(\hat{\xi}))$ at the coordinate $\hat{\xi}$
4. Compute the distance from the tip $\rho := \left\| \mathbf{x}(\hat{\xi}) - \mathbf{x}^{\lambda} \right\|$ and determine the enrichment function $\varpi_{kM}^{I}(\mathbf{x}^{\lambda}, \mathbf{x}(\hat{\xi}))$
5. Evaluate the integrand of Eq. (E.3) and multiply it by the weight corresponding to the integration point. Increment the value of the integral
6. Take the next integration point η and return to 2

If the tip element contains the source point, Telles' transformation (Section (C.2)) can be used to regularise the weakly singular integrand that appears due to the singularity of the fundamental solution U_{ij}^{*}. Note that since discontinuous NURBS are adopted to model the crack and interface surfaces, there is no collocation point at the crack tip ($\rho = 0$). Therefore, the singularity arising from U_{ij}^{*} when the tip element contains the source point $\mathbf{x}'$ does not occur at the same singular point of ϖ_{kM}^{I}.